KINETICS OF THE FORMATION OF MAGNESIUM ALUMINATE INCLUSIONS

KINETIC MODELLING FOR THE FORMATION OF MAGNESIUM ALUMINATE INCLUSIONS IN THE LADLE METALLURGY FURNACE

By

ALAN GALINDO, B. Eng.

A Thesis Submitted to the School of Graduate Studies

in Partial Fulfilment of the Requirements for the Degree

Master of Applied Science

McMaster University

MASTER OF APPLIED SCIENCE (2015)

Department of Materials Science and Engineering

McMaster University

Hamilton, Ontario, Canada

TITLE: Kinetic modelling for the formation of Magnesium Aluminate Inclusions in the Ladle Metallurgy Furnace

AUTHOR: Alan Galindo
B. Eng. (Materials Engineering, Instituto Tecnólogico de Querétaro, Mexico)

SUPERVISOR: Dr. Gordon A. Irons

NUMBER OF PAGES: xxx, 307

Abstract

Magnesium aluminate spinel inclusions are a concern in the steelmaking industry since these particles affect the processing and the properties of steel. During the refining of low carbon aluminum killed steel in the ladle furnace; the initial alumina inclusions shift their composition towards higher contents of MgO and eventually they become magnesium aluminate spinel inclusions.

This research developed a kinetic model for the transformation of alumina inclusions to spinel in liquid steel. The aspects of simultaneous deoxidation and of solid state cation counterdiffusion were addressed in the model.

Coupling the model for spinel inclusions to a kinetic model for the slag-steel reactions in the ladle furnace allowed verifying the modeled concentrations in the inclusions with the plant data measurements of ArcelorMittal Dofasco operations. Good agreement between the experimental and calculated Mg contents in the inclusions was obtained for most of the industrial heats analyzed.

Finally, a sensitivity analysis of the coupled kinetic model was performed to compare the effect of the different processing conditions and mass transfer rates on the amount of Mg and spinel in the inclusions. Several results from this work indicate that the rate limiting step on the formation of magnesium aluminate spinel inclusions is the supply rate of dissolved [Mg] from the slag-steel reaction; the supply of [Mg] is in turn controlled by the changes at the slag-steel interface.

Acknowledgements

Thanks to life and its incredible ways and wisdom for giving me the opportunity of pursuing this research project and for allowing me to live this unforgettable academic, professional and personal experience.

I am extremely grateful with my supervisors for giving me the opportunity of working on this Master's research project. The outcomes of this thesis are not only academic and scientific but also there are life lessons and there is the personal growth that I gained during this research to become a better engineer and a better person.

I am truly thankful with my supervisor Dr. Gordon Irons for his continuous and active guidance and assistance during the course of my research at the university. I really value and appreciate the freedom, confidence and trust that Dr. Irons gave me during the development of the kinetic model for the inclusions. Also, the results of this thesis project were possible thanks to all the weekly meetings that we had for academic discussion.

I appreciate and thank the analysis and discussions that I had with my co-supervisor Dr. Kenneth Coley; his comments and observations were very helpful on the implementation of the coupled kinetic model.

I would like to thank to my co-supervisor Dr. Stanley Sun from ArcelorMittal Dofasco for his observations and his support on the several enquires that I made

about the characteristics of the industrial process and the procedures for sampling and measurement of the ladle furnace operations. The inputs from his industrial experience were very important for this research.

The assistance regarding the industrial process and plant measurements that Liao Dongsheng from ArcelorMittal Dofasco offered is also acknowledged and appreciated.

I appreciate and thank the discussions about my project that I had with Dr. Dmitri Malakhov and Dr. Anthony Petric, both professors from the MSE department at the university. Their observations and comments were useful and helpful for this project.

I want to thank and acknowledge to Dr. Diego Ayala for his very helpful comments and discussions on the numerical solution of the diffusion equation for the inclusions and on the numerical implementation of the boundary conditions. The inputs from his observations oriented the mathematical strategies of the kinetic model for the inclusions in the right direction.

The financial supports provided by the Natural Sciences and Engineering Research Council of Canada (NSERC) and by the National Council for Science and Technology of Mexico (CONACYT) are greatly appreciated.

Thanks to my supervisors Dr. Irons and Dr. Coley for giving me the opportunity of attending the 6th International Congress on the Science and Technology of

Steelmaking (ICS 2015) in Beijing, China. It was a great experience for me to give an oral presentation of my research project at an international conference.

As a very important mention, I deeply appreciate and thank all the moral support and constant encouragement that I received from my family throughout all the time that I was working on my master's project. Thanks to my mom, my sister, my brother and my dad. The values, principles and the lessons that my family taught me were key reminders and references to complete this project.

Thanks to all the friends and nice people that I met at the university and in the city of Hamilton. Their company, the conversations, the celebrations, the projects, the activities and the stories that we shared made me remember that acquiring good and happy memories with other people is a very important part of being alive.

Most importantly, I dedicate this research work and effort to all the people in the world that in recent decades have been affected on their quality of life or that have suffered abuses and violations to their human rights because of the social inequality and economic inequality that exists and that has been increasing in our society. During my time doing this project, I realized that there are many people that will enthusiastically collaborate with their knowledge on science and technology to provide real alternatives and solutions to the severe challenges of our current human society. I have faith on myself and on the persons that live in the world, independently of their origin and occupation, in that we can work and progress to assure the justice and the respect that all human lives must receive.

Contents

List of figures

Chapter 2

Chapter 3

Chapter 4

List of tables

Chapter 4

List of symbols

$*$	Indicates a value at the contact interphase between two phases
$,$	Value at the phase boundary between the unreacted Al_2O_3 core and the spinel product layer
a_i	Activity of component *i*
A	Reaction area [m^2]
b	Indicates a value at the bulk of the phase
b_i	Mobility of species *i*
C_i	Molar concentration of species *i* [mol/m^3]
C_S'	Modified sulphide capacity in the slag
Cv_m	Total molar concentration of the metal phase [mol/m^3]
Cv_{sl}	Total molar concentration of the slag phase [mol/m^3]
D_i	Diffusivity of component *i* [m^2/sec]
d	Particle diameter [m]
f_i	Activity coefficient of dissolved species *i* in liquid steel
F	Faraday's constant [C/mol]
f_A	Correlation factor for diffusion of cation A as component
h_i	Henrian activity of the dissolved species *i* in liquid steel
h	Radial distance between two consecutive discretizing nodes [mm]
$Inclus$	Inclusions
J_i	Molar flux of species *i* [$mol \cdot m^{-2} \cdot s^{-1}$]
K	Equilibrium constant of reaction
k_m^i	Mass transfer coefficient of the dissolved species *i* in steel [m/s]
k_{sl}^i	Mass transfer coefficient of the species *i* in slag [m/s]

L_s	Equilibrium partition coefficient for desulphurization with the slag, $L_s = \frac{(wt\%\ S)^*}{[wt\%\ S]^*}$.
L'_s	Equilibrium partition coefficient for desulphurization with the slag, $L'_s = \frac{(X^*_{S,sl})}{[X^*_{S,st}]}$.
M	Metallic species in the steel
$\%Mg$	Calculated total atomic percentage of Mg in the inclusions
Mw_i	Molecular weight of species *i* [gr/mol]
M_xO_y	Oxide component in the slag
n_i	Number of moles of component *i* [mol]
$n_{Oxygen-bonded}$	Moles of oxygen bonded to the oxide inclusions [mol]
N_i	Mass transfer rate of species *i* [mol/sec]
N_p	Total number of particles/inclusions in the steel
O_{inclus}	Content of oxygen chemically bonded to the inclusions [ppm]
O_T	Total oxygen content in the steel [ppm]
Q	Argon gas flowrate [Nm^3/sec]
r	Radial distance in the inclusions [m]
R	Gas constant [$J \cdot mol^{-1} \cdot K^{-1}$]
r_M	Rate of addition of spinel lattice molecules at the steel-inclusions interface [mol/sec]
Sl	Slag
Sl_{mass}	Total mass of slag in the ladle [kg]
St	Steel
St_{mass}	Total mass of steel in the ladle [kg]
T	Temperature [K]
t	Time [sec]
Tol	Mathematical tolerance in the numerical method

Δt_q	Time step for the time integration of the kinetic model [sec]
t_q	Time coordinate in the kinetic model [sec]
U_i	Spatial and time discretization node for the concentration of Mg^{2+} in the spinel product layer, $C_{Mg^{2+}}(i,q) = U(r_i, t_q)$
V	Volume of the phase [m^3]
v_i	Velocity of species i [m/sec]
V_m	Molar volume [m^3/mol]
$[wt\%\ i]$	Weight percent of dissolved species *i* in steel
$(wt\%\ i)$	Weight percent of component *i* in the slag
X_i	Molar fraction of component *i*
z_i	Net charge of species *i*
δ	Index for Mg in the nonstoichiometric magnesium aluminate spinel $Mg_\delta Al_\nu O_4$
ε	Effective gas stirring energy [W/tonne]
ε_i^j	First order interaction parameter of Wagner's thermodynamic formalism
γ_i	Activity coefficient of component *i*
η_i	Electrochemical potential of the charges species *i* [J/mol]
φ_i	Electrical potential of component *i* [J/C]
μ_i	Chemical potential of component *i* [J/mol]
ν	Index for Al in the nonstoichiometric magnesium aluminate spinel $Mg_\delta Al_\nu O_4$
ρ	Density [Kg/m^3]
ρ_i^{ij}	Second order interaction parameter of Wagner's thermodynamic formalism
ξ	Position coordinate with respect to the immobile oxygen lattice in spinel

Declaration of Academic Achievement

This master's thesis was written by Alan Galindo under the supervision of Dr. Gordon Irons. The committee members and co-supervisors of this research project were Dr. Kenneth Coley and Dr. Stanley Sun.

The original contribution to this project was made by Alan Galindo and consists on the theoretical analysis and mathematical development of a kinetic model for the transformation of alumina inclusions to magnesium aluminate inclusions in liquid steel. A computational program with the kinetic model for the inclusions was also developed by Alan Galindo. The kinetic model for spinel inclusions was coupled to the kinetic model for slag-steel reactions of Graham & Irons (2010). The results of the coupled kinetic model were verified with the processing conditions and plant data measurements made by Graham (2008) at ArcelorMittal Dofasco. This work also obtained a sensitivity analysis of the coupled kinetic model that identifies the main processing parameters and conditions that affect the formation of spinel inclusions.

The supervisor of this research project Dr. Gordon Irons participated actively on offering guidance, orientation and discussion analysis to achieve the objectives of this research. Dr. Coley gave important inputs and suggestions on the development of the coupled kinetic model. Dr. Stanley Sun provided information and insights relevant to the industrial aspects of the metallurgical process being modeled as well as on the plant data measurements.

The description of the coupled model for spinel inclusions and some of the results from this work were presented as conference papers and oral presentations at the 6th International Congress on the Science and Technology of Steelmaking (ICS 2015, Beijin, China) and at the symposium Challenges and Transformative Solutions to Sustainable Steelmaking and Casting For Environment-Friendly Metallurgical Innovation (CTSSC-EMI 2015, Tokyo, Japan).

All the chapters and appendices of this thesis were written by Alan Galindo. The complete document was reviewed and approved by all the committee members.

But now he pays attention, he notices something about the bush that he thinks he has missed those other times. How tangled up in itself it is, how dense and secret. It's not a matter of one tree after another, it's all the trees together, aiding and abetting one another and weaving into one thing. A transformation, behind your back.

– Alice Munro, *Too Much Happiness*

The aim of life is not to prosper, but to transform oneself. When you launch yourself into the unknown is when you are saved

– Elena Poniatowska, *Leonora*

Textbooks and Heaven only are Ideal;
Solidity is an imperfect state.
Within the cracked and dislocated Real
Nonstoichiometric crystals dominate.

– John Updike, *The Dance of the Solids*

Chapter 1

Introduction

1.1 Background of the research

Non-metallic inclusions are always present in steel. These particles vary in terms of amount, size, morphology, source and chemical composition. In this aspect, the concept of clean steel refers to the steel for which the population and type of non-metallic inclusions does not affect the properties and performance of that steel in a specific application.

In the case of Low Carbon Aluminum Killed steels, most of the found non-metallic inclusions are oxides. These oxide inclusions form during the refining of liquid steel in the Ladle Metallurgy Furnace. At the beginning of the process aluminum is used to deoxidize the liquid steel and the immediate products of this reaction are solid alumina inclusions.

Reported industrial observations indicate a change in the inclusions composition during ladle treatment of aluminum killed steels. The alumina inclusions increase their content of magnesium and transform into solid magnesium aluminate spinel inclusions. This formation of magnesium aluminate spinel inclusions represents a concern and issue that affects both the processing of liquid steel and the properties of the solidified end products.

Although several laboratory studies have been made on the formation of spinel inclusions, there are just a few reported projects that consider the variations in the industrial process. In general, steelmaking metallurgists agree on the strong effect that the ladle slag composition has on the formation of spinel inclusions.

In this work a kinetic model for the slag-steel reactions in the ladle furnace was extended to include the transformation of alumina inclusions to magnesium aluminate spinel inclusions. The applicability of the model was then evaluated by comparing the model results with industrial measurements. This research aims to further understand the processing conditions and factors that promote the formation of spinel inclusions during ladle treatment of liquid steel.

1.2 Objectives of the research

The objectives of this research project are:

- Develop a mathematical kinetic model for the transformation of alumina inclusions to magnesium aluminate spinel inclusions in liquid steel.
- Couple the model for spinel inclusions to a kinetic model for the slag-steel reactions during ladle treatment of steel.
- Use the processing parameters from the industrial operations at ArcelorMittal Dofasco to verify the coupled kinetic model. This verification is made by comparing the calculated composition of the inclusions with the respective industrial analysis of the inclusions.

- Perform a sensitivity analysis of the coupled kinetic model in order to prioritize the impact of the different conditions and factors involved in the formation of spinel inclusions during refining of steel in the ladle furnace.

1.3 Outline of the thesis

This thesis is divided in five chapters. The present Chapter 1 introduces and describes the topic of this research and the main objectives of pursuing this thesis work.

A literature review of the topics from Secondary steelmaking that are involved in the refining of low carbon aluminum killed steel is part of Chapter 2. The state of the art on the thermodynamics and kinetics of magnesium aluminate inclusions formation is also in this chapter. The main concepts of the kinetic theory for the solid state formation of spinel type oxides are mentioned. Finally, the literature review includes a general description of the previously developed kinetic model for slag-steel reactions.

Chapter 3 explains the proposed kinetic model for the transformation of alumina inclusions to spinel. This model considers only the thermodynamic and kinetic interaction of the dissolved [Mg], [Al] and [O] in steel with the inclusions. The detailed mathematical analysis for the calculations in the model are in Appendices A and B.

Chapter 4 describes the methodology to couple the model for the inclusions to the kinetic model for slag-steel reactions in the ladle furnace. The modeling of industrial refining heats in the ladle furnace and the further comparison with the sampled compositions of the slag, steel and inclusions is discussed. For the seven industrial heats analyzed, the details on their processing conditions, model results and industrial measurements are in Appendix C. Finally, Chapter 4 includes a sensitivity analysis of the coupled model for spinel inclusions formation. The effects of several processing conditions and of the diffusion and mass transfer parameters are compared.

Chapter 5 summarizes the main conclusions and results, suggestions for future work are also included.

Chapter 2

Literature Review

2.1 Secondary Steelmaking and Steel cleanliness

2.1.1 Process Metallurgy of Steelmaking

Modern Steel production is composed of several stages known as ironmaking, steelmaking, casting, hot rolling and finishing. For steelmaking metallurgy it is possible to differentiate the two main practices to obtain crude steel: Oxygen Steelmaking and the Electric Arc Furnace (EAF). Both processing routes vary on the raw materials used, the methods to transform them and the production scales, Figure 2-21.

Integrated Steelmaking plants produce liquid hot metal by reducing iron ore in the Blast Furnace. Afterwards, the hot metal and steel scrap are charged into the Oxygen Converter in order to obtain low-carbon molten steel. In the case of the Electric Arc Furnace route, the main function of the EAF is to melt the charge to produce molten steel. Most of the EAF operations work only by recycling steel scrap, however depending on the availability of the scrap some plants may use other materials like direct reduced iron (DRI), solid pig iron or hot metal in the charge.

Primary Steelmaking refers then to the production of molten steel from either the Oxygen Converter or the EAF. Even though this crude steel is low in

carbon, it contains high concentrations of dissolved impurities like sulphur and oxygen that must be removed. Additionally, adjustments in the chemical composition and temperature of the steel are required before it is teemed into the Tundish for continuous casting and solidification.

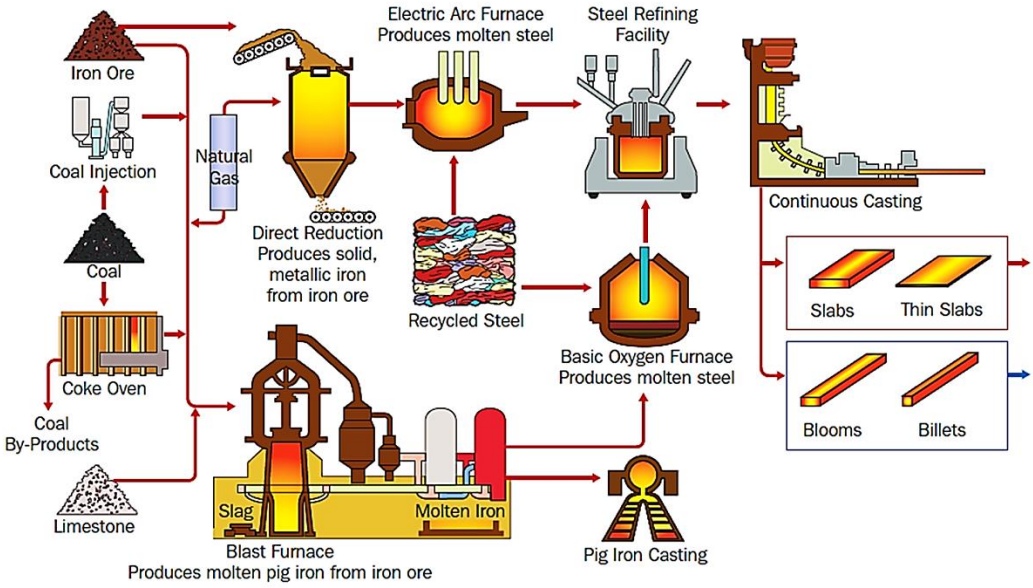

Figure 2-1. Processing routes in modern Ironmaking and Steelmaking. (AISI, Technology Roadmap Research Program for the Steel Industry, Final Report, 2011.)

All the different processes applied to the liquid steel in the ladle before casting it are known as Secondary Steelmaking or Ladle Metallurgy. The detailed objectives of Secondary Steelmaking are (Lange, 1988) :

i. Homogenization of the steel in terms of temperature and composition

ii. Alloying and chemical compositional control within narrow limits

iii. Desulphurization, deoxidation, inclusions control, improvement of steel cleanliness, dephosphorization.

iv. Decarburization

v. Degassing for hydrogen removal and nitrogen control

vi. Attainment of prescribed teeming temperatures within narrow limits

vii. Acting as a buffer between primary steelmaking and the casting unit.

Furthermore, the industrial installations where Secondary Metallurgy tasks are performed can be divided into processes with and without application of vacuum.

2.1.2 Treatment of steel in the Ladle Metallurgy Furnace

One of the most common processes in Secondary Metallurgy is the Ladle Metallurgy Furnace (LMF); mostly because this unit is an excellent place to desulphurize with the slag, carry out Ca - treatment, and to make other alloying and trimming additions (Holappa, 2014).

After the liquid steel coming from primary steelmaking is tapped into the ladle, a new non-oxidizing synthetic slag is formed; this top slag protects the steel against the oxidizing atmosphere and participates in the refining operations. Homogenization is obtained typically by injecting argon from the bottom of the ladle; however some plants apply electromagnetic stirring instead. The processing temperature is maintained by heating with graphite electrodes, Figure 2-2. The LMF station is also used to incorporate alloying elements to the steel, basic

alloying is performed during tapping of the steel and minor additions are then made during the ladle treatment.

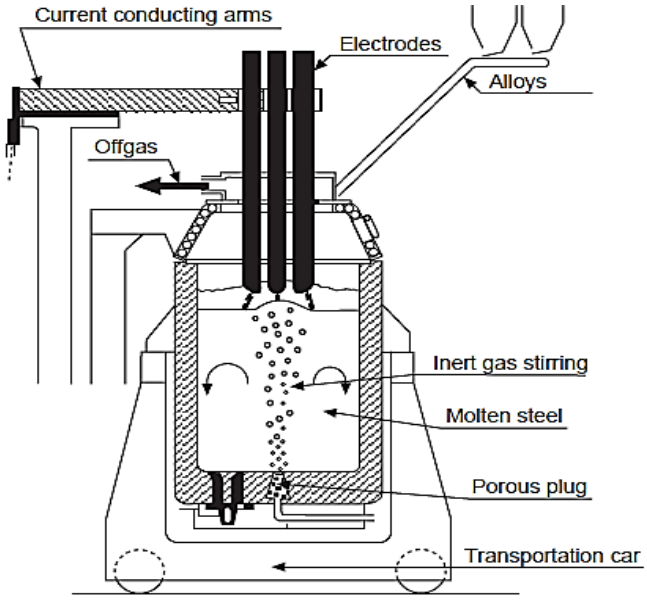

Figure 2-2. Scheme of the Ladle Metallurgy Furnace (Kor & Glaws, 1998)

Most Ladle Metallurgy furnaces are equipped with devices for controlled additions which are based on steel sampling. For small alloy additions, wire-injection is generally used.

2.1.2.1 Deoxidation

After the Oxygen Converter or the EAF processes, the content of dissolved oxygen in the liquid steel [O] goes from 200 to 800 ppm. However once steel solidifies the solubility of oxygen drops drastically, for Austenite at 1773 K it is 30 ppm or less. Therefore, during solidification the dissolved oxygen cannot

stay in the solid phase and it diffuses to the remaining liquid where it increases its concentration; oxygen then reacts with the dissolved carbon according to:

$$[\mathrm{C}] + [\mathrm{O}] = \mathrm{CO}_{(g)} \tag{2-1}$$

The steel that is not deoxidized is said to be 'unkilled', and contains porosity because of the CO gas formed during solidification. Furthermore, most steel production requires fully deoxidized grades; these are 'killed' steels without CO porosity, which is a key requirement if the continuous casting process is used. In order to lower the oxygen dissolved, strong deoxidizing elements are required. The most common industrial practice is to use aluminum for the production of killed steels; this is because aluminum is an efficient and low cost element to attain values from 2 to 6 ppm of dissolved oxygen.

From a thermodynamic point of view when deoxidation is carried out by addition of only one deoxidizer is referred to as 'simple' and when more than one deoxidizer is used it becomes a process of 'complex deoxidation' (Ghosh, 2000). The reaction for the simple deoxidation is represented as:

$$\mathrm{x[M]} + \mathrm{y[O]} = \left(\mathrm{M_X O_y}\right) \tag{2-2}$$

Where [M] is the dissolved deoxidizer and $\left(\mathrm{M_X O_y}\right)$ is the deoxidation product, the respective heterogeneous equilibrium is:

$$K_{M-O} = \frac{\left(a_{M_X O_y}\right)}{[f_M \cdot wt\%M]^x [f_O \cdot wt\%O]^y} \tag{2-3}$$

Values for the deoxidation constants K_{M-O} as a function of temperature have been measured and reported, while in the case of a multicomponent alloy such as liquid steel, the henrian activity coefficients f_M and f_O can be calculated from the Wagner formalism of interaction in dilute solutions (Hino & Ito, 2010).

While thermodynamics provides information about the lowest equilibrium concentration of oxygen that can be obtained, the kinetics of the process are important to know how the deoxidation products grow and are removed from the melt. A practical indirect measurement to follow the kinetics of deoxidation is the Total Oxygen, this value is the sum of the free dissolved oxygen and the oxygen combined in the non-metallic inclusions; these inclusions are mostly the deoxidation products. The general process of deoxidation, Figure 2-3, can be divided in the following stages, (Holappa, 2014):

i. addition, melting, and dissolution of the deoxidizing element(s) into the steel
ii. chemical reaction with dissolved oxygen, nucleation of oxide inclusions
iii. diffusion growth of inclusions
iv. collision growth of inclusions
v. separation and removal of inclusions to the top slag and refractory walls

In practice, the dissolved oxygen decreases rapidly due to chemical reaction and nucleation, the slowest and most critical step to reduce the total oxygen content is the removal of inclusions from the liquid steel.

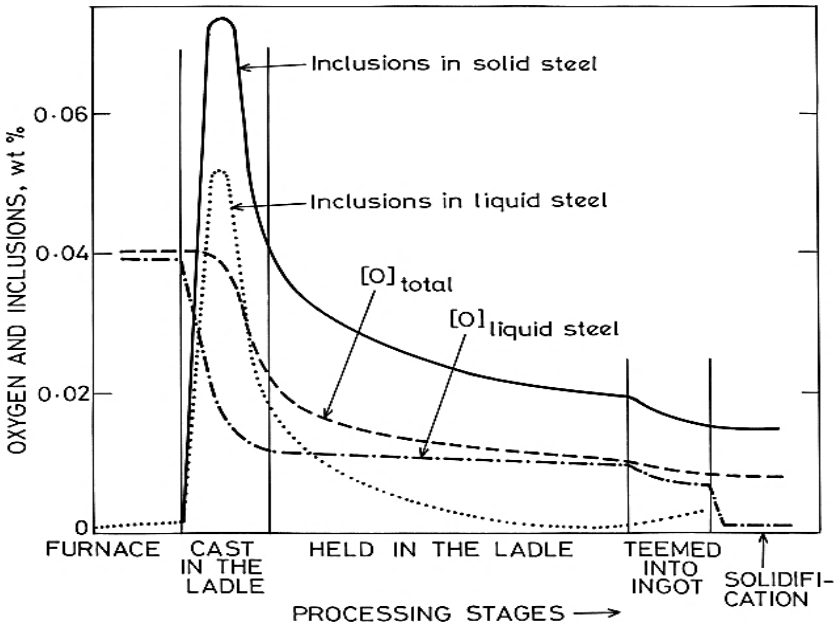

Figure 2-3. Oxygen and inclusions content during deoxidation(Ghosh,2000)

2.1.2.2 Desulphurization

Dissolved sulphur concentrations at the end of the EAF process ranges from 150 to 400 ppm and 100 to 200 ppm if the steel comes from the Oxygen Converter. Because of the detrimental effects of the sulphide inclusions on the mechanical and corrosion properties of steel, sulphur contents below 20 ppm are generally required. The mechanisms and technologies for desulphurization have been extensively reviewed (Ghosh, 2000; Lehmann & Nadif, 2011). In the Ladle Furnace, steel desulphurization with the top slag occurs as an electrochemical exchange reaction at the slag-steel interface according to:

$$[S] + (O^{2-}) = (S^{2-}) + [O] \quad (2\text{-}4)$$

The corresponding equilibrium is:

$$K_{(2-4)} = \frac{(\gamma_{S^{2-}})(wt\%S\,)[h_O]}{[f_S \cdot wt\%S](a_{O^{2-}})} \tag{2-5}$$

The equilibrium distribution of sulphur between the slag and the steel L_S is then:

$$L_S = \frac{(wt\%S)^*}{[wt\%S]^*} = \frac{K_{(2-4)}\,(a_{O^{2-}})\,f_S^*}{(\gamma_{S^{2-}})[h_O^*]} = \; C_S' \cdot \frac{f_S^*}{[h_O^*]} \tag{2-6}$$

Where C_S' is known as the modified sulphide capacity and it represents the ability of the slag to absorb sulphur. The sulphide capacity is an intrinsic property of the slag that at a given temperature depends only on the slag composition; specifically, the sulphide capacity increases with a higher slag basicity. Higher values of the sulphur distribution are beneficial for desulphurization; therefore expression (2-6) demonstrates the importance of having a low oxygen potential at the slag-steel interface, this is achieved with a well deoxidized steel and low contents of easily reducible oxides in the slag, specifically FeO and MnO since these components supply oxygen to the steel.

The kinetics of many reactions at steelmaking temperatures is mass transfer controlled; this is because the chemical reactions are very fast. According to the theory and concepts of desulphurization kinetics, the removal of [S] by using a top slag in the ladle follows a first-order reversible process if the processing conditions provide large values of the equilibrium partition coefficient L_S, (Deo & Boom, 1993; Ghosh, 2000). Therefore, the equation for the change in the bulk content of sulphur can be written as:

$$\frac{d[wt\%S]}{dt} = -\frac{k_m \cdot A}{V}\left[[wt\%S] - \left[wt\%S_{equilib}\right]\right] \quad (2\text{-}7)$$

The rate constant k_m is the mass transfer coefficient for sulphur in the liquid metal [m/sec] and it is a function of the stirring intensity, A is the slag-steel interfacial area [m^2] and V is the volume of the steel [m^3]. For interphase mass transfer between the steel and the slag in ladles, it has been noted that in general the $k_m \cdot A$ value is a function of the stirring power ε.

2.1.2.3 Gas stirring in the ladle furnace

Stirring with argon bubbling in ladles has several purposes: homogenization of the composition and temperature in the melt, steel cleanliness improvement by removal of inclusions and it also promotes mass transfer for the slag-steel reactions. The moderate argon flow rates in the LMF are obtained using porous refractory plugs located in the bottom of the ladle. Homogenization is caused by the dissipation of the buoyant energy of the injected gas, where the effective stirring energy or effective stirring power ε [W/tonne] can be calculated for example with the expression derived by Pluschkell, (Pluschkell, 1981):

$$\varepsilon = \left(\frac{101330}{273}\right) \cdot \left(\frac{Q \cdot T}{M}\right) \cdot ln\left(1 + \frac{\rho \cdot g \cdot h}{101330}\right) \quad (2\text{-}8)$$

M is the total mass of steel, Q is the Argon gas flow rate [Nm^3/sec], T is the temperature in Kelvin degrees, ρ is the steel density [kg/m^3] and h is the depth of gas injection [m].

When gas stirring is used, the slag-steel interfacial area is affected by the degree of agitation in the bath which is determined by the stirring power. Additionally, it has been noted that in general, for interphase mass transfer between the slag and steel, the capacity coefficient of mass transfer $k_m \cdot A$ increases with the gas flow rate Q, and since the stirring energy ε is proportional to Q, the expression is formulated as:

$$k_m \cdot A \propto \varepsilon^n \tag{2-9}$$

Several correlations for the $k_m \cdot A$ values between two liquids as a function of ε have been reported, the case of desulphurization with top slag has also been analyzed. These correlations specify the conditions and flow rate ranges to be used, however it is important to stress out that all these correlations are empirical Furthermore, the mass transfer coefficients in the slag phase do not only depend on the stirring energy but also on the properties of the slag.

2.1.3 Non-Metallic Inclusions and Clean steel

2.1.3.1 Origin and classification of inclusions

Non-metallic inclusions are particles that are present in steel and alloys. By their composition, non-metallic inclusions are classified as oxides, sulfides, oxy-sulfides, nitrides, carbides and carbonitrides. In terms of their origin, the inclusions that form due to reaction of the dissolved species in the molten steel or during solidification are called “indigenous”; if the particles form in solid steel

then they are “precipitates”. Also, during the processing of liquid steel, particles that come from external sources such as erosion of the refractories or slag entrapment are known as “exogenous”. In general, indigenous inclusions are small, numerous, uniformly distributed and their composition depends on the grade of steel processed, exogenous inclusions on the contrary are larger and scarce (Ghosh, 2000).

The amount and type of non-metallic inclusions has great relevance because it affects different properties in steel (Holappa & Wijk, 2014). In this sense, inclusions have a direct influence on mechanical properties such as strength and fatigue, ductile and brittle fracture, hot shortness and tearing, welding properties, machinability, surface finishing and corrosion resistance.

During the refining of Low Carbon Aluminum-Killed (LCAK) liquid steel the sources of non-metallic inclusions are, (Zhang & Thomas, 2003):

i. Deoxidation products, in this case Alumina inclusions are the majority of indigenous inclusions in LCAK steel. Alumina inclusions are dendritic when formed in a high oxygen environment, Figure 2-4a and 2-4b; these inclusions also may form from the collision of smaller particles Figure 2-4c.
ii. Reoxidation products such as alumina are generated when the dissolved [Al] in the liquid steel is oxidized by FeO, MnO, SiO_2 and other oxides in the slag and refractory linings. Exposure of the steel to the atmosphere also produces reoxidation.

iii. Slag entrapment during addition of fluxes forms exogenous liquid inclusions which are usually spherical, Figure 2-4d.

iv. Exogenous inclusions from other sources including loose dirt, broken refractory and ceramic lining. These are large particles with irregular shape and might serve as sites for heterogeneous nucleation of alumina (central particle in Figure 2-4c).

v. Chemical reactions, these are oxide inclusions that initially were alumina but have been modified during the process by reaction with dissolved species in the steel to form complex oxide inclusions.

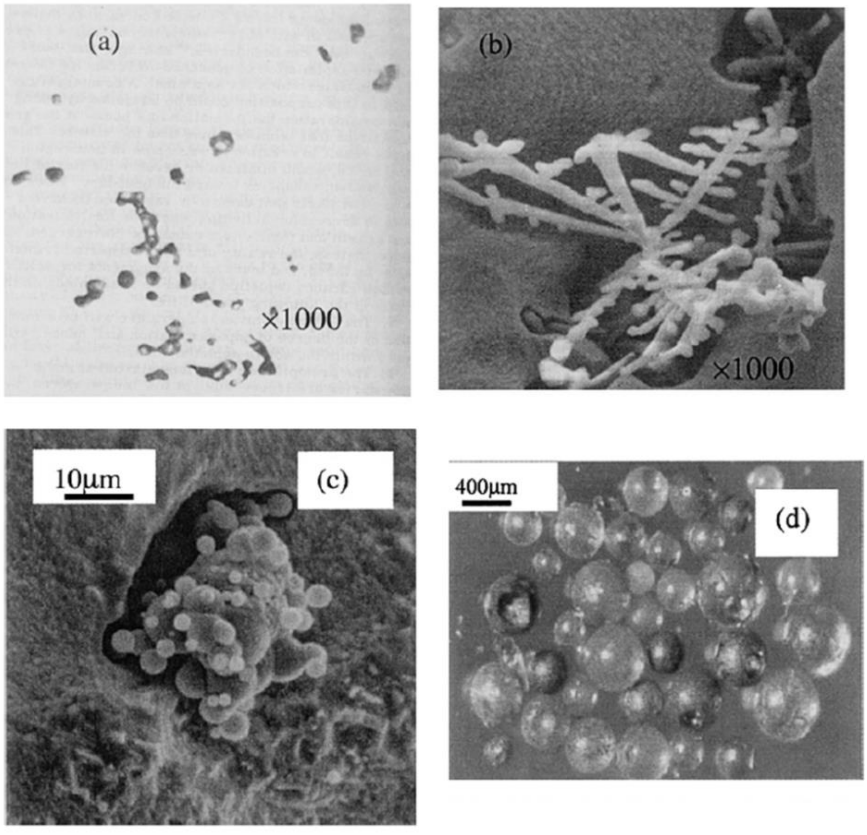

Figure 2-4. Typical inclusions in LCAK steels, (Zhang & Thomas, 2003)

2.1.3.2 Steel Cleanliness control

A definition of steel cleanliness is not the same for all the different steel grades and their end applications. Even though the concept of "clean steel" is closely linked to the amount of non-metallic inclusions in the steel and the concentration of dissolved impurities like [O], [S] and [N]; the concept of clean steel is also related to the type, size, shape and distribution of the non-metallic inclusions, (Holappa & Wijk, 2014). Furthermore, adequate cleanliness implies that the amount and characteristics of the inclusions formed do not affect negatively the properties required for a given steel product.

The assessment of steel cleanliness can be made using direct methods that are more accurate but more expensive or represent difficulties in the sample preparation and indirect methods that are faster and inexpensive but work only as indicators of the cleanliness condition, Figure 2-5. Literature reviews on the characteristics of these methods have been published (Kaushik, et al, 2009; Zhang & Thomas, 2003). A more recent review (Kaushik, Lehmann, & Nadif, 2012) summarizes the tools for cleanliness analysis for use in research and industrial plant studies in order to diagnose the root cause of industrial problems.

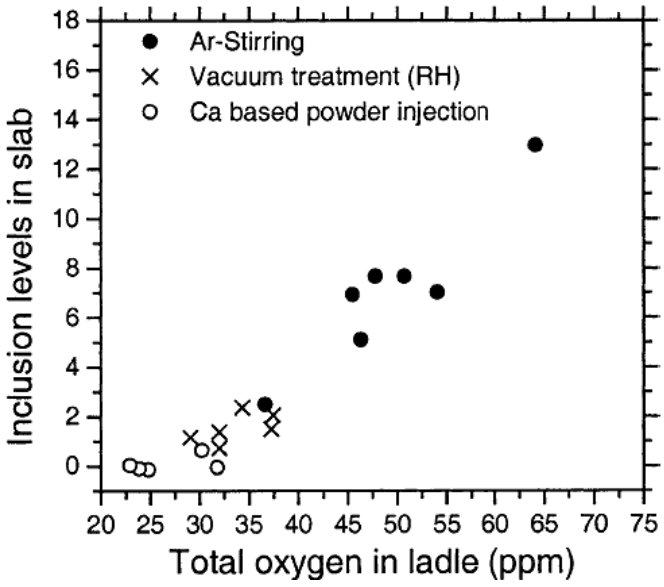

Figure 2-5. Influence of different ladle treatments on the level of inclusions in the cast slab. (Lange, 1988)

Direct methods are techniques based on the characterization of steel samples and include metallographic examination by Scanning Electron Microscope (SEM), Automated SEM microscopy, Optical Emission Spectrometry with Pulse Discrimination Analysis (OES-PDA), Confocal Scanning Laser Microscope, Remelt buttons, Ultrasonic testing and others. These techniques have been more used in the past decade; however the selection of a direct method depends on its applicability either as a test method or an inspection technique during production, the requirements of time and the problem to be solved (Kaushik et al., 2009).

Indirect methods are more commonly used since the information they provide can be used to estimate the steel cleanliness of the heat (Zhang & Thomas, 2003). These methods include total oxygen measurements (O_T) and the

analysis of process variables such as changes in the slag composition, nitrogen pick-up and frequency of clogging of the casting nozzle.

As mentioned by Kaushik et al (2009), cleanliness control practices during steel refining are critical for continuous improvement in the quality of the of the finished products and casting operations. These authors further pointed out that in practice steel cleanliness is measured using an index that can be monitored to realize improvements for process control. Such index must be reliable, repetitive and useful to evaluate the success or failure of a trial for the development and modification of the secondary refining and casting practices.

2.1.3.3 Reoxidation and steel cleanliness in the ladle furnace

In LCAK steel most of the indigenous inclusions are alumina particles that result from the deoxidation process applied after primary steelmaking. However, there are several factors during the secondary refining processes and the casting operations that cause reoxidation of the steel which in turn increases the amount of oxide inclusions and affect the steel cleanliness. During ladle treatment, the two main sources of reoxidation include reaction of the steel with the atmosphere and an oxidized slag (Holappa & Wijk, 2014; Zhang & Thomas, 2003).

Reoxidation due to reaction with the atmosphere occurs when high intensity argon gas stirring is applied and the ascending plume of bubbling gas exposes an area of the liquid steel so the top slag does not cover it, this region is called an ‘open eye’. The eye area has been extensively studied and analyzed in

terms of the stirring parameters (Krishnapisharody & Irons, 2007). When the steel is in contact with the atmosphere, oxygen and nitrogen from the air can dissolve in the steel as impurities, furthermore the extra dissolved [O] can form new oxide inclusions which affect the steel cleanliness.

The top slag is considered to be oxidized when it contains high FeO and MnO concentrations; this occurs if the ladle slag is contaminated with slag carryover from the previous furnaces. These oxides can be easily reduced with the dissolved aluminum [Al] in the steel and thus they generate aluminum loses and produce additional alumina inclusions. Therefore, a higher FeO and MnO content in the slag promotes reoxidation and affect the cleanliness, Figure 2-6.

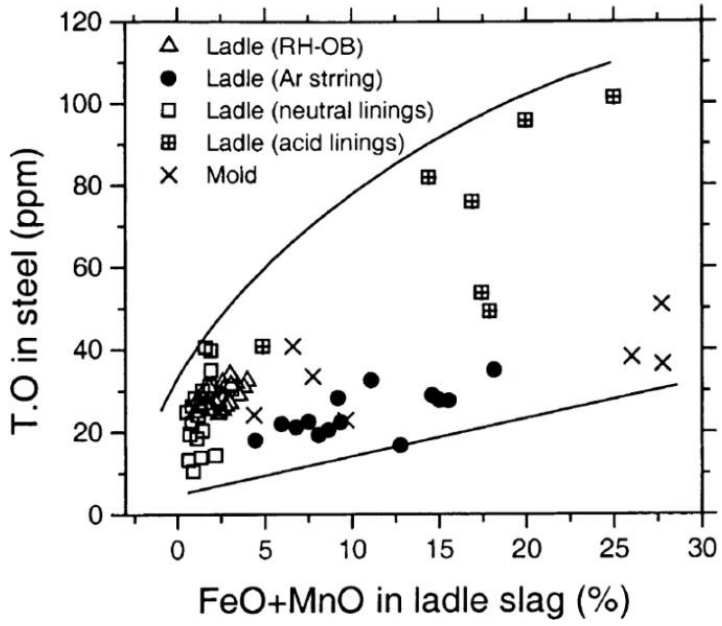

Figure 2-6. Relation between FeO+MnO content and Total Oxygen in the steel for different ladle furnaces and in the casting mold (Zhang & Thomas, 2003).

2.2 Magnesium Aluminate Spinel Inclusions

During the process of deoxidation and desulphurization in the Ladle Metallurgy Furnace, the content of dissolved magnesium [Mg] in the liquid steel increases, leading to a transformation of the initial indigenous inclusions of alumina to Magnesium Aluminate Spinel inclusions $MgAl_2O_4$, Figure 2-7. For ladle treatment of LCAK steel, this change in the inclusions composition has been reported and reviewed by several authors (Graham & Irons, 2010; Pretorius, Oltmann, & Schart, 2013; Story, Smith, & Fruehan, 2004; Yang et al., 2013).

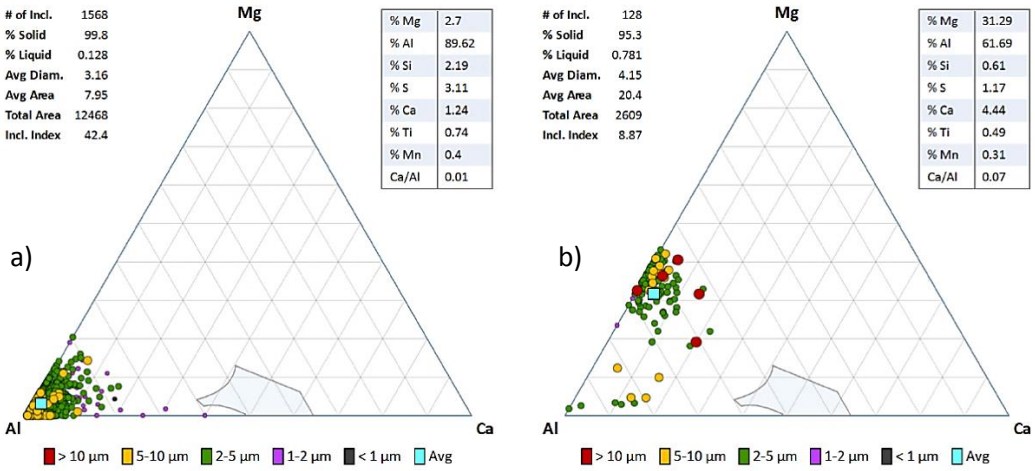

Figure 2-7. Distribution of the inclusions composition. a) Just after Al-deoxidation, b) After desulphurization of the steel. (Pretorius, et al, 2013)

2.2.1 Impact of Magnesium Aluminate Spinel Inclusions on the steel

Magnesium Aluminate Spinels (MA Spinel) as non-metallic inclusions, have negative effects on the properties of the final steel products as well as in the processing of those products (Park & Todoroki, 2010; Yang, Wang, Zhang, Li, & Peaslee, 2012). Because MA spinel inclusions have a high hardness, they cannot

be elongated when the steel is cold formed. Some examples of these defects include a cold rolled 430 stainless steel deoxidized with aluminum; in Figure 2-8 the failure was initiated by oxide particles with the composition of MA spinel. Additionally, the swollen defect appears in the case of deeply drawn products, Figure 2-9, in this case the defect was caused by MA spinel inclusions.

Additionally, MA spinel inclusions affect the continuous casting operations; this problem arises because spinel inclusions tend to adhere to the inner wall of the submerged entry nozzle. The buildup of inclusions can form accretions that reduce the flow of molten steel and even can lead to complete shutdown of operations in the caster due to 'clogging' (Frank, 2001).

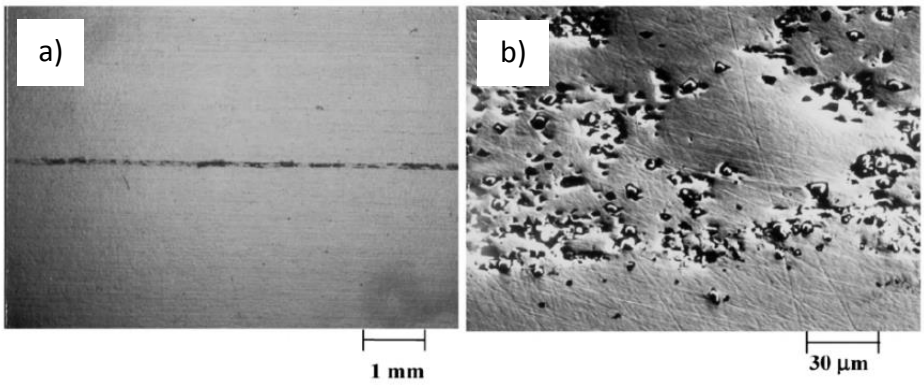

Figure 2-8. a) Sliver defect on the strip surface of a cold rolled steel b) SEM image inside the defect. Inclusions identified as MA spinel.
(Park & Todoroki, 2010)

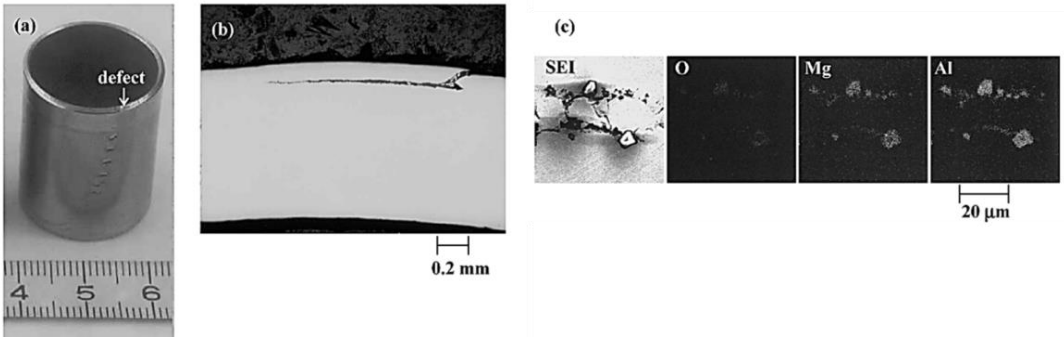

Figure 2-9. a) Swollen defect on a deep-drawn product, b) cross-sectional view, c) element distribution of the inclusions. (Park & Todoroki, 2010)

2.2.2 Thermodynamics of Magnesium aluminate spinel inclusions

The formation of indigenous spinel inclusions can be predicted by the equilibria among the dissolved species [Al], [Mg], [O] and the oxides Al_2O_3 and MgO. The respective deoxidation reactions are:

$$2[Al] + 3[O] = (Al_2O_3) \quad (2\text{-}10)$$

$$[Mg] + [O] = (MgO) \quad (2\text{-}11)$$

Values for the change in the standard Gibbs free energy of reaction as well as the first and second order interaction parameters to calculate the henrian coefficients f_{Al}, f_{Mg} and f_O, have been reviewed thoroughly by the Japan Society for the Promotion of Science (Hino & Ito, 2010), the calculated equilibrium at 1873 K is shown in Figures 2-10 and 2-11. The formalism used to calculate the henrian activity coefficients is the Wagner-Lupis-Elliot formalism (Lupis, 1983).

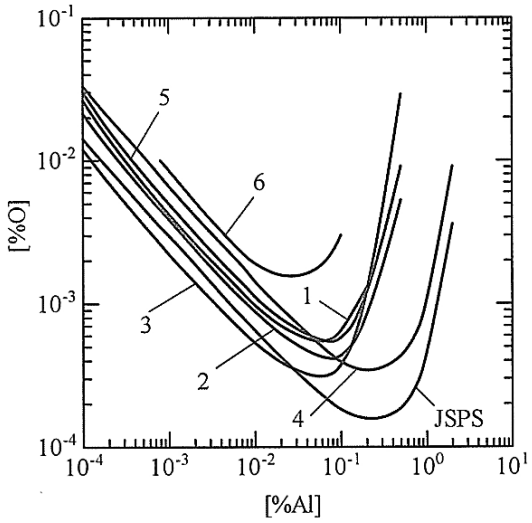

References for Figure 2-10	
JSPS	Hino & Ito, 2010
1	Gustafsson & Mellberg, 1980
2	Cho & Suito, 1994
3	Dimitrov, Weyl, & Janke, 1995
4	Itoh, Hino, & Ban-Ya, 1997
5	Seo, Kim, & Lee, 1998
6	Fujiwara, Hattori, & Ichise, 1999

Figure 2-10. Comparison of values for equilibrium between [%Al] and [%O] in Iron at 1873 K (Hino & Ito, 2010).

The phase diagram of the quasi binary system Al_2O_3-MgO shows that magnesium aluminate spinel is the only intermediate compound, Figure 2-12. Because spinel has a range of nonstoichiometry due to the solubility of Al_2O_3 and MgO in this phase, it is commonly described as $MgO \cdot xAl_2O_3$, where the molar ratio x represents the degree of nonstoichiometry. At steelmaking temperatures (1873 K), x ranges from 0.85 to 2.22.

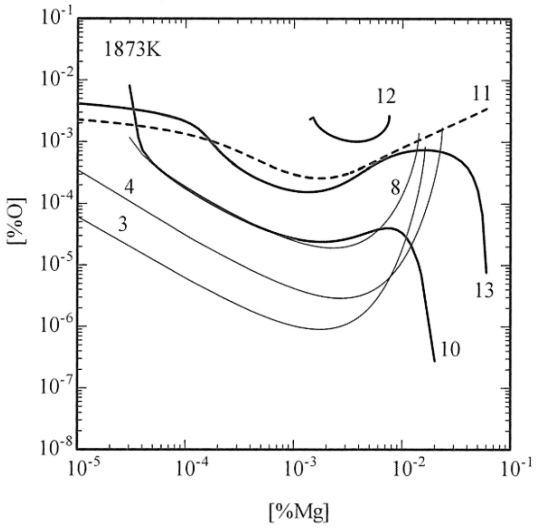

References for Figure 2-11	
3	Gorobets, 1980
4	Kulikov, 1985
8	Inoue & Suito, 1994
10	Ohta & Suito, 1997
11	Itoh et al., 1997
12	Han, Zhou, & Xiang, 1997
13	Seo & Kim, 2000

Figure 2-11. Comparison of values for equilibrium between [%Mg] and [%O] in Iron at 1873 K (Hino & Ito, 2010).

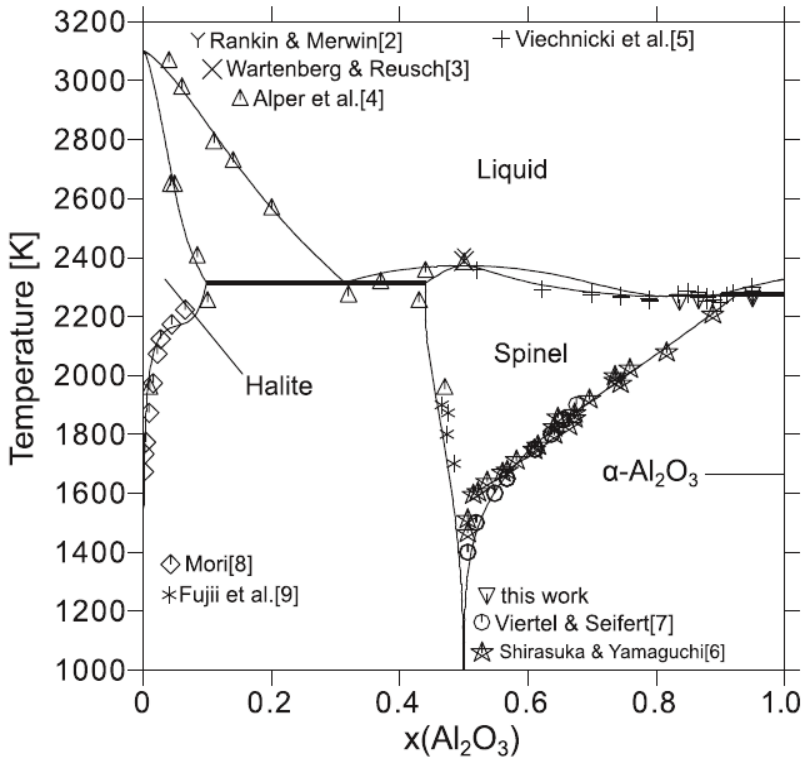

Figure 2-12. Calculated quasi binary system MgO-Al_2O_3 together with experimental data (Zienert & Fabrichnaya, 2013).

For the spinel solid solution, the activities of the components Al_2O_3 and MgO as a function of composition can be obtained by using the different thermodynamic assessments (Hallstedt, 1992; I.-H. Jung, Decterov, & Pelton, 2004b; Zienert & Fabrichnaya, 2013). Experimental values for the change of the component activities in spinel were reported by Fujii et al.(2000) at temperatures of 1800 and 1873 K.

In order to analyze the simultaneous deoxidation equilibrium between MgO, Al_2O_3 and spinel with the [Al], [Mg] and [O] in the steel, several researches have calculated phase stability diagrams (Fujii et al., 2000; Itoh et al., 1997; Jung, et al., 2004; Ohta & Suito, 1997; Seo & Kim, 2000) These phase diagrams are based on thermodynamic evaluations of the {Fe}-[Al]-[Mg]-[O] system considering the different reactions among the components. For the equilibrium between spinel and MgO, two reactions have been proposed (Itoh et al., 1997; Todoroki & Mizuno, 2004):

$$4\mathrm{MgO}\ (\mathrm{s}) + 2[\mathrm{Al}] = \mathrm{MgO} \cdot \mathrm{Al_2O_3}\ (\mathrm{s}) + 3[\mathrm{Mg}] \quad (2\text{-}12)$$

$$\mathrm{MgO}\ (\mathrm{s}) + 2[\mathrm{Al}] + 3[\mathrm{O}] = \mathrm{MgO} \cdot \mathrm{Al_2O_3}\ (\mathrm{s}) \quad (2\text{-}13)$$

For the Al_2O_3 and spinel equilibrium, two reactions have been mentioned:

$$4\mathrm{Al_2O_3}\ (\mathrm{s}) + 3[\mathrm{Mg}] = 3\mathrm{MgO} \cdot \mathrm{Al_2O_3}\ (\mathrm{s}) + 2[\mathrm{Al}] \quad (2\text{-}14)$$

$$\mathrm{Al_2O_3}(\mathrm{s}) + [\mathrm{Mg}] + [\mathrm{O}] = \mathrm{MgO} \cdot \mathrm{Al_2O_3}\ (\mathrm{s}) \quad (2\text{-}15)$$

Itoh et al. (1997) calculated the stability region at 1873 K for spinel and the equilibrium iso-oxygen concentration lines by assuming that the activities of MgO and Al_2O_3 behave ideally in the spinel solid solution, Figure 2-13a. Fujii et al. (2000) considered their experimental results in the calculation of the stability diagram by including the non-ideal variation of the activities of MgO and Al_2O_3 in spinel, Figure 2-13a. Jung et al. (2004) used the associate model formalism for the dissolved species in steel and the FactSage software database (Bale et al., 2009) to produce the phase stability diagram, Figure 2-13b. Based on thermodynamic calculations using the FactSage software Yang, et al., (2012) reported that at the lower temperature of 1773 K the region of stability for spinel increases and the MgO region shrinks.

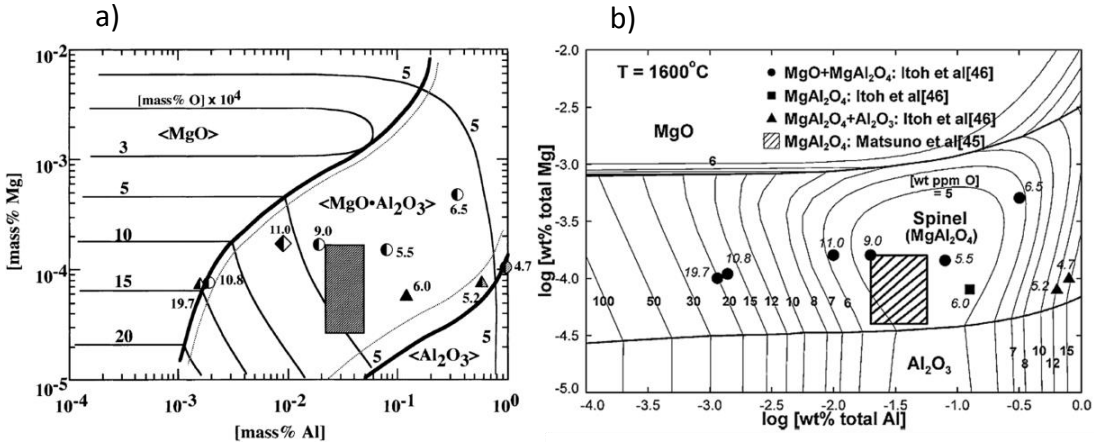

Figure 2-13. Inclusions phase stability diagrams for MgO, Al_2O_3 and spinel formation in liquid steel at 1873 K. a) Fine dotted lines for spinel phase boundaries: Itoh et al., 1997. Bold solid lines: Fujii et al., 2000. b) FactSage group assessment and calculations: Jung et al., 2004.

Additional thermodynamic studies have been reported based on measurements or calculations that aim to analyze the effect of other dissolved species on the spinel formation, for example: high Cr steels (Jo, Song, & Kim, 2002), Ti additions (Ono, et al., 2010) and Ca treatment (Yang et al., 2013).

2.2.3 Sources of spinel inclusions during steelmaking

The transformation of the alumina inclusions to spinel in LCAK steel requires a source of dissolved [Mg]; this is shown in reactions (2-14) and (2-15). In this sense, spinel formation is unlikely to occur in the Oxygen Converter or the EAF because the highly oxidizing conditions remove any trace of dissolved magnesium (Story, et al., 2004). However, during the reducing conditions in the ladle furnace the possible [Mg] sources include: 1) the top slag, 2) contamination of Mg if an aluminum alloy is used for deoxidation and 3) the refractory lining. Discarding the mistake of deoxidizing the steel using Al alloys with harmful Mg contents the other two sources have been more studied (Yang et al., 2012).

The use of MgO-C bricks for refractory lining in the ladle is a common practice. Brabie (1996) proposed that at steelmaking temperatures an internal oxidation-reduction occurs within the brick:

$$\mathrm{MgO\ (s) + C\ (s) = Mg\ (g) + CO\ (g)} \qquad (2\text{-}16)$$

Both the Mg and CO gases diffuse through the pores of the brick to the steel where dissolution reactions occur at the brick-steel interface according to:

$$CO(g) = [C] + [O] \quad (2\text{-}17)$$

$$Mg\ (g) = [Mg] \quad (2\text{-}18)$$

Afterwards, the dissolved [Mg], [O] and [Al] can form a thin layer of MgO or Al_2O_3 at the brick-steel interface or, alternatively, [Mg] can diffuse into the steel and react with alumina inclusions to produce spinel.

Regarding the mechanism of [Mg] supply from the top slag, known as Al-reduction model, Nishi & Shinme (1998) performed laboratory experiments of 18%Cr - 5%Ni stainless steel deoxidized with aluminum using a CaO-Al_2O_3-MgO-SiO_2 slag. They reported an increase in the MgO content of the inclusions with longer processing times and for higher values of the CaO/SiO_2 ratio. These researchers related the origin of the Mg in the inclusions to the reduction of MgO from the slag and to the slag composition. For aluminum killed steels, the slag-steel reaction to supply [Mg] is:

$$3(MgO)_{Slag} + 2[Al] = (Al_2O_3)_{Slag} + 3[Mg] \quad (2\text{-}19)$$

A similar laboratory study was performed by Okuyama et al. (2000) by using a 16%Cr ferritic aluminum killed stainless steel under a CaO-Al_2O_3-SiO_2-MgO slag. They reported higher levels of [Si] and [Mg] concentrations with longer processing times. Also, the rate of accumulation of MgO in the inclusions increased as the basicity, CaO/SiO_2 and CaO/Al_2O_3, of the top slag increased. This higher [Mg] supply was linked to changes on the activity of MgO in the slag.

Furthermore, the mechanism for formation of spinel was claimed to be made of two processes: 1) reaction between the metal and the slag according to reaction (2-19) and 2) reaction between the steel and the alumina inclusions, Figure 2-14. This study concluded that the rate controlling step for the spinel formation on the whole system is the supply of [Mg] from the slag.

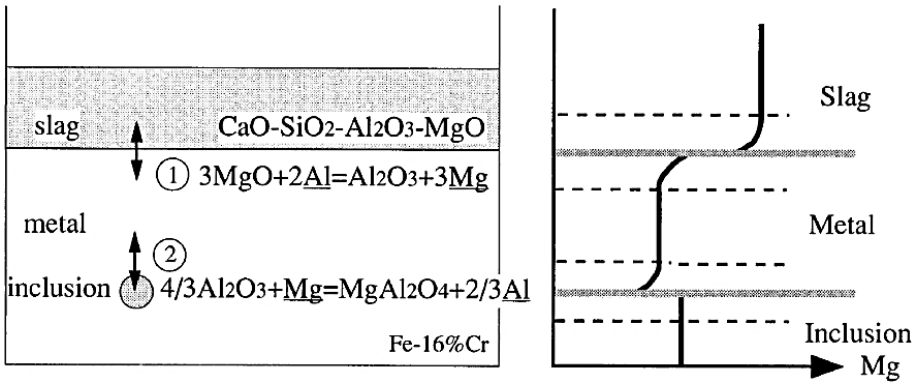

Figure 2-14. Schemes of the reactions among slag, steel and inclusions and of the Mg content in slag, metal and inclusions (Okuyama, et al., 2000).

Mizuno et al, (2001), showed that spinel inclusions increased in the case of a 18%Cr-8%Ni stainless steel when the deoxidizer contains more aluminum. Todoroki & Mizuno (2004) reported for laboratory experiments with an Al-killed 304 stainless steel, that higher contents of SiO_2 in the slag reduces the amount of [Mg] and [Ca] supplied from the slag which in turn affects the composition of the spinel inclusions.

From and industry perspective, it has been demonstrated that during ladle treatment of LCAK steel, the Al-reduction mechanism promotes spinel formation

if the highly fluid basic slag is well deoxidized (Figure 2-15) and during periods of high stirring (Pretorius et al., 2013). The effect of the slag deoxidation level is further reflected on the increase of dissolved [Si] during the progress of the heat (Pretorius, et al, 2010), since no [Si] is added during the ladle treatment, the [Si] pickup means that SiO_2 from the slag is reduced.

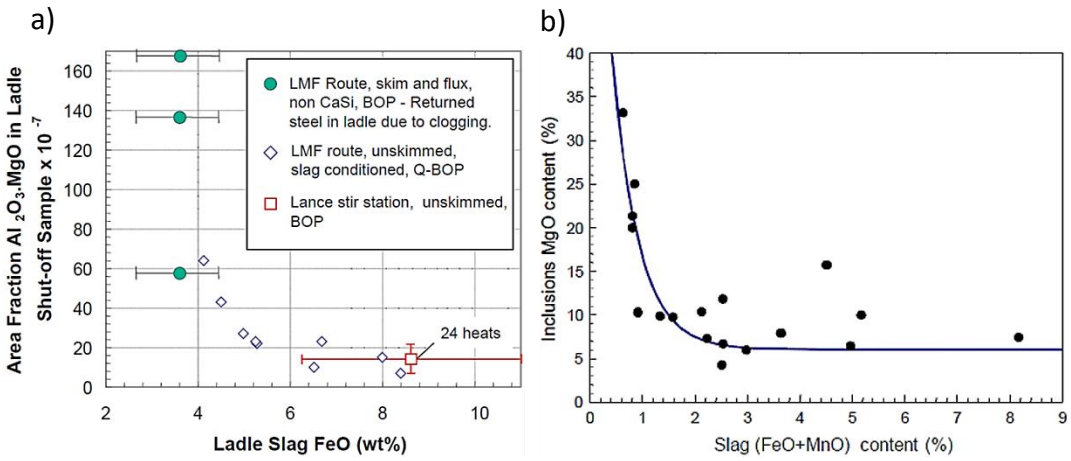

Figure 2-15. Effect of deoxidation level of the ladle slag on the spinel inclusions content. a) Spinel area fraction vs FeO in slag (Story et al., 2004), b) FeO+MnO in the slag vs the MgO content in the inclusions (Mendez, et al , 2012)

Finally, Story et al (2004) reported the possibility that the application of electrical arcing can increase the spinel inclusions by a reaction between the MgO in the slag and the carbon graphite electrodes:

$$(\mathrm{MgO})_{\mathrm{Slag}} + \mathrm{C} = \mathrm{CO\ (g)} + \mathrm{Mg\ (g)} \qquad (2\text{-}20)$$

The produced Mg gas dissolves in the steel according to reaction (2-18) where then it can react with the inclusions.

Among the different sources of [Mg] during ladle treatment of LCAK steel, Pretorius et al. (2010) mentioned that the kinetics of slag-metal reactions is typically much faster than the one of refractory-metal reactions, therefore it is more likely for the Al-reduction mechanism to be the main source of spinel inclusions.

2.2.4. Kinetics studies for the alumina to spinel transformation of inclusions

From their laboratory experiments, Okuyama et al (2000) analyzed the kinetic effect of the top slag on the rate of spinel inclusions formation. For the slag-metal reactions they implemented the kinetic model of Robertson et al (1984) that considers multicomponent interphase mass transfer based on the double boundary layer diffusion mechanism. With this approach, the [Mg] content in the bulk of the steel is controlled by the slag-steel interfacial concentration [Mg*], which in turn depends on the interfacial values of the MgO activity in the slag $a_{MgO}*$, and the oxygen activity in the steel, h_O^*.

For the change in the oxide inclusions composition two different scenarios were formulated. First, with a spherical geometry, a spinel product layer was assumed to form on top of the unreacted alumina core, Figure 2-16a. The increase of MgO concentration in the inclusions was calculated by using the following diffusion equation for the spinel product layer:

$$\frac{d(MgO)}{dt} = \frac{D_s}{r^2}\ \frac{d}{dr}\left[r^2 \cdot \frac{d(MgO)}{dr}\right] \qquad (2\text{-}21)$$

In this model the MgO concentration at the spinel-alumina interface and at the spinel-steel interface were kept constant. The second model assumed that diffusion in the inclusions is much faster and the rate limiting step is the transport of dissolved [Mg] across the boundary layer at the steel-inclusions interface, the content of (Mg) in the inclusions is obtained from the mass balance:

$$\frac{d}{dt}\left[\frac{4\pi}{3}{R_O}^3 \cdot (Mg) \cdot \rho_s\right] = 4\pi \cdot {R_O}^2 \frac{D_m \cdot \rho_m}{R_O}\left[[Mg] - \frac{(Mg)'}{L}\right] \qquad (2\text{-}22)$$

In this case, L is the equilibrium partition ratio at the inclusions-steel interface.

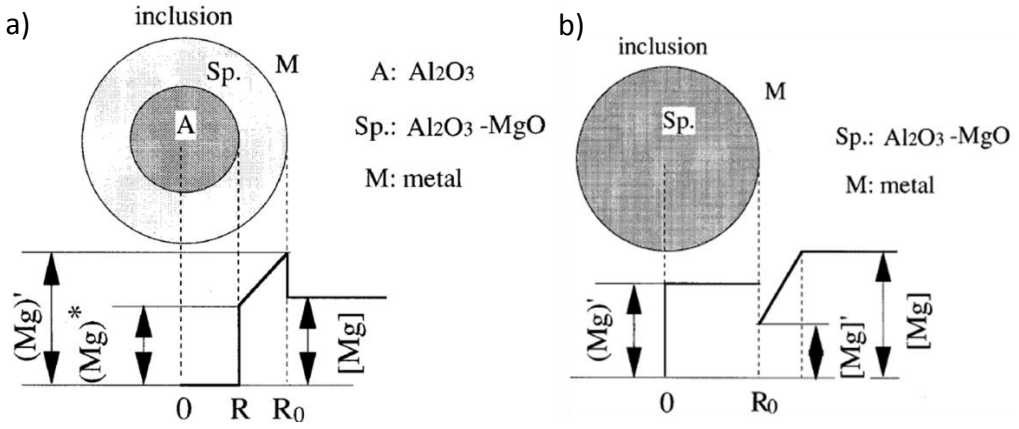

Figure 2-16. a) Mg distribution in the inclusions with a spinel product layer, b) Rate limiting is step is in the steel boundary layer, (Okuyama et al., 2000)

Comparing both inclusion models and the times to reach saturation Okuyama et al found that diffusion in the steel boundary layer is slower than in the product layer. However, since the experimental and calculated contents of [Mg] from the slag-steel reaction required more time to reach equilibrium, it was concluded that the rate limiting step for spinel formation of the whole system is

the slag-metal reaction. Using the same assumptions, a slightly different mathematic method to solve equation (2-22) was proposed (Wu & Zhang, 2008).

For the heterogeneous reaction of solid particles with a fluid, the assumption of a shell-core structure and the different assumptions for diffusion models have been discussed (Szekely & Themelis, 1971; Wen, 1968). Experimentally, there is evidence of the formation of a spinel product layer for the transformation of alumina inclusions to spinel. Takata et al (2007) injected magnesium vapor into aluminum killed steel; from the EDS line analysis of the inclusions they reported an increase of magnesium concentration in the periphery of the inclusions, Figure 2-17.

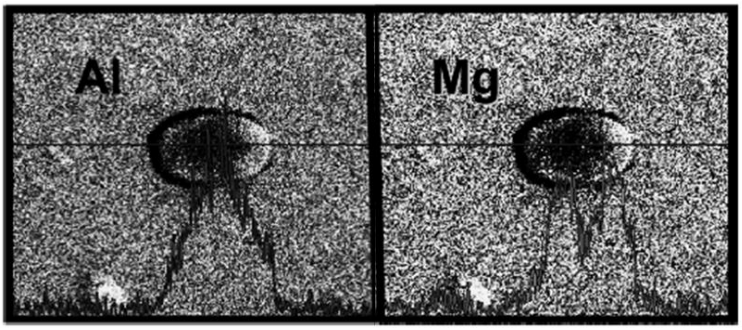

Figure 2-17. EDS analyses of an Alumina-Spinel inclusion, (Takata et al, 2007).

Park and Kim (2005) obtained similar results by equilibrating Fe-16Cr melts with different $CaO-Al_2O_3-MgO$ slags. The analysis of the inclusions formed shows a gradient in the Mg and Al concentrations, Figure 2-18. This indicates that the initial MgO inclusions reacted with [Al] in the steel to become $MgAl_2O_4$ spinel. Based on these results, the authors suggested a mechanism for inclusions

modification that involves cationic diffusion and ionic exchange reactions at the core-product layer interface and at the product layer-steel interface.

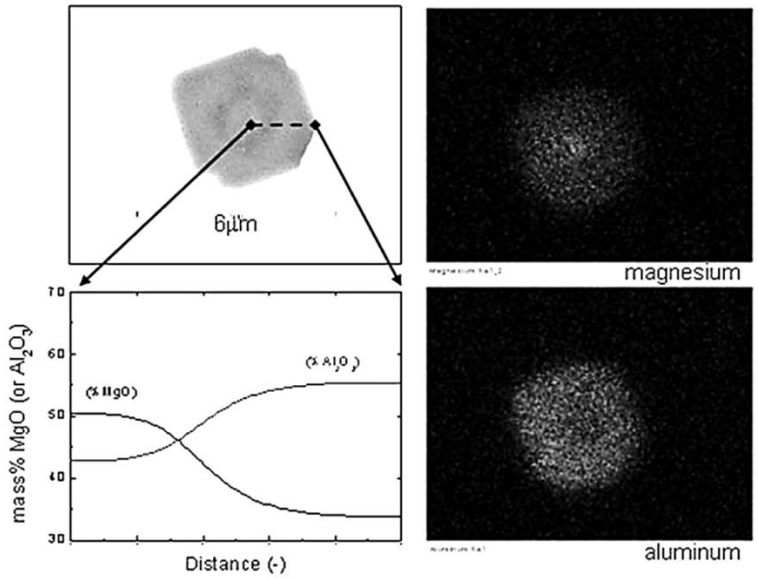

Figure 2-18. Morphology and element mapping of the spinel-type inclusions in Fe-16Cr melts equilibrated with the $CaO-Al_2O_3-MgO$ slags, (Park & Kim, 2005).

2.3 Cation counterdiffusion mechanism for spinel formation

2.3.1 Solid state reaction mechanism for spinel

Spinels are a type of ionic compounds formed from strongly electropositive metal ions and strongly electronegative nonmetals ions. These compounds commonly exist as oxides, sulfides or iodides and are distinguished by its crystallographic structure (Armijo, 1969). Aluminate oxides like $ZnAl_2O_4$ and $NiAl_2O_4$ belong to the spinels group. The solid state reaction mechanism to

form spinel was first proposed by Koch and Wagner (Koch & Wagner, 1936) and states that the formation of spinel occurs by counterdiffusion of cations through a rigid and compact anion sublattice, Figure 2-19. This mechanism has been verified for several spinel compounds, for example, $ZnFe_2O_4$, $ZnCr_2O_4$, $NiCr_2O_4$, Zn_2SnO_4 and $ZnAl_2O_4$ (Bengtson & Jagitsch, 1947; Lindner & Åkerström, 1956).

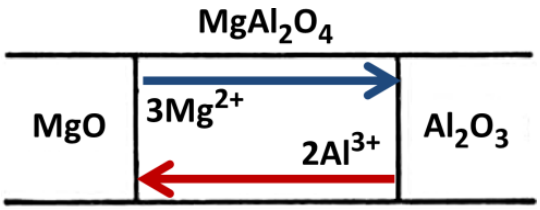

Figure 2-19. Schematic of the mechanism for the spinel solid state reaction

For magnesium aluminate spinel, the counterdiffusion of Mg^{2+} and Al^{3+} was first demonstrated with experiments between solid Al_2O_3 and Mg gas (Carter, 1961; Navias, 1961). From these, it was concluded that spinel forms at the alumina-spinel and spinel-$Mg_{(gas)}$ interfaces, also variations in composition across the spinel rim were reported, this was attributed to the range of solubility of alumina in spinel.

Solid state diffusion couples between Al_2O_3 and MgO have been analyzed by several researchers and confirmed Wagner's mechanism: (Rossi & Fulrath, 1963; Yamaguchi & Tokuda, 1967; Whitney & Stubican, 1971a, 1971b; Zhang, Debroy, & Seetharaman, 1996; Watson & Price, 2002; Götze et al., 2009). Based on their results, the different authors stablished stoichiometries of the

semireactions at each interface. For the studies that measured the concentration profiles across the spinel layer, the results demonstrated that both spinel interfaces have equilibrium compositions, Figure 2-20a. Also, in terms of diffusion, the calculations of Zhang et al (1996) showed that the interdiffusion coefficient has a negligible change as a function of composition in the spinel layer, Figure 2-20b.

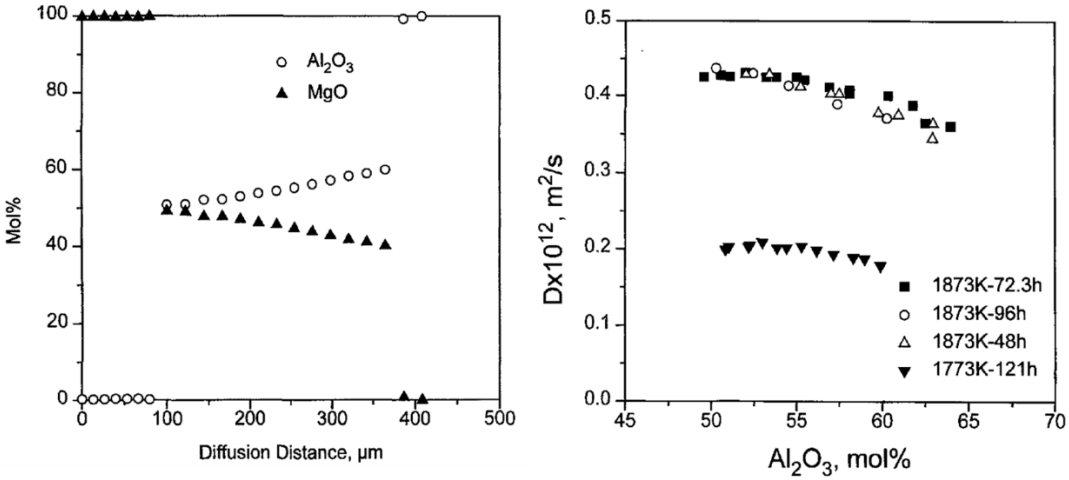

Figure 2-20. a) Concentration profiles in the spinel layer, b) Interdiffusion coefficients across the spinel product layer (Zhang et al., 1996).

The study of Martinelli et al (1986) on the mobilities of Mg^{2+} and Al^{3+}, concluded that Mg^{2+} is the predominant ionic current carrier during the formation of spinel. Similarly, by using atomic scale computer simulations Murphy et al (2009) concluded that Mg^{2+} ions are more mobile than Al^{3+} ions in $MgAl_2O_4$ Additionally, the self diffusion coefficient of Mg^{2+} was measured by Sheng et al (1992) by placing single crystals of stoichiometric spinel in contact with oxide melts ^{28}Mg doped, made of CaO, MgO and SiO_2.

One of the main assumptions in Wagner's mechanism is that the anion sublattice of oxygen in spinel is immobile. To verify this, Nakano et al (1971) measured the diffusivity of oxygen by using solid diffusion couples and MgO enriched with the stable isotope ^{18}O. Ando and Oishi (1974) and Reddy and Cooper (1981) measured the diffusivity of oxygen by using atmospheres enriched with ^{18}O. In general, the reported diffusivities for oxygen in spinel are several orders of magnitude smaller than the diffusivities of the cations. Reviews have been published for the self-diffusion and interdiffusion coefficient values in magnesium aluminate spinel (Benameur, et al, 2011; Reimanis & Kleebe, 2009; Rubat Du Merac, et al, 2013; Van Orman & Crispin, 2010). Figure 2-21 is a comparison of the different self-diffusivity values reported in the literature.

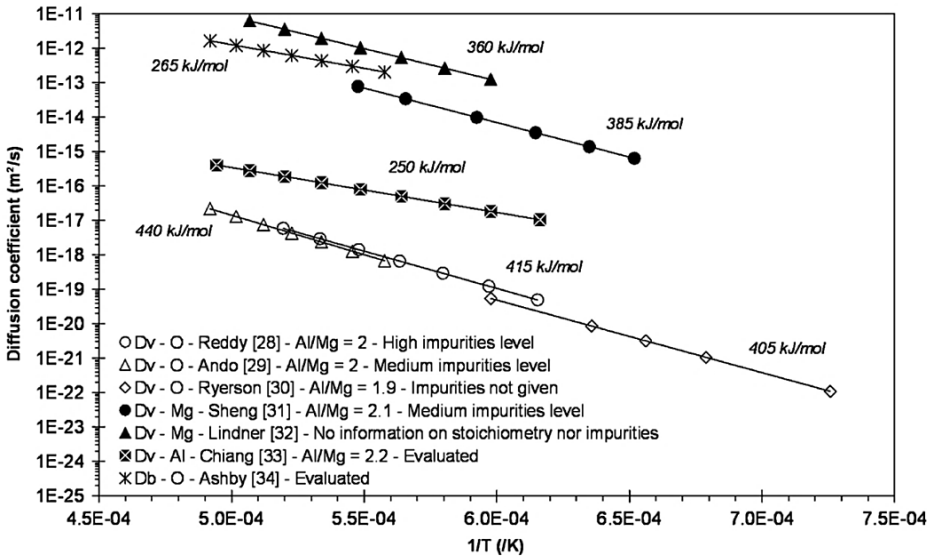

Figure 2-21. Self-diffusion coefficients for O^{2-}, Mg^{2+} and Al^{3+} in spinel taken from the literature. Dv is for volume/bulk diffusion and Db for grain-boundary diffusion. The stoichiometry level (Al/Mg ratio) and the impurity content are specified (Benameur et al., 2011).

2.3.2 Ionic transport in oxides

The chemical potential μ_i of species i in a phase is defined thermodynamically as the work needed to bring a mole of that species into the bulk of that phase, therefore $d\mu_i$ is the driving force that causes the flow of mass in a chemical process. However, this definition is of limited validity for oxides since the concept of chemical potential only applies to neutral species or uncharged media (Barsoum, 2002). For ions in oxides the appropiate function to use is the molar electrochemical potential η_i , which is defined for a particle of net charge $z_i \cdot e$ by:

$$\eta_i = \mu_i + z_i F \varphi_i \tag{2-23}$$

Where μ_i is the chemical potential [J/mol], φ_i is the electrical potential [J/C] and F is Faraday's constant. From this definition, the driving force for diffusion of charged species is the gradient in its electrochemical potential. In this way, compositional equilibrium is reached when the gradient in electrochemical potential for every species vanishes (Barsoum, 2002; Schmalzried, 1995) that is:

$$d\eta_i = 0 \tag{2-24}$$

From a phenomenological and macroscopic point of view, the irreversible processes of diffusion, electrical conduction and heat flow can be described with the theory of non-equilibrium thermodynamics. As reviewed by Mehrer (2007) the major assumptions of non-equilibrium thermodynamics are:

1. The transport equations of atoms, heat, and electrons are linear relations between the fluxes J_i and the thermodynamic driving forces $\boldsymbol{X}_i$. The phenomenological response for the complete set of n fluxes has a linear form, Equation (2-25). L_{ij} are the transport coefficients. The matrix of coefficients is called the Onsager matrix:

$$J_i = \sum_{j=1}^{n} L_{ij}\boldsymbol{X}_j \tag{2-25}$$

2. The Onsager matrix is composed in part of diagonal terms, L_{ii} that connect each driving force with its conjugate flux and it also contains off-diagonal coefficients, L_{ij} that determine the influence of a driving force on a non-conjugate flux, this is known as a 'cross effect'.
3. The central idea of non-equilibrium thermodynamics is that each of the thermodynamics forces acting with its flux response dissipates free energy and produces entropy. The rate of entropy production, σ, can be written as:

$$T\sigma = \sum_{i}^{n} J_i\boldsymbol{X}_i \; + \; J_q\boldsymbol{X}_q \tag{2-26}$$

Where J_i denotes the flux of atoms *i* and J_q the flux of heat. For isothermal diffusion in a closed, isobaric, magnetic field-free n-component system, it is found that $\boldsymbol{X}_i = -\nabla\eta_i$, (Schmalzried, 1995). Therefore the component fluxes are given by:

$$J_i = -\sum_{i=1}^{n} L_{ij}\nabla\eta_i \tag{2-27}$$

Additionally, it is customary to omit the difficulties of the cross effects by assuming that L_{ij} = 0 for $i \neq j$. As mentioned by Pfeiffer and Schmalzried (1989) this last assumption, although not quite correct, allows a quantitative treatment of the problem. Also, since the flux of species *i* is the product of the concentration times its velocity, the equation reads:

$$J_i = C_i \cdot (v_i - w) \tag{2-28}$$

Where C_i is the molar concentration [mole/m^3], ν_i is the velocity vector of particles i and w is the reference velocity frame. For the given velocity framework the velocity of the particles can be expressed as:

$$v_i = b_i \cdot \boldsymbol{K_i} \tag{2-29}$$

Here b_i represents the mobility of the species *i* and $\boldsymbol{K_i}$ is the force vector that drives the movement of the particles. Considering that $\nabla\eta_i$ is the only force for diffusion, it is concluded that the transport coefficient L_{ii} actually correspond to the product of the concentration C_i times the mobility b_i (Schmalzried, 1995). In many cases of transport of solids, the atoms (ions) of one sublattice in the crystal are almost immobile which sets the velocity reference frame, therefore:

$$L_{ii} = b_i \cdot C_i \tag{2-30}$$

Considering the Nernst-Einstein equation, equation (2-30) becomes:

$$L_{ii} = \frac{D_i C_i}{RT} \tag{2-31}$$

In the case of binary ionic solids AX where A represents the cation and X the anion, diffusion of ions and vacancies is possible by point defects jumps. If the sublattice of anions is almost immobile, cross effects are neglected and there is at low concentration of point defects, the flux of point defects is then:

$$J_p = -L_{pp}\nabla\eta_p = -\frac{D_p C_p}{RT}\nabla\eta_p \tag{2-32}$$

The respective flux of A^+ cations is:

$$J_{A^+} = -\frac{D_{A^+} C_{A^+}}{RT}\nabla\eta_{A^+} \tag{2-33}$$

For electronic defects (excess of electrons and electron holes)

$$J_{el} = -\frac{D_{el} C_{el}}{RT}\nabla\eta_{el} \tag{2-34}$$

If anions are mobile, there is a flux of X^- in the lattice reference frame

$$J_{X^-} = -\frac{D_{X^-} C_{X^-}}{RT}\nabla\eta_{X^-} \tag{2-35}$$

As mentioned by Schmalzried (1995), in order to know the magnitude of the fluxes it is necessary to set boundary conditions depending on the specific transport situations. For the theory of cationic diffusion additional introductory references include the textbook of Kofstad and Truls (2007) and reference books for the diffusion in solids from the perspective of irreversible thermodynamics (Mehrer, 2007; Rickert, 1982; Young, 2008).

2.3.3 Wagner-Schmalzried model for spinel formation

The kinetics of spinel formation from the binary oxides AO and B_2O_3 ($AO + B_2O_3 = AB_2O_4$) was first explained quantitatively by Wagner (1938) where A and B can represent a variety of different elements such as Mg, Fe, Ni, Co and Al, Ga, Cr respectively; the formation of silicates, double sulfides and double halides also belong to the spinel category. Later on Wagner's mechanism was expanded for different conditions of spinel formation (Pfeiffer & Schmalzried, 1989; Schmalzried & Pfeiffer, 1986). As summarized by Armijo (1969) the assumptions of the Wagner-Schmalzried model are:

1. The reaction layer is dense, and does not contain nonequilibrium defects such as dislocations or grain boundaries.
2. Interface reactions are faster than the transport of ions through the spinel.
3. Diffusing species are coupled only by the requirements of local equilibrium and electroneutrality, and otherwise move independently.
4. Thermodynamic equilibrium exists at the phase boundaries.
5. All the oxides involved are assumed to be semiconductors, that is: $D_{el} \cdot C_{el} >> D_{ion} \cdot C_{ion}$. The subscript 'el' denotes electronic carriers: electron and holes.

Pfeiffer and Schmalzried (1986) classified the different possible cases for the formation of spinel from oxides, Figure 2-22. Three main limiting cases can be evaluated; if Δ denotes the difference across the spinel product layer, the three

scenarios are: 1) $\Delta\mu_{AO} \neq 0$, $\Delta\mu_O = 0$, 2) $\Delta\mu_{AO} = 0$, $\Delta\mu_O \neq 0$ and 3) $\Delta\mu_{AO} \neq 0$, $\Delta\mu_O \neq 0$. Also, the availability of AO, B_2O_3 and oxygen O_2 at the interfaces determine the transport behaviour for a given process, that is, whether or not the interfaces are open or closed for these constituents affects the spinel reaction rate.

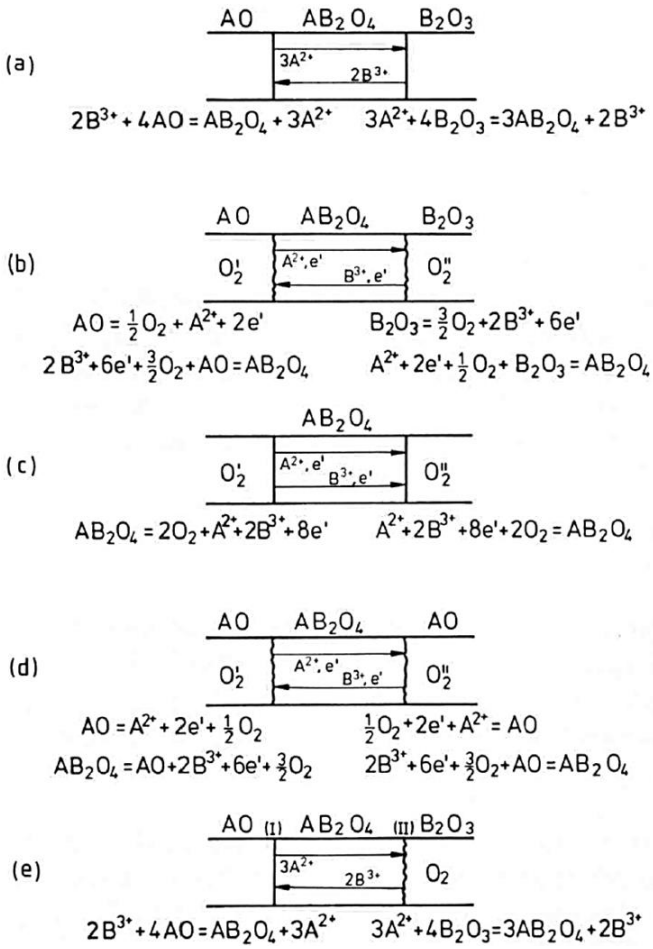

Figure 2-22. Scheme of fluxes and chemical potentials for different boundary conditions for spinel formation. a) O_2 is excluded from both interfaces, b) Oxygen of a given potential has access to both interfaces, c) Only O_2 is available at both interfaces, d) Oxygen is available at both interfaces, only one reactant AO is present at both interfaces, e) O_2 is available at one interface, also B_2O_3. AO is available at the other interface, but no O_2 (Schmalzried & Pfeiffer,1986).

If there is access of oxygen at the interfaces, lattice molecules (M) of spinel can be added to or substracted from the spinel crystal (Pfeiffer & Schmalzried, 1989). Therefore if ξ represents distance and ξ^p is the position of the interface open to oxygen, the rate of addition or loss of spinel molecules r_M is:

$$\frac{\partial n_M}{\partial t} = r_M \qquad (\xi^p, t) \tag{2-36}$$

With the molar volume of spinel V_m and the cross sectional area q, the increase in spinel thickness with time due to uptake of oxygen, for a planar geometry, becomes:

$$\frac{\partial \xi^p}{\partial t} = r_M \cdot \left(\frac{V_m}{q}\right) \tag{2-37}$$

The assumption that all the oxides involved are semiconductive compounds implies that the electrochemical gradient of electrons or holes cannot be mantained and eventually disappears, therefore for electric carriers $\nabla\eta_{el} = 0$, then:

$$\nabla \mu_{e^-} = F \cdot \nabla \varphi \tag{2-38}$$

Assuming that spinel forms by counterdiffusion of cations and neglecting cross terms, the fluxes of the electrical charged species are formulated as:

$$J_i = -\frac{D_i C_i}{RT} \cdot \frac{\partial \eta_i}{\partial \xi} \tag{2-39}$$

Where for one-dimensional conditions, ξ is the position coordinate refering to the immobile oxygen lattice frame for spinel. If local thermodynamic

equilibrium at the interfaces is assumed then it is possible to replace the electrochemical potential of A^{2+} and B^{3+} by the chemical potentials of the neutral species A and B, considering:

$$A = A^{2+} + 2e^{-} \tag{2-40}$$

The variation in the chemical potential of A becomes:

$$\partial\mu_A = \partial\mu_{A^{2+}} + 2\partial\mu_{e^-} \tag{2-41}$$

The gradient in the electrochemical potential of A^{2+} is by definition:

$$\frac{\partial\eta_{A^{2+}}}{\partial\xi} = \frac{\partial\mu_{A^{2+}}}{\partial\xi} + 2F\frac{\partial\varphi}{\partial\xi} \tag{2-42}$$

From equations (2-38), (2-41) and (2-42)

$$\frac{\partial\eta_{A^{2+}}}{\partial\xi} = \frac{\partial\mu_A}{\partial\xi} \tag{2-43}$$

Therefore the flux of cations, Equation (2-39), can be expressed using the gradient of the neutral species across the spinel product layer, for A^{2+} :

$$J_{A^{2+}} = -\frac{D_A C_A}{RT}\cdot\frac{\partial\mu_A}{\partial\xi} \tag{2-44}$$

Similarly for B^{3+} :

$$J_{B^{3+}} = -\frac{D_B C_B}{RT}\cdot\frac{\partial\mu_B}{\partial\xi} \tag{2-45}$$

Furthermore, these fluxes can be expressed in terms of independent thermodynamic chemical potentials (μAO, μB_2O_3 and μO) by considering the individual formation reactions:

$$A + O = AO \tag{2-46}$$

$$2B + 3O = B_2O_3 \tag{2-47}$$

The respective changes in chemical potential are:

$$\partial\mu_A + \partial\mu_O = \partial\mu_{AO} \tag{2-48}$$

$$2\partial\mu_B + 3\partial\mu_O = \partial\mu_{B_2O_3} \tag{2-49}$$

From equations (2-44) and (2-48):

$$J_{A^{2+}} = -\frac{D_A C_A}{RT} \cdot \left[\frac{\partial\mu_{AO}}{\partial\xi} - \frac{\partial\mu_O}{\partial\xi}\right] \tag{2-50}$$

From equations (2-45) and (2-49):

$$J_{B^{3+}} = -\frac{D_B C_B}{RT} \cdot \frac{1}{2}\left[\frac{\partial\mu_{B_2O_3}}{\partial\xi} - 3\frac{\partial\mu_O}{\partial\xi}\right] \tag{2-51}$$

As mentioned by Schmalzried & Pfeiffer (1986), the driving forces for cation diffusion in equations (2-50) and (2-51) are expressed in terms of neutral chemical potentials and they are completely general, except for the semiconduction assumption that there is not external electrical current in the process. Therefore, these ecuations can be applied under the different boundary conditions of spinel formation, Figure 2-22.

2.4 Kinetic models for ladle metallurgy furnace operations

A process model is a system of mathematical equations and parameters that are solved computationally to make quantitative predictions about some aspects of a real process. The different reasons to develop a process model include

(Thomas & Brimacombe, 1997): increasing fundamental understanding of a process, assisting in scale-up, design of experiments, evaluation of experimental results, quantifying propetry measurements, On-line process control, optimization and technology transfer.

In order to describe the compositional changes in the slag and steel phases during liquid steel treatment in the LMF several kinetic models have been proposed (Andersson et al, 2000; Brooks et al, 2009; Harada et al, 2013; Peter et al, 2005). The model of Graham and Irons (2010) retrieves the processing parameters in the LMF and calculates the compositional changes in the slag and steel based on the model of Robertson et al (1984). Furthermore, the model of Graham and Irons (Graham & Irons, 2010; Graham, 2008) was validated with extensive sampling of the slag, steel and inclusions during the progress of the heats, the study was conducted at ArcelorMittal Dofasco in order to model a 165t LMF used for the refining of liquid steel coming from the EAF; this model will be reviewed more in detail since it was used, adpated and extended for this thesis project.

2.4.1 Thermodynamic formalisms in the kinetic model of Graham and Irons

For the activities of the different components in the multicomponent molten slag Graham and Irons (2010) used the Cell Model. This model belongs to the group of Quasichemical formalisms for liquid slags. The Cell Model was initially formulated for binary and ternary silicate melts by Kapoor and Frohberg

(Kapoor & Frohberg, 1973) and then was further extended and generalized for multicomponent slags by the research group of ArcelorMittal Maizières, formerly IRSID (Gaye, et al, 1992; Gaye & Welfringer, 1984; Lehmann & Gaye, 1993). As mentioned by Lehmann and Gaye (1992), the model considers two sublattices in the slag: an anionic sublattice filled with divalent anions and a cationic sublattice filled with the different cations in decreasing order of their charge. The structure of the slag is then described in terms of symetric (i-A-i) and asymetric cells (i-A-j), which consists in a central anion surrounded by two cations, the mole number of cells i-k-j is R_{ij}^{k} . Two types of parameters are used and they are binary parameters assumed temperature independent:

Formation parameters

- W_{ij}^{A} , associated for each anion to the formation of asymmetric cells from the corresponding symetric ones:

$$\frac{1}{2}(\mathrm{i}-\mathrm{A}-\mathrm{i}) + \frac{1}{2}(\mathrm{j}-\mathrm{A}-\mathrm{j}) = (\mathrm{i}-\mathrm{A}-\mathrm{j}) \qquad (2\text{-}52)$$

- W_{ii}^{A} , represents the stability of the A-symmetric cell relative to the oxygen symmetric cell:

$$(\mathrm{i}-\mathrm{O}-\mathrm{i}) + \mathrm{A} = (\mathrm{i}-\mathrm{A}-\mathrm{i}) + \mathrm{O} \qquad (2\text{-}53)$$

Interaction parameters

- E_{ij}^{A} , interaction between cells (i-A-i) and (i-A-j). In the liquid oxide model, only one independent cell interaction parameter is used per binary system.
- E_{i}^{A} , in polyanionic systems it represents the interaction between (i-A-i) and (i-B-i) cells.

The Gibbs free energy of the system is obtained by calculating the mole number of cells R_{ij}^{k}, this is achieved by maximization of the partition function under mass balance constraints for the anions and cations. After calculating the Gibbs free energy the chemical potential and activities of the different components are calculated using classical thermodynamic expressions for multicomponent systems.

The activities for the dissolved species in the steel are calculated with the Unified Interaction Parameter Formalism, UIPF, which is a modification of the Wagner interaction parameter formalism (Carl Wagner, 1952) that has been frequently used for dilute solutions in iron-based alloys. Pelton and Bale (1986) reviewed the shortcomings of Wagner's formalism and its thermodynamic inconsistency at higher solute concentrations. They proposed the UIPF which has the following characteristics (Bale & Pelton, 1990; Pelton & Bale, 1986):

1. Is thermodynamically consistent at finite concentrations in binary, ternary, and multicomponent systems.
2. Can be derived from general Margules-type polynomial expressions.
3. Reduces to the standard first-order Wagner's interaction parameter formalism at infinite dilution.
4. Reduces to the standard second-order interaction Lupis and Elliot parameter formalism at infinite dilution (Lupis, 1983).
5. Reduces to the quadratic Darken's formalism which is thermodynamically consistent at finite concentrations.

6. Can be employed with existing compilations of interaction parameters or Gibbs energy expressions.

The modified activity coefficients for the components in an Fe-based solution are:

$$ln\, f_i = \sum_{j=1}^{N} \varepsilon_{ij} X_j + \sum_{j,\, k=1}^{N} \varepsilon_{ijk} X_j X_k + ln\, f_{Fe} \tag{2-54}$$

$$ln\, f_{Fe} = -\frac{1}{2} \sum_{j,k=1}^{N} \varepsilon_{jk} X_j X_k \; - \; \frac{2}{3} \sum_{j,k,l=1}^{N} \varepsilon_{jkl} X_j X_k X_l \tag{2-55}$$

The parameters ε_{ij} and ε_{ijk} of the UIPF can be calculated from the reported first order ε_i^j, and second order ρ_i^{ij}, interaction parameters of Wagner's formalism (Hino & Ito, 2010).

2.4.2 Coupled kinetic model of Graham and Irons for the LMF

The work of Graham and Irons (2010) has great relevance in the area of process modeling for the LMF, particularly since it represents the first study that demonstrated the coupled nature of the simultaneous slag-steel reactions during ladle treatment at the industrial scale. For the kinetics of the process, Graham and Irons implemented the model of Robertson et al (1984) which allows to predict the kinetics of coupled multicomponent slag-steel reactions by relating the mass transfer of the different species in both phases with the thermodynamic equilibrium that is assumed at the slag-steel interface. As reviewed by Robertson (1995) the model has been applied to the study of several processes including

desulphurization of pig iron, refining of stainless steel, the fuming of zinc from slags and the production of low carbon ferromanganese.

The model of Robertson et al (1984) assumes formation reactions between oxides in the slag and the respective species in the steel according to:

$$\mathrm{x[M] + y[O] = (M_xO_y)_{slag}} \tag{2-56}$$

These type of reactions were considered for the slag oxides FeO, MnO, CaO, MgO, TiO_2, SiO_2 and Al_2O_3 in the work of Graham and Irons. The respective heterogeneous equilibrium that is assumed for all reactions at the slag-steel interface is:

$$K_{M-O} = \frac{\left(\gamma^*_{M_xO_y}\right) \cdot \left(X^*_{M_xO_y}\right)}{[f^*_M X^*_M] \cdot [f^*_O X^*_O]} \tag{2-57}$$

Where $X^*_{M_xO_y}$, X^*_M and X^*_O are the equilibrium concentrations in molar fraction. Assuming that the kinetics is controlled only by transport of the species from the bulk of the phases to the interphase, the expression for the mass diffusion considering the double boundary layer theory for each reaction is:

$$k^M_m Cv_m (X^b_M - X^*_M) = k^{M_xO_y}_{sl} Cv_{sl} \left(X^*_{M_xO_y} - X^b_{M_xO_y}\right) \tag{2-58}$$

Cv_m and Cv_{sl} are the total molar concentrations of the metal and slag phase respectively while k^M_m and $k^{M_xO_y}_{sl}$ are the mass transfer coefficients for convective transport in the metal and slag. The model of Robertson et al (1984) couples all the reactions with the balance for oxygen:

$$k^O_m Cv_m (X^b_O - X^*_O) = \sum_{i=1}^{n} y_i \, k^{M_xO_y}_{sl} Cv_{sl} \left(X^*_{M_xO_y} - X^b_{M_xO_y}\right) \tag{2-59}$$

This last equation allows to solve the nonlinear system of equations for the 15 unknown interfacial concentrations. At each time step the concentrations in the bulk of the steel and slag are updated using first-order time integration of equations (2-60) and (2-61) for each species:

$$\frac{dX_{M_xO_y}}{dt} = -k_{sl}^{M_xO_y}\left(\frac{A}{V_{St}}\right)\left(X_{M_xO_y}^{b} - X_{M_xO_y}^{*}\right) \tag{2-60}$$

$$\frac{dX_{M}}{dt} = -k_{m}^{M}\left(\frac{A}{V_{Sl}}\right)\left(X_{M}^{b} - X_{M}^{*}\right) \tag{2-61}$$

From the industrial measurements at ArcelorMittal Dofasco and assuming metal transfer control for desulphurization, Graham and Irons (2010) reported an empirical correlation for the mass transfer coefficient of [S] in the steel for a 165 tonnes industrial ladle:

$$k_m^S \cdot A = 0.006 \pm 0.002\ \varepsilon^{1.4 \pm 0.002} \tag{2-62}$$

Where the effective stirring power ε [Watt/tonne] is calculated with Pluschkell's correlation, equation (2-8). The mass transfer coefficients for all the species in steel were assumed to be the same while the ones for the species in the slag were obtained from ratios k_m^M / $k_{sl}^{M_xO_y}$ that fitted the experimental results. The reported mass transfer ratios ratios ranged between 7 to 20 for FeO, MnO, and Al_2O_3, and 50 to 100 for SiO_2 (Graham & Irons, 2010).

Desulphurization in the ladle is modeled with the respective balance for the transfer of sulphur from the metal to the slag:

$$k_m^S Cv_m\left(X_{S,m}^{b} - X_{S,m}^{*}\right) = k_{sl}^S Cv_{sl}\left(X_{S,Sl}^{*} - X_{S,Sl}^{b}\right) \tag{2-63}$$

The interfacial concentrations are related by means of the equilibrium partition coefficient for desulphurization in molar fraction, L'_S:

$$L'_S = \frac{X^*_{S,sl}}{X^*_{S,m}} = \frac{C'_S \cdot f^*_S \cdot K_s}{h^*_O} \tag{2-64}$$

Where C'_S is the slag sulphide capacity calculated with the empirical expressions proposed by Young, et al, (1992) as a function of the optical basicity in the slag, f^*_S is the interfacial activity coefficient for [S], K_s is the equilibrium constant for the desulphurization reaction (2-4) and h^*_O is the interfacial activity for oxygen that satisfies the multicomponent equilibria for the coupled reactions at the slag-steel interface. Graham and Irons (2010) pointed out the importance of using the interfacial oxygen activity h^*_O for the calculation of L'_S since other oxygen activities cannot represent the simultaneous effect of the deoxidation level in the slag and the steel. Figure 2-23 shows the diagram of the numerical routine implemented for the multicomponent kinetic model.

An additional study in the work of Graham and Irons was focused on the analysis of the oxide inclusions during the refining process. From the compositional analysis of the inclusions using Automated SEM, the activities of MgO and Al_2O_3 in the spinel inclusions were obtained with the Cell model; these values were then compared with the respective activities at the slag-steel interface considering the slag composition and the interfacial activity of oxygen using the method of kinetic coupled reactions, Figure 2-24. The thermodynamic parameters

for the [Al]-[Mg]-[O] equilibrium were taken from the values of Nadif and Gatellier (1986).

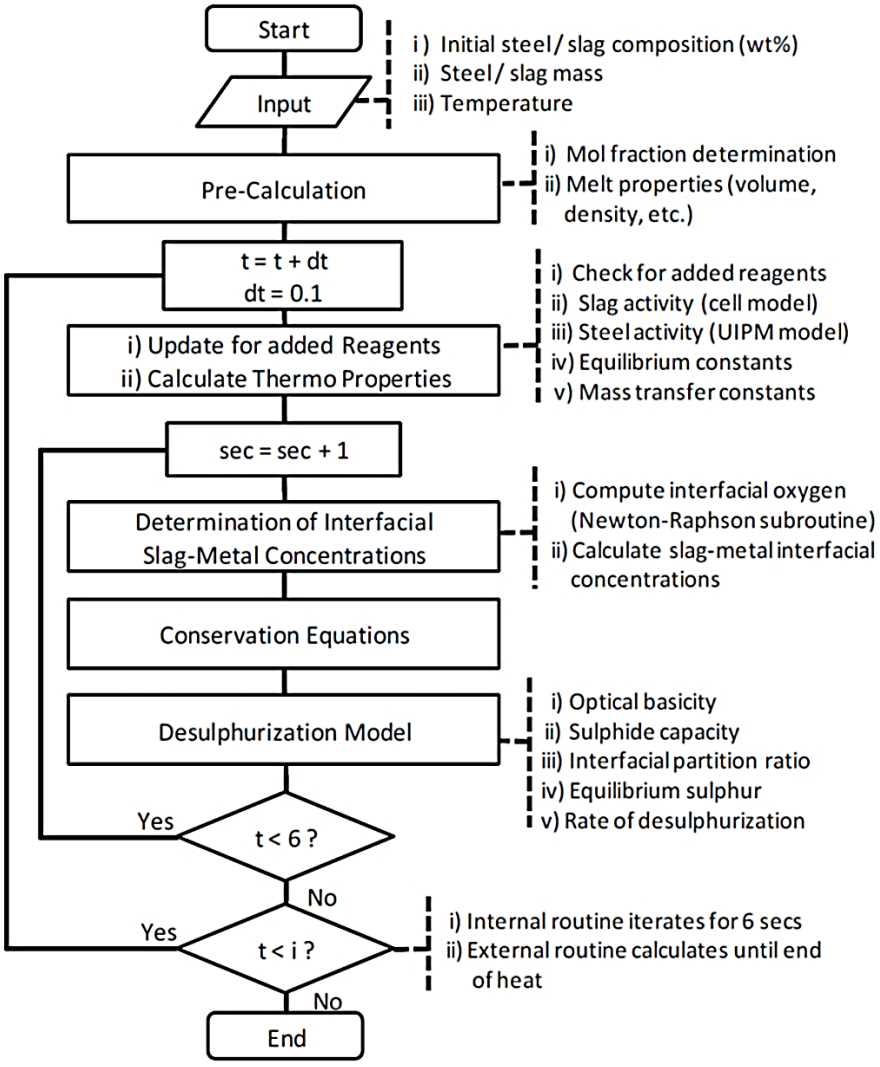

Figure 2-23. Schematic of multicomponent kinetic model (Graham, 2008)

From their calculations of the slag-steel equilibrium the dissolved magnesium contents in steel ranged between 50 to 200 ppm. Furthermore, the authors pointed out that the overall system moves towards a state of slag-metal-inclusion equilibrium during the refining process in the LMF; finally they also

suggested that magnesium reduction from the ladle slag is the main source of magnesium contamination to produce spinel inclusions.

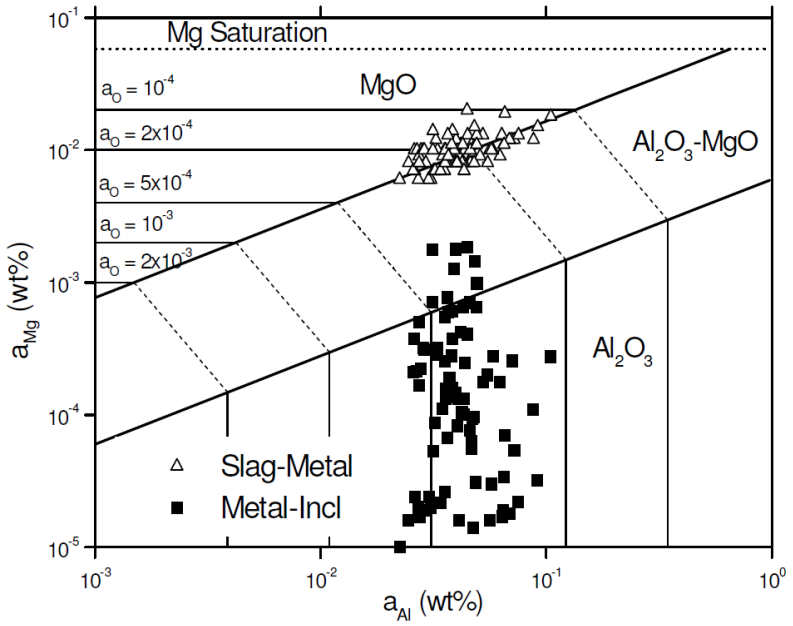

Figure 2-24. [Al]-[Mg]-[O] equilibrium diagram in liquid steel at 1873 K using the thermodynamic data of Nadif & Gatellier (1986). Dissolved magnesium levels were calculated on the basis of slag-metal (■), and metal-inclusion (Δ) equilibrium (Graham & Irons, 2010)

Recently, a kinetic coupled model to describe industrial operations in the ladle furnace was proposed by Harada et al (2013). This is a complex model that considers: 1) reactions between steel and slag based on the multicomponent kinetic model of Robertson et al (1984), 2) reactions between steel and inclusions originating from slag entrapment, 3) deoxidation caused by the additions, 4) dissolution of the refractory into the slag phase and 5) formation, flotation and agglomeration of inclusions. Rates for slag entrapment, agglomeration of

inclusions and inclusions flotation are described with constant ratios, Figure 2-25. At each time step the composition of the different phases is updated. The model was validated with the reported results of Graham and Irons (2010).

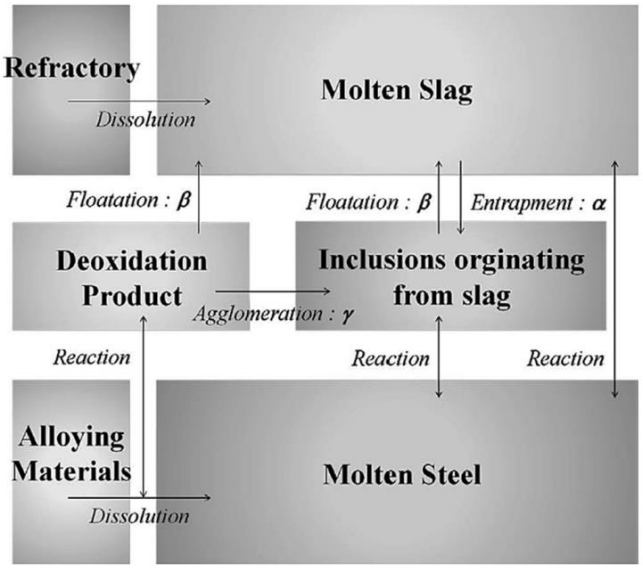

Figure 2-25. Schematic of the kinetic model proposed by Harada, et al., (2013)

The activities of the components in the slag were obtained using the software FactSage 6.3 (Bale et al., 2009) and ChemApp (Petersen & Hack, 2007). The inclusions composition was calculated considering deoxidation reactions for [Al], [Ca], [Mg] and [Si]. The possible deoxidation products were $MnO{\cdot}SiO_2$, Al_2O_3, $MgO{\cdot}Al_2O_3$ and $CaO{\cdot}Al_2O_3$. Also, the activities of the individual components for a given oxide system of the inclusions were fixed, for example in spinel $MgO\text{-}Al_2O_3$, the activity of MgO was 0.5 and for Al_2O_3 was 0.08. After the addition of a deoxidizer, the free energy of formation for each deoxidation

reaction is calculated, an iterative procedure was used where the composition in the steel and the inclusions is modified until all the ΔG of reaction become positive.

With their developed model, Harada et al (2013b) compared the influence of the different factors that affect the amount of spinel inclusions; sensitivity analysis were made for different parameters including: ratio of slag entrapment, flotation rate, rate of agglomeration of inclusions, amount of aluminum added for deoxidation, MgO content in the slag and slag basicity. From this analysis the authors suggested that spinel formation can be reduced with the control in conjunction of the Al-deoxidation, MgO in slag and the slag basicity.

Chapter 3

Kinetic model for the oxide inclusions

3.1 Chemical kinetics of particle-fluid systems

Solid-fluid reactions are present in several industrial operations and the respective kinetic analysis is of utmost importance in order to optimize operations. As mentioned by Sohn (2014), heterogeneous reactions occur at phase boundaries, unlike homogeneous reactions that take place over the entire volume of a given phase. Therefore, heterogeneous reactions always involve the transfer of mass and heat between the reaction interface and the bulk phase. The reaction in a solid-fluid system consists of the following steps (Sohn, 2014; Wen, 1968):

1. Diffusion of the fluid reactants across the fluid film surrounding the solid
2. Diffusion of the fluid reactants within the pores of the solid, if the solid contains open porosity.
3. Chemical reaction between the fluid reactant and the solid at the fluid–solid interface.
4. Diffusion of the product away from the reaction surface through the porous solid media and through the fluid film surrounding the solid.
5. Transfer of the reaction heat within the solid.
6. Transfer of heat between the external surface of the solid and the surroundings by convection and radiation.

7. Changes in the structure of the solid due to chemical reaction and heat.

There are several types of solid-fluid reactions of metallurgical interest; gas-solid reactions have been reviewed by Szekely, et al., (1976), while processes of extractive metallurgy have been reviewed by Sohn and Wadsworth (1979). As mentioned by Sohn (2014) the most common case in metallurgical operations occurs when an initially non-porous solid reacts with a fluid to form a product layer (ash) around the unreacted portion of the solid and the reaction progresses from the outer surface of the solid toward its interior, the chemical reaction takes place then at the sharp interface between the reacted and the unreacted zone. This topochemical reaction mechanism is modeled on the basis of a shrinking-core structure, Figure 3-1.

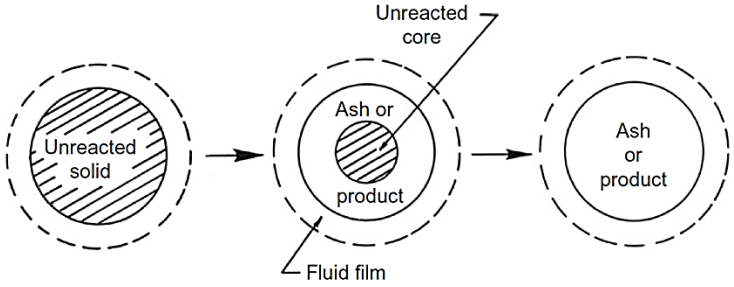

Figure 3-1. Shrinking-core reaction mechanism (Sohn & Wadsworth, 1979)

The general rate equations for each kinetic step of the shrinking-core model and the different kinetic limiting cases have been reviewed by Levenspiel (1998), Szekely & Themelis (1971) and Wen (1968). As mentioned by Levenspiel (1998), a key assumption of the shrinking-core mechanism is that the reaction occurs at a sharp interface between the product layer and the unreacted solid. The

model has limited applicability for cases when the reactant solid is very porous and when the solid is converted by the effect of heat even without the presence of fluid.

3.2 Description of the model for oxide inclusions

In this thesis a kinetic model is proposed to describe the transformation of the alumina inclusions to magnesium aluminate inclusions in liquid steel. The model calculates the compositional changes in the oxide inclusions and in the liquid steel. The formation of spinel is assumed to occur as a product layer in the oxide particles.

3.2.1 Assumptions of the model

The kinetic steps, geometry and phase interfaces of the model are shown in the diagram of Figure 3-2. The main assumptions of the kinetic model for the oxide inclusions are:

1. The kinetics of the process is mass transfer controlled.
2. Transport of the dissolved species [Mg], [Al] and [O] from the bulk of the liquid steel phase to the interface of each inclusion occurs across a respective boundary layer.
3. A spherical geometry for the oxide inclusions is assumed during all the process. A product layer of magnesium aluminate spinel is formed over the unreacted alumina core; the shrinking core-model mechanism is assumed to

prevail. The dimensions of the inclusions change due to the chemical reactions and mass balance relationships.

4. A sharp interface divides the unreacted alumina core and the spinel layer. At this interface the concentration of the spinel components Al_2O_3 and MgO correspond to the thermodynamic equilibrium between alumina and spinel.
5. The activities of the spinel components Al_2O_3 and MgO are in local thermodynamic equilibrium with the dissolved [Mg], [Al] and [O] at the inclusion-steel interface.

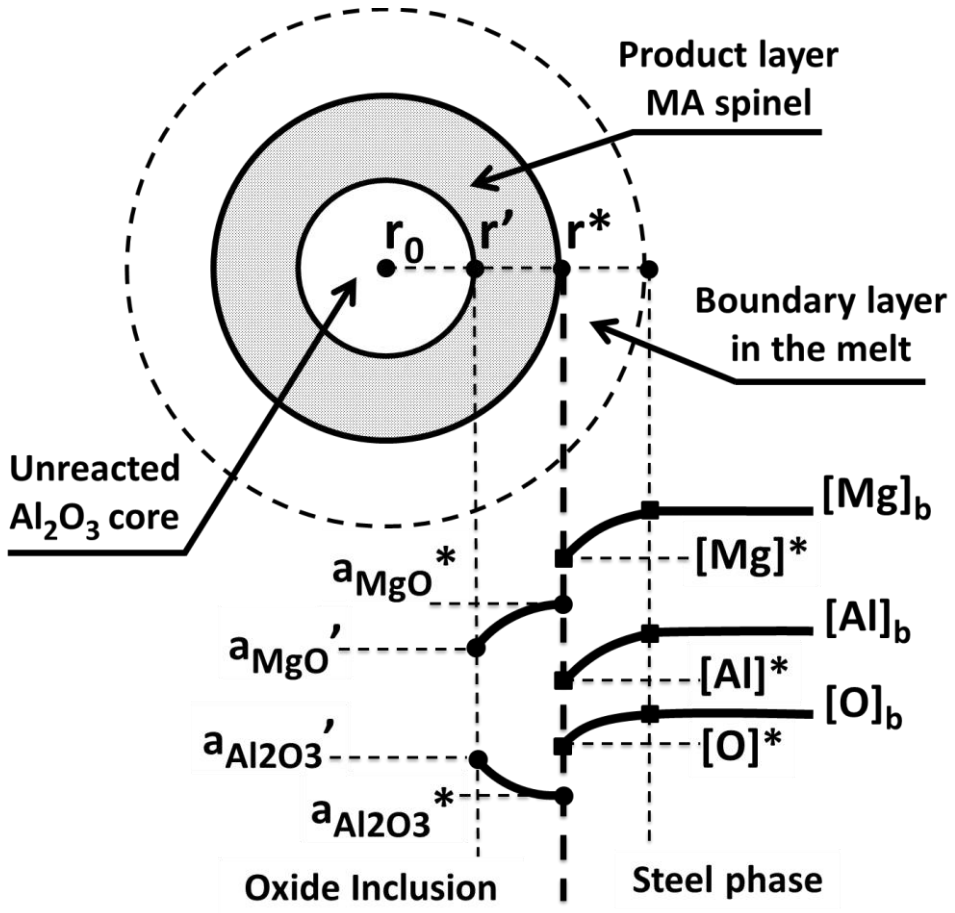

Figure 3-2. Diagram of the kinetic model for the oxide inclusions.

6. Mass transport at the boundary fluid layer and at the spinel product layer is isothermal with the liquid steel temperature.
7. Solid state cationic counterdiffusion of Mg^{2+} and Al^{3+} in the spinel product layer is described based on the Wagner-Schmalzried theory for spinel formation.
8. The alumina and spinel phases are dense.

The rate equation for each step of the model is solved considering the boundary conditions of the system as well as the thermodynamic and kinetic constraints.

3.2.2 Mass transfer of the species dissolved in liquid steel

As reviewed by Oeters (1994) and Szekely & Themelis (1971) during the mass transfer between a fluid and a condensed phase, solid or liquid, there is a region adjacent to the interface in which the concentration differs from that in the bulk of the fluid; this region is known as the diffusion boundary layer and it is analogous to the velocity and temperature boundary layers at interfaces for momentum and heat transfer. If the fluid is in movement and well stirred the transport resistance within the bulk in the fluid is negligible so that the concentration of species is virtually uniform and the only resistance for mass transfer exists in the boundary layer.

Szekely and Themelis (1971) also mention that in many mass transfer problems it is not necessary to calculate the concentration profiles in the boundary

layer, instead of that the knowledge of the mass transfer rate between a solid and a fluid or between two fluids is more useful, Figure 3-3.

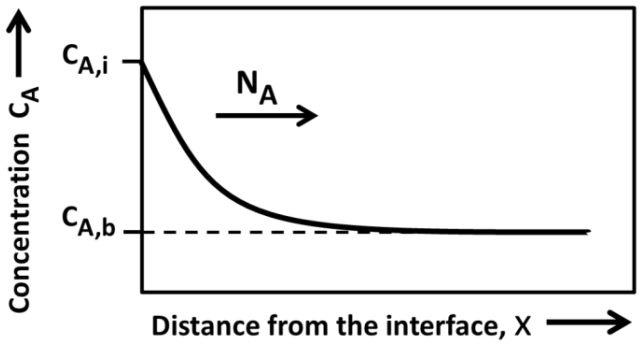

Figure 3-3. Scheme of the concentration profile in the boundary layer close to the interface for mass transfer in the fluid.

The equation for the mass transfer rate through the boundary layer from the bulk of the fluid to the surface of a spherical particle is:

$$N_A = 4\pi r^{*2} \cdot k_A C \, (X_A^b - X_A^*) \tag{3-1}$$

Where k_A is the mass transfer coefficient across the boundary layer, r* is the particle radius, C is the total molar concentration in the fluid phase, X_A^b is the mole fraction of the species A in the bulk of the fluid phase and X_A^* is the mole fraction of the species A at the surface of the particle. Since Equation 3-1 neglects the effect of the bulk flow, the expression only applies to systems involving either equimolar counterdiffusion or small concentrations of the diffusing species. The mass transfer coefficient k_A is related to the fluid flow conditions, the geometry of the system and the properties of the system. From the dimensionless analysis, k_A is obtained with the Sherwood number that is defined as:

$$Sh = \frac{k_A d}{D_{[A]}} \tag{3-2}$$

Here d is the particle diameter and $D_{[A]}$ is the diffusivity of the species in the fluid. Szekely & Themelis (1971) mention that in the limiting case of a spherical particle in a motionless fluid the Sherwood number at steady state conditions is equal to 2. Oeters (1994) further explained that for liquid steel if there is flow of the melt, its effect on the Sherwood number does not need to be considered if the particle diameter is smaller than 14 μm because for those particle sizes the flow field no longer contributes to the mass transfer and Sh = 2. In both scenarios, this assumption implies that at the boundary layer only mass transport by diffusion is possible and that there is no convective contribution.

In the inclusion-steel model the oxide inclusions are assumed to be spherical, Figure 3-2. Also, the model is designed to study indigenous inclusions during ladle furnace treatment where the inclusions of more interest are smaller than 10 μm (Story, et al., 2008). The mass transfer coefficients are calculated assuming that the Sherwood number is 2 and with the published diffusivities of the species in liquid iron, the values used are: $D_{[Mg]} = 3 \times 10^{-9}\, m^2 \cdot s^{-1}$ (Irons, et al., 1978), $D_{[Al]} = 3.5 \times 10^{-9}\, m^2 \cdot s^{-1}$ (Nagata, et al., 1988) and $D_{[O]} = 3.1 \times 10^{-9}\, m^2 \cdot s^{-1}$ (Lu, 1992). Therefore, the equations for the mass transfer rate through the boundary layer for [Mg], [Al] and [O] diffusing from the bulk of the liquid steel phase to the inclusions surface are:

$$N_{[Mg]} = 4\pi r^{*2} \cdot k_{Mg} C_{Vm} \left(X_{Mg}^{b} - X_{Mg}^{*}\right) \tag{3-3}$$

$$N_{[Al]} = 4\pi r^{*2} \cdot k_{Al} C_{Vm} (X_{Al}^{b} - X_{Al}^{*}) \tag{3-4}$$

$$N_{[O]} = 4\pi r^{*2} \cdot k_{O} C_{Vm} (X_{O}^{b} - X_{O}^{*}) \tag{3-5}$$

C_{Vm} is the total molar concentration in the steel phase; X_{Mg}^{b}, X_{Al}^{b} and X_{O}^{b} are the bulk mole fractions while X_{Mg}^{*}, X_{Al}^{*} and X_{O}^{*} are the mole fraction concentrations at the interface between each inclusion and the steel.

3.2.3 Cationic diffusion in the spinel product layer

Mass transfer in the magnesium aluminate spinel product layer is assumed to occur by counterdiffusion of Mg^{2+} and Al^{3+}. The diffusion equations are based on the Wagner-Schmalzried theory for spinel formation. At a given point in the spinel product layer and with the frame of reference of an immobile sublattice of oxygen, the mass transfer rates of Mg^{2+} and Al^{3+} are driven by the gradient in the electrochemical potential with respect to the radial position, therefore:

$$N_{Mg^{2+}} = 4\pi r^{2} \cdot \frac{D_{Mg} C_{Mg}}{RT} \left(\frac{\partial \eta_{Mg^{2+}}}{\partial r} \right) \tag{3-6}$$

$$N_{Al^{3+}} = 4\pi r^{2} \cdot \frac{D_{Al} C_{Al}}{RT} \left(\frac{\partial \eta_{Al^{3+}}}{\partial r} \right) \tag{3-7}$$

Where D_{Mg} and D_{Al} are the chemical diffusivities of Mg^{2+} and Al^{3+} in magnesium aluminate spinel and C_{Mg} and C_{Al} are the molar concentration of the cations. For the chemical diffusivities Wagner (1975) referred to them as ‘component diffusivities’; furthermore, it is mentioned that for cationic diffusion in oxides and sulphides the diffusivity of a species as component is related to its

self-diffusion coefficient D_A^* also known as tracer diffusion coefficient according to the relation:

$$D_{A(component)} = \frac{D_A^*}{\mathrm{f}_A} \tag{3-8}$$

Here $\mathrm{f_A}$ is the correlation factor that depends on the crystalline structure of the spinel and on the diffusion mechanism of the cations that can be either interstitial or via vacancies. On the other hand, the correlation factor is of the order of unity (Ganguly, 2002; C Wagner, 1975). For the inclusions model the diffusivity values of Götze et al., (2009) are used in equations (3-6) and (3-7), these values were calculated from solid state spinel rim growth experiments at 1623 K and considering simultaneous diffusion of Mg^{2+} and Al^{3+} as well as the coupling of fluxes to keep electroneutrality. Götze et al., (2009) reported the diffusion coefficients as effective component diffusivities since they include a relative contribution of grain boundary diffusion and of volume diffusion to bulk material transport, their values are: $D_{Mg(component)} = 1.4 \times 10^{-15}\, m^2 \cdot s^{-1}$ and $D_{Al(Component)} = 3.7 \times 10^{-16}\, m^2 \cdot s^{-1}$. Furthermore, because of the temperature and experimental conditions to measure the diffusivities used for this model and since the reported component diffusivities in magnesium aluminate are limited; a sensitivity analysis of the different kinetic parameters was included in this thesis project.

Assuming that there is no resistance for the flow of electrons or electron holes, the driving forces for cation diffusion become the gradients in the chemical potential of the neutral components Mg and Al in the product layer:

$$N_{Mg^{2+}} = 4\pi r^2 \cdot \frac{D_{Mg} C_{Mg}}{RT} \left(\frac{\partial \mu_{Mg}}{\partial r} \right) \tag{3-9}$$

$$N_{Al^{3+}} = 4\pi r^2 \cdot \frac{D_{Al} C_{Al}}{RT} \left(\frac{\partial \mu_{Al}}{\partial r} \right) \tag{3-10}$$

Considering the formation reactions for MgO and Al_2O_3, the chemical potentials of Mg and Al and O are related by:

$$\mu_{Mg} + \mu_O = \mu_{MgO} \tag{3-11}$$

$$2\mu_{Al} + 3\mu_O = \mu_{Al_2O_3} \tag{3-12}$$

With equations (3-11) and (3-12) the mass transfer rates of Mg^{2+} and Al^{3+} become:

$$N_{Mg^{2+}} = 4\pi r^2 \cdot \frac{D_{Mg} C_{Mg}}{RT} \left[\frac{\partial \mu_{MgO}}{\partial r} - \frac{\partial \mu_O}{\partial r} \right] \tag{3-13}$$

$$N_{Al^{3+}} = 4\pi r^2 \cdot \frac{D_{Al} C_{Al}}{RT} \left[\frac{1}{2} \frac{\partial \mu_{Al_2O_3}}{\partial r} - \frac{3}{2} \frac{\partial \mu_O}{\partial r} \right] \tag{3-14}$$

For the spinel formation in the indigenous inclusions the inner interface of the spinel product layer is in contact with the Al_2O_3 shrinking core, at that point there is no additional access of oxygen. On the contrary, at the spinel-steel interface there is access of the dissolved Mg, Al and Oxygen. Under those conditions of the inner and external interfaces Schmalzried & Pfeiffer (1986)

proposed that the variation in the chemical potential of oxygen can be obtained by coupling the mass transfer rates of $N_{Mg^{2+}}$ and $N_{Al^{3+}}$ where electroneutrality is maintained according to:

$$2N_{Mg^{2+}} = -3N_{Al^{3+}} \tag{3-15}$$

Using expressions (3-13) and (3-14) and relating them according to (3-15), the gradient of the chemical potential for oxygen in the product layer becomes:

$$\frac{\partial \mu_O}{\partial r} = RT \frac{D_{Mg} C_{Mg} \frac{\partial \mu_{MgO}}{\partial r} + \frac{3}{4} D_{Al} C_{Al} \frac{\partial \mu_{Al_2O_3}}{\partial r}}{D_{Mg} C_{Mg} + \frac{9}{4} D_{Al} C_{Al}} \tag{3-16}$$

At steelmaking temperatures magnesium aluminate spinel has a range of solubility with Al_2O_3 and its composition deviates from the stoichiometric spinel $MgAl_2O_4$. Several forms to express the nonstoichiometry in spinel have been used in the literature, one of the most common formulae is $MgO{\cdot}nAl_2O_3$ where n is the molar ratio. With the same molar ratio n, an equivalent formula is $Mg_{\frac{4}{3n+1}}Al_{\frac{8n}{3n+1}}V_{\frac{n-1}{3n+1}}O_4$ where V represents the concentration of cation vacancies (Mitchell, 1999; Viertel & Seifert, 1979; Wei, et al., 1998). Watson & Price (2002) used the formula $Mg_{1-3x}Al_{2+2x}\square_xO_4$ where □ is a cation vacancy. For this thesis, the spinel is described as $Mg_\delta Al_\upsilon O_4$ where the indexes δ and υ are related to the mole fraction of alumina $X_{Al_2O_3}$ assuming that spinel only varies in the quasi-binary system Al_2O_3-MgO, therefore:

$$\delta = \frac{4 - 4X_{Al_2O_3}}{1 + 2X_{Al_2O_3}} \tag{3-17}$$

$$\upsilon = \frac{8X_{Al_2O_3}}{1 + 2X_{Al_2O_3}} \tag{3-18}$$

On the other hand, the molar volume of spinel V_m^{Sp} slightly changes when the solubility with Al_2O_3 increases (Ganesh, 2013), for this thesis the value $V_m^{Sp} = 41.419$ [mm^3/mmol] reported by Fiquet, et al., (1999) at T = 1889 K is assumed constant; the molar concentrations of Mg^{2+} and Al^{3+} in spinel are:

$$C_{Mg^{2+}} = \frac{\delta}{V_m^{Sp}} \tag{3-19}$$

$$C_{Al^{3+}} = \frac{\upsilon}{V_m^{Sp}} \tag{3-20}$$

From its definition, the variation of the chemical potential of a component in a system is related to the change in the activity of the component:

$$d\mu_i = RT\, d\ln a_i \tag{3-21}$$

With the expressions for cationic concentration and the change in chemical potential, equation (3-16) for the gradient in the chemical potential is:

$$\frac{\partial \mu_O}{\partial r} = RT \frac{\delta \cdot D_{Mg}\left(\frac{\partial \ln a_{MgO}}{\partial r}\right) + \frac{3}{4}\upsilon \cdot D_{Al}\left(\frac{\partial \ln a_{Al_2O_3}}{\partial r}\right)}{\delta \cdot D_{Mg} + \frac{9}{4}\upsilon \cdot D_{Al}} \tag{3-22}$$

With equation (3-22), the mass transfer rates of Mg^{2+} and Al^{3+} at a given point in the spinel product layer become:

(3-23)

$$N_{Mg^{2+}} = 4\pi r^2 qea \cdot \frac{\delta\, \upsilon \cdot D_{Mg} D_{Al}}{4\delta \cdot D_{Mg} + 9\upsilon \cdot D_{Al}} \left(\frac{1}{V_m^{Sp}}\right)\left[9\left(\frac{\partial \ln a_{MgO}}{\partial r}\right) - 3\left(\frac{\partial \ln a_{Al_2O_3}}{\partial r}\right)\right]$$

(3-24)

$$N_{Al^{3+}} = 4\pi r^2 \cdot \frac{\delta\, \upsilon \cdot D_{Mg} D_{Al}}{4\delta \cdot D_{Mg} + 9\upsilon \cdot D_{Al}} \left(\frac{1}{V_m^{Sp}}\right)\left[2\left(\frac{\partial \ln a_{Al_2O_3}}{\partial r}\right) - 6\left(\frac{\partial \ln a_{MgO}}{\partial r}\right)\right]$$

Equations (3-23) and (3-24) express the coupled cationic mass transfer rates at a point in the spinel product layer driven by the gradients in the activities of the components of the Al_2O_3-MgO system.

3.2.4 Calculation of the inclusion-steel interfacial equilibrium

Thermodynamic equilibrium at the inclusion-steel interface is calculated based on the simultaneous deoxidation equilibria of [Mg] and [Al] in steel with the components in spinel Al_2O_3 and MgO. The calculation is possible by coupling the interfacial mass transfer rates of the different components involved. In order to consider the change in the bulk concentration of the dissolved oxygen due to the inclusions a special consideration is required. Because the anion sublattice of oxygen is assumed to be immobile in the spinel product layer, it is not possible to formulate an expression for oxygen diffusion as in the case of Mg^{2+} and Al^{3+}. However, since there is access of the dissolved oxygen [O] at the spinel-steel interface then lattice molecules of spinel with composition $Mg_{\delta^*}Al_{\upsilon^*}O_4$ can be added to or subtracted from the spinel product layer at a given molar rate r_M.

In this case, δ∗ and ν∗ indicate the composition of spinel in equilibrium with steel at the radial position r*. Pfeiffer and Schmalzried (1989) defined the balance of lattice molecules M at the interface as:

$$\frac{\partial n_M}{\partial t} = r_M \quad (r^*, t) \tag{3-25}$$

In this way, the molar rate r_M at the interface is related to the mass transfer of oxygen in the liquid steel boundary layer by:

$$r_M = \frac{1}{4} N_{[O]} \tag{3-26}$$

Furthermore, the addition or subtraction rate of spinel with composition $Mg_{\delta^*}Al_{\upsilon^*}O_4$ at the interface r* must be considered in the rates of consumption or release of dissolved [Mg] and [Al] in the steel; for magnesium this is:

$$N_{[Mg]} = N_{Mg^{2+}}\Big|_{r*} + \frac{\delta^*}{4} N_{[O]} \tag{3-27}$$

The balance of the mass transfer rates for aluminum is:

$$\frac{\upsilon^*}{4} N_{[O]} = -N_{Al^{3+}}|_{r*} + N_{[Al]} \tag{3-28}$$

Where $N_{Mg^{2+}}\Big|_{r*}$ and $N_{Al^{3+}}|_{r*}$ are the mass transfer rates in the product layer at the inclusion-steel interface r*. Equations (3-27) and (3-28) are the most important expressions for the calculation of the interfacial concentrations in the formation of spinel. For example, with a source of dissolved [Mg] and if the mass transfer of [O] is small then the change of Al_2O_3 inclusions to spinel will occur mostly by consumption of [Mg] and release of some [Al] to the steel.

$N_{Mg^{2+}}\big|_{r*}$ and $N_{Al^{3+}}|_{r*}$ are calculated by considering the spinel composition in equilibrium with steel and the activity gradients in the product layer evaluated at the interface, therefore:

(3-29)

$$N_{Mg^{2+}}\big|_{r*} = 4\pi r^{*2}\frac{\delta^* v^* \cdot D_{Mg}D_{Al}}{4\delta^* D_{Mg} + 9v^* D_{Al}} \cdot \frac{1}{V_m^{Sp}}\left[9\frac{\partial \ln a_{MgO}}{\partial r}\Big|_{r*} - 3\frac{\partial \ln a_{Al_2O_3}}{\partial r}\Big|_{r*}\right]$$

(3-30)

$$N_{Al^{3+}}|_{r*} = 4\pi r^{*2}\frac{\delta^* v^* \cdot D_{Mg}D_{Al}}{4\delta^* D_{Mg} + 9v^* D_{Al}} \cdot \frac{1}{V_m^{Sp}}\left[2\frac{\partial \ln a_{Al_2O_3}}{\partial r}\Big|_{r*} - 6\frac{\partial \ln a_{MgO}}{\partial r}\Big|_{r*}\right]$$

Since the diffusion equations in the product layer are solved numerically, the derivatives for the radial change of $a_{Al_2O_3}$ and a_{MgO} in equations (3-29) and (3-30) are discretized using spatially equidistant nodes and a fourth-order backward finite difference approximation that takes only the local values at the interface as shown in Figure 3-4:

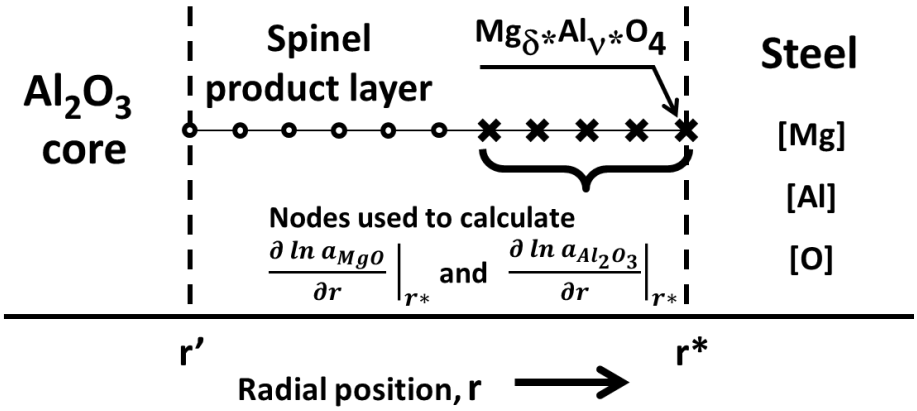

Figure 3-4. Scheme of the spatial discretization in the product layer and location of the nodes adjacent to the interface used for the equilibrium calculations.

Considering the heterogeneous equilibrium for the deoxidation reactions with [Mg] and with [Al] the interfacial activities are related according to:

$$K_{MgO} = \frac{a_{MgO}\ *}{[f_{Mg}^{*} \cdot\ wt\%Mg^{*}][f_{O}^{*} \cdot\ wt\%O^{*}]} \tag{3-31}$$

$$K_{Al_2O_3} = \frac{a_{Al_2O_3}\ *}{[f_{Al}^{*} \cdot\ wt\%Al^{*}]^2[f_{O}^{*} \cdot\ wt\%O^{*}]^3} \tag{3-32}$$

Where K_{MgO} and $K_{Al_2O_3}$ are the equilibrium constants of deoxidation; $a_{Al_2O_3}$* and a_{MgO}* are the interfacial activities in spinel; wt%Mg*, wt%Al* and wt%O* are the interfacial concentrations of the species in steel and f_{Mg}^{*}, f_{Al}^{*}, and f_{O}^{*} are the henrian activity coefficients calculated at the inclusion-steel interface calculated with the Unified Interaction Parameter Formalism.

The concentrations of the dissolved [Mg], [Al] and [O] can be expressed in the respective mole fractions X_{Mg}^{*}, X_{Al}^{*} and X_{O}^{*}, therefore:

$$K_{MgO} = \frac{a_{MgO}\ *}{\left[\frac{X_{Mg}^{*} f_{Mg}^{*} \cdot n_T Mw_{Mg} \cdot 100}{St_{mass}}\right]\left[\frac{X_{O}^{*} f_{O}^{*} \cdot n_T Mw_{O} \cdot 100}{St_{mass}}\right]} \tag{3-33}$$

$$K_{Al_2O_3} = \frac{a_{Al_2O_3}\ *}{\left[\frac{X_{Al}^{*} f_{Al}^{*} \cdot n_T Mw_{Al} \cdot 100}{St_{mass}}\right]^2\left[\frac{X_{O}^{*} f_{O}^{*} \cdot n_T Mw_{O} \cdot 100}{St_{mass}}\right]^3} \tag{3-34}$$

Where n_T are the total number of moles in the steel phase; Mw_{Mg}, Mw_{Al}, and Mw_{O} are the molar weights of the species and St_{mass} is the total mass of the steel phase. The set of thermodynamic data used to calculate the deoxidation

equilibrium with [Mg] and [Al] were taken from the published values of Seo, et al., (1998) and Seo & Kim (2000), therefore: $K_{Al_2O_3} = 12.32 - 47400/T$ and $K_{MgO} = -7.21$ at 1873 K. The first and second order interaction parameters are: $e_{Al}^{O} = -6.90,\ r_{Al}^{O} = 7.60,\quad e_{O}^{Al} = 15.57 - 36500/T,\ r_{O}^{Al} = 2.67,\ e_{Mg}^{O} = -560,$ $r_{Mg}^{O} = 145000,\ e_{O}^{Mg} = -370,\ r_{O}^{Mg} = 5900$. Additional interaction parameters for the effect of other elements were taken from the review of the Japan Society for the Promotion of Science (Hino & Ito, 2010). Although there are variations in the literature values for deoxidation with [Mg]; the reported results of Seo and Kim (2000) were used for this model since that thermodynamic study was considered by Jung, et al., (2004) in their assessment for deoxidation. Jung, et al., (2004) preferred these values because of the experimental procedure used and with their agreement with the results of Han, et al., (1997).

The variations of the activities $a_{Al_2O_3}$ and a_{MgO} in the Al_2O_3-MgO system were represented with sigmoidal functions empirically fitted to the measured values at 1873 K of Fujii, et al. (2000), the respective functions are shown in Figure 3.5. The function for the change in $a_{Al_2O_3}$ with the mole fraction $X_{Al_2O_3}$ is:

$$a_{Al_2O_3} = a_1 - (a_1 - b_1) \cdot exp\left[-\left(k_1 \cdot X_{Al_2O_3}\right)^{d_1}\right] \qquad (3\text{-}35)$$

Where the parameters are: a_1 = 1, b_1 = 0.034, k_1 = 1.862 and d_1 = 15.131. The activity of MgO as a function of $X_{Al_2O_3}$ is calculated with:

$$a_{MgO} = \frac{b_2}{\left[1 + \left(\frac{c_2}{X_{Al_2O_3}}\right)^{h_2}\right]^{s_2}} \tag{3-36}$$

The respective parameters are: b_2 = 1, c_2 = 0.462, h_2 = -143.245 and s_2 = 0.127. Figure 3-5 shows how the fitted functions compare with the activities calculated using the database of the software FactSage 6.4 (C. W. Bale et al., 2009) that contains the thermodynamic assessment of Jung, et al., (2004b) for the Al_2O_3-MgO system.

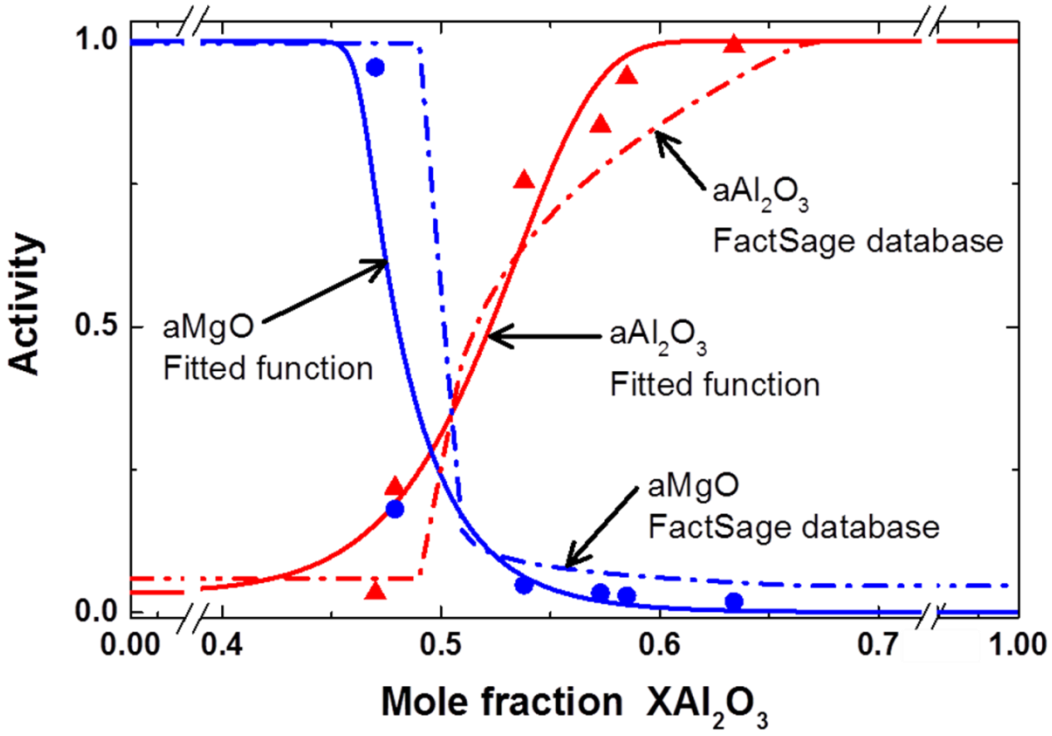

Figure 3-5. Activities of the components in the system Al_2O_3-MgO at 1873 K. Experimental measurements from Fujii, et al., (2000): ●⟶ a_{MgO} and ▲⟶$a_{Al_2O_3}$. Fitted functions from equations (3-35) and (3-36) and values obtained with FactSage 6.4

In order to find the equilibrium activities, concentrations and spinel composition $Mg_{\delta^*}Al_{\upsilon^*}O_4$ at the inclusion-steel interface; equations (3-27) and (3-28) for the interfacial mass balances are solved in conjunction with the equilibrium conditions (3-33), (3-34) and the functions for the activities (3-35) and (3-36). Appendix A outlines the procedure in which the non-linear system of six equations is solved numerically for the six unknowns X^*_{Mg}, X^*_{Al}, X^*_O, $a_{Al_2O_3}{}^*$, $a_{MgO}{}^*$ and $X_{Al_2O_3}{}^*$ that allow to calculate the interfacial mass transfer rates.

3.2.5 Unsteady state diffusion model for the spinel product layer

Diffusion across the product layer of magnesium aluminate spinel is driven by the gradient in the chemical potentials of the neutral components $\frac{\partial \mu_{Mg}}{\partial r}$ and $\frac{\partial \mu_{Al}}{\partial r}$. For this dynamic system the concentration and mass transfer rates of Mg^{2+} and Al^{3+} change with position and time. The accumulation model for cationic unsteady state diffusion in the product layer is described according to:

$$4\pi r^2 \frac{\partial C_{Mg^{2+}}}{\partial t} = \frac{\partial}{\partial r}\left(N_{Mg^{2+}}\right) \qquad r' \leq r \leq r^* \tag{3-37}$$

Here $C_{Mg^{2+}}$ is the molar concentration of Mg^{2+} in spinel. The domain of the diffusion equation goes from the inner interface at the radial position r' where spinel is in contact with the alumina core to the interface r^* where the product layer is in contact with liquid steel. From the Wagner-Schmalzried theory the

mass transfer rate $N_{Mg^{2+}}$ is defined with equation (3-9), therefore the model for one-dimensional diffusion is:

$$\frac{\partial C_{Mg^{2+}}}{\partial t} = \frac{1}{r^2} \cdot \frac{\partial}{\partial r}\left[r^2 \frac{D_{Mg} C_{Mg}}{RT} \left(\frac{\partial \mu_{Mg}}{\partial r} \right) \right] \tag{3-38}$$

After expansion of the terms and assuming that the diffusivity D_{Mg} is constant the model becomes:

$$\frac{\partial C_{Mg^{2+}}}{\partial t} = \frac{D_{Mg}}{RT} \left[\frac{2}{r} C_{Mg} \left(\frac{\partial \mu_{Mg}}{\partial r} \right) + \left(\frac{\partial C_{Mg}}{\partial r} \right) \left(\frac{\partial \mu_{Mg}}{\partial r} \right) + C_{Mg} \left(\frac{\partial^2 \mu_{Mg}}{\partial r^2} \right) \right] \tag{3-39}$$

$$r' \leq r \leq r^*$$

Examination of the partial differential equation (3-39) shows that three different effects are involved in the model and that these effects contain the non-linear variation of the chemical potential μ_{Mg} with composition in spinel. Therefore the model in (3-39) is a non-linear second order PDE that requires two boundary conditions to fully describe the process.

An efficient alternative to solve non-linear time dependent PDE equations such as (3-39) is the numerical discretization using the Method of Lines. (Silebi & Schiesser, 1992; Wouwer, et al., 2001). For the general time dependent PDE problem in the form:

$$\boldsymbol{u}_t = \mathbf{f}(\boldsymbol{u}), \qquad \boldsymbol{x}_L < \boldsymbol{x} < \boldsymbol{x}_R\,, \quad t > 0 \tag{3-40}$$

In this case $\boldsymbol{u}_t = \frac{\partial \boldsymbol{u}}{\partial t}$, $\boldsymbol{u}$ is the vector of dependent variables, t is the initial value independent variable, $\boldsymbol{x}$ are the boundary value independent variables, $\boldsymbol{f} = \boldsymbol{f}(\boldsymbol{x}, t, \boldsymbol{u}, \boldsymbol{u}_x, \boldsymbol{u}_{xx}, \cdots)$ is the spatial differential operator and $\boldsymbol{u}(t = 0)$ is known. The Method of Lines (MOL) is a computational approach for solving PDE problems of the form of equation (3-40) that proceeds in two separate steps (Wouwer et al., 2001):

1. Spatial derivatives $\boldsymbol{u}_x, \boldsymbol{u}_{xx}, \cdots$ are approximated using finite difference (FD) or finite element (FE) techniques.
2. The resulting system of semi-discrete ordinary differential equations in the initial value variable is integrated in time, t.

Therefore, by first discretizing with a spatial grid of N nodes, then a large system of N initial value ODEs can be integrated with an ODE integrator. The values of each node correspond to the solution u at a grid point as a function of time, Figure 3-6.

As mentioned by Hundsdorfer and Verwer, (2007) the MOL approach is very popular for its simplicity and flexibility as well as for the fact that is easy to model various combined effects for advection and diffusion with reaction terms. Another practical point in favor of this method is that many well developed ODE solver methods are freely available.

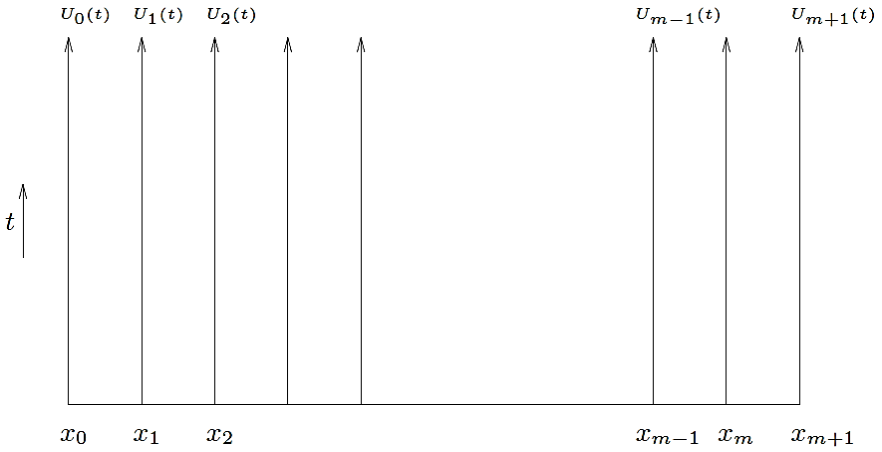

Figure 3-6. Method of lines interpretation. $u_i(t)$ is the solution along the line forward in time at the grid point x_i, (LeVeque, 2007).

For the diffusion model in the product layer the spatial domain is discretized with equidistant nodes U_i according to:

$$C_{Mg}(i,q) = U(r_i,\ t_q) \tag{3-41}$$

The equidistant nodes $U_i = U(r_i)$ are located across the product layer with the expressions:

$$h = \frac{r^* - r'}{n-1} \tag{3-42}$$

$$r_i = r' + (i-1)h \qquad i = 1, \dots, n \tag{3-43}$$

Here n is the total number of nodes and h is the distance between each node. The kinetic model assumes that the initial condition of the system is $C_{Mg}(i, t=0) = C_{Mg}^{eq}$ for all the nodes; where C_{Mg}^{eq} corresponds to the equilibrium composition of Al_2O_3 with spinel in the Al_2O_3-MgO binary system located at $X_{Al_2O_3}^{eq} = 0.68$. In order to simplify the model the initial nucleation

process of spinel on the alumina inclusions is neglected. Therefore, the model assumes that a small homogeneous shell of spinel is already formed at $t = 0$, the total number of Mg^{2+} moles per inclusion particle is then:

$$n_{Mg^{2+}} = \frac{4\pi}{3}\frac{\delta_{eq}}{V_m^{Sp}}\left(r'^3 - r^{*3}\right) \tag{3-44}$$

The total initial number of Al^{3+} moles per inclusion must consider the content in the homogeneous spinel product layer and the content in the alumina core, therefore:

$$n_{Al^{3+}} = \frac{4\pi}{3}\frac{\upsilon_{eq}}{V_m^{Sp}}\left(r'^3 - r^{*3}\right) + \frac{4\pi}{3}r'^3\left(\frac{2}{V_m^{Al_2O_3}}\right) \tag{3-45}$$

Here $\delta_{eq}$and υ_{eq} are the stoichiometric indices of the spinel composition that is in equilibrium with alumina at $X_{Al_2O_3}^{eq}$. V_m^{Sp} and $V_m^{Al_2O_3}$ are the molar volumes of spinel and alumina respectively. Furthermore, the initial total atomic percentage of Mg in the inclusions is related to the moles of Mg^{2+} and Al^{3+} per inclusion with:

$$\%Mg|_{t=0} = \left(\frac{n_{Mg^{2+}}|_{t=0}}{n_{Mg^{2+}}|_{t=0} + n_{Al^{3+}}|_{t=0}}\right) \times 100 \tag{3-46}$$

If the initial atomic percentage of Mg in the inclusions $\%Mg|_{t=0}$ and the diameter of the inclusions particles is known, then thickness of the initially homogeneous spinel layer and the position of r' can be calculated with equations (3-44), (3-45) and (3-46):

(3-47)

$$r' = \left[\frac{r^{*3}\left[\frac{\delta_{eq}}{V_m^{Sp}} - \left(\frac{\%Mg}{100}\right)\left(\frac{\upsilon_{eq}}{V_m^{Sp}}\right) - \left(\frac{\%Mg}{100}\right)\left(\frac{\delta_{eq}}{V_m^{Sp}}\right)\right]}{\frac{\delta_{eq}}{V_m^{Sp}} - \left(\frac{\%Mg}{100}\right)\left(\frac{\upsilon_{eq}}{V_m^{Sp}}\right) + \left(\frac{\%Mg}{100}\right)\left(\frac{2}{V_m^{Al_2O_3}}\right) - \left(\frac{\%Mg}{100}\right)\left(\frac{\delta_{eq}}{V_m^{Sp}}\right)} \right]^{\frac{1}{3}}$$

Once the domain of the product layer and the nodes U_i are specified at a time step t, it is possible to calculate the activities $a_{Al_2O_3}(i,t)$ and $a_{MgO}(i,t)$ as well as the value of the terms $\left.\frac{\partial \mu_{Mg}}{\partial r}\right|_{i,t}$, $\left.\frac{\partial^2 \mu_{Mg}}{\partial r^2}\right|_{i,t}$ and $\left.\frac{\partial C_{Mg}}{\partial r}\right|_{i,t}$ for the PDE (3-39) at each node. The detailed procedure based on finite differences approximations is described in Appendix B of this thesis.

3.2.5.1 Interfacial boundary conditions for the cationic diffusion model

Since the diffusion model in equation (3-39) is described with a second order PDE then two boundary conditions must be specified in addition to the initial condition of the system. For the interaction of the spinel product layer with the liquid steel the boundary condition imposed is known as an interfacial boundary condition or boundary condition of the fourth type (Luikov, 1968; Taler & Duda, 2006).

As mentioned by Luikov (1968), the boundary condition of the fourth kind applies when there is heat transfer between a solid body and liquid through convective transfer. For the mass transfer process of cationic diffusion the PDE

model is expressed in terms of the change in molar concentration in spinel C_{Mg} , therefore the two boundary conditions at the interface r^* for a given time step are:

$$\left.\frac{\partial C_{Mg^{2+}}}{\partial r}\right|_{t,\ r^*} = \left(\frac{\partial C_{Mg^{2+}}}{\partial r}\right)^* \tag{3-48}$$

$$C_{Mg^{2+}}(r^*, t) = C_{Mg^{2+}}^{equilib} \tag{3-49}$$

Here $\left(\frac{\partial C_{Mg^{2+}}}{\partial r}\right)^*$ is the gradient of C_{Mg} in the spinel product layer at the interface with steel; therefore it is a function of the cationic mass transfer $N_{Mg^{2+}}\big|_{r*}$ which is obtained from the simultaneous deoxidation equilibria and the interfacial mass balance calculated at each time step. Additionally, $C_{Mg^{2+}}^{equilib}$ corresponds to the molar concentration of Mg in the product layer in equilibrium with the steel. The calculation to obtain the values of the interfacial boundary conditions from the results of the simultaneous equilibrium is described in Appendix B of this thesis. Additionally, the procedure to enforce the boundary conditions in the spatial discretization of the PDE model is described in Appendix B.

3.2.5.2 Time integration of the diffusion model

After the diffusion equation (3-39) has been spatially discretized at a given time step, each node is integrated in time from t_q to t_{q+1}. Since the model is non-linear an explicit Runge-Kutta method was selected in order to simplify the calculations. The general scheme of an explicit *m*-stage Runge-Kutta method for

the ODE problem $\dot{y} = F(t, y)$ and initial condition $y(0) = y_0$ is described as (Gustafsson, 1991; Hairer, et al., 2011) :

$$\dot{Y}_1 = F\left(t_q, y_n\right) \tag{3-50.1}$$

$$\dot{Y}_i = F\left(t_q + c_i \Delta t_q\,, y_n + \Delta t_q \sum_{J=1}^{i-1} a_{iJ} \dot{Y}_J\right) \qquad i = 2, \ldots, m \tag{3-50.2}$$

$$y_{q+1} = y_q + \Delta t_q \sum_{J=1}^{m} b_j \dot{Y}_J \tag{3-50.3}$$

$$t_{q+1} = t_q + \Delta t_q \tag{3-50.4}$$

The real coefficients a_{iJ}, b_J and c_i depend on the specific Runge-Kutta method while Δt_n is the time step used. For each time integration an estimation of the error is necessary; as mentioned by Hairer et al., (2011) the error estimations ensure that Δt_i is chosen to be sufficiently small to maintain the required precision and stability of the computed results; additionally, they ensure that the step sizes are large enough to avoid unnecessary computational work. A practical approach is to use embedded Runge-Kutta formulas that allow calculation of the numerical approximation y_1 and a second approximation $\hat{y}_1$ by sharing the results of the stages in the step. In this way, the difference $\|y_1 - \hat{y}_1\|$ provides an estimate of the local error for the less accurate approximation which then can be used for step size control.

For the diffusion model several embedded Runge-Kutta methods were tested including the method of Fehlberg RKF45 (Hairer et al., 2011), the Strong

Stability Preserving method SSPRK(9,3) (Gottlieb, et al., 2011) and the 8th order method of Prince & Dormand DOP853 described in (Hairer et al., 2011) and (Hairer & Wanner, 2002). From all these explicit integrators, the method DOP853 was chosen since it proved to be the best in terms of accuracy and number of iterations per modeling case. The adaptive time step control strategy is based on the modified PI method proposed by Gustafsson (1991) and further described by Söderlind (2002) and (Hairer & Wanner, 2002). The specifics of the Runge-Kutta time integration and the time step control are in Appendix B.

3.2.6 Displacement of boundaries in the spinel product layer

3.2.6.1 Movement of the interface between Al_2O_3 and the spinel product layer

Under the assumption of the shrinking core model it is necessary to determine, at each time step, the location of the interface between the unreacted alumina core and the spinel product layer. In this kinetic model the moving boundary is denoted with the radial position r', Figure 3-2.

The progress of the Al_2O_3-spinel interface is determined based on the assumption that there is a sharp interface where the two phases in contact reach local thermodynamic equilibrium; this has been experimentally demonstrated for solid state diffusion couples (Götze et al., 2009; Navias, 1961; Zhang, et al., 1996). Therefore, from the Al_2O_3-MgO binary system the equilibrium composition of Al_2O_3 with spinel C_{Mg}^{eq} at 1873 K corresponds to the mole

fraction $X_{Al_2O_3}^{eq} = 0.68$ (Fujii, et al., 2000; Zienert & Fabrichnaya, 2013). A scheme of the Mg concentration profile in the product layer obtained with the PDE model and the displacement of the boundary is shown in Figure 3-7.

Defining the alumina-spinel equilibrium composition at r' as $Mg_{\delta'}Al_{\upsilon'}O_4$ the indexes δ' and υ' are obtained with $X_{Al_2O_3}^{eq}$. Considering that there is no additional source of oxygen, the interfacial reaction at r' is:

$$\delta' Mg^{2+} + \frac{4}{3}Al_2O_3 = Mg_{\delta'}Al_{\upsilon'}O_4 + \left(\frac{8}{3} - \upsilon'\right)Al^{3+} \tag{3-51}$$

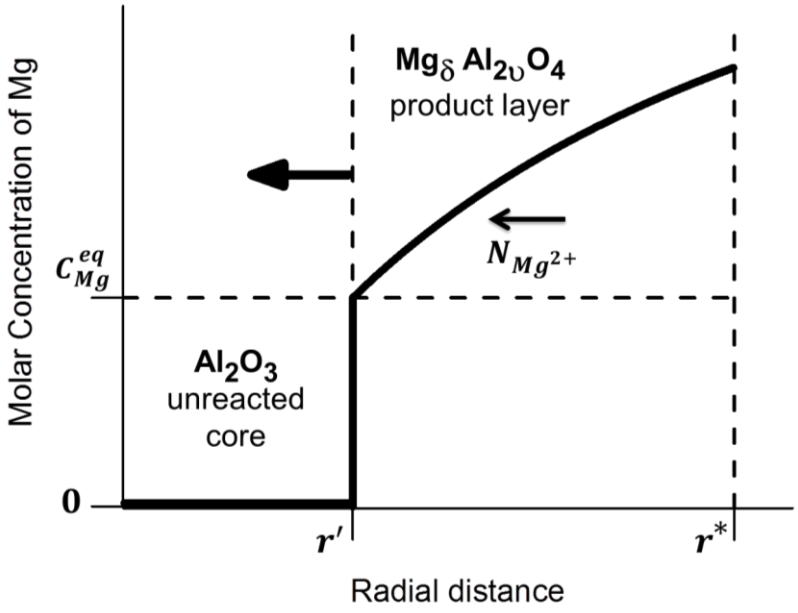

Figure 3-7. Concentration profile of Mg in the spinel product layer and position r' of the interfacial composition in equilibrium with alumina at a given time step.

A characteristic of the displacement of $r'(t)$ with time is that this problem belongs to the group of Stefan problems for heat or mass transfer (Crank, 1987). The solution of the inner moving boundary of the spinel product layer is based on

the stoichiometric mass balance and on the strategies proposed by Crank & Gupta (1972) that include displacement of the discretization grid and interpolation using cubic splines.

With the known concentrations and activities at each node it is possible to calculate the mass transfer rate of $N_{Mg^{2+}}$ at r' in the product layer at each time step. Therefore, the number of moles of Mg^{2+} transferred at r' during the lapse of a time integration step is approximated with:

$$n_{Mg^{2+}}\Big|_{t_q} = \left(N_{Mg^{2+}}\Big|_{r',\ t_q}\right) \cdot \Delta t_q \tag{3-52}$$

From reaction (3-51) at r' and expression (3-52), the change in the number of moles of the alumina core consumed during the time step per inclusion is:

$$\Delta n_{Al_2O_3}\Big|_{t_q} = -\frac{4}{3\delta'} \cdot N_{Mg^{2+}}\Big|_{r',\ t_q} \cdot \Delta t_q \tag{3-53}$$

The respective volume of alumina core reacted per inclusion per time step is obtained with the molar volume of alumina $V_m^{Al_2O_3}$:

$$\Delta V_{Al_2O_3}\Big|_{t_q} = -\frac{4}{3\delta'} V_m^{Al_2O_3} \cdot N_{Mg^{2+}}\Big|_{r',\ t_q} \cdot \Delta t_q \tag{3-54}$$

Simultaneously, the number of moles of non-stoichiometric spinel with composition $Mg_{\delta'}Al_{v'}O_4$ that is produced at r' during the time step is:

$$\Delta n_{Mg_{\delta'}Al_{v'}O_4}\Big|_{t_q} = \frac{1}{\delta'} \cdot N_{Mg^{2+}}\Big|_{r',\ t_q} \cdot \Delta t_q \tag{3-55}$$

The respective volume of the spinel produced at r' is:

$$\Delta V_{Mg_{\delta'}Al_{v'}O_4}\Big|_{t_q} = \frac{1}{\delta'} V_m^{Sp} \cdot N_{Mg^{2+}}\Big|_{r',\ t_q} \cdot \Delta t_q \tag{3-56}$$

Due to the difference in the molar volumes, the transformation of alumina to magnesium aluminate spinel implies a volumetric expansion; this effect has an impact on the position of the discretizing nodes. For this model, such change is considered as an increase on the distance Δr_{Sp} that occurs from time t_q to t_{q+1}. On solving a similar diffusion problem Crank & Gupta (1972) suggested to move the complete discretizing grid and transfer the information of the concentration values of each node to a new grid. Additionally, Wouwer et al., (2001) used adaptive grids for the Method of lines (MOL) when the PDE models involve moving boundaries. Wouwer et al., (2001) proposed the use of cubic splines as the interpolation technique to transfer the data from the old to the new grid, the information in the new nodes is the initial condition for the next time integration of the system.

If r'_{t_q} is the position of the inner boundary at the time step t_q and $r'_{t_{q+1}}$ is the new position at t_{q+1} the volume change of the alumina core from (3-54) is related according to:

$$\Delta V_{Al_2O_3} = \frac{4}{3}\pi\left[\left(r'_{t_{q+1}}\right)^3 - \left(r'_{t_q}\right)^3\right] \tag{3-57}$$

The volume of the spinel produced during the time step from equation (3-56) is considered with:

$$\Delta V_{Mg_{\delta'}Al_{\upsilon'}O_4} = \frac{4}{3}\pi\left[\left(r^{Sp}_{t_{q+1}}\right)^3 - \left(r'_{t_{q+1}}\right)^3\right] \tag{3-58}$$

In this last expression $r_{t_{q+1}}^{Sp}$ allows to calculate the increase on the radial distance Δr_{Sp} due to volumetric expansion, Figure 3-8:

$$\Delta r_{Sp} = r_{t_{q+1}}^{Sp} - r'_{t_q} \tag{3-59}$$

In the discretization of the product layer the first node U_1 is located at the alumina-spinel interface. Therefore, its location at the next time step is:

$$U_1|_{t_{q+1}} = r'_{t_{q+1}} \tag{3-60}$$

The position of the rest of the nodes U_i is updated according to:

$$r_i|_{t_{q+1}} = r_i|_{t_q} + \Delta r_{Sp} \qquad i = 2, \dots, n \tag{3-61}$$

The displacement of nodes is illustrated in Figure 3-8.

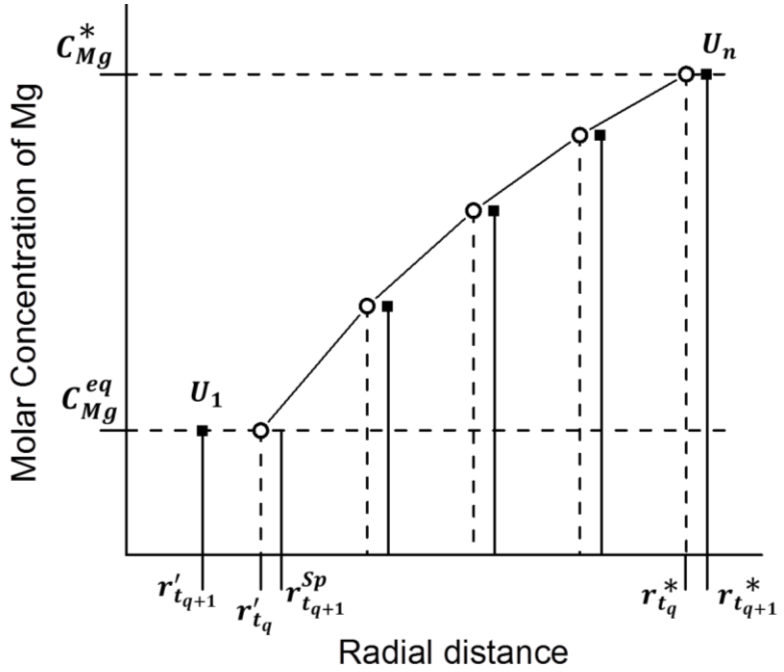

Figure 3-8. Procedure to update the location of the inner boundary. The equidistant nodes before displacement are indicated with ○. All the nodes except U_1 are shifted the distance Δr_{Sp} due to the volumetric change. The new position of the nodes is indicated with ■.

Because of the change in the inner boundary, the discretizing mesh and the position of the nodes become non-uniform. In order to have all the nodes equidistant an interpolation is made in order to transfer the information of the updated concentration profile to a new equidistant mesh for the next time integration. The interpolation is made using cubic splines; the procedure is shown in Figure 3-9.

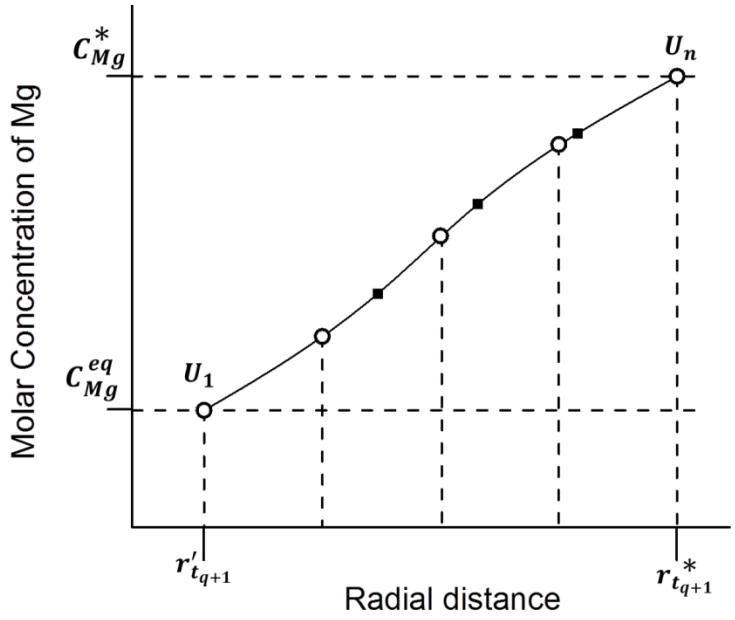

Figure 3-9. Cubic splines interpolation calculated with the updated nodes ■ in order to obtain a new mesh of equidistant nodes ○.

As the thickness of the product layer increases the distance between the nodes h increases as well. When $h \geq 2h_{min}$ the total number of nodes changes from (n) to $(n+1)$, this is shown in Figure 3-10. Here, h_{min} is the minimum distance that can exist between two consecutive nodes. In this way, the location

and the number of nodes adapts to the growth or reduction of the spinel product layer depending on the conditions of the system.

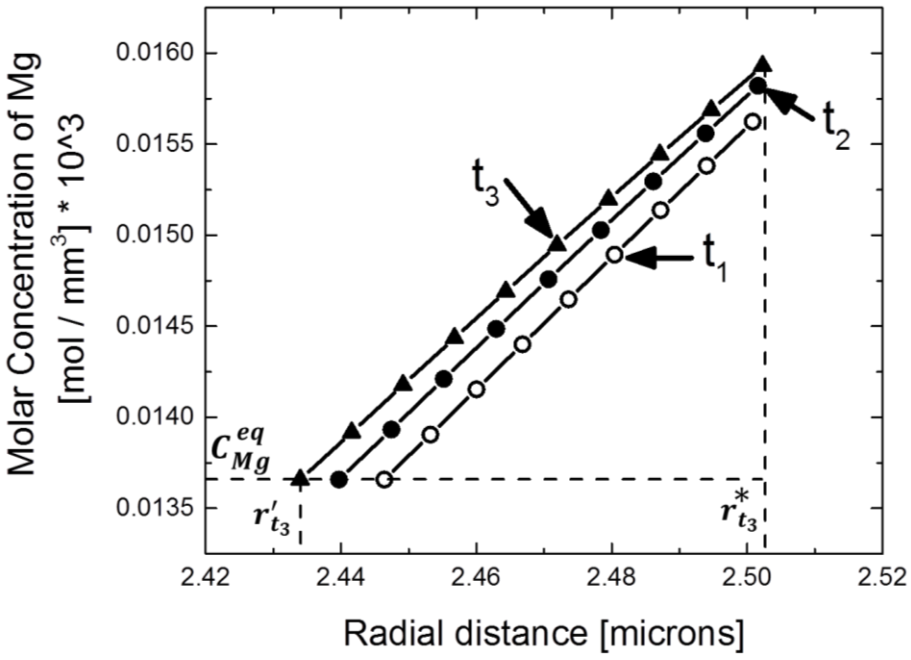

Figure 3-10. Evolution of the concentration profile with adaptation of the equidistant mesh. The distance between nodes increases from t_1 to t_2 using nine nodes. At t_3 an extra node is added.

3.2.6.2 Movement of the external boundary of the spinel product layer

In the calculation of the thermodynamic equilibrium for the simultaneous steel deoxidation with [Mg] and [Al], a mass balance at the spinel-steel interface is considered. The result of such calculations at each time step is the concentration of spinel in equilibrium with steel $Mg_{\delta^*}Al_{\upsilon^*}O_4$, as well as the activities and concentration of the species that satisfy the spinel-steel equilibrium. From these values the mass transfer rate of dissolved oxygen in steel to each inclusion can be easily calculated with equation (3-5). Therefore, the number of moles of spinel

that precipitate over the product layer during the lapse of the time integration step Δt_q is approximated with:

$$\Delta n_{Mg_{\delta^* Al_{\upsilon^*} O_4}}\Big|_{t_q} = \frac{1}{4} \cdot N_{[O]} \cdot \Delta t_q \tag{3-62}$$

The respective volume of the formed deoxidation product per particle is:

$$\Delta V_{Mg_{\delta^* Al_{\upsilon^*} O_4}}\Big|_{t_q} = \frac{1}{4} V_m^{Sp} \cdot N_{[O]} \cdot \Delta t_q \tag{3-63}$$

This additional change in volume is considered with the displacement of the interfacial node U_n located at the external boundary of the product layer $r^*_{t_q}$, Figure 3-10:

$$\Delta V_{Mg_{\delta^* Al_{\upsilon^*} O_4}} = \frac{4}{3}\pi \left[\left(r^*_{t_{q+1}} \right)^3 - \left(r^*_{t_q} \right)^3 \right] \tag{3-64}$$

The concentration value of the interfacial node C^*_{Mg} is kept constant and only its position is updated to $r^*_{t_{q+1}}$ from (3-64). In order to have all nodes equidistant the interpolation with cubic splines is repeated and a new mesh is obtained.

3.3 Unsteady state kinetic model for the formation of spinel inclusions in steel

With assumption that the diffusion process of an individual inclusion is the same for all the inclusions in a multiparticle system, it is possible to model the compositional changes in the inclusions phase and the steel phase by updating the concentration of [Mg], [Al] and [O] in steel as well as the concentration profile in the spinel product layer. Here, the steel and the oxide inclusions are a closed

system with defined initial composition. The initial size of the inclusions and the number of inclusions is also known.

The initial number of inclusions is obtained from the total oxygen concentration of the system O_T in ppm; this value comprises the parts per million [ppm] of dissolved oxygen in steel $[O]$ and the parts per million [ppm] of oxygen bonded to the oxide inclusions O_{inclus} .

$$O_T = [O] + O_{inclus} \tag{3-65}$$

With the assumed initial atomic percentage of Mg in the inclusions $\%Mg|_{t=0}$ and the initial diameter of the inclusions the thickness of the spinel product layer is calculated using expression (3-47). Therefore, the number of moles of oxygen bonded per inclusion is:

$$n_{Oxygen} = \left[\frac{4}{3}\pi\left(\frac{4}{V_m^{Sp}}\right)\cdot((r^*)^3 - (r')^3) + \frac{4}{3}\pi\left(\frac{4}{V_m^{Al_2O_3}}\right)(r')^3\right] \times 10^3 \tag{3-66}$$

The distances are in millimeters and the molar volumes V_m^{Sp} and $V_m^{Al_2O_3}$ are in mmols per mm^3. The initial number of particles is then:

$$Np = (O_{inclus} \times 10^{-4})\left(\frac{St_{mass}}{100}\right)(10^3)\left(\frac{1}{Mw_O}\right)\left(\frac{1}{n_{Oxygen}}\right) \tag{3-67}$$

The number of moles of Mg per inclusion at a given time step is quantified with the concentration profile $C_{Mg}(r)$ across the spinel product layer:

$$n_{Mg} = \left[4\pi\int_{r'}^{r^*} r^2\ \left(C_{Mg}(r)\right)dr\right] \times 10^3 \tag{3-68}$$

Here, the molar concentration $C_{Mg}(r)$ is in mmols per mm^3 and the radial distance is in millimeters. The total moles of Al per inclusion at a given time step considers the content in the product layer as well as the unreacted alumina core:

$$n_{Al} = \left[4\pi \int_{r'}^{r^*} r^2 \left(C_{Al}(r)\right) dr + \frac{4}{3}\pi(r')^3 \cdot \frac{2}{V_m^{Al_2O_3}} \right] \times 10^3 \qquad (3\text{-}69)$$

The integrals in (3-68) and (3-69) are calculated with the concentration values of Mg and Al at the equidistant nodes in the product layer and using Simpson's 3/8 rule for the numerical integration.

The change in moles of dissolved magnesium in steel $\Delta[Mg]$ being removed or added from the steel due to the oxide inclusions during a time step is quantified according to:

$$\Delta[Mg] = -\left(n_{Mg}\big|_{t_{q+1}} - n_{Mg}\big|_{t_q}\right) Np \qquad (3\text{-}70)$$

Here, $n_{Mg}\big|_{t_q}$ is the number of moles of Mg per inclusion before the time integration of the diffusion model in the product layer and $n_{Mg}\big|_{t_{q+1}}$ is the Mg content per particle after the concentration profile and position of the boundaries in the spinel product layer is updated. A similar expression is used for the change in moles of dissolved aluminum in steel during a time step:

$$\Delta[Al] = -\left(n_{Al}|_{t_{q+1}} - n_{Al}|_{t_q}\right) Np \qquad (3\text{-}71)$$

The change in moles of dissolved oxygen in steel during a time step is:

$$\Delta[O] = -N_{[O]}\big|_{t_q} \cdot Np \cdot \Delta t_q \qquad (3\text{-}72)$$

In expression (3-72) $N_{[O]}\big|_{t_q}$ is the mass transfer rate of dissolved [O] in moles per second per inclusion from the bulk of steel to the inclusion-steel interface and Δt_q is the time step used for the integration of the diffusion equation in the product layer.

The concentration in moles of the dissolved species in moles is updated for the next time step using first order time integration:

$$[Mg]_{t_{q+1}} = [Mg]_{t_q} + \Delta[Mg] \tag{3-73}$$

$$[Al]_{t_{q+1}} = [Al]_{t_q} + \Delta[Al] \tag{3-74}$$

$$[O]_{t_{q+1}} = [O]_{t_q} + \Delta[O] \tag{3-75}$$

With the new concentrations in the steel the thermodynamic equilibrium between the inclusions and the steel is recalculated which in turn provides the value of the boundary conditions for the time integration of the diffusion model in the spinel product layer. The atomic percentage of Mg in the inclusions $\%Mg|_{t_q}$ is calculated at each time step from the values of expression (3-68) and (3-69) according to:

$$\%Mg|_{t_q} = \frac{n_{Mg}\big|_{t_q}}{n_{Mg}\big|_{t_q} + n_{Al}|_{t_q}} \times 100 \tag{3-76}$$

The stepping procedure for updating the concentration in both phases at each time step is the basis of the kinetic model for the formation of spinel inclusions in steel. An scheme of the algorithm is shown in Figure 3-11.

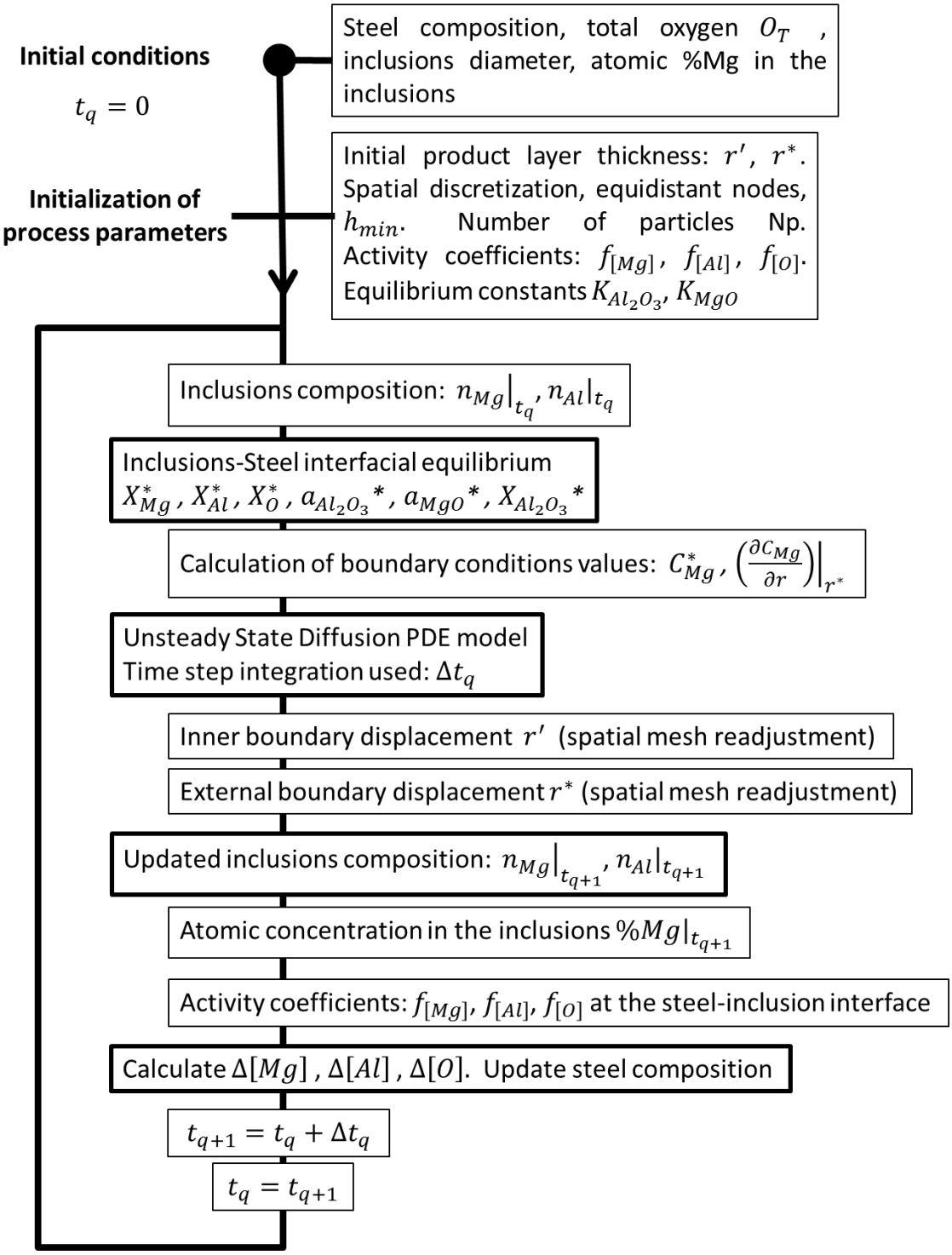

Figure 3-11. Scheme of the time step procedure of the kinetic model for the formation of magnesium aluminate spinel inclusions.

3.4 Quasi-steady state approximation for diffusion in the inclusions

In the solution of the kinetic model an additional assumption can be made for the changes in the spinel product layer. If the diffusion process in the product layer is considered to occur much faster than other processes in the system, then the product layer in each inclusion can reach a condition of steady state during a given time step. Mathematically, this assumption is expressed based on the fact that during steady state diffusion there is no change of concentration with time, therefore for the cationic diffusion model:

$$\frac{\partial C_{Mg^{2+}}}{\partial t} = 0 \qquad r' \leq r \leq r^* \qquad (3\text{-}77)$$

In this way, the concentration C_{Mg} in the product layer varies only with distance but not with time. Furthermore, if steady-state diffusion is reached, the mass transfer rate $N_{Mg^{2+}}$ is constant across the product layer and its value becomes steady as well:

$$\frac{\partial N_{Mg^{2+}}}{\partial r} = 0 \qquad r' \leq r \leq r^* \qquad (3\text{-}78)$$

On the other hand, the kinetic model describes a dynamic system in which the concentrations of the steel and the inclusions vary during the deoxidation process with [Mg] and [Al]. Therefore, the mass transfer rate through the product layer can be assumed constant and equal to the steady state value only during a time step of the kinetic model. This modeling approach known as Pseudo-steady state or Quasi-steady state approximation is a very good approximation of the shrinking-core model for systems of solid particles reacting with a gas (Szekely &

Themelis, 1971; Wen, 1968). In the case of solid particles reacting with liquids the applicability of the Quasi-steady state assumption has been analyzed and reviewed by Wen (1968) and Liddell (2005).

In order to find the steady state solution of the non-linear PDE diffusion model (3-39), the method of false transients is used. The method of false transients is based on the spatial and temporal discretization of the method of lines (MOL). As described by Schiesser (1991) this numerical approximation allows the PDE solution to proceed to essentially infinite time and converge if the solution is stable.

For a given time in the kinetic model the interfacial equilibrium between the steel and the inclusions is calculated. This allows the calculation of the interfacial boundary conditions (3-48) and (3-49) as well as the mass transfer rates of the different species for the balance at the external interface r^*. All these interfacial values are assumed constant during the Quasi-steady state step. The inner displacement of the spinel product layer and the volumetric change in the alumina core per inclusion is calculated using the mass transfer $N_{Mg^{2+}}$ at the external interface r^* , since this value must be the same all across the product layer then:

$$\Delta V_{Al_2O_3}\big|_{\Delta t} = -\frac{4}{3\delta'}\, V_m^{Al_2O_3} \cdot N_{Mg^{2+}}\big|_{r^*,\ \Delta t} \cdot \Delta t \qquad (3\text{-}79)$$

In expression (3-79) Δt refers to the length of the Quasi-steady state time step.

The new position of the inner boundary $r'_{t_{new}}$ is computed from:

$$\Delta V_{Al_2O_3}\big|_{\Delta t} = \frac{4}{3}\pi\left[\left(r'_{t_{new}}\right)^3 - \left(r'_{t_{old}}\right)^3\right] \tag{3-80}$$

The Quasi-steady state solution to the PDE model is obtained by iterating the MOL spatial and temporal discretization with as many false transient steps as necessary to reach an steady concentration profile that also satisfies the requirement of the new inner boundary position $r'_{t_{new}}$. The displacement and adjustment of the discretizing mesh is applied at each iteration. A scheme of the false transient steps is shown in Figure 3-12.

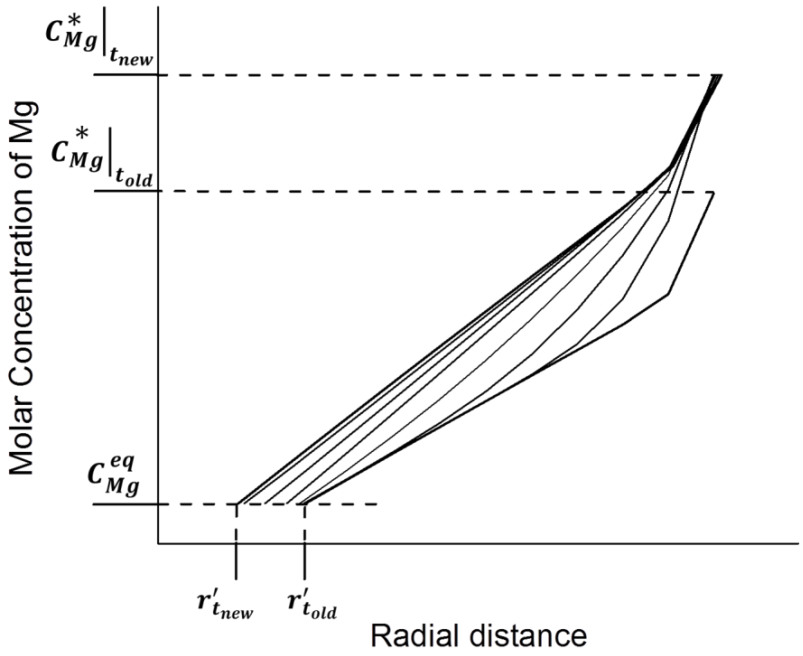

Figure 3-12. False transient time step iterations between two Quasi-steady state concentration profiles for diffusion in the spinel product layer.

The convergence of the steady state solution is assured by evaluating the relative difference in the concentration C_{Mg} at each node between two consecutive iterations:

$$max \left| \frac{C_{Mg}(i\ ,\ t_q)}{C_{Mg}(i\ ,\ t_{q+1})} - 1 \right| \leq Tol_1 \qquad i = 1, \dots, n \tag{3-81}$$

Additionally, the change in concentration with time at each node has to be less than the accuracy of the steady state solution, therefore:

$$max \left| \left(\frac{\partial C_{Mg^{2+}}}{\partial t} \right)_i \right| \leq Tol_2 \qquad i = 1, \dots, n \tag{3-82}$$

The displacement of the inner boundary continues until the value of r' during the iterations is close enough with the final displacement for the Quasi-steady state step in expression (3-80), this is measured with:

$$\left| \frac{r'_{t_q}}{r'_{t_{new}}} - 1 \right| \leq Tol_3 \tag{3-83}$$

When the conditions in (3-81), (3-82) and (3-83) are satisfied simultaneously the iterations for the concentration profile stop and the procedure for external growth of the product layer is applied with the Quasi-steady time step Δt .

$$\Delta V_{Mg_{\delta^* Al_{\upsilon^*} O_4}}\big|_{\Delta t} = \frac{1}{4} V_m^{Sp} \cdot N_{[O]} \cdot \Delta t \tag{3-84}$$

Finally, the total number of moles of Mg and Al per inclusion are calculated for the new concentration profile and the composition in the steel phase is updated. An outline of the kinetic model with the Quasi-steady state assumption for the inclusions is in Figure 3-13.

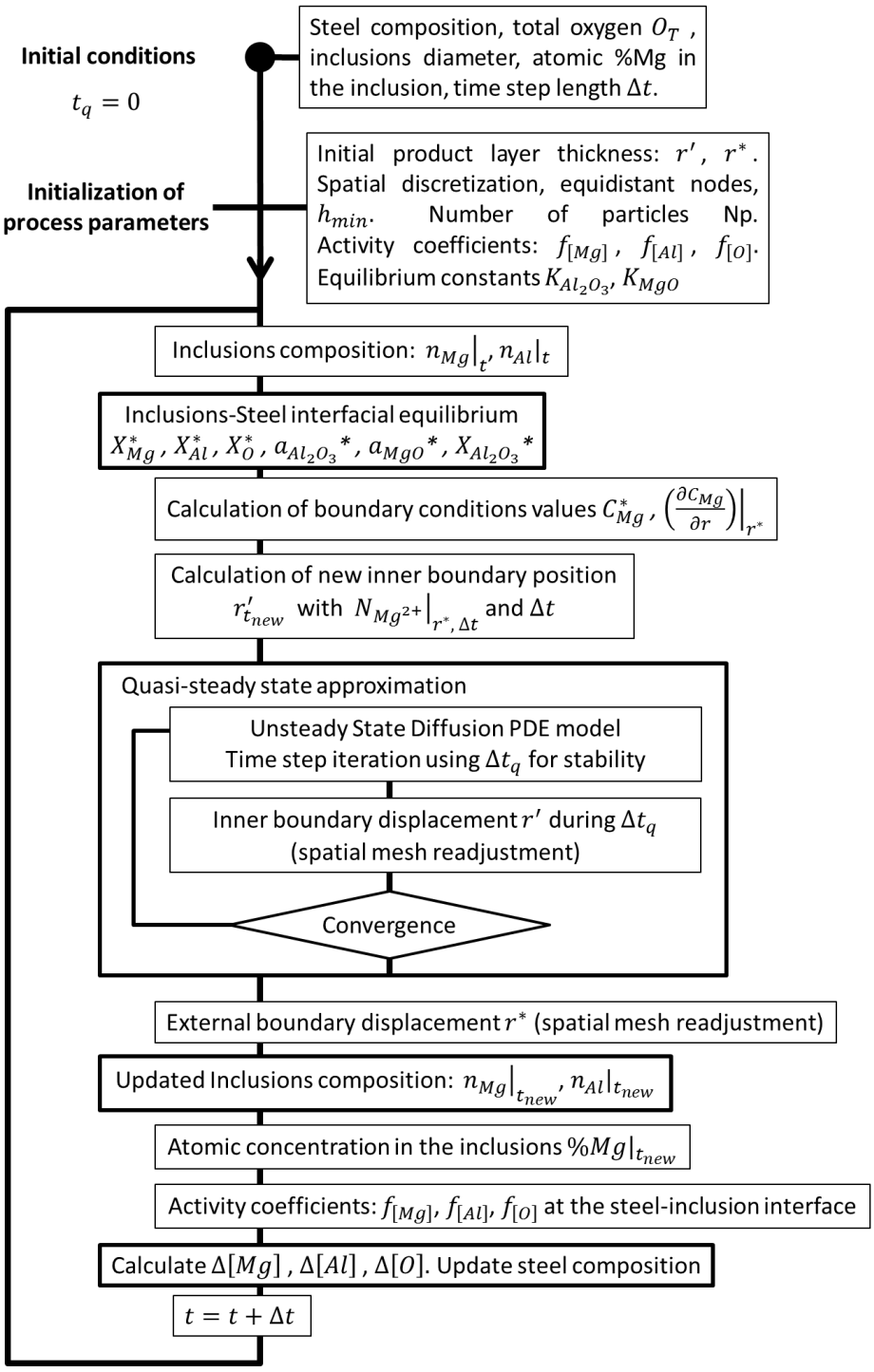

Figure 3-13. Outline of the kinetic model with the Quasi-steady approximation for diffusion in the spinel product layer.

3.5 Results from the kinetic model for the oxide inclusions

3.5.1 Results from the model for unsteady state cationic diffusion

The performance of the kinetic model was evaluated in order to analyze the compositional changes in the steel and the oxide inclusions. For simplification of the system, the steel composition was assumed to contain only dissolved [Mg], [Al] and [O]. In these calculations, the mass of the steel was 160000 kg, the temperature was kept constant at 1873 K, the total oxygen of the system was 40 ppm, the initial diameter of the inclusions was 5 microns and the initial concentration of magnesium in the inclusions was 1% atomic Mg. The only dissolved species in steel considered were [Mg], [Al] and [O]; with the initial concentrations of [Al] = 0.03 wt% and [Mg] = 3 ppm. The initial dissolved oxygen in the bulk of steel was assumed to be the equilibrium concentration from deoxidation with pure alumina $a_{Al_2O_3} = 1$, therefore [O]= 8.18 ppm.

The total concentration of the inclusions in atomic % of Mg shows that the initial high rate of Mg pickup slows down with time and eventually reaches equilibrium with the steel, Figure 3-14. In Figure 3-15, the mass transfer rates at the spinel-steel interface r^* for $N_{Mg^{2+}}$ and $N_{Al^{3+}}$ multiplied by the total number of particles Np, indicate that the diffusion rate decreases with time until the system reaches equilibrium, additionally the counterdiffusion process of cations maintains electroneutrality during all the process by coupling the mass transfer rates according to $N_{Mg^{2+}} = -\frac{3}{2} N_{Al^{3+}}$.

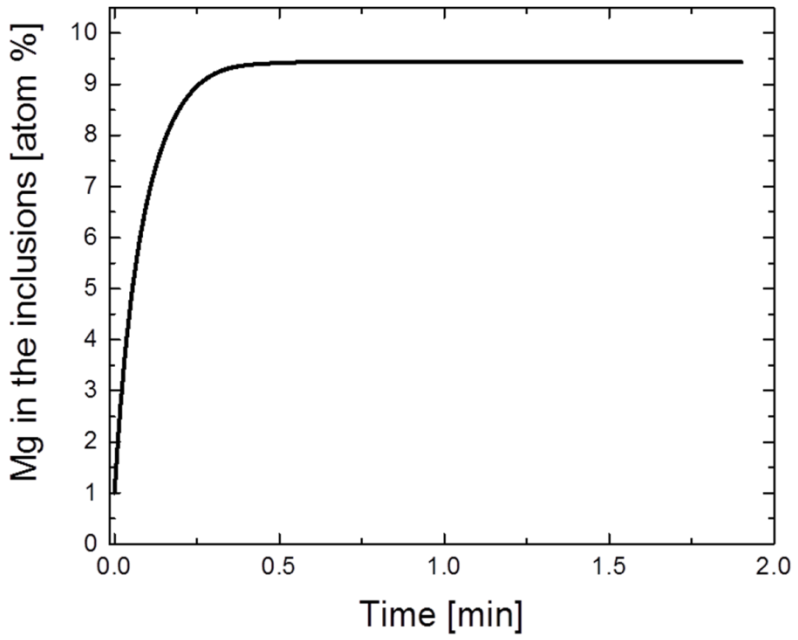

Figure 3-14. Change in the overall content of Mg in the inclusions with time

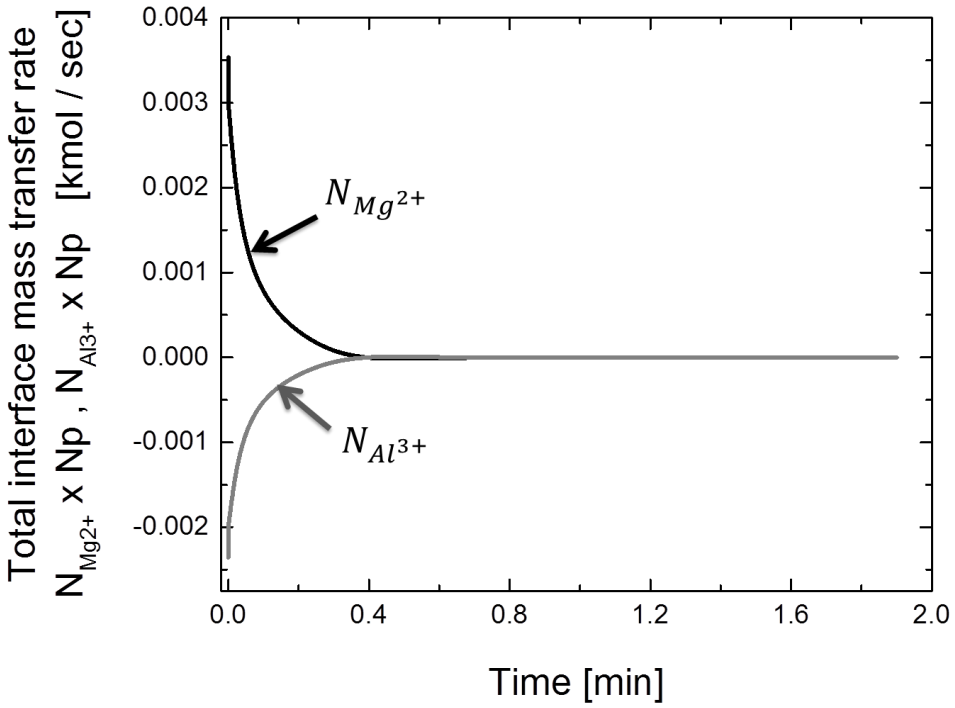

Figure 3-15. Total interface mass transfer of Mg^{2+} and Al^{3+} with time.

The change in the composition of spinel in equilibrium with steel is shown in Figure 3-16 from the variation of the interfacial mole fraction $X_{Al_2O_3}{}^*$. The rapid initial change occurs because magnesium is a stronger deoxidizer than aluminum in steel and the assumed initial product layer with composition $X_{Al_2O_3} = 0.68$ has a lower activity of MgO than the one for deoxidation with 3 ppm [Mg], this represents a driving force for the rapid change at the interface. The interfacial composition of spinel returns to the composition in equilibrium with alumina since the inclusions are not completely transformed and the dissolved [Mg] decreases with time.

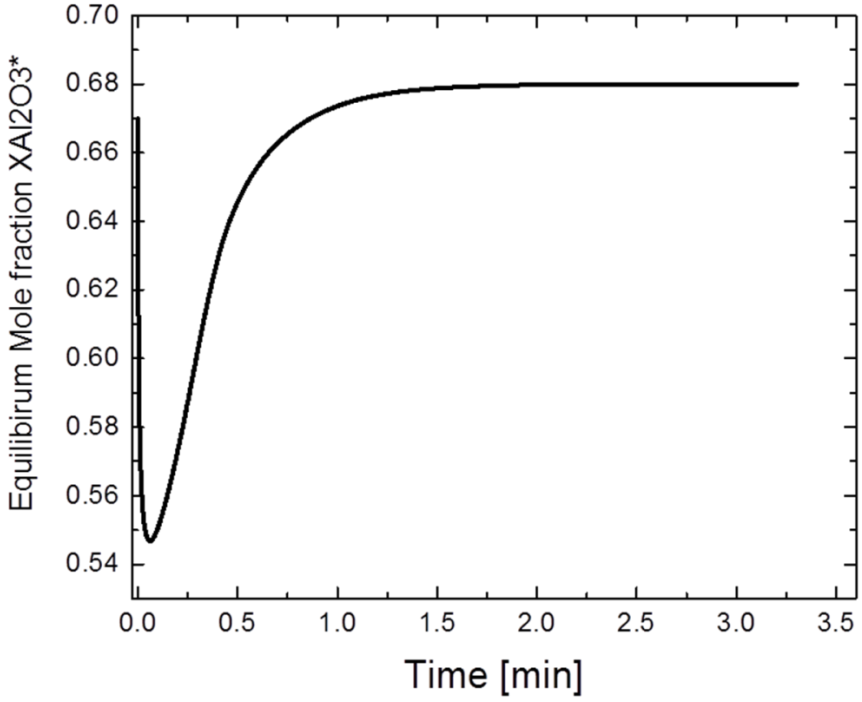

Figure 3-16. Time variation in the composition of spinel in equilibrium with steel

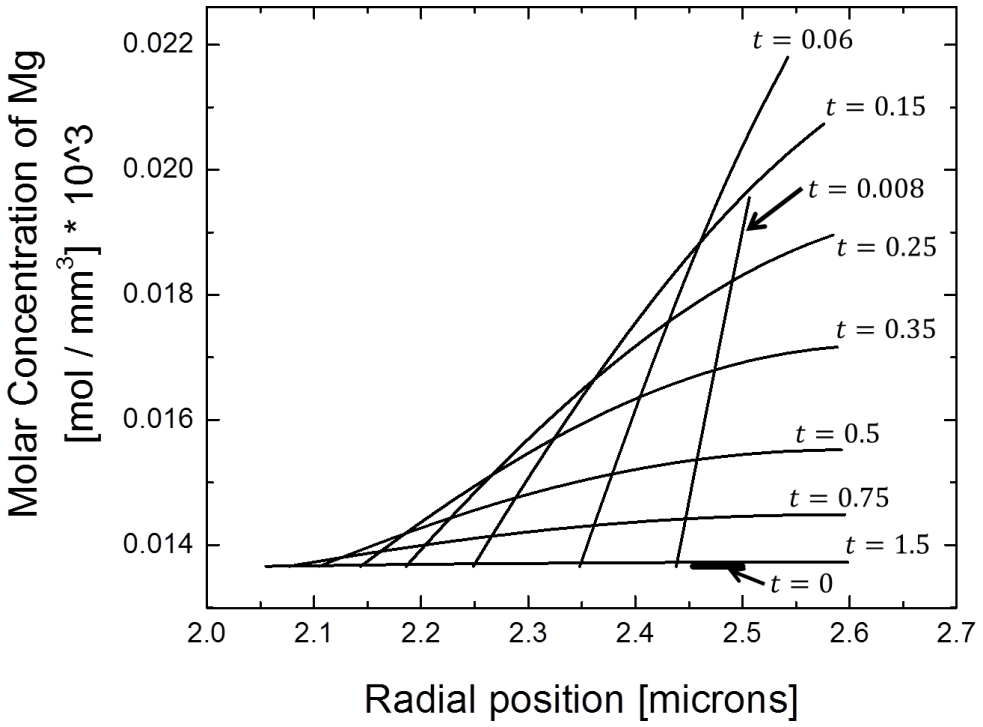

Figure 3-17. Mg concentration profile in the spinel product layer, time in minutes.

The evolution of the concentration profile in the spinel product layer in Figure 3-17 shows the change of the concentration in equilibrium with steel at r^*. After 1.5 minutes of the process, the concentration profile has the equilibrium concentration of spinel with the remaining alumina core. The calculated positions of the inner and external boundaries of the product layer are in Figure 3-18.

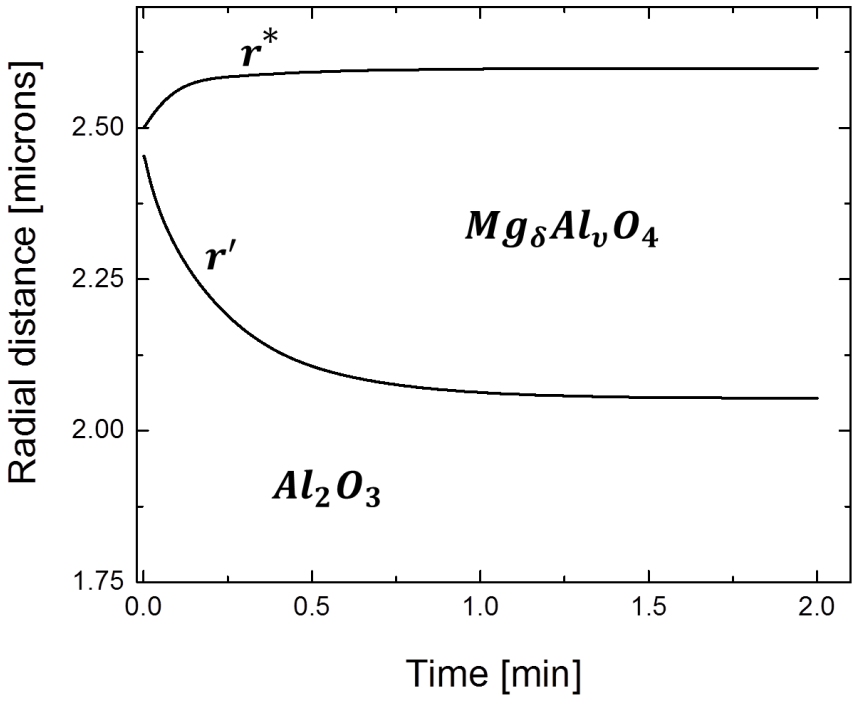

Figure 3-18. Calculated variation in the thickness of the spinel product layer

The different concentration profiles across the spinel product layer at time $t = 0.06$ minutes of the simulation were plotted. Figure 3-19 shows the variations in mole fraction $X_{Al_2O_3}$; Figure 3-20 and 3-21 show the variation in the stoichiometry indexes δ and υ of the non-stoichiometric spinel; Figure 3-22 and 3-23 illustrate the radial variation in the activities of the components a_{MgO} and $a_{Al_2O_3}$ respectively. The calculated mass transfer rates of $N_{Mg^{2+}}$ and $N_{Al^{3+}}$ across the spinel product layer showing the ratio to maintain electroneutrality are plotted in Figure 3-24.

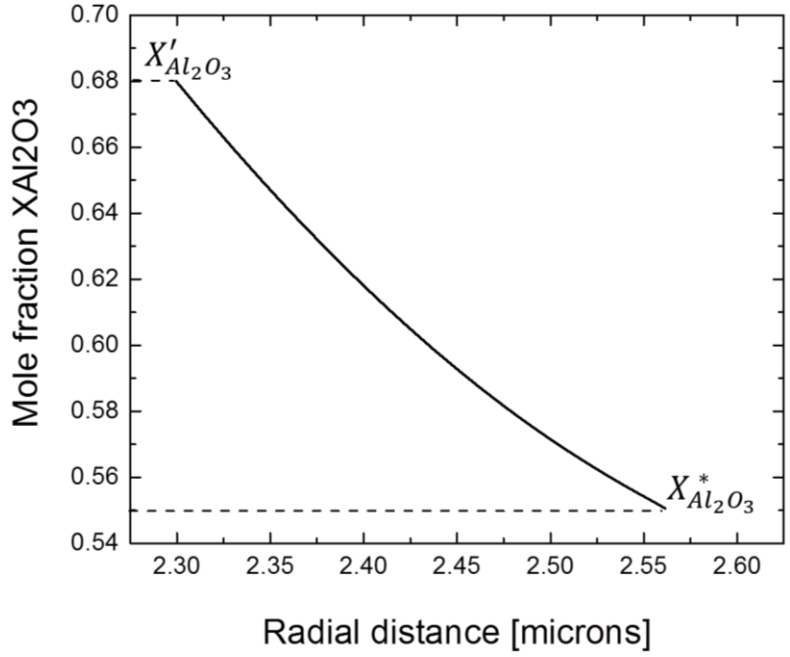

Figure 3-19. Variation of $X_{Al_2O_3}$ across the product layer at time $t = 0.06$ minutes

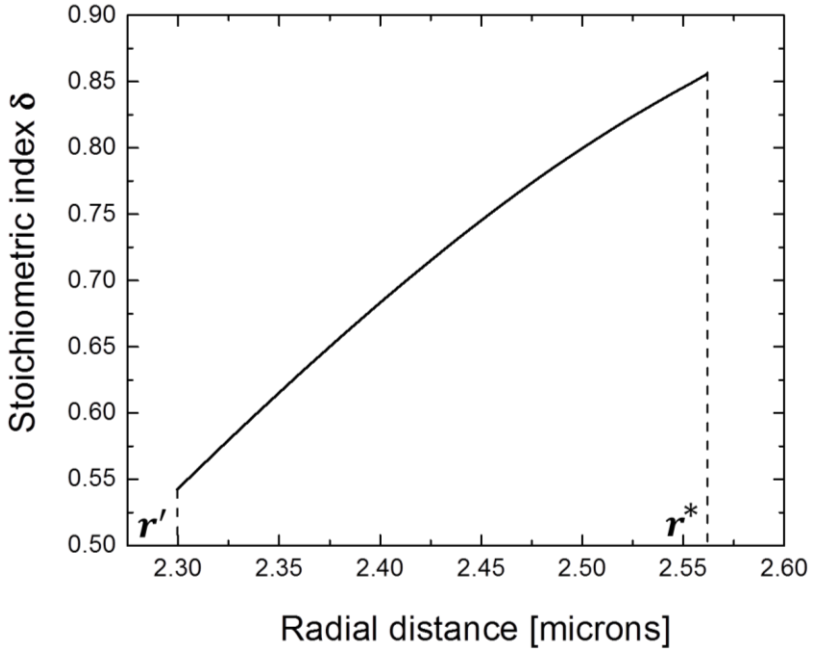

Figure 3-20. Stoichiometric index δ for magnesium aluminate spinel $Mg_\delta Al_\upsilon O_4$ at time $t = 0.06$ minutes

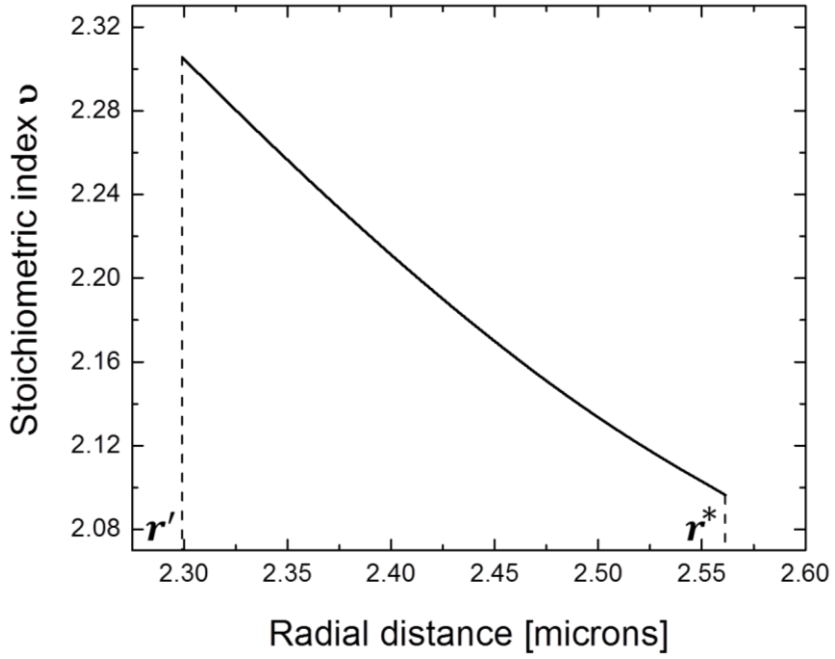

Figure 3-21. Stoichiometric index υ for magnesium aluminate spinel $Mg_{\delta}Al_{\upsilon}O_4$ at time $t = 0.06$ minutes

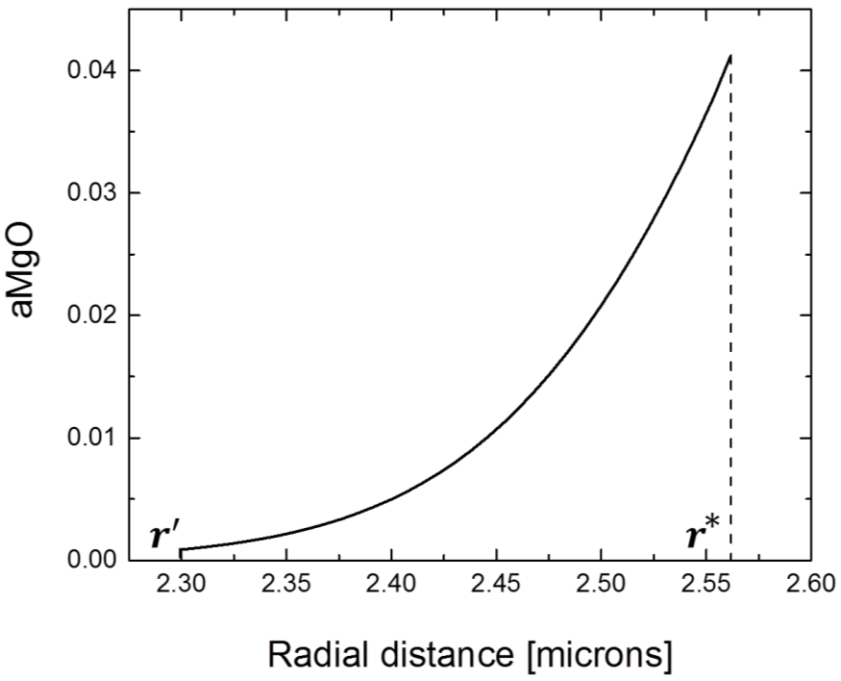

Figure 3-22. Radial variation in the activity of the MgO component at time $t = 0.06$ minutes

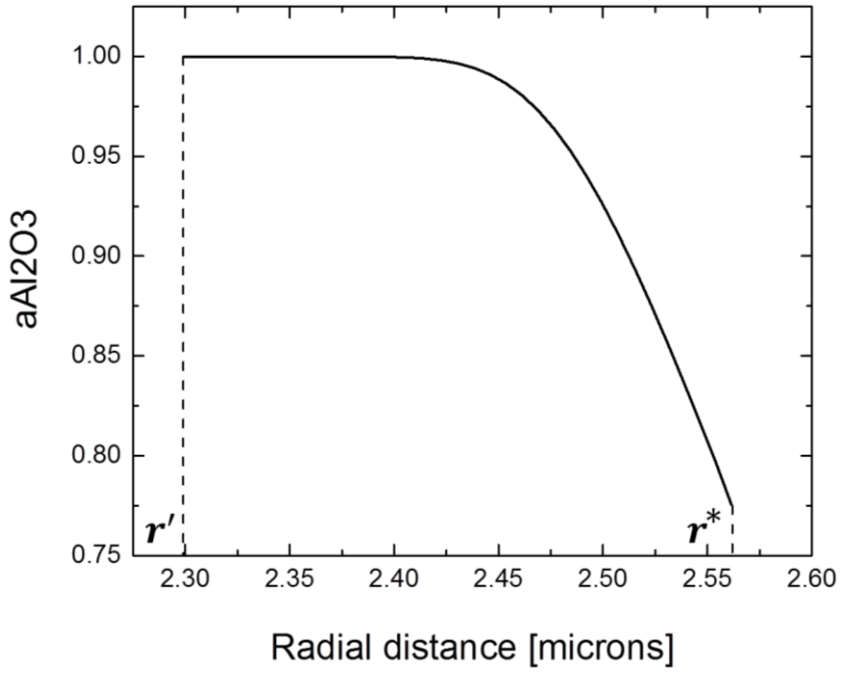

Figure 3-23. Radial variation in the activity of the Al_2O_3 component at time $t = 0.06$ minutes

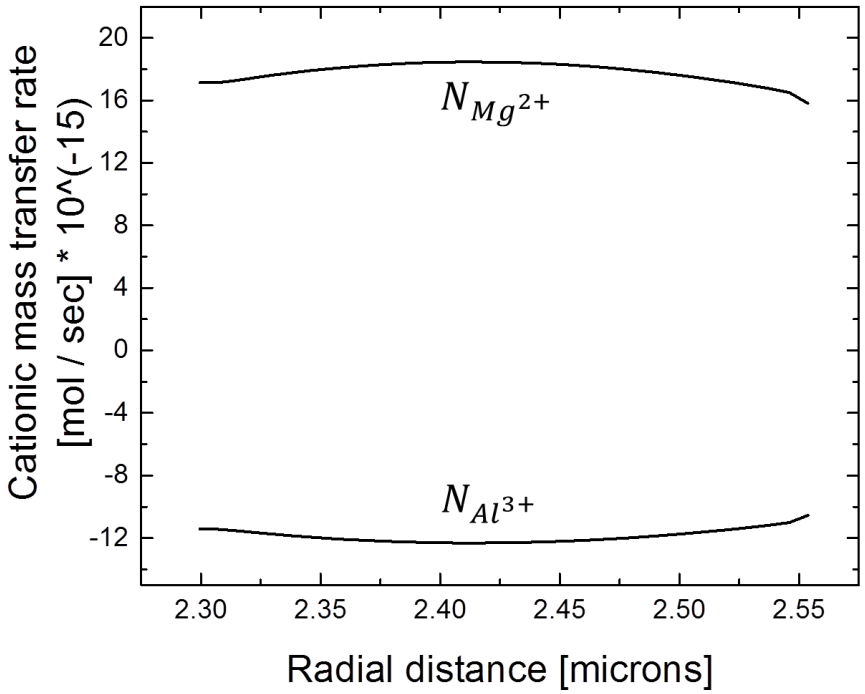

Figure 3-24. Cationic mass transfer rates across the boundary layer at time $t = 0.06$ minutes

The change in the bulk concentrations of the dissolved [Mg], [Al] and [O] is compared with the equilibrium concentrations at the interface between the each inclusion and steel in Figures 3-25 to 3-27.

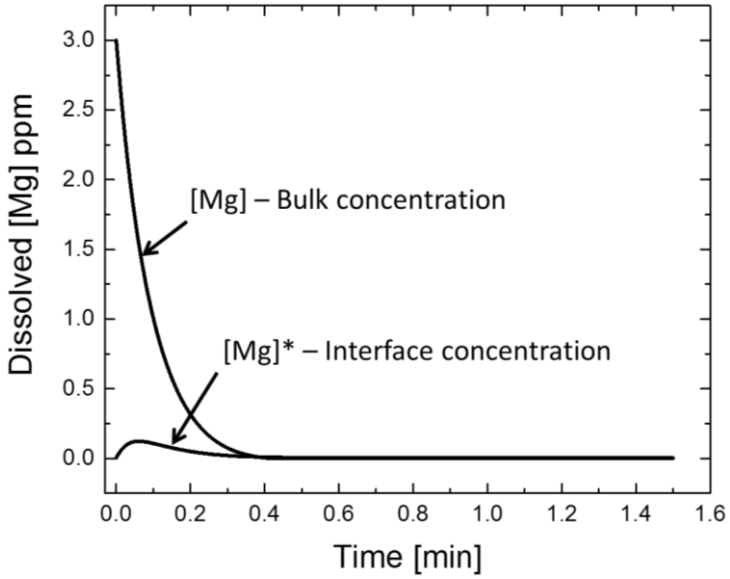

Figure 3-25. Variation in the concentration of dissolved [Mg] in steel

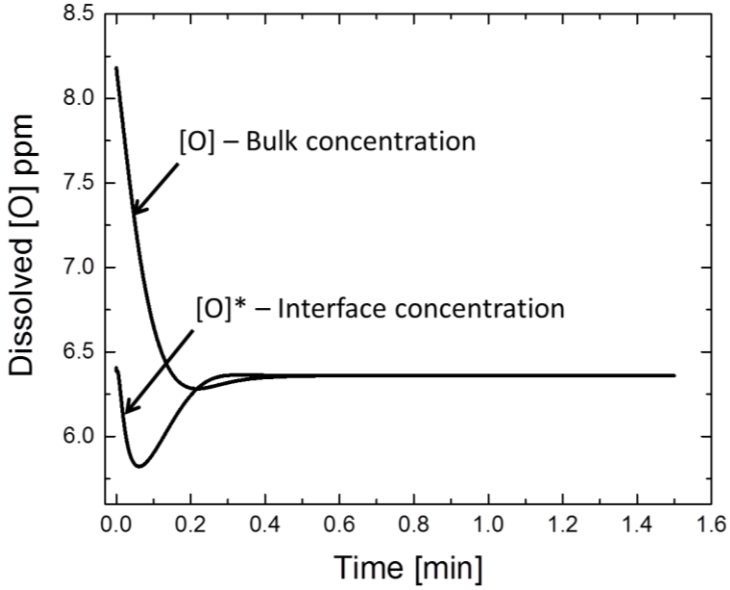

Figure 3-26. Variation in the concentration of dissolved [O] in steel

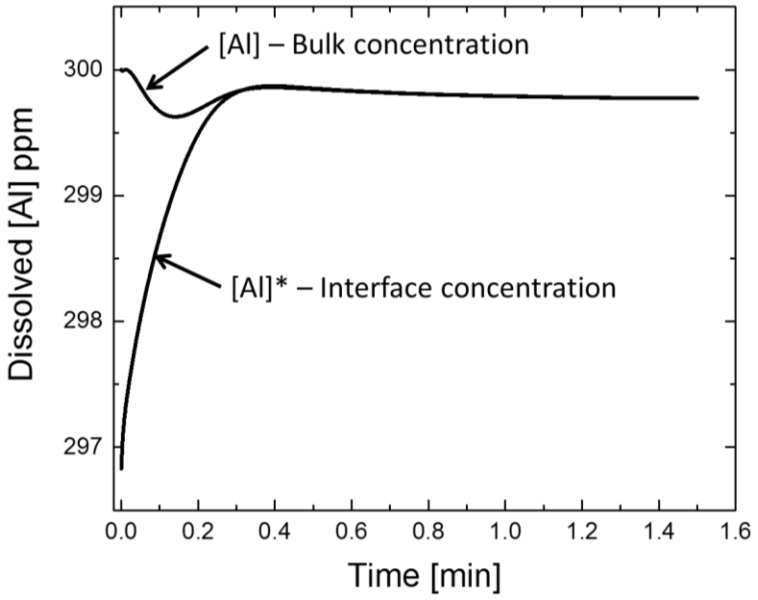

Figure 3-27. Variation in the concentration of dissolved [Al] in steel

The changes in the equilibrium activities in spinel at the interface with steel are plotted in figures 3-28 and 3-29.

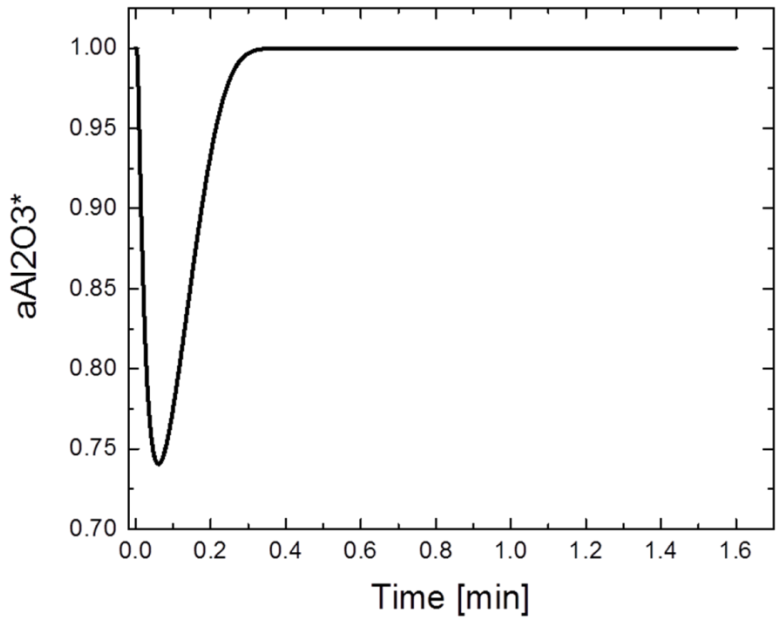

Figure 3-28. Interfacial activity of Al_2O_3 in equilibrium with steel.

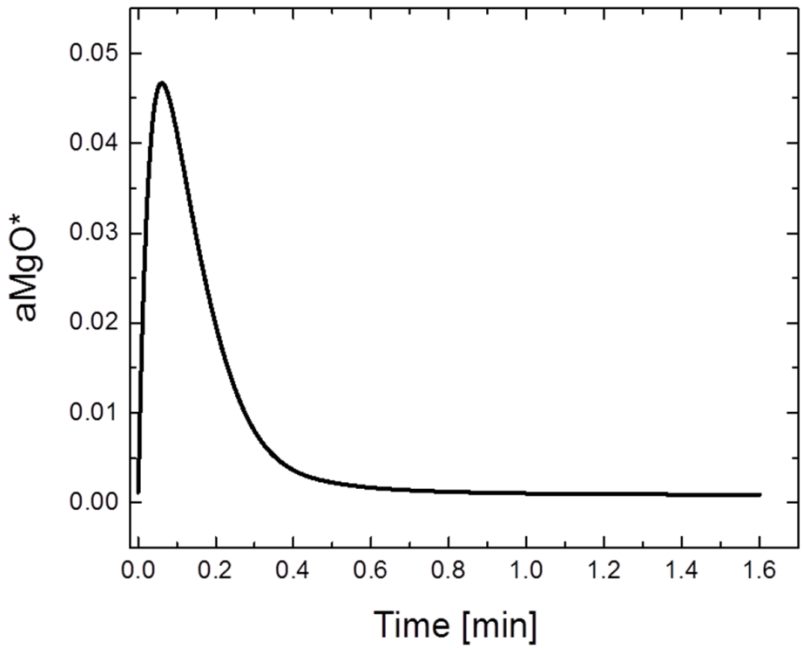

Figure 3-29. Interfacial activity of MgO in equilibrium with steel.

Figures 3-16, 3-28 and 3-29 demonstrate the utility of the sigmoidal functions used to describe the activities of the components in spinel since activity values for $a_{Al_2O_3}$ close to unity are in the vicinity of the mole fraction $X_{Al_2O_3} = 0.68$ which is the composition of alumina in equilibrium with spinel at 1873 K.

3.5.2 Effect of initial size of the inclusions

An analysis of the effect of the initial diameter of the inclusions was performed with the kinetic model using the unsteady state solution for diffusion in the product layer. The initial content of [Mg] dissolved in steel is 1 ppm, [Al] = 0.03 wt% and [O] was assumed in equilibrium with pure alumina. The Total oxygen concentration was set to 40 ppm. The simulation was repeated with

different values for the initial diameter of the inclusions, the values considered were: 2 μm, 5 μm, 10 μm and 15 μm. Figure 3-30 shows the changes in the content of Mg in the inclusions with time.

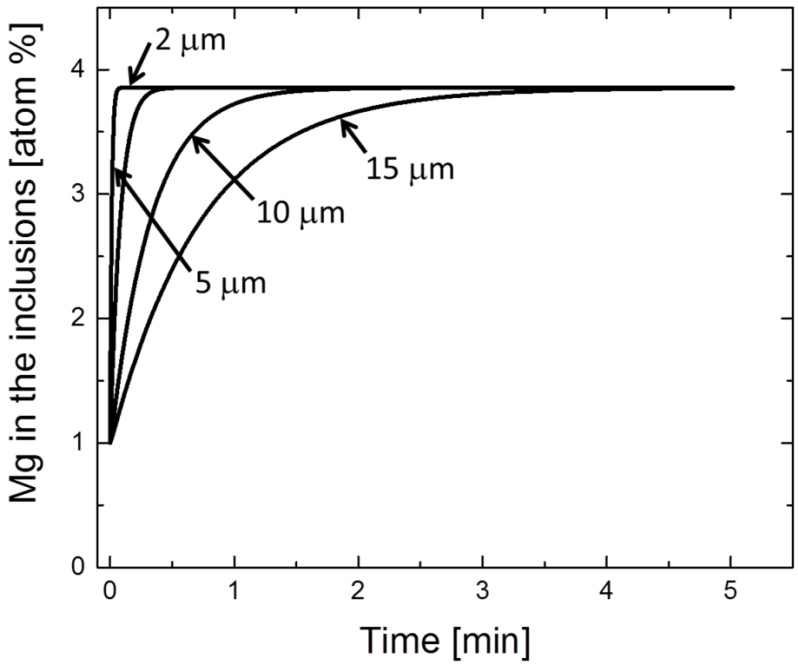

Figure 3-30. Overall content of Mg in the inclusions with time for different initial diameter of the inclusions.

The longer time required for the larger inclusions to reach the equilibrium concentration in figure 3-30 is due to the differences in the number of particles Np as well as due to the different mass transfer coefficients for diffusion in the interface boundary layer in steel. Furthermore, in the calculation with smaller inclusions the interfacial area of contact between the inclusions and the steel increases which in turn accelerates the process. Figure 3-31 illustrates the change in the content of dissolved [Mg] for the different particle sizes. Figure 3-32 shows the change in the spinel composition at the interface in contact with steel.

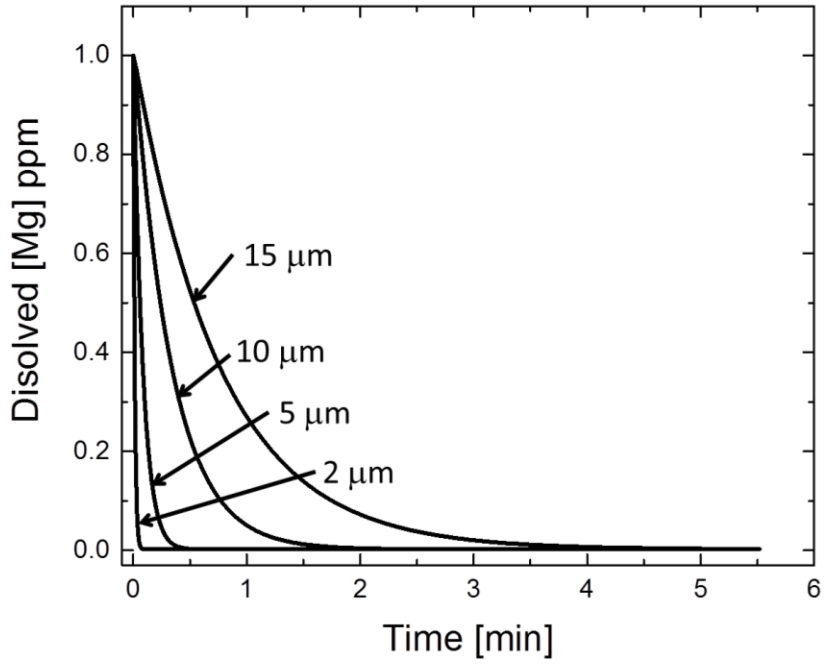

Figure 3-31. Effect of initial particle diameter on the content of [Mg] in steel

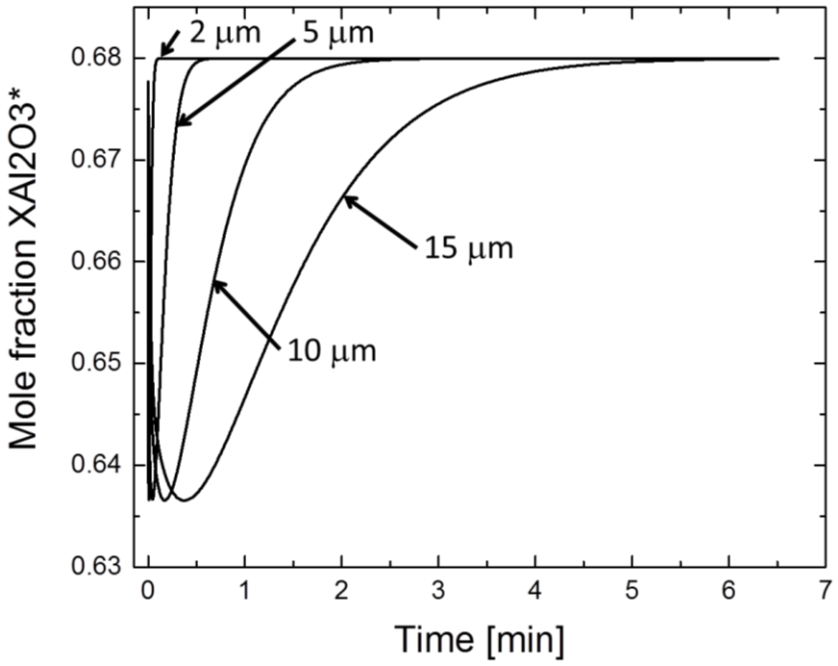

Figure 3-32. Effect of initial particle diameter on the spinel in equilibrium with steel, concentration in mole fraction $X_{Al_2O_3}{}^*$.

The dissolved magnesium in the steel is not enough to transform the inclusions completely. Therefore, the end point steady state concentration is the same for all the cases considering that the final spinel concentration is in equilibrium with the remaining alumina core. Figure 3-33 shows the variations in the activity of MgO at the interface between the spinel and steel.

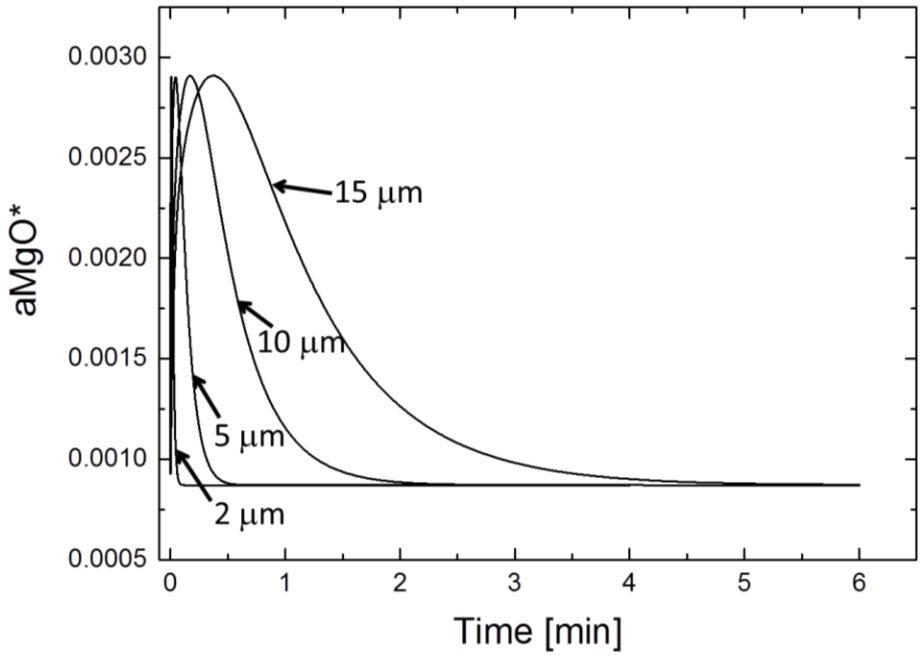

Figure 3-33. Interfacial activity of MgO in equilibrium with steel.

3.5.3 Results from the Quasi-steady state diffusion approximation

To compare the results of the Quasi-steady state approximation for diffusion in the product layer the kinetic model was used considering different initial concentrations of dissolved [Mg]. The initial diameter of the inclusions was set to 5 microns. The number of particles was kept constant and based on a Total Oxygen content of 40 ppm. In the calculations, the initial aluminum dissolved in

steel is 0.03 wt% and the content of oxygen is in equilibrium with pure alumina. The initial concentrations of [Mg] are: 0.5, 1, 2, 5 and 10 ppm. The initial content of Mg in the inclusions is 1% atomic Mg. Figure 3-34 and Figure 3-35 show the different final concentrations of Mg in the inclusions calculated with the Unsteady-state and Quasi-steady state models.

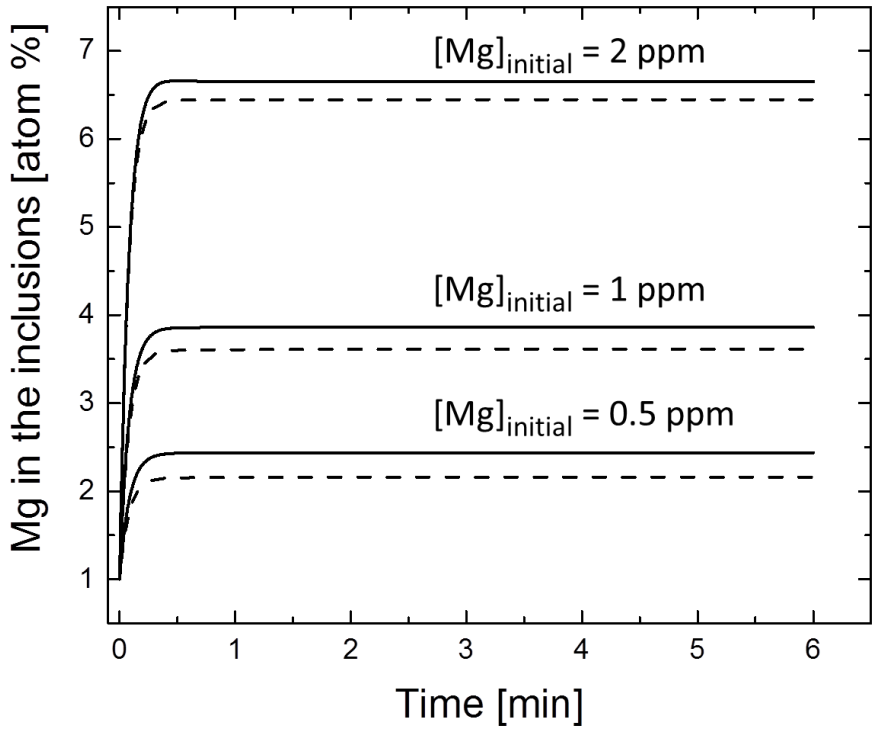

Figure 3-34. Mg content in the inclusions from 0.5, 1 and 2 ppm initial concentration of [Mg] in steel. Continuous lines calculated with the Unsteady-state diffusion model. Dashed lines from the Quasi-steady state approximation.

The discrepancies between the Unsteady and Quasi-steady solutions are due to the differences in the concentration profiles across the product layer and the displacement of the boundaries as shown in Figure 3-36. Additionally, the Unsteady state solution calculates the changes for the variation of Mg in the

product layer to update the steel composition as well as the interface boundary conditions a greater number of times than the Quasi-steady approximation, this also improves the accuracy of the solution. Since the spinel product layers in both models are not exactly the same, then the changes of [Mg] and [Al] in steel also vary, Figure 3-37 and 3-38; this in turn affects the interfacial equilibrium and the deoxidation rates, Figure 3-39.

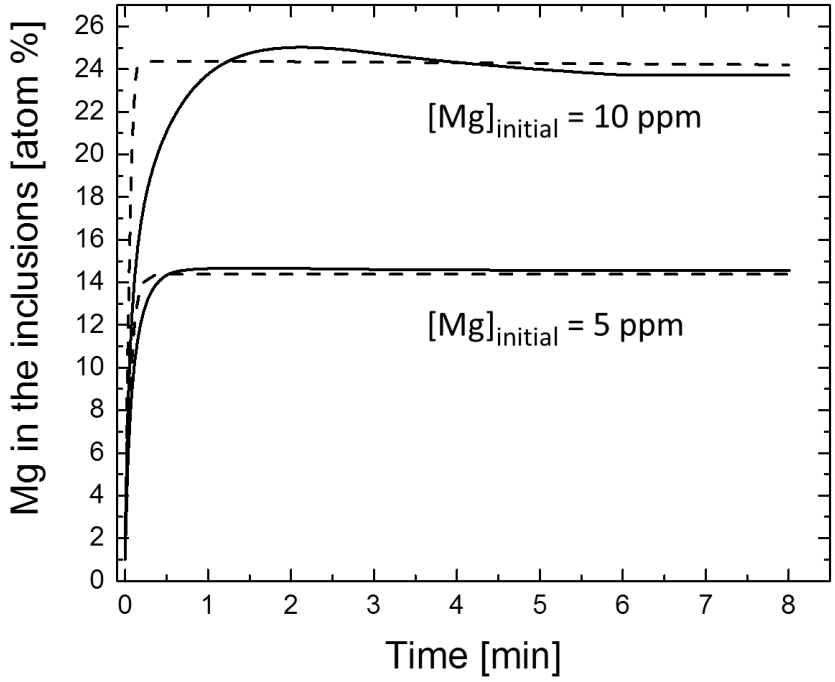

Figure 3-35. Mg content in the inclusions from 5 and 10 ppm of initial [Mg] in steel. Continuous lines calculated with the Unsteady-state diffusion model. Dashed lines from the Quasi-steady state approximation.

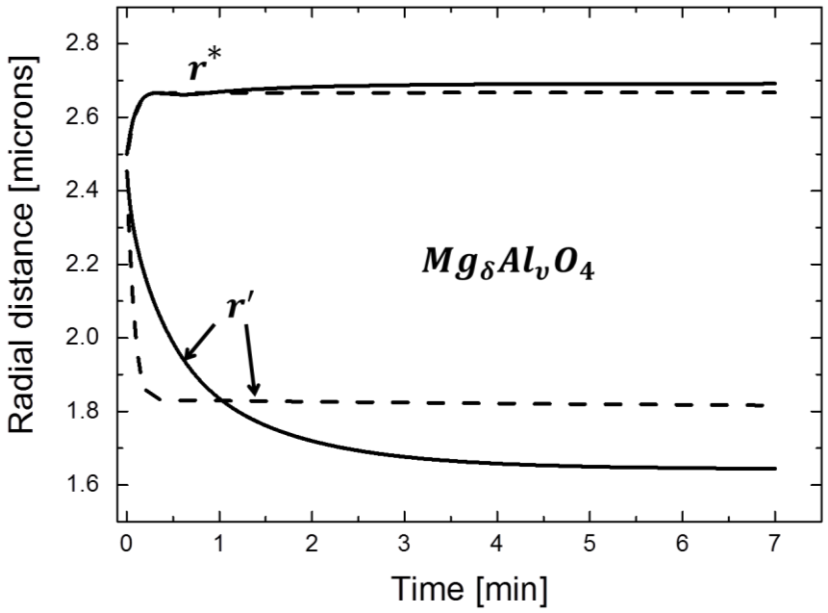

Figure 3-36. Calculated thickness of the spinel product layer for 5 ppm of initial [Mg] in the steel. Continuous lines from the Unsteady-state diffusion model. Dashed lines from the Quasi-steady state approximation.

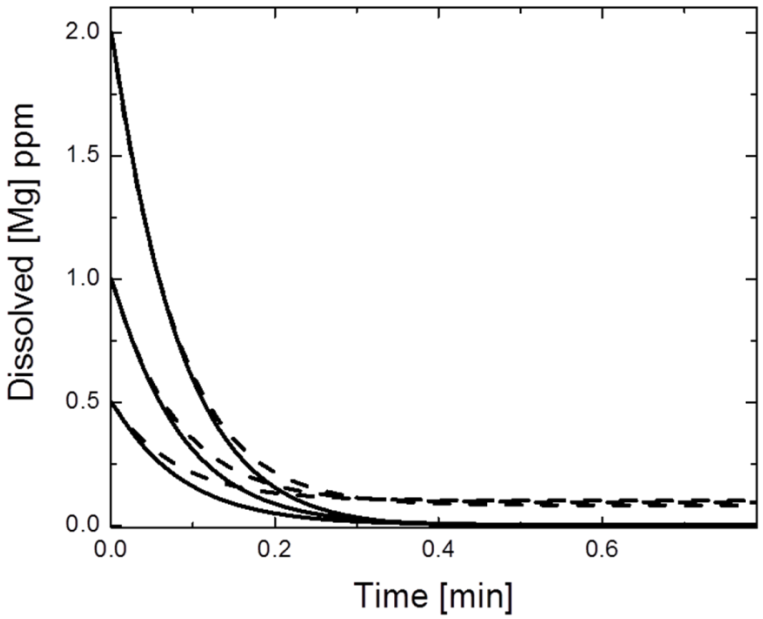

Figure 3-37. Variation of [Mg] in steel for 0.5, 1 and 2 ppm initial [Mg]. Continuous lines from the Unsteady-state model. Dashed lines from the Quasi-steady state approximation.

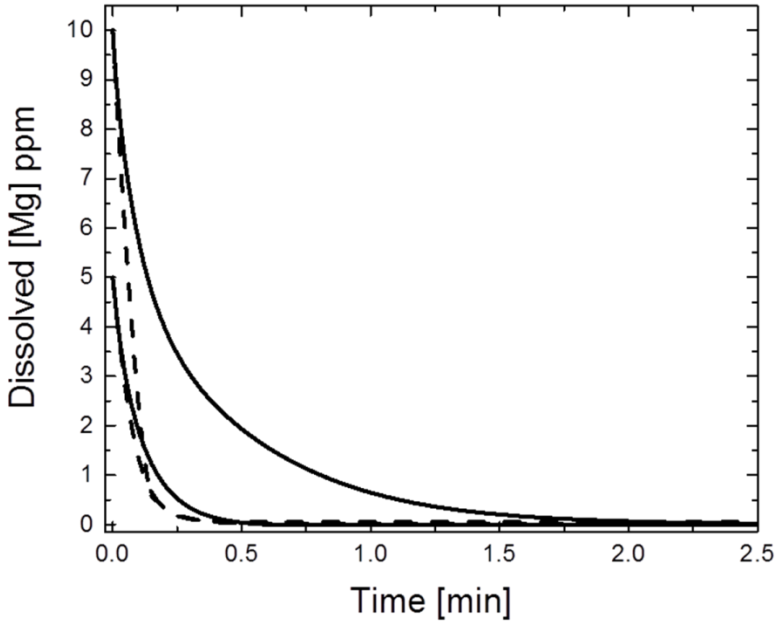

Figure 3-38. Variation of [Mg] in steel for 5 and 10 ppm initial [Mg]. Continuous lines from the Unsteady-state model. Dashed lines from the Quasi-steady state approximation.

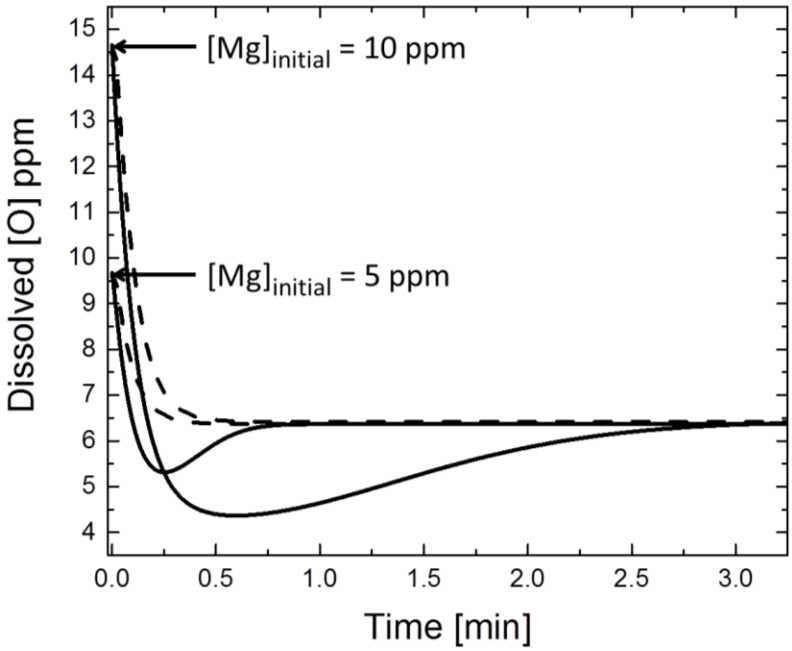

Figure 3-39. Variation of [O] in steel for 5 and 10 ppm initial [Mg]. Continuous lines from the Unsteady-state model. Dashed lines from the Quasi-steady state approximation.

Although the Unsteady-state model is more accurate, the computation of the Quasi-steady state solution requires less iterations to complete the simulations. In most of industrial applications, the Quasi-steady state assumption represents a valid and useful approximation to analyze and optimize diffusional processes. Additional discussion on the differences between these solutions is included in chapter four of this thesis for the modeling of the oxide inclusions considering the industrial operations in the ladle metallurgy furnace.

Chapter 4

Coupled kinetic model for the oxide inclusions in the ladle metallurgy furnace

4.1 Kinetic model for the slag-steel reactions

The transformation of indigenous alumina inclusions to magnesium aluminate spinel during the refining of low carbon aluminum steel LCAK in the ladle metallurgy furnace LMF is linked to the interaction between the top slag and the steel. According to the Al-reduction mechanism, proposed by Nishi & Shinme (1998), the source of [Mg] for the inclusions transformation is the MgO dissolved in the slag.

The effect of the slag composition on the formation of spinel has been analyzed in several laboratory experiments (Mizuno, et al., 2001; Okuyama, et al., 2000; Todoroki & Mizuno, 2004). The kinetic study of Okuyama et al. (2000) for the compositional changes in the slag, steel and the oxide inclusions was validated with laboratory experiments; in that work slag-steel reactions were described with the multicomponent kinetic model of Robertson, et al., (1984). A drawback from the work of Okuyama et al. (2000) was that they did not have the model for the inclusions coupled to the slag-steel calculations. However, from their comparison between the experimental and the mathematical analysis they concluded that the rate limiting step for spinel inclusions formation is the slag-steel reaction for the release of [Mg]. In general, all the laboratory studies on spinel formation are

characterized by the fact that the easily reducible oxides FeO and MnO were not included in the slag compositions.

From an industrial perspective, the deoxidation level of the top slag and the gas stirring rate strongly affect the rate of spinel formation during ladle treatment of LCAK steel (Pretorius, et al., 2013; Story, et al., 2004). The industrial sampling at ArcelorMittal Dofasco and its respective analysis made by Graham & Irons (2010) showed that the oxide inclusions shift their concentration towards higher Mg contents during the course of the refining heats, the inclusions analysis of this study and thermodynamic calculations suggested that the main source of [Mg] in steel is the slag. The kinetic model of Harada et al., (2013) also uses the model of Robertson, et al., (1984) for slag-steel reactions while a method of iterative variation in the composition is used for the changes in the oxide inclusions. Harada et al., (2013) validated their model with the reported values of Graham & Irons (2010). From a sensitivity analysis, this study proposed a combined control of the deoxidation with aluminum, slag basicity and MgO in the slag in order to reduce the amount of spinel inclusions (Harada, et al., 2013b). Although Harada, et al., (2013b) made a detailed analysis of several important parameters that influence spinel inclusions formation, they did not conclude on what is the rate control mechanism for the process.

For this thesis project the supply of [Mg] to the steel from the slag during ladle treatment is calculated with the kinetic model of Graham & Irons (2010) described in greater detail by Graham (2008) and briefly described in chapter two.

In this model, the kinetics of slag –steel reactions is based on the model of Robertson, et al., (1984) that couples the oxidation-reduction reactions between the species dissolved in the steel and the respective oxide components in the slag. The activities of the components in the slag are calculated with the Cell model formalism while for the species in steel the Unified Interaction Parameter formalism is used. A scheme of the mass transport process for the slag-steel reaction between (MnO), [Mn] and [O] is shown in Figure 4-1. The driving force for mass transfer is the difference between the bulk concentrations and the concentrations at the interface were local thermodynamic equilibrium is assumed.

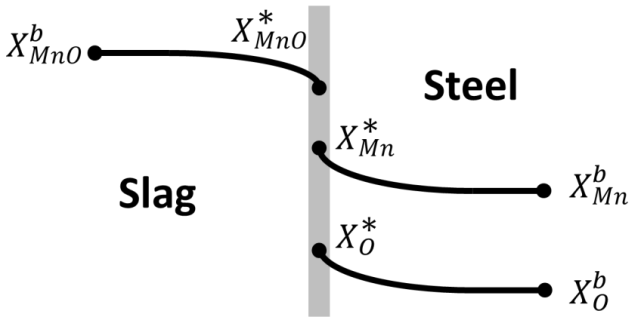

Figure 4-1. Mass transfer of the species from the bulk of the slag and steel phases to the slag-steel interface.

The slag-steel reactions considered in the kinetic model of Graham & Irons (2010) that describe the compositional changes of the main components in the slag and steel are:

$$(\mathrm{FeO}) = \{\mathrm{Fe}\} + [\mathrm{O}] \quad (4\text{-}1.1)$$

$$(\mathrm{MnO}) = [\mathrm{Mn}] + [\mathrm{O}] \quad (4\text{-}1.2)$$

$$(\mathrm{CaO}) = [\mathrm{Ca}] + [\mathrm{O}] \quad (4\text{-}1.3)$$

$$(\mathrm{MgO}) = [\mathrm{Mg}] + [\mathrm{O}] \quad (4\text{-}1.4)$$

$$(\mathrm{SiO_2}) = [\mathrm{Si}] + 2[\mathrm{O}] \quad (4\text{-}1.5)$$

$$(\mathrm{TiO_2}) = [\mathrm{Ti}] + 2[\mathrm{O}] \quad (4\text{-}1.6)$$

$$(\mathrm{Al_2O_3}) = 2[\mathrm{Al}] + 3[\mathrm{O}] \quad (4\text{-}1.7)$$

For sulphur, the equilibrium partition coefficient L_S' for desulphurization with the top slag is calculated with:

$$L_S' = \frac{X_{S,sl}^*}{X_{S,m}^*} = \frac{C_S' \cdot f_S^* \cdot K_s}{h_O^*} \quad (4\text{-}2)$$

In expression (4-2) h_O^* is the activity of dissolved [O] in steel at the slag-steel interface that satisfies the multicomponent thermodynamic equilibrium of all the reactions (4-1.1) to (4-1.7), C_S' is the modified sulphide capacity calculated from the empirical correlation as a function of the optical basicity of the slag with the parameters of Young, et al, (1992), K_s is the equilibrium constant for desulphurization with the top slag and f_S^* is the activity coefficient of dissolved [S] at the slag-steel interface. The mass transfer balance for desulphurization is:

$$k_m^S Cv_m\left(X_{S,m}^b - X_{S,m}^*\right) = k_{sl}^S Cv_{sl}\left(X_{S,Sl}^* - X_{S,Sl}^b\right) \quad (4\text{-}3)$$

With the equilibrium partition coefficient L_S' and the bulk concentrations of sulphur in steel $X_{S,m}^b$ and in slag $X_{S,Sl}^b$ for equation (4-3) the interfacial concentrations $X_{S,m}^*$ and $X_{S,Sl}^*$ are obtained. Once all the interfacial mole fraction

values are calculated at a time step t_q, the update of the slag and steel bulk concentrations proceeds with a first order time integration:

$$M_xO_y\big|_{t_{q+1}} = M_xO_y\big|_{t_q} + \Delta M_xO_y\big|_{t_q} \tag{4-4}$$

$$M|_{t_{q+1}} = M|_{t_q} + \Delta M|_{t_q} \tag{4-5}$$

The values in equations (4-4) and (4-5) are in moles of the respective species, the changes in moles for the composition during a time step Δt_q are calculated according to:

$$\Delta M_xO_y\big|_{t_q} = -k_{sl}^{M_xO_y} \cdot A \cdot Cv_{sl}\left(X^b_{M_xO_y} - X^*_{M_xO_y}\right) \cdot \Delta t_q \tag{4-6}$$

$$\Delta M|_{t_q} = -k_m^M \cdot A \cdot Cv_m(X_M^b - X_M^*) \cdot \Delta t_q \tag{4-7}$$

Cv_m and Cv_{sl} are the total molar concentrations of the metal and slag phase respectively while k_m^M and $k_{sl}^{M_xO_y}$ are the mass transfer coefficients in m/sec for convective transport in the metal and slag. The mass balance update of sulphur in the slag and steel includes an additional effect considering that [O] is released to the steel mostly in accordance to:

$$(\mathrm{CaO}) + [\mathrm{S}] = (\mathrm{CaS}) + [\mathrm{O}] \tag{4-8}$$

Assuming that the oxygen released at the interface reacts with [Al], then:

$$3(\mathrm{CaO}) + 3[\mathrm{S}] + 2[\mathrm{Al}] = 3(\mathrm{CaS}) + (\mathrm{Al_2O_3}) \tag{4-9}$$

From (4-6), (4-7) and (4-9) the total amounts in moles for the change in bulk concentration of (CaO), [Al] and (Al_2O_3) during a time step are:

$$\Delta(CaO)|_{t_q} = \Delta(CaO) + \Delta[S] \tag{4-10}$$

$$\Delta[Al]|_{t_q} = \Delta[Al] + \frac{2}{3}\Delta[S] \tag{4-11}$$

$$\Delta(Al_2O_3)|_{t_q} = \Delta(Al_2O_3) + \frac{1}{2}\Delta(CaS) \tag{4-12}$$

4.1.1 Mass transfer coefficients in the slag and steel phases

The mass transfer coefficients k_m^M for all the dissolved species in steel are assumed to be equal since the diffusivities of the solutes in molten steel have the same order of magnitude. The empirical correlation proposed by Graham & Irons (2010) for the mass transfer coefficient of dissolved [S] as a function of the gas stirring energy ε in [W/tonne] is:

$$k_m^S \cdot A = 0.006 \pm 0.002\ \varepsilon^{1.4 \pm 0.002} \tag{4-13}$$

Correlation (4-13) is based on the industrial sampling of the operations in a 165 tonnes ladle metallurgy furnace in ArcelorMittal Dofasco. The mass transfer coefficients of the components in the slag $k_{sl}^{M_xO_y}$ are calculated from individual ratios with the mass transfer coefficient of the species in steel $k_{sl}^{M_xO_y} / k_m^M$ this approach was proposed in the model of Robertson, et al., (1984) and also used in the kinetic models of Kitamura et al., (1991), Okuyama et al., (2000) and Harada, et al., (2013).

As summarized by Szekely & Themelis (1971), the interphase mass transfer between two immiscible liquids involves the addition of the mass transfer

resistances in each phase. For the case of a molten slag and liquid steel, the overall mass transfer rate of a diffusing species B can be expressed as:

$$N_B = \frac{\frac{C^b_{B,\,sl}}{L_B} - C^b_{B,m}}{\frac{1}{k_m} + \frac{1}{L_B k_{sl}}} \tag{4-14}$$

In expression (4-14) $C^b_{B,\,sl}$ and $C^b_{B,\,m}$ represent the bulk concentrations in the slag and steel phases respectively; k_{sl} and k_m are the mass transfer coefficients for the species A in the slag and steel while L_B is the equilibrium partition coefficient at the slag-steel interphase:

$$L_B = \frac{C^*_{B,\,sl}}{C^*_{B,\,m}} \tag{4-15}$$

$C^*_{B,\,sl}$ and $C^*_{B,\,m}$ are the concentrations for the equilibrium between the two phases. The numerator in (4-14) represents the overall driving force, while the denominator corresponds to the overall resistance to mass transfer, therefore:

$$\frac{1}{k_{OV}} = \frac{1}{k_m} + \frac{1}{L_B \cdot k_{sl}} \tag{4-16}$$

As explained by Szekely & Themelis (1971) equation (4-16) indicates that for many cases the overall transfer between the slag and steel is controlled by resistance in the steel phase; even though the diffusivities and mass transfer coefficients in steel are greater than in the slag. This condition of metal control is due to the large value of the partition coefficient L_B for the slag-steel reaction.

In this kinetic model, the assumption of transport control in the steel side is applied by equating the ratios of the mass transfer coefficients k_{sl}^{CaO} / k_m^{Ca} , k_{sl}^{MgO} / k_m^{Mg} and $k_{sl}^{Al_2O_3} / k_m^{Al}$ to unity. In this way, the resistance for transport of the components CaO, MgO and Al_2O_3 is neglected because of the large value of the partition coefficients for reactions (4-1.3), (4-1.4) and (4-1.7).

Due to the smaller partition coefficients for reactions (4-1.1), (4-1.2) and (4-1.5) as well as the lower diffusivity of the SiO_2 species in the molten slag, the ratios k_{sl}^{FeO} / k_m^{Fe} , k_{sl}^{MnO} / k_m^{Mn} and $k_{sl}^{SiO_2} / k_m^{Si}$ were fitted for each modelling case in order to obtain agreement with the experimental values. Furthermore, a sensitivity analysis for the effect of k_{sl}^{FeO}, k_{sl}^{MnO} and $k_{sl}^{SiO_2}$ is included in this chapter.

4.1.2 Retrieving of processing parameters from the ladle furnace operations

The kinetic model of Graham & Irons (2010) was validated with the industrial results for refining LCAK steel in the ladle metallurgy furnace at ArcelorMittal Dofasco. As described by Graham (2008), the kinetic model considers the processing parameters applied at each heat. The information retrieved to reproduce the conditions in the ladle furnace include: initial mass of steel in the ladle furnace, estimation of the slag volume based on slag depth measurement, temperaure measurements, argon gas flow rate of the 2 bottom porous plugs and energy applied for heating with electrical arcing.

The chemical compositions of the slag, steel and the indigenous inclusions at the beginning of the ladle treatment were also measured. During the course of each heat additional samples of the slag, steel and inclusions were taken to monitor the refining process.

4.1.2.1 Slag and steel additions and gas stirring flow rate

The mass of the fluxes for the slag and additions for the steel as well as the time at which they are added is reported in the process data sheet of the ladle metallurgy furnace, this information is included in the input values of the kinetic model for all the different materials listed in Figure 4-2.

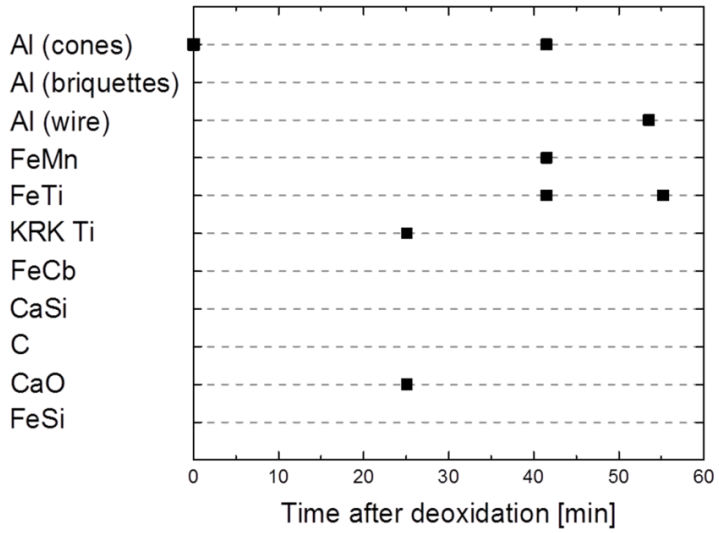

Figure 4-2. Additions for the slag and steel during treatment of Heat 2 in the LMF

For all the industrial heats analyzed, the source of primary molten steel is the EAF process. An initial deoxidation with aluminum is performed during tapping of steel from the EAF to the ladle by using the agitation of steel to

homogenize and to float out the deoxidation products to the new slag. Once the ladle arrives to the treatment station a second deoxidation is carried out, this aluminum addition is indicated in Figure 4-2 at $t = 0$ min and sets the initial time of ladle treatment.

Argon gas stirring is applied with two bottom porous plugs. The variations in the gas flow rate, Figure 4-3, are included in the kinetic model to calculate the stirring power ε with the expression derived by Pluschkell, (Pluschkell, 1981).

$$\varepsilon = \left(\frac{101330}{273}\right) \cdot \left(\frac{Q \cdot T}{M}\right) ln\left(1 + \frac{\rho \cdot g \cdot h}{101330}\right) \quad (4\text{-}17)$$

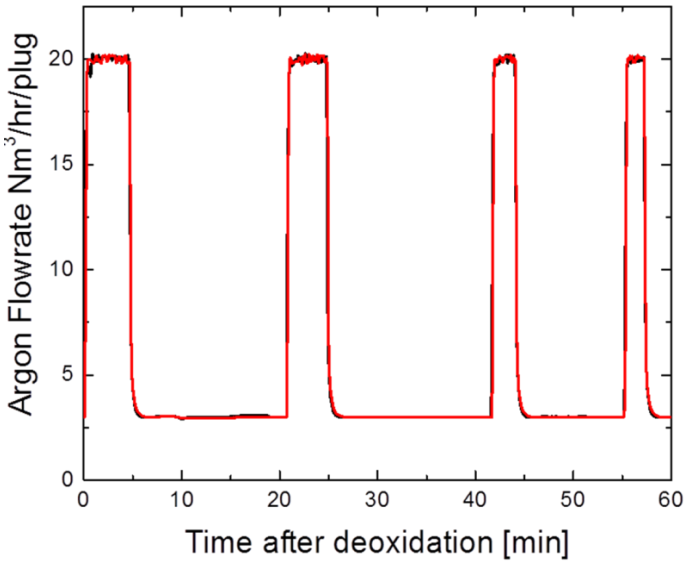

Figure 4-3. Gas stirring during treatment of Heat 2

4.1.2.2 Temperature update due to electrical arcing

The periods of heating with electrical arcing are included for the update of the temperature, Figure 4-4. From the analysis of 41 industrial heats for ladle treatment of LCAK steel, Graham (2008) calculated the rate of bath temperature

gain with electrical heating to be 3.35 °C / min. When electrical heating is not applied the rate of temperature loss is 1.33 °C / min.

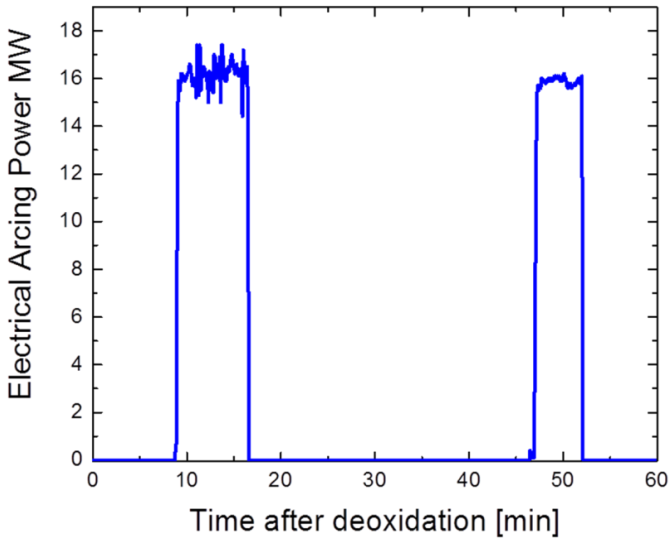

Figure 4-4. Electrical heating during treatment of Heat 2 in the LMF

4.1.2.3 Reoxidation due to electrical arcing

Application of the electric arc increases the content of dissolved [O] in steel and the FeO in the slag due to oxidation of the metal. This effect was mentioned in the analysis of the industrial heats made by Graham (2008); the observed oxygen pick-up during arcing was proposed to explain the occurrence of sulphur reversion when electrical heating is on. Similar evidence of reoxidation due to electrical arcing has been reported. Paar et al., (2014) compared the different types of electric current on experimental studies of Electro-Slag-Remelting and its effect on oxygen pick-up and cleanliness level. Sheshukov et al., (2014) performed laboratory experiments in order to evaluate the relation

between the slag composition and the voltage of the arc applied, this study concluded that higher levels of FeO in the slag and [O] in steel are obtained with higher voltages.

From the study of Graham (2008), the rate of oxygen pick-up during arcing was reported to be 0.1134 ppm of dissolved [O] per minute. Reoxidation was not included in the model of Graham & Irons (2010), for this model the stoichiometry of reoxidation during electrical heating is assumed as:

$$O_2 + \{Fe\} = (FeO) + [O] \tag{4-18}$$

The stoichiometry in reaction (4-18) is a simplification to describe the industrial experience and evidence that both [O] in steel and (FeO) in slag increase during electrical arcing. In this case, the stoichiometry in reaction (4-18) assumes a similar increase in moles for (FeO) and [O]. It is important to note that this reoxidation of the bulk of steel and slag is a non equilibrium phenomenon since the oxygen potential at the slag-steel interface is much lower given the aluminum [Al] content in the steel.

From (4-18) the increase in moles of dissolved [O] in steel and (FeO) in slag during a time step with arcing is:

$$\Delta[O]_{reox} = (0.1134 \times 10^{-4}) \left(\frac{St_{mass}}{100}\right) \left(\frac{1}{Mw_O}\right) \left(\frac{1}{60}\right) \cdot \Delta t_q \tag{4-19}$$

$$\Delta(FeO)_{reox} = \Delta[O]_{reox} \tag{4-20}$$

The composition update in moles is the sum of the update from the multicomponent kinetic model (4-6) and (4-7) and the reoxidation effect:

$$\Delta[O]|_{t_q} = \Delta[O] + \Delta[O]_{reox} \tag{4-21}$$

$$\Delta(FeO)|_{t_q} = \Delta(FeO) + \Delta(FeO)_{reox} \tag{4-22}$$

If $[wt\%\ O]|_{t_q}$ is the known concentration of dissolved oxygen at a given time then it is possible to estimate the mass of steel oxidized due to arcing:

$$St_{reox} = (0.1134 \times 10^{-4}) \cdot St_{mass} \left(\frac{1}{[wt\%\ O]|_{t_q}}\right)\left(\frac{1}{60}\right) \cdot \Delta t_q \tag{4-23}$$

The change in mols of [Mn] oxidized during a time step with arcing is also considered:

$$\Delta[Mn]_{reox} = -St_{reox} \left(\frac{[wt\%\ Mn]|_{t_q}}{100}\right)\left(\frac{1}{Mw_{Mn}}\right)\left(\frac{1}{60}\right) \cdot \Delta t_q \tag{4-24}$$

In (4-24) $[wt\%\ Mn]|_{t_q}$ is the concentration of dissolved [Mn] in steel. The respective MnO increase in moles for the slag update is:

$$\Delta(MnO)_{reox} = -\Delta[Mn]_{reox} \tag{4-25}$$

4.1.3 Industrial sampling for validation of the kinetic model

The validation of the slag-steel model for the LMF operations at ArcelorMittal Dofasco was made by taking simultaneous samples of the slag and steel as well as measurements of the bath temperature and dissolved oxygen with Celox oxygen probes. The sampling was made before and after any process change; that is, argon strring, alloy or slag addition and electrical arcing.

Additionally, an estimation of the amount of slag carryover from the EAF furnace was perfomerd by using the AMEPA TDS (AMEPA, Wuerselen-Aachen, Germany) slag detection system. The details on the sampling procedure, the analytical techniques for chemical analysis and the slag carryover control are described by Graham (2008). Figure 4-5 illustrates the timing of the different samples taken during the course of Heat 2.

For the analysis of the indigenous inclusions, steel samples were sent to the RJ Lee Group (Monroeville, PA) to be analyzed using an automated scanning electron microscope known as the Automated Steel Cleanliness Analysis Tool (ASCAT), Graham (2008). This and other automated SEM inclusions equipment are direct methods to evaluate steel cleanliness, now in common use for inclusion analysis (Kaushik et al., 2009). As summarized by Kaushik et al., (2009) and Story et al., (2004), the computer controlled SEM is designed to rapidly analyse steel samples by locating the inclusions on a polished steel surface, measure their size and obtain their elemental analysis with the integrated energy-dispersive X-ray spectroscopy (EDX). The compositional data results from the EDX chemical analysis are presented as average values for all the inclusions found in the sample independently of the size or type of inclusion. Alternatively, the same EDX data per inclusion analyzed are processed by a software system to classify and to organize the found inclusions into categories of compositional phases or mixtures.

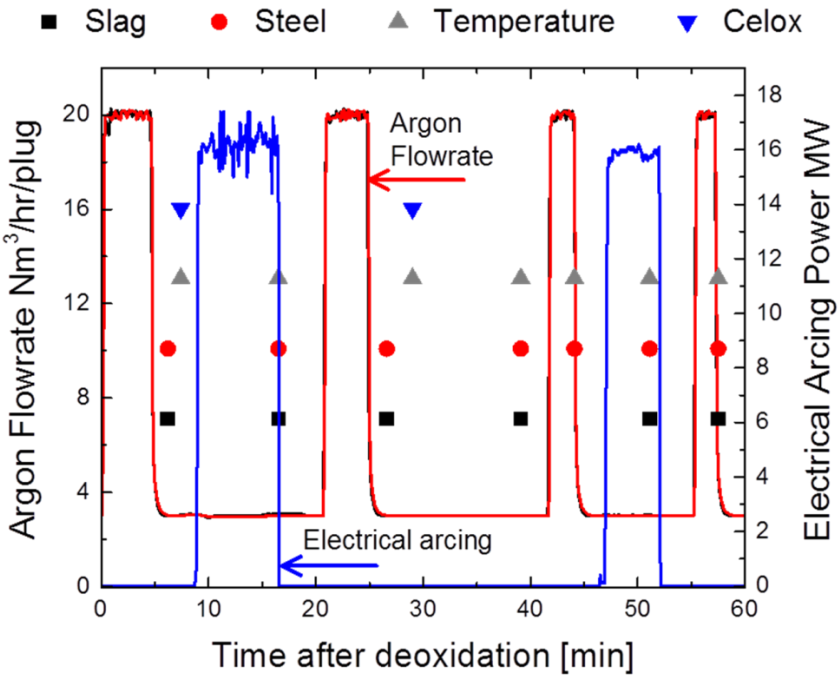

Figure 4-5. Location of samples taken during treatment of Heat 2 in the LMF

4.2 Kinetic model for spinel inclusions formation in the ladle furnace

The coupling of the kinetic model for the slag-steel reactions in the ladle furnace and the model for formation of spinel is made through the variation in the bulk concentration of [Mg], [Al] and [O] in the steel during a time step Δt_q with a first order time update:

$$[Mg]_{t_{q+1}} = [Mg]_{t_q} + \Delta[Mg]_{t_q,\ Sl-St} + \Delta[Mg]_{t_q,\ St-Inclus} \quad (4\text{-}26)$$

$$[Al]_{t_{q+1}} = [Al]_{t_q} + \Delta[Al]_{t_q,\ Sl-St,\ Desulph} + \Delta[Al]_{t_q,\ St-Inclus} \quad (4\text{-}27)$$

$$[O]_{t_{q+1}} = [O]_{t_q} + \Delta[O]_{t_q,\ Sl-St,\ \ arcing} + \Delta[O]_{t_q,\ St-Inclus} \quad (4\text{-}28)$$

The update for [Mg] includes the variation due to the slag-steel reaction and mass transfer to the inclusions. In the case of [Al] the update considers the

balance for the slag-steel reactions and desulphurization from equation (4-11) as well as the mass transfer to the inclusions. For dissolved [O] the model considers the slag-steel reactions and reoxidation during electrical arcing from equation (4-21) as well as mass transfer to the inclusions.

4.2.1 Coupled model with the unsteady state solution for spinel formation

The time step length Δt_q in seconds for the progress of the slag-steel reactions model depends on the scheme for diffusion in the spinel product layer, i.e. Unsteady state solution or Quasi-steady state approximation. For unsteady state diffusion in the inclusions, the adaptive time step strategy sets the $\Delta t_{q_{Inclus}}$ that maintains stability in the evolution of the concentration profile of Mg^{2+}. Therefore, the same step size for the inclusions must be used to update the bulk concentrations of the slag-steel model. This implies that the time scales for the slag-steel process and the inclusions-steel interaction are coupled.

On the other hand, it is important to mention that the retrieve of the industrial processing conditions occurs every six seconds; this is due to the characteristics of the process data sheet supplied by ArcelorMittal Dofasco that registers the processing parameters every 0.1 minutes. A scheme with the organization of the coupled kinetic model for the three phases is in Figure 4-6.

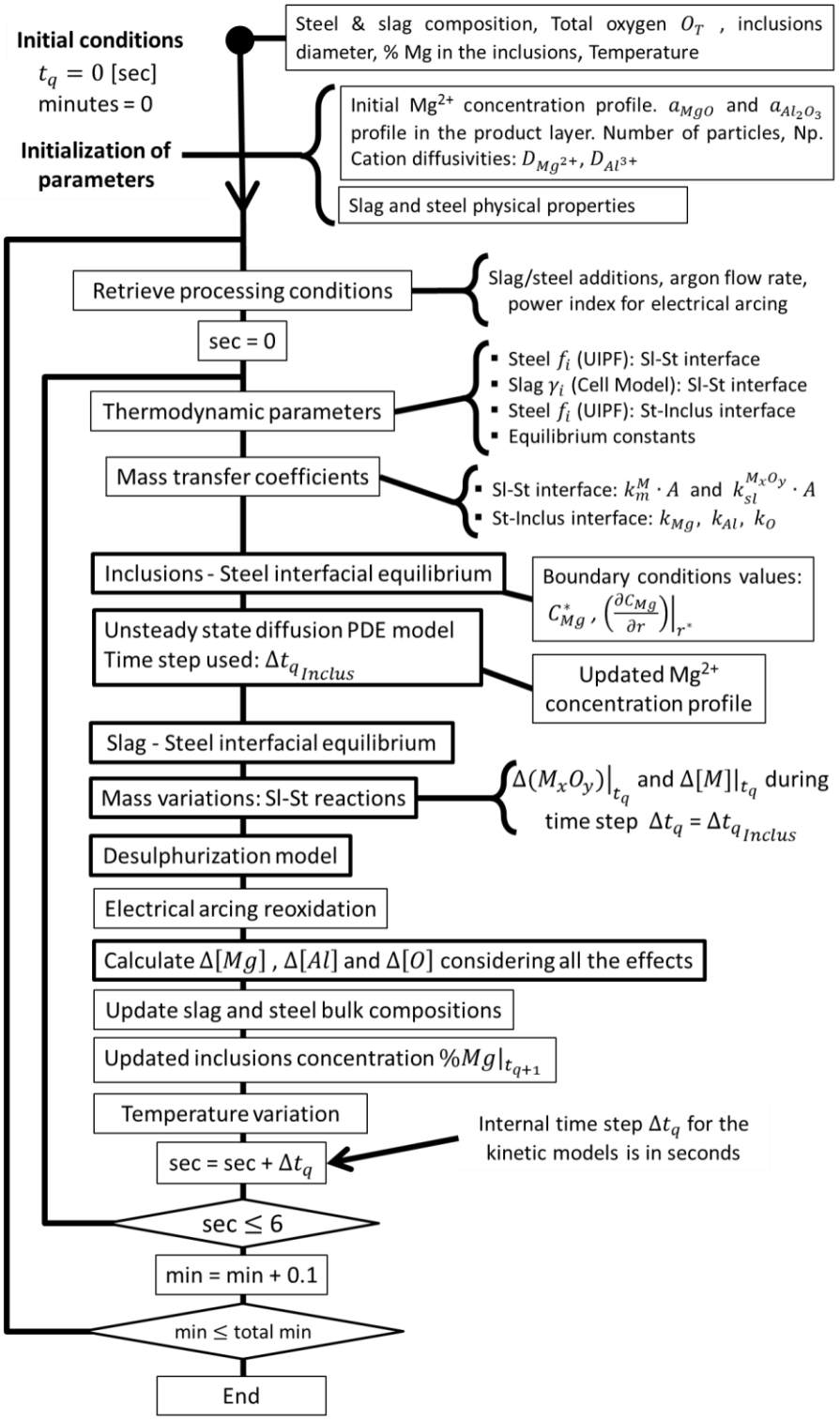

Figure 4-6. Coupled kinetic model for the slag, steel and Unsteady state diffusion in the oxide inclusions

4.2.2 Coupled model with the Quasi-steady state solution for spinel formation

The application of the Quasi-steady state solution for diffusion in the inclusions assumes that changes in the spinel product layer are much faster than the compositional variations due to the slag-steel model. Under this condition, the time step Δt_q in seconds used to proceed with the updates in the bulk of the slag and steel is independent of the several internal and smaller time steps $\Delta t_{q_{Inclus}}$ used to find convergence of the concentration profile of Mg^{2+} in the Quasi-steady state scheme. Therefore, the time scales of both processes are separated; additional details on the implementation of this scheme are in Chapter 3.

Figure 4-7 outlines the organization of the kinetic model for the three phases with the Quasi-steady state approximation.

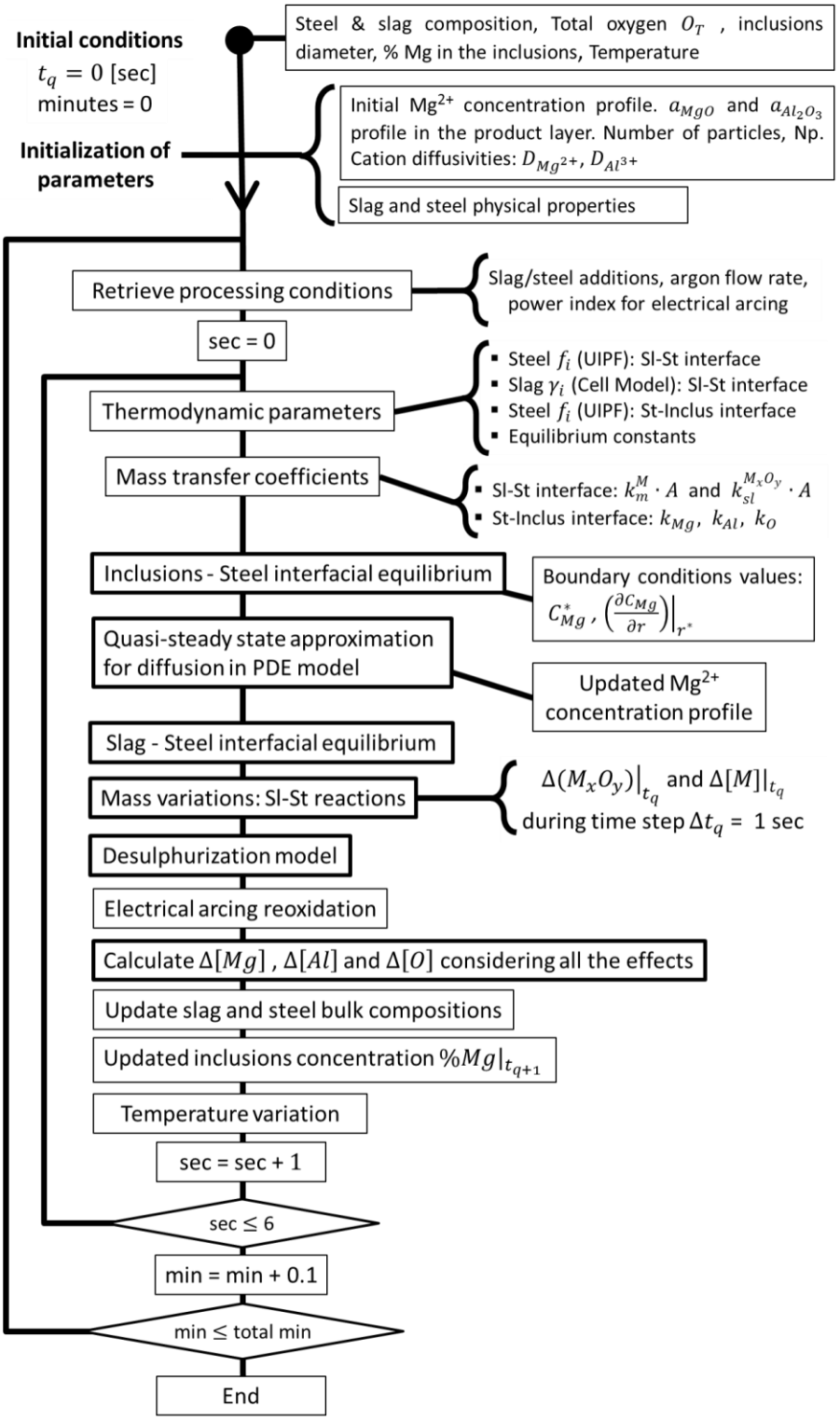

Figure 4-7. Coupled kinetic model for the slag, steel and Quasi-steady state diffusion in the oxide inclusions

4.3 Results from the analysis of industrial heats

The coupled kinetic model for the slag-steel-inclusions was used considering the industrial processing conditions of the refining heats without calcium treatment. The initial mass of the oxide inclusions was assumed the same for all the heats and was calculated based on 40 ppm of Total Oxygen O_T which comprises the oxygen bonded to the inclusions and the oxygen dissolved in steel [O]. The 40 ppm O_T value was chosen since it is within the range of measurements of total oxygen from the industrial sampling of the Ladle Furnace station in the study of Graham (2008).

The initial diameter of the inclusions was assumed to be 5 microns, this is due to plant results from the Automated SEM inclusions analysis (Graham, 2008) that indicate that most of indigenous inclusions are in the size range of 2.5 to 5 microns in diameter. Finally, the total number of inclusions N_p calculated at the start of every modeled heat was kept constant throughout the process.

Results of the calculated concentrations and the industrial sampling for Heat 7 are shown in figures 4-8 to 4-10. Additional results showing the validation of the coupled kinetic model as well as the processing parameters for this and all the heats analyzed are included in Appendix C of this thesis.

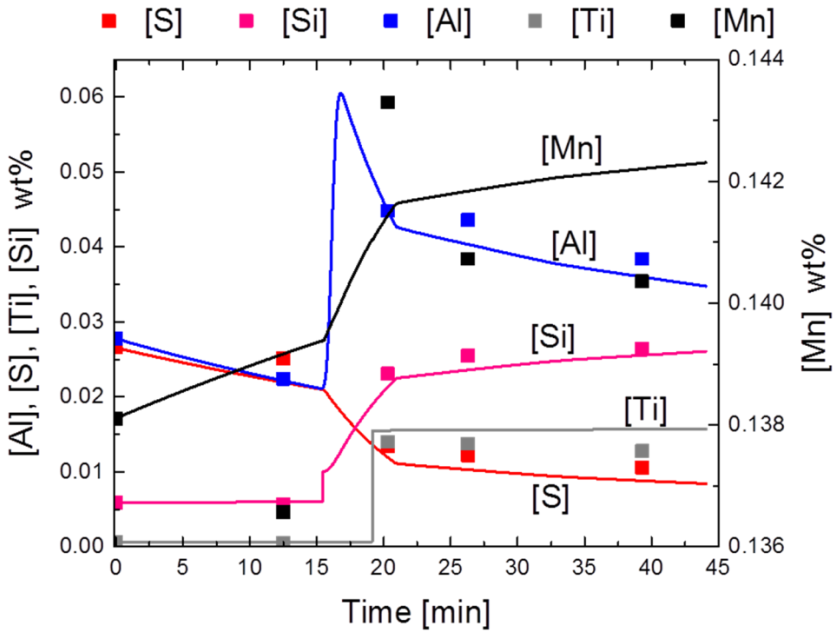

Figure 4-8. Calculated and measured bulk concentrations of dissolved species in the steel, Heat 7.

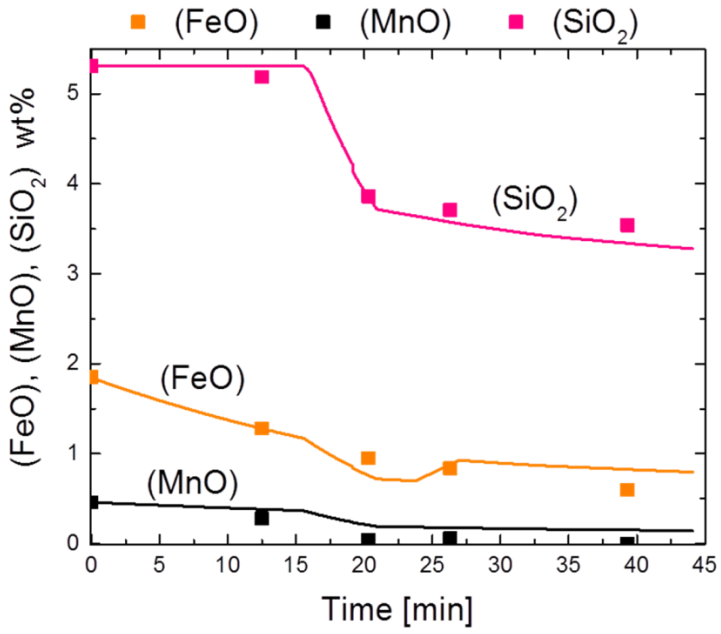

Figure 4-9. Calculated and measured bulk concentrations of FeO, MnO and SiO_2 in the slag, Heat 7.

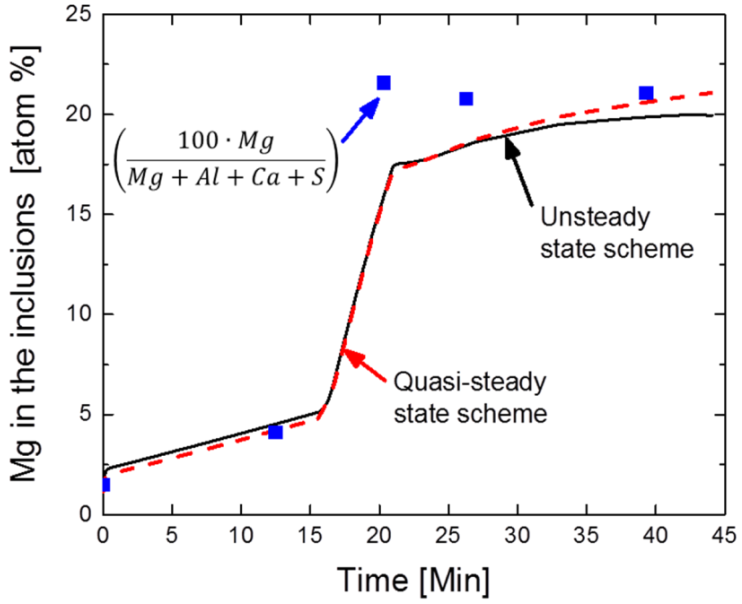

Figure 4-10. Calculated and measured content of Mg in the oxide inclusions, Heat 7.

In Heat 7 there is good agreement of the calculations with the measured values of the three phases: steel desulphurization, slag deoxidation, release of [Si] and inclusions analysis. At $t = 0$ $[min]$ the slag does not have a very high content of FeO and MnO, this allows some reduction of MgO that in turn slightly increases the %Mg of the inclusions. Afterwards, from $t = 16$ to $t = 21$ $[min]$ a higher flow rate of Ar gas is injected and aluminum cones are added for further deoxidation and desulphurization; during this period of time, the rate of Mg pickup in the inclusions increases but then it slows down during the subsequent low stirring regime.

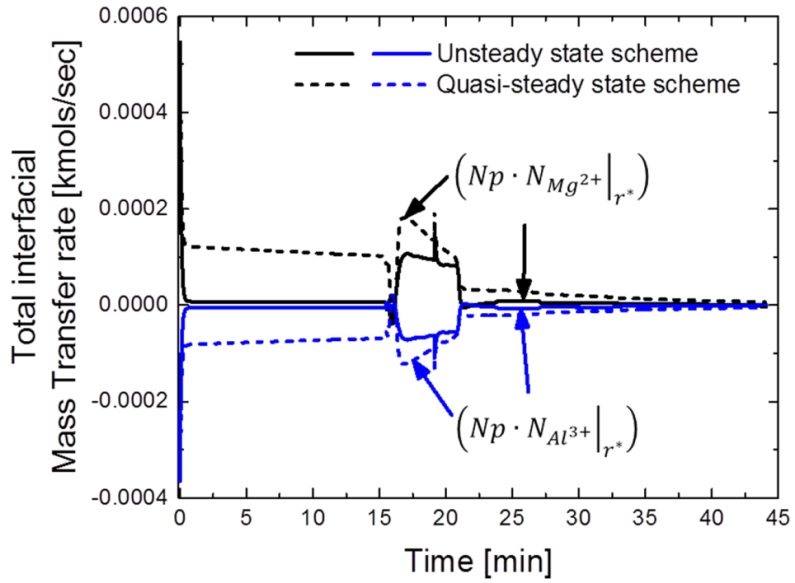

Figure 4-11. Calculated total interfacial mass transfer rates of Mg^{2+} and Al^{3+}, Heat 7. Np is the total number of particles.

The lapse of higher release of [Mg] from the slag to the steel increased the chemical potential μ_{Mg} for spinel formation; this can be detected in the calculated mass transfer rates of Mg^{2+} and Al^{3+} at the inclusions-steel interface, Figure 4-11.

Figure 4-10 compares the calculated atomic percentage of Mg in the inclusions (%Mg) with the fraction of measured Mg respect to the contents of Al, Mg, Ca and S in the inclusions; the minor contents of other elements as shown in Figure 4-12 are discarded. The measured element concentrations in Figure 4-12 that were also used for the fraction of Mg in Figure 4-10 correspond to the average element contents in all the inclusions found in each sample; this is independent of the size or type of oxide inclusion.

Furthermore, the comparison in Figure 4-10 is adequate for this system; this is due to the fact that the indigenous oxide inclusions during ladle refining of

LCAK steel change its composition mainly along the different mixtures and solid solutions of the oxides and oxisulphides with Al, Mg and Ca.

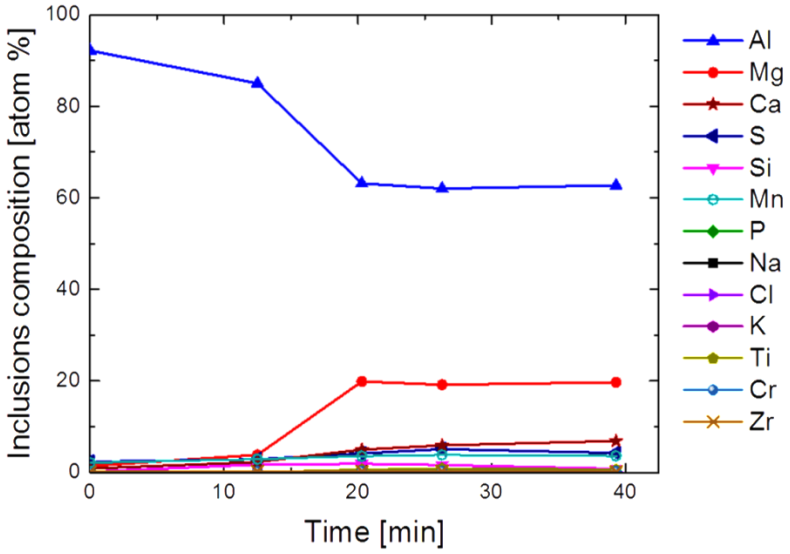

Figure 4-12. Automated SEM analysis, measured average composition of the indigenous inclusions during ladle treatment of Heat 7.

The calculated variation in the composition of spinel at the inclusion-steel interface is shown in Figure 4-13. Although there are local differences in the calculated equilibrium mole fraction $X_{Al_2O_3}$*, the average concentration of Mg in the inclusions behave in a similar way for both the steady and Quasi-steady state schemes as depicted in Figure 4-10.

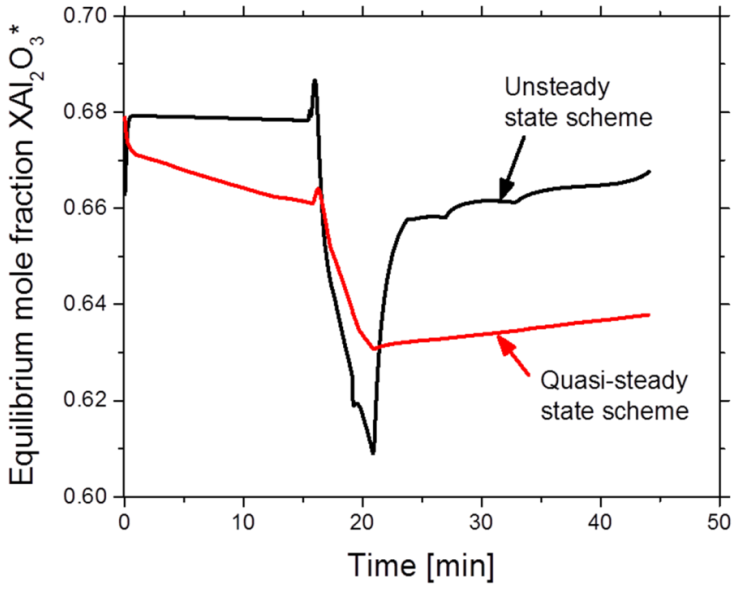

Figure 4-13. Calculated composition of spinel in the Al_2O_3-MgO system. Equilibrium mole fraction at the inclusions - steel interface, Heat 7.

The validation for the Mg content in the case of Heat 6 is in Figure 4-14. As reported in Appendix C, Heat 6 was processed under very similar conditions to Heat 7: steel mass, slag mass, contents of [Al] in the range of 0.03 to 0.06 wt% and a period of high stirring with the addition of Aluminum cones and Ferrotitanium. However, small differences in the behavior of the Mg pickup by the inclusions can be explained with the changes in the contents of the easily reduced oxides in the slag of Heat 6 shown in Figure 4-15.

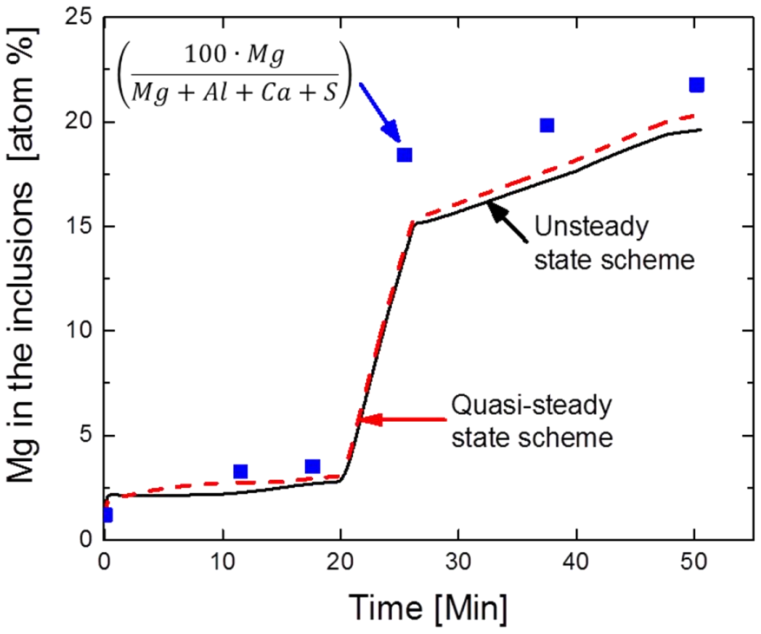

Figure 4-14. Calculated and measured content of Mg in the oxide inclusions, Heat 6.

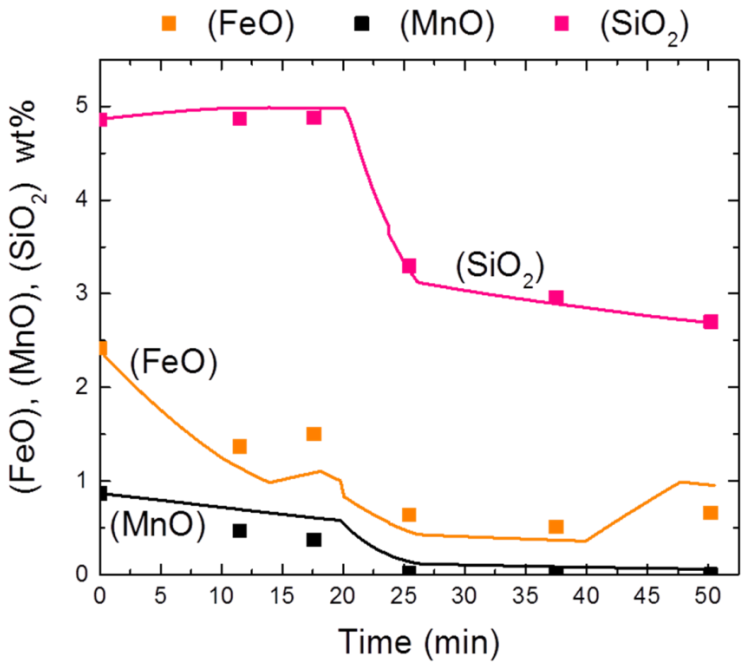

Figure 4-15. Calculated and measured bulk concentrations of FeO, MnO and SiO_2 in the slag, Heat 6.

Before the high stirring period, the slag in Heat 6 contained more FeO and MnO than Heat 7; this is reflected with a lower rate of Mg pickup in Heat 6 for the calculated and measured results. On the contrary, after the high stirring period Heat 6 is lower than Heat 7 in FeO and MnO, this explains the higher rate of Mg pickup during the second half of the process for the inclusions in Heat 6.

The validation results of the coupled model for the steel phase, the easily reduced oxides in the slag and the inclusions of Heat 15 are in figures 4-16 to 4-18. The respective processing conditions are shown in Figure 4-19.

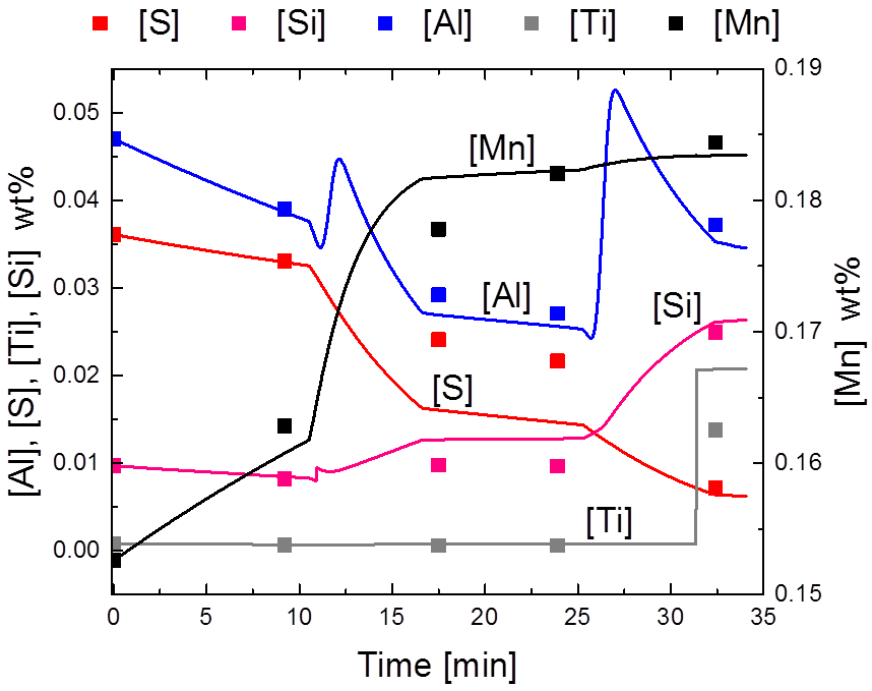

Figure 4-16. Calculated and measured bulk concentrations of dissolved species in the steel, Heat 15.

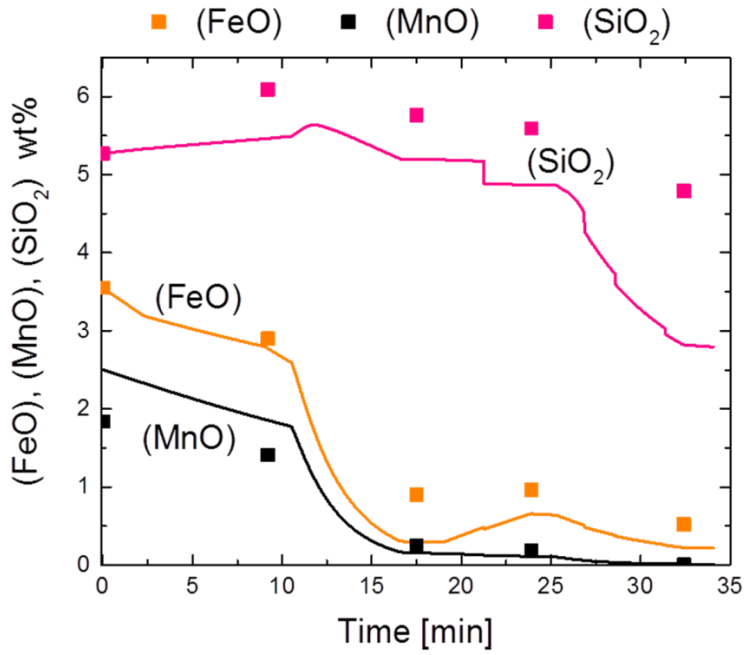

Figure 4-17. Calculated and measured bulk concentrations of FeO, MnO and SiO_2 in the slag, Heat 15.

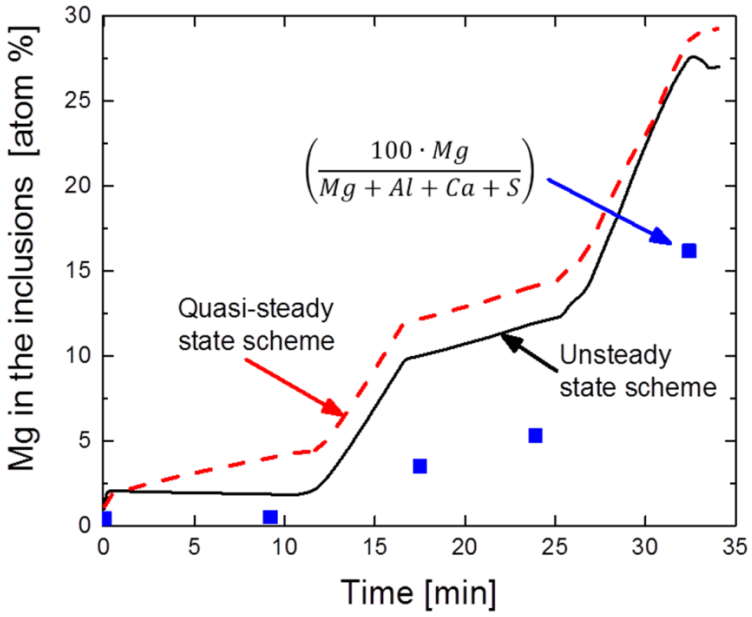

Figure 4-18. Calculated and measured content of Mg in the oxide inclusions, Heat 15.

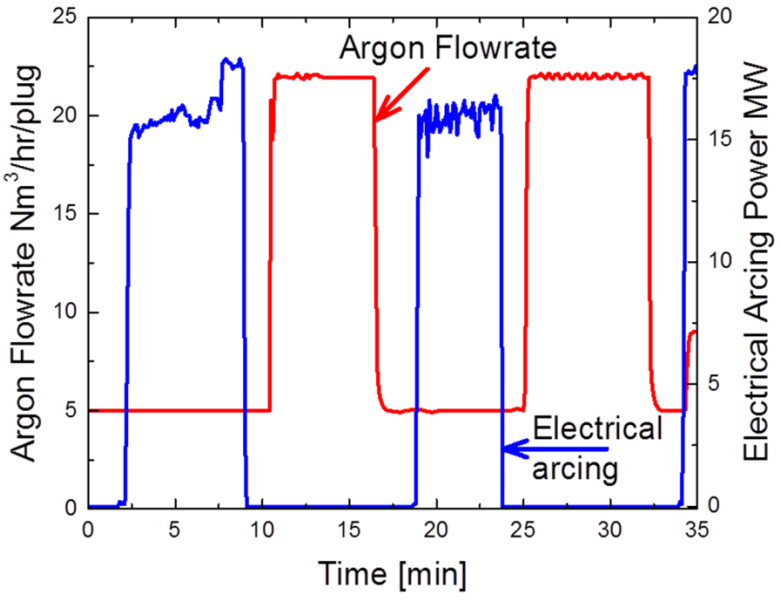

Figure 4-19. Argon gas stirring and electrical heating during treatment in the LMF, Heat 15.

Heat 15 had a higher content of FeO and MnO at the beginning that initially provided more oxidizing conditions for the dissolved [Si] in steel which caused an increase in the calculated and measured (SiO_2) in slag. However, the first period of high stirring from $t = 10.5$ to $t = 16.5$ $[min]$ included an addition of [Al] which drastically reduced the FeO and MnO in slag and shifted the system to favorable conditions to start the SiO_2 reduction.

Figure 4-18 illustrates that discrepancies between the calculated and measured final Mg content in the inclusions for Heat 15 are more evident during the first period of stirring. It is also important to notice for the first stirring period, that the calculated sulphur in the steel is below the measured values. The higher rate of steel desulphurization in the model from $t = 10.5$ to $t = 16.5$ $[min]$ can

be due to the calculation of an oxygen activity too low for the multicomponent interfacial equilibria at the slag-steel interface.

After the first high stirring the agitation is reduced and the slag is well deoxidized by the beginning of the second half of the refining heat. The second [Al] addition and the increase on the gas flowrate further promoted the formation of magnesium aluminate spinel in the inclusions. The more rapid release of [Mg] from the slag had an impact on the calculated mass transfer rates of Mg^{2+} and Al^{3+} at the inclusions-steel interface, Figure 4-20, as well as at the interfacial concentration of spinel in equilibrium with steel, Figure 4-21.

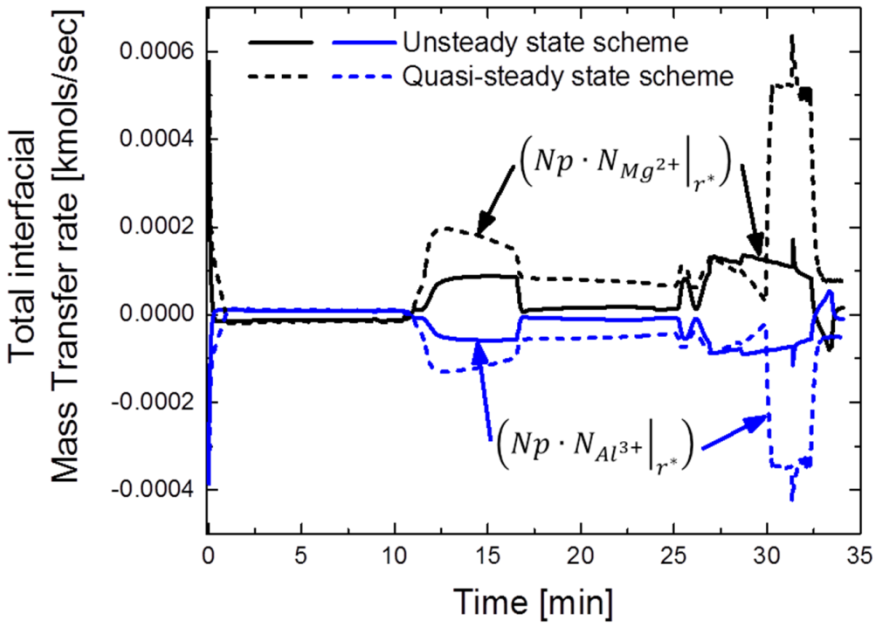

Figure 4-20. Calculated total interfacial mass transfer rates of Mg^{2+} and Al^{3+}, Heat 15. Np is the total number of particles.

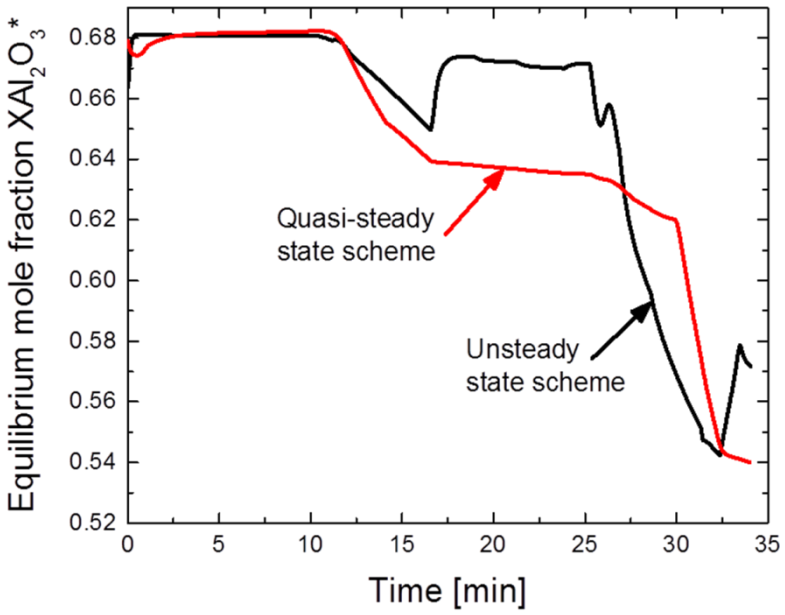

Figure 4-21. Calculated composition of spinel in the Al_2O_3-MgO system. Equilibrium mole fraction at the inclusions - steel interface, Heat 15.

The results from figures 4-18, 4-20 and 4-21 corroborate that the differences in the interfacial mass transfer rates of Mg^{2+} and Al^{3+} and the equilibrium composition of spinel calculated with the unsteady and quasi-steady state schemes are actually local differences. When the behavior of the total Mg content in the oxide inclusions in the overall system is compared for both schemes, Figure 4-18, very similar results are obtained. This supports and it is consistent with the argument that the kinetics of alumina to spinel transformation in the inclusions is controlled by the release of [Mg] from the slag and the kinetically coupled slag-steel reactions.

The validation results for Heat 18 are in figures 4-16 to 4-18. The particularity of Heat 18 is the higher initial [Al] content of 0.068 wt% which made unnecessary to add more [Al] during the process.

Despite the good agreement for the species in the slag and steel, the largest discrepancy for the rate of Mg pickup by the inclusions occurs during the application of a higher gas stirring flowrate. Simultaneously, another effect that contributes for the disagreement of the measured (%Mg) in the inclusions is the release of [Ca] due to the much lower oxygen potential at the slag- steel interface; these few ppm of dissolved [Ca] are absorbed by the inclusions to form calcium aluminates and mixtures of calcium and magnesium aluminates as shown in the inclusions analysis of sample 6: Figure 4-25 and Figure 4-26.

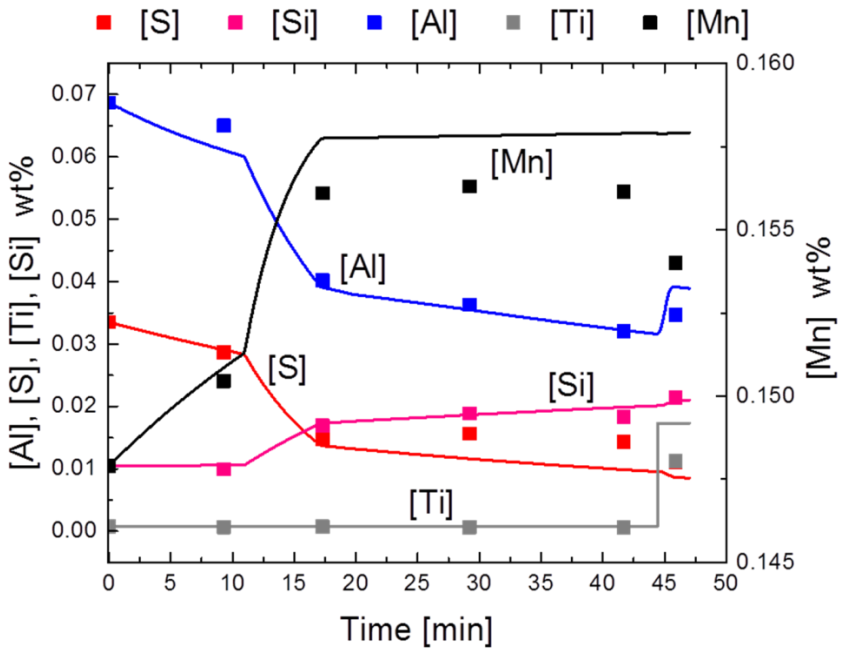

Figure 4-22. Calculated and measured bulk concentrations of dissolved species in the steel, Heat 18.

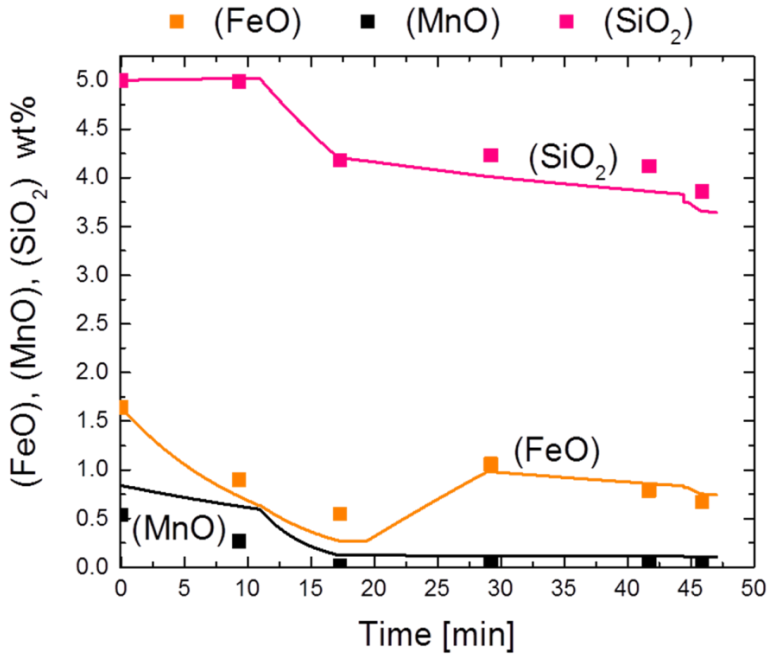

Figure 4-23. Calculated and measured bulk concentrations of FeO, MnO and SiO_2 in the slag, Heat 18.

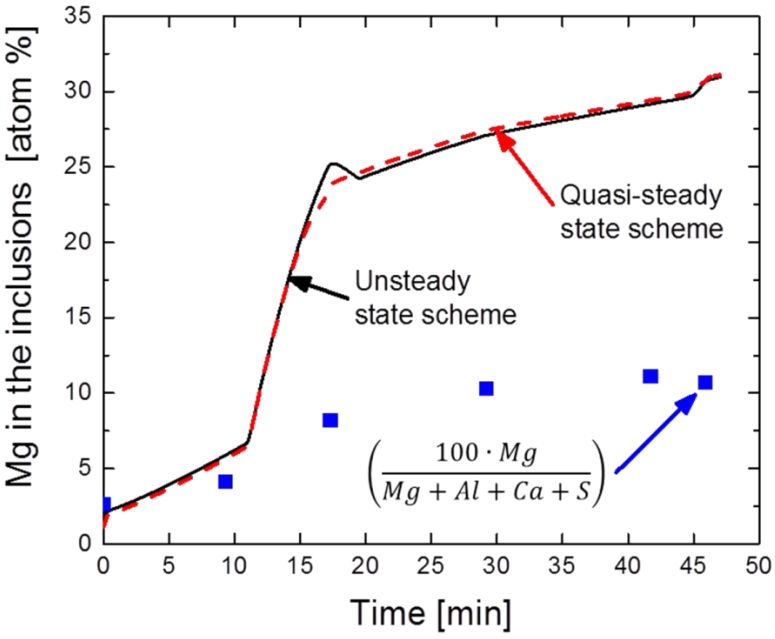

Figure 4-24. Calculated and measured content of Mg in the oxide inclusions, Heat 18.

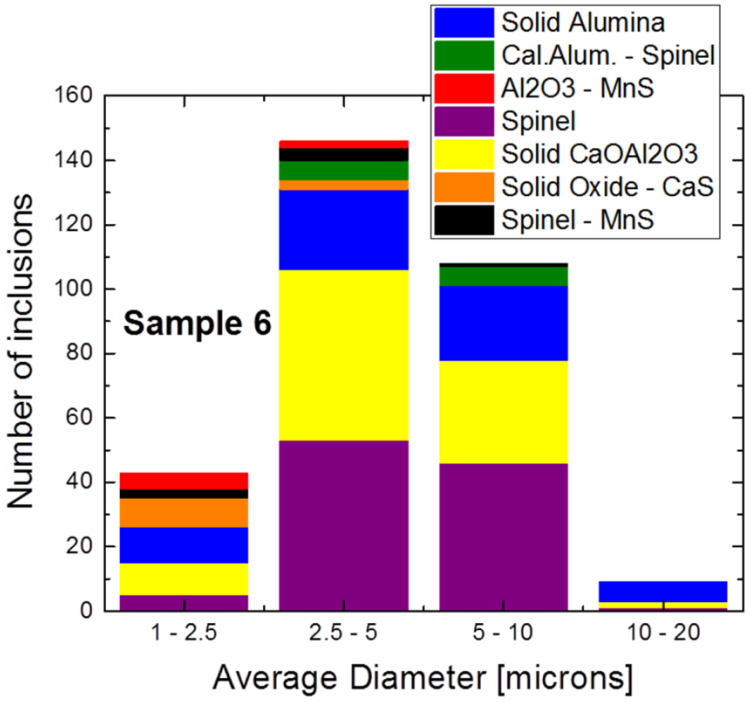

Figure 4-25. Measured results from the automated SEM inclusions analysis.

Number Distribution by average diameter (microns). Heat 18, sample 6.

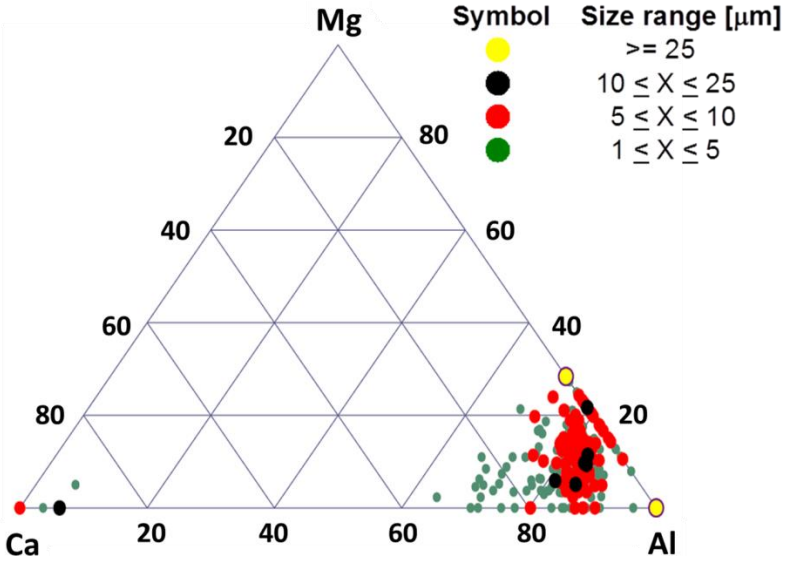

Figure 4-26. Measured results from the automated SEM inclusions analysis.

Ternary diagram for the Al-Mg-Ca percentage contents. Heat 18, sample 6.

The composition displacement in Heat 18 towards phases and mixtures with higher Ca contents in the inclusions cannot be modeled under the thermodynamic and kinetic assumptions of the current kinetic model on the formation of magnesium aluminate spinel. The present model can only describe variations across the Al_2O_3-MgO system for the inclusions.

In terms of a general analysis, introducing the effect of reoxidation due to electrical arcing improved the description of FeO in the slag as shown in Figure 4-15 for Heat 6, Figure 4-17 for Heat 15, and Figure 4-23 for Heat 18. However, even with this effect in the model, the discrepancies between the measured and modeled rates of Mg pickup by the inclusions prevailed during the periods of high stirring. Similarly, discrepancies on the calculated rates of steel desulphurization were mostly found during high stirring periods.

If the calculated oxygen activity at the slag-steel interface h_O^* is too low then the equilibrium activity and equilibrium concentration of X_{Mg}^* rises and induces a higher rate for [Mg] release to the steel. Similarly, a lower calculated h_O^* gives larger values of the equilibrium partition coefficient L_S' which promotes higher desulphurization rates. This in turn suggests the possibility of atmospheric reoxidation of the steel when a high gas flowrate is used for stirring. Such atmospheric reoxidation is favored when the steel exposes an 'open eye' which is an area not covered by the top slag. The oxygen potential at the slag-steel interface might then be affected by the partial pressure of oxygen in the

atmosphere. The comparison between measured and calculated Mg content in the inclusions for Heat 8, 10, and 17 is shown in figures 4-27 to 4-29.

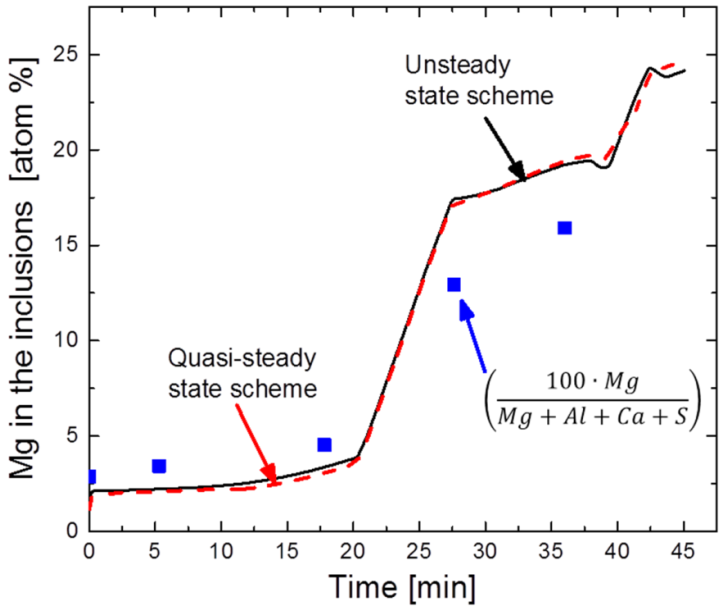

Figure 4-27. Calculated and measured content of Mg in the oxide inclusions, Heat 8.

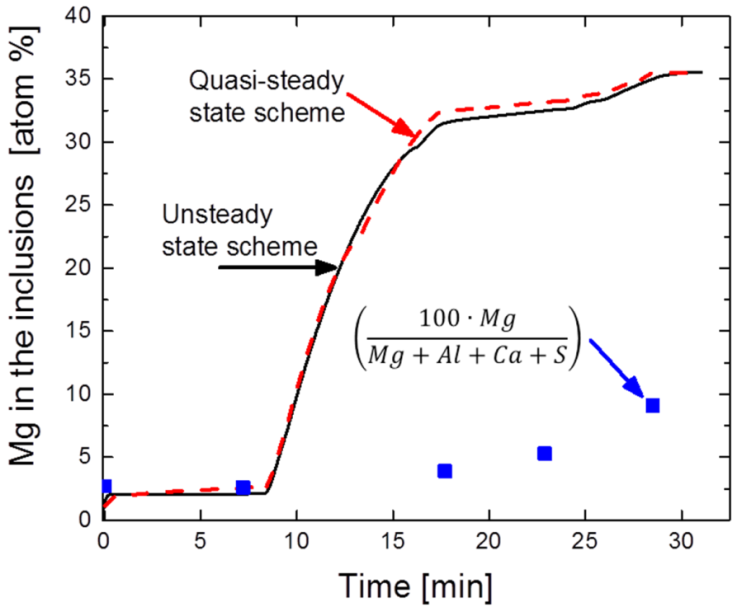

Figure 4-28. Calculated and measured content of Mg in the oxide inclusions, Heat 10.

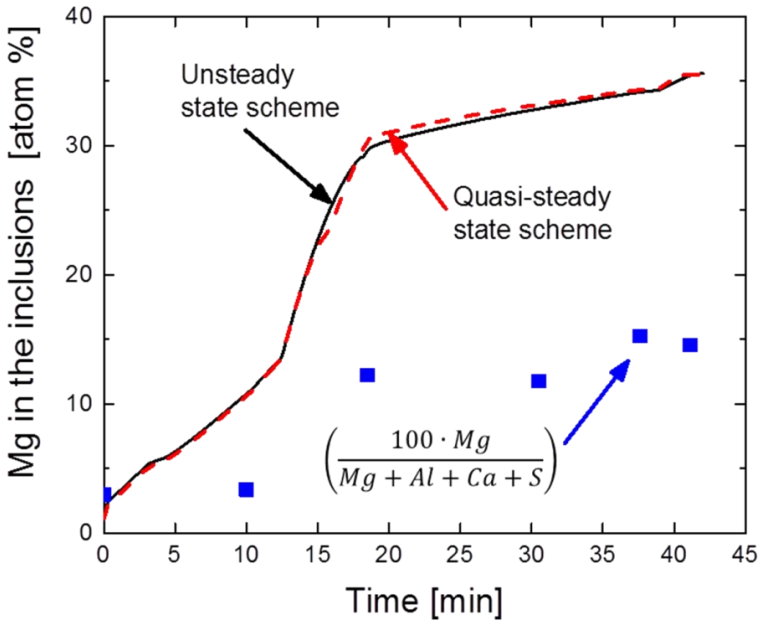

Figure 4-29. Calculated and measured content of Mg in the oxide inclusions, Heat 17.

Further sources of discrepancy between the measured and modeled amounts of Mg in the inclusions that are important to be mentioned include:

- Instrumental error and variation in the quantification of chemical elements from the Automated SEM analysis. This has been reported by Kaushik, Lehmann, & Nadif (2012) and Verma et al., (2012).
- Uncertainty in the thermodynamic parameters for steel deoxidation with [Mg] and [Al].
- Thermodynamics of the activities $a_{Al_2O_3}$ and a_{MgO} in the inclusions and the effect of other minor components in the Al_2O_3-MgO system.
- Changes in the amount of inclusions during the refining heats. This effect impacts the content of spinel mainly during periods of high Ar stirring since

a part of the formed spinel inclusions can be removed by flotation. Furthermore, new alumina inclusions can be incorporated into the steel due to reoxidation.

- Effect of atmospheric reoxidation
- The sampling procedure.

Some of these effects or parameters are further analyzed as part of the sensitivity analysis in this thesis project.

4.4 Analysis of the industrial heats with variations in the kinetic model

The previous results for the validation of the kinetic model with the industrial heats were obtained by specifying a constant number of particles N_p throughout the calculations of a given heat and assuming that the all particles have the same size. This is a simplification to the variations in the size and amount of oxide inclusions during ladle treatment; the implications of such assumptions were analyzed by repeating the calculations with the kinetic model and retrieving the industrial processing parameters but changing the number of inclusions, that is the cleanliness level. Furthermore, the same industrial conditions of certain heats were used but considering a distribution of particle sizes for the inclusions.

Additionally, there is a strong interest from the present study on magnesium aluminate spinel inclusions as well as from ArcelorMittal Dofasco on finding strategies to minimize the spinel formation without a negative impact on

the desulfurization efficiency. An alternative to this was analyzed by repeating the kinetic modeling of industrial heats but with a lower content of MgO in the slag; this is relevant since the slag is the only supplier of [Mg] in the current model for the formation of spinel in the inclusions.

4.4.1 Analysis for the total number of inclusions in the model validation

The more realistic conditions for the number and size distribution of the oxide inclusions during steel refining involve processes for the removal and the return of inclusions to the steel during the different operations in the ladle furnace. Because of the inclusions size, the liquid steel and the inclusions move as a unit. In this way, inclusions can be removed from the steel by reaching the slag-steel interface where they can be absorbed in the slag. Also, the number of inclusions decreases if they become attached to the refractory walls, Holappa (2014).

As reviewed by Fruehan & Pistorius (2013), gas stirring of the melt promotes inclusion removal simply by moving steel and the inclusions towards the slag–steel interface. Furthermore, direct interaction of inclusions with gas bubbles may also contribute to inclusion removal since inclusions tend to attach to gas bubbles in the case they collide each other. On the other hand, the processes which create new inclusions or return inclusions to the steel are reoxidation, washing of inclusions resting at the steel–slag interface back into the bulk steel and erosion of ladle walls. Unfortunately, both reoxidation and inclusion washing occur at higher rates if gas stirring is stronger.

The current kinetic model does not contain a model to quantify the different removal and source terms for the inclusions during ladle furnace operations. The measurements of Total Oxygen O_T from the sampling made by Graham (2008) of the industrial heats at ArcelorMittal Dofasco are shown in Figure 4-30.

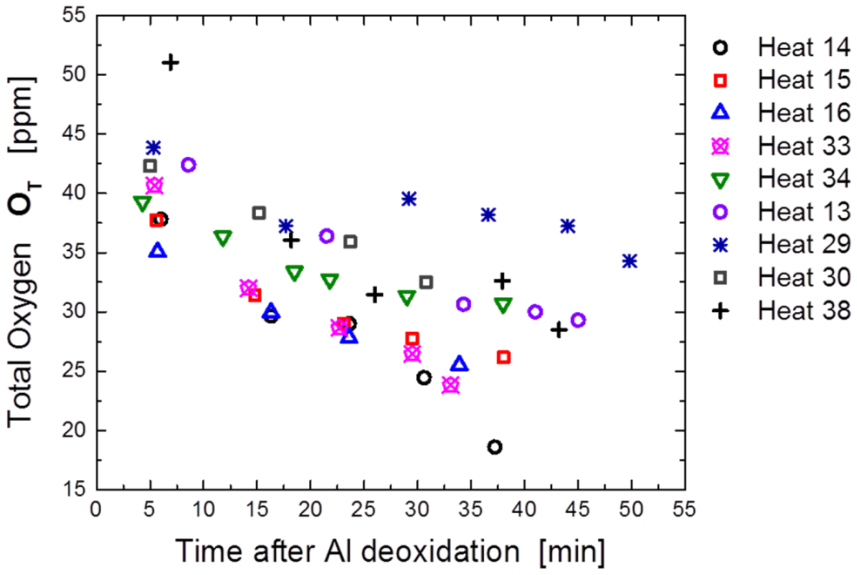

Figure 4-30. Measurements of Total Oxygen after Al deoxidation for non-calcium treated heats, values from Graham (2008).

The decrease in total oxygen for most of the heats indicates that the number of inclusions reduces during the course of a heat although there are differences and scatter in the removal rates for each heat. In the calculations with the coupled kinetic model the number of inclusions N_p is fixed. Furthermore, N_p is obtained by specifying the initial total oxygen and the initial diameter of the inclusions. During the calculations, both the total oxygen and the inclusions

diameter change; this is due to the mass transfer of [O] between the slag and the steel and between the steel and the inclusions. The sensitivity of the kinetic model to the number of inclusions was analyzed for Heats 8 and 15 by repeating the calculations but with the values of N_p for 20 ppm and 50 ppm of initial total oxygen. The initial diameter of the inclusions was the same as the previously used of 5 microns; the results are in Figures 4-31 and 4-32.

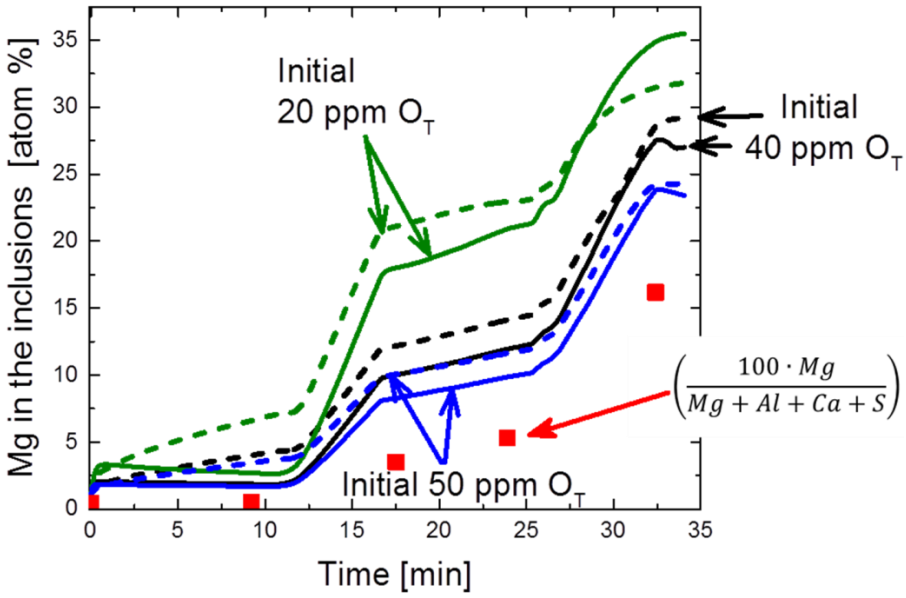

Figure 4-31. Mg content in the oxide inclusions for various initial O_T contents. The solid and dotted lines are the unsteady state and quasi-steady state solutions, respectively. The points are the data from SEM measurements, Heat 15.

As the number of inclusions decreases the [Mg] released from the slag is distributed among fewer particles, this in turn increases the content of Mg absorbed per particle and the amount of spinel formed in the inclusions. The

similar behavior for the solution with the unsteady and quasi-steady scheme supports again that the rate limiting step is the release of [Mg] from the slag.

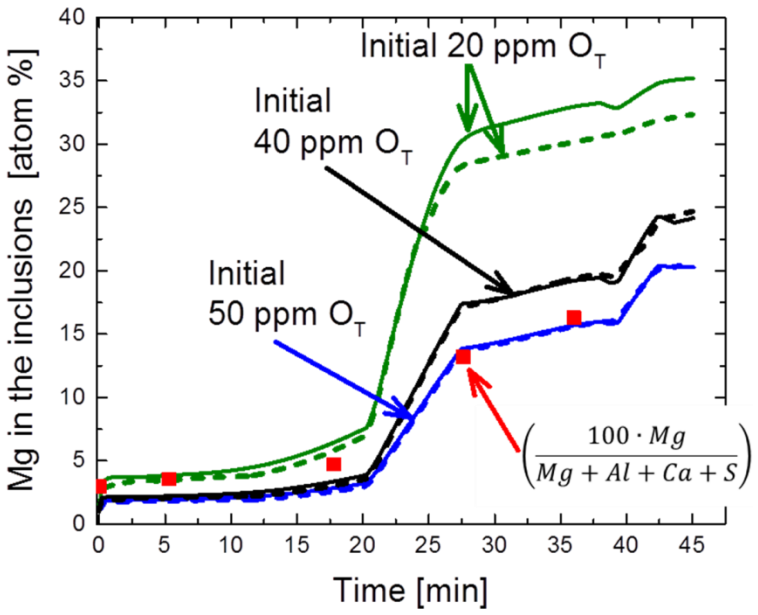

Figure 4-32. Mg content in the oxide inclusions for various initial O_T contents. The solid and dotted lines are the unsteady state and quasi-steady state solutions, respectively. The points are the data from SEM measurements, Heat 8.

The calculations with 40 and 50 ppm of initial total oxygen for Heats 10 and 17 are shown in figures 4-33 and 4-34. The results indicate that even with a higher number of particles, the disagreement for these heats during the period of high stirring is not enough compensated. This in turn suggests that other effects for the loss of [Mg] can be involved, including the possibility of atmospheric reoxidation and the release of Mg vapour.

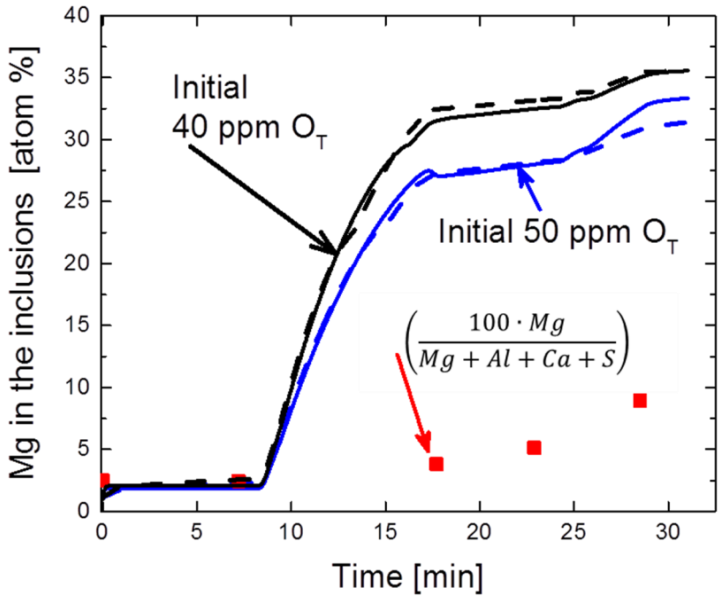

Figure 4-33. Mg content in the oxide inclusions for 40 and 50 ppm of initial O_T. The solid and dotted lines are the unsteady state and quasi-steady state solutions, respectively. The points are the data from SEM measurements, Heat 10.

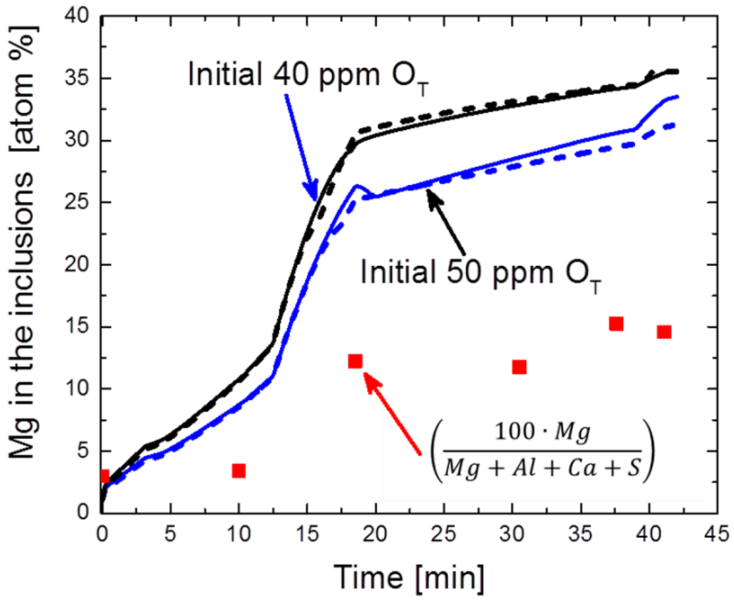

Figure 4-34. Mg content in the oxide inclusions for 40 and 50 ppm of initial O_T. The solid and dotted lines are the unsteady state and quasi-steady state solutions, respectively. The points are the data from SEM measurements, Heat 17.

4.4.2 Analysis for the size distribution of the inclusions

The measurements from the automated SEM analysis also include the distribution of particle sizes for all the inclusions found in a sample. The results specify the number of inclusions that belong to one of the four size ranges: 1-2.5 μm, 2.5-5 μm, 5-10 μm and 10-20 μm. Additionally, the classification is made by compositional phase. As shown in Figure 4-25 for Heat 6, most of particles are in the range of 2.5 to 5 μm. This condition is similar for all the heats studied; given this situation the calculations with the kinetic model assumed that the initial diameter was 5 μm, afterwards in the model during the progress of a heat the size of the calculated inclusions changes due to the volumetric variations between alumina and spinel as well as due to the deoxidation of steel.

With the total number of particles for each sample it is possible to calculate the fraction of particles in a given size range. Considering that indigenous inclusions are in the range of 1 to 10 microns, three fractions of particle sizes were identified according to:

$$fr\_a = \frac{1\ to\ 2.5\ \mu m\ inclusions}{Total\ number\ of\ inclusions} \tag{4-29}$$

$$fr\_b = \frac{2.5\ to\ 5\ \mu m\ inclusions}{Total\ number\ of\ inclusions} \tag{4-30}$$

$$fr\_c = \frac{5\ to\ 10\ \mu m\ inclusions}{Total\ number\ of\ inclusions} \tag{4-31}$$

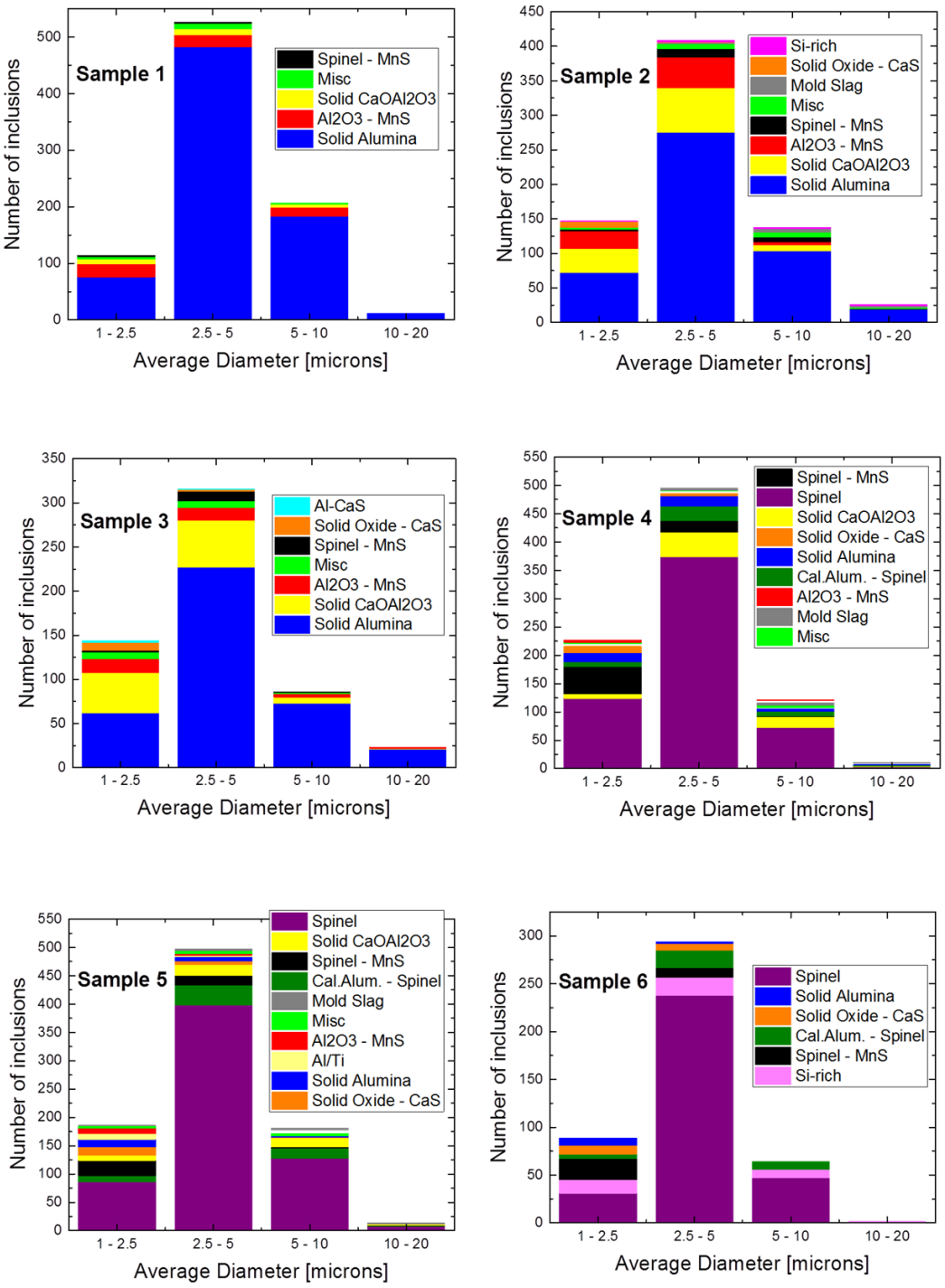

Figure 4-35. Measured results from the automated SEM inclusions analysis. Number Distribution by average diameter (microns), Heat 6. Sample numbers correspond to the sequence of process sampling as in Figure 4-14.

The variations in the fractions of particle sizes for Heat 6 are shown in Figure 4-36.

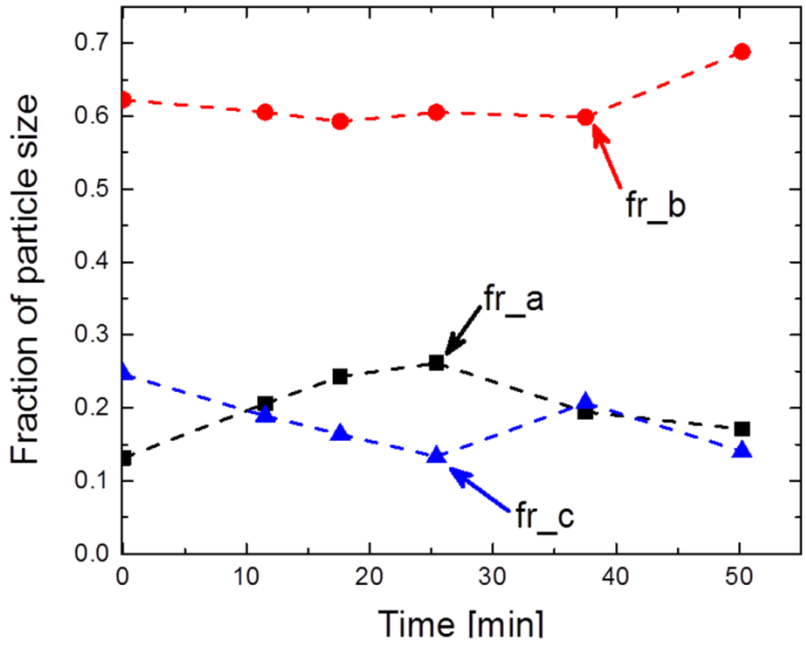

Figure 4-36. Changes in the fractions of particle sizes during the course of Heat 6

In order to investigate the effect of considering three inclusions sizes for the calculations with the current kinetic model, three initial diameters were assumed: $Diameter\_a = 2\ \mu m$, $Diameter\_b = 4\ \mu m$ and $Diameter\_c = 8\ \mu m$. An initial linear concentration profile for the respective product layers of each inclusion size was assumed. With the volume of each particle and the thickness of the initial spinel product layer it is possible to know the number of moles of oxygen per inclusion type, the procedure for these calculations is described in Chapter 3. The moles of oxygen per individual particle type are then identified as: $n_{Oxygen\_}a$, $n_{Oxygen\_}b$ and $n_{Oxygen\_}c$.

For these calculations the Total Oxygen O_T was assumed the same as in the calculations with a single type of inclusions size, therefore 40 ppm O_T was used. By subtracting the ppm of dissolved oxygen [O] in steel, the moles of oxygen bonded to the oxide inclusions are obtained and defined as $n_{Oxygen-bonded}$. The number of particles for each inclusion size is defined as: N_p_a, N_p_b and N_p_c. Then, balance for the moles of oxygen in the total mass of all inclusions is:

$$n_{Oxygen}\_a \times N_p\_a \; + \; n_{Oxygen}\_b \times N_p\_b \; + \; n_{Oxygen}\_c \times N_p\_c \; = \; n_{Oxygen-bonded} \tag{4-32}$$

From the previous definition of the fractions of particle sizes, the oxygen balance in equation (4-32) can be expressed as:

$$n_{Oxygen}\_a \times fr_a \cdot N_p \; + \; n_{Oxygen}\_b \times fr_b \cdot N_p + n_{Oxygen}\_c \times fr_c \cdot N_p = \; n_{Oxygen-bonded} \tag{4-33}$$

In equation (4-33) the total number of particles N_p is:

$$N_p\_a \; + N_p\_b \; + N_p\_c \; = \; N_p \tag{4-34}$$

To simplify the calculations, the average values of the variations in each fraction size during the course of a heat were used. For Heat 6 in Figure 4-36, the average values are: $\overline{fr\_a} = 0.204$, $\overline{fr\_b} = 0.614$ and $\overline{fr\_c} = 0.181$. The balance for oxygen in the total mass of all the inclusions can be expressed then as:

$$n_{Oxygen}\_a \times \overline{fr\_a} \cdot N_p \; + \; n_{Oxygen}\_b \times \overline{fr\_b} \cdot N_p + n_{Oxygen}\_c \times \overline{fr\_c} \cdot N_p = \; n_{Oxygen-bonded} \tag{4-35}$$

The number of particles N_p was obtained from equation (4-35) and with the known values of the moles of oxygen per individual particle, the average values of the fractions size and the moles of oxygen bonded to the inclusions. After N_p was calculated, the total number of particles N_p_a, N_p_b and N_p_c was obtained by using the average values of the fractions size. These initial calculations set the values of N_p_a, N_p_b and N_p_c that remain constant throughout the modeling of an industrial heat.

The modification of considering three particle sizes makes necessary to solve three interfacial calculations for the simultaneous deoxidation equilibria. Furthermore, three concentration profiles must be integrated with time to describe the growth of the product layers. In order to do so, first the time step to maintain stability for each concentration profile was calculated, that is: Δt_q_a, Δt_q_b and Δt_q_c. Then the integration time step Δt_q for the three inclusions sizes and for the slag-steel model was set the same and equal to the minimum of the three individual time steps. In this way, stability is preserved for all the concentrations profiles and the progress for all the inclusions and the slag-steel model was at the same pace. The results of the calculations with multiple particle sizes are in Figure 4-37 by showing the %Mg in each particle size. With the known number of moles of Mg and Al per inclusion size in the model, it was possible to calculate the content of Mg in the total mass of the inclusions as it is reported in the automated SEM analysis which is independent of the inclusions sizes. The numbers of moles of Mg and Al per individual inclusion type were defined as:

n_{Mg}_a, n_{Mg}_b, n_{Mg}_c, n_{Al}_a, n_{Al}_b and n_{Al}_c. Therefore, with the number of particles of each inclusion size, the total numbers of moles of Mg and Al in all the inclusions being modeled are:

$$Total\, n_{Mg} = n_{Mg}\_a \times N_p\_a + n_{Mg}\_b \times N_p\_b + n_{Mg}\_c \times N_p\_c \quad (4\text{-}36)$$

$$Total\, n_{Al} = n_{Al}\_a \times N_p\_a + n_{Al}\_b \times N_p\_b + n_{Al}\_c \times N_p\_c \quad (4\text{-}37)$$

The respective %Mg in all the mass of the inclusions that can be used for comparison with the automated SEM analysis is obtained with:

$$\%Mg_{All\ inclusions} = \frac{Total\, n_{Mg}}{Total\, n_{Mg} + Total\, n_{Al}} \times 100 \quad (4\text{-}38)$$

The %Mg calculated with only one particle size and assuming 5 microns of initial diameter is also presented in Figure 4-37. It is important to recall that for the single particle calculation and for the multiple particle size calculation the initial total mass of the inclusions is the same and is based on 40 ppm of Total Oxygen O_T.

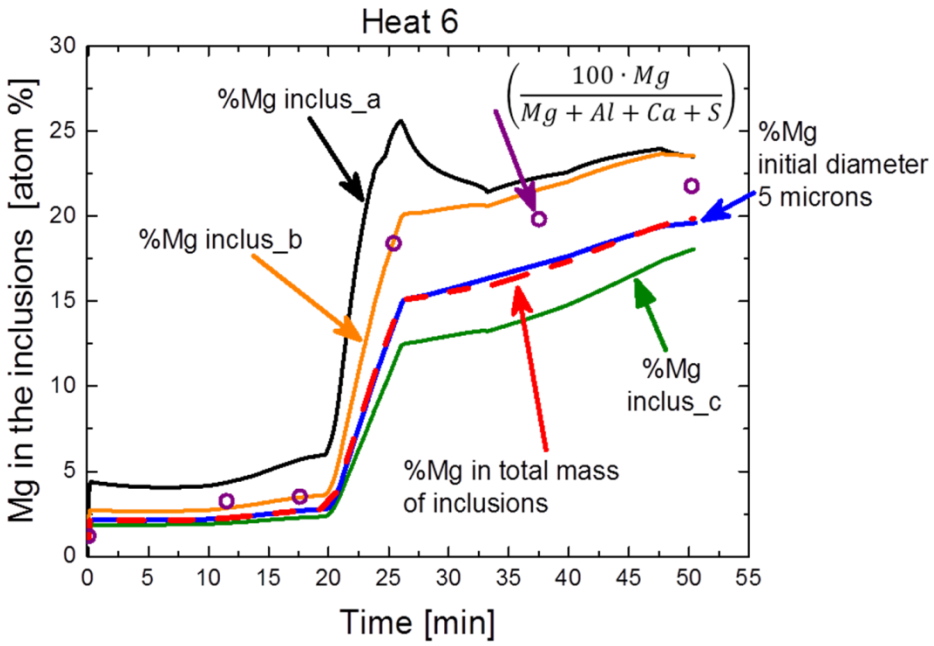

Figure 4-37. Calculated %Mg for each particle size in the simultaneous multiparticle model. The dashed line is the respective %Mg in all the mass of inclusions. The %Mg from the model with a single particle size is also included as well as the fraction of Mg from the industrial measurements. Heat 6.

The results in Figure 4-37 indicate that the smaller particles reach a higher concentration of magnesium while the larger particles have a lesser extent of transformation to spinel. During the period of high stirring it is noticeable that the rate of Mg pickup by the inclusions increases as the size of the inclusions decreases. The calculated interfacial concentration of spinel for the three inclusions sizes is shown in Figure 4-38.

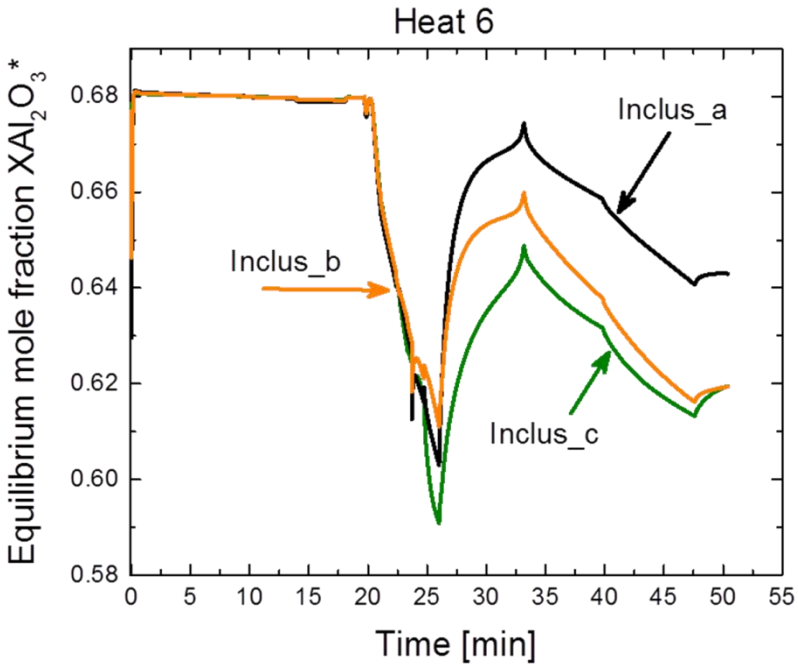

Figure 4-38. Calculated composition of spinel in the Al_2O_3-MgO system. Equilibrium mole fraction at the inclusions - steel interface. Simultaneous multiparticle model, Heat 6.

The variations in particle size fractions for Heat 7 are in Figure 4-39, the respective average values used for the kinetic model are: $\overline{fr\_a} = 0.195$, $\overline{fr\_b} = 0.598$ and $\overline{fr\_c} = 0.206$. The results of %Mg for each particle size, the Mg concentration for all the inclusions and for the single particle size model as well as the SEM measurements are in Figure 4-40. Similarly for Heat 15, the particle size fractions are in Figure 4-41. The average values used for the model are: $\overline{fr\_a} = 0.187$, $\overline{fr\_b} = 0.597$ and $\overline{fr\_c} = 0.214$. Finally, the results of %Mg for each particle size, the Mg concentration for all the inclusions and for the single particle size calculation are in Figure 4-42.

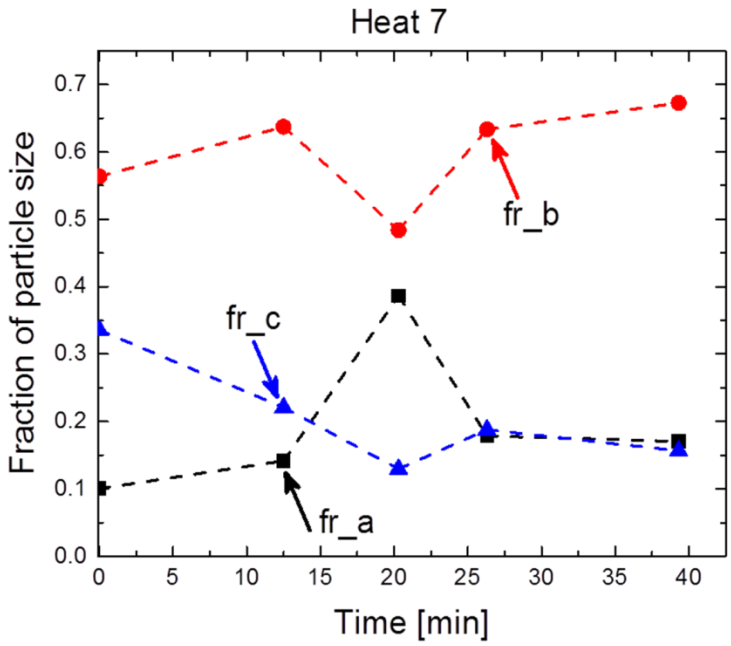

Figure 4-39. Changes in the fractions of particle sizes during the course of Heat 7

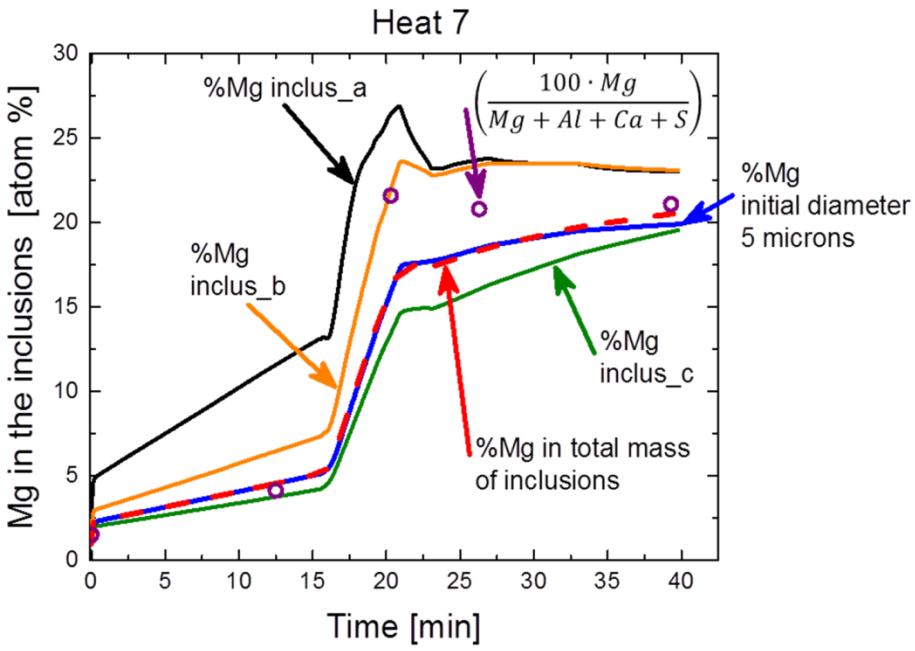

Figure 4-40. Calculated %Mg for each particle size in the simultaneous multiparticle model. The dashed line is the respective %Mg in all the mass of inclusions. The %Mg from the model with a single particle size is also included as well as the fraction of Mg from the industrial measurements. Heat 7.

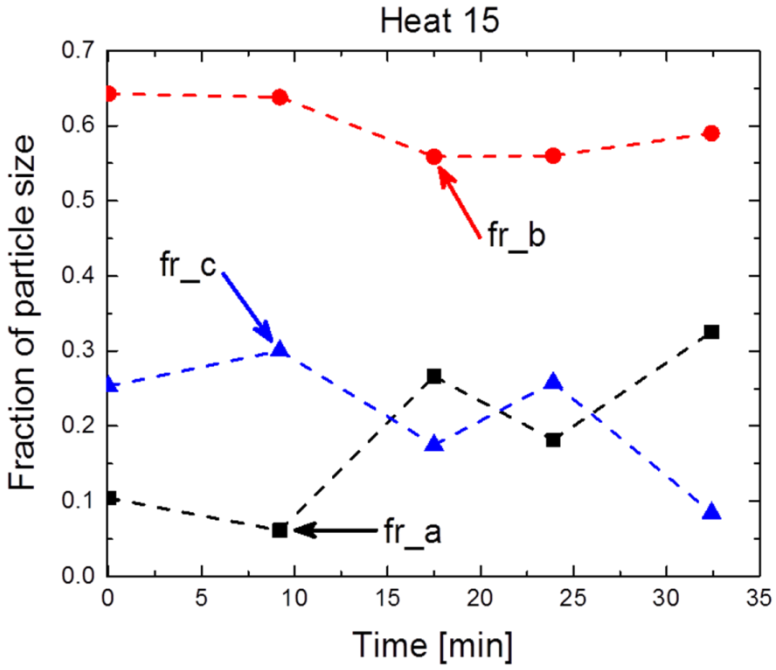

Figure 4-41.Changes in the fractions of particle sizes during the course of Heat 15

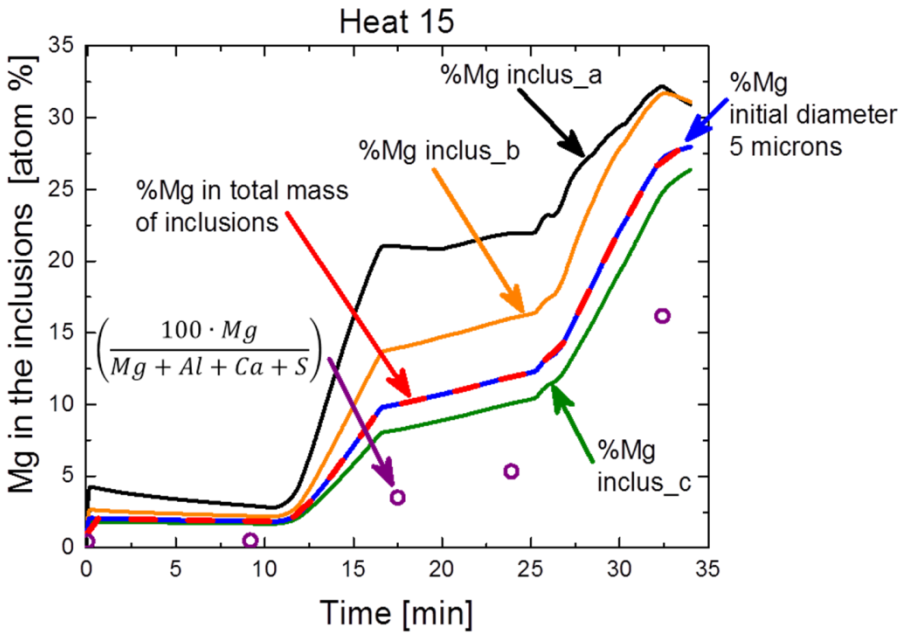

Figure 4-42. Calculated %Mg for each particle size in the simultaneous multiparticle model. The dashed line is the respective %Mg in all the mass of inclusions. The %Mg from the model with a single particle size is also included as well as the fraction of Mg from the industrial measurements. Heat 15.

An important conclusion from the results of these heats is the fact that the calculated %Mg in all the mass of inclusions from the multiparticle model has almost an identical behavior to the %Mg obtained with the model that assumes that all inclusions have the same size. Also, assuming 5 μm for initial diameter is appropriate in the single particle size model. These conclusions imply that considering a particle size distribution in the model does not impact the amount of Mg pickup by the complete mass of inclusions. The results indicate that this is true as far as the total mass of inclusions is the same, which in these scenarios it was always based on 40 ppm of total oxygen. It is important to recall that these kinetic models do not consider the changes due to flotation of inclusions. On the contrary, the effect of the mass of inclusions in the system was previously analyzed by varying the total oxygen O_T and it was shown to have a greater impact on the extent of spinel formation.

4.4.3 Analysis on the MgO content in the top slag

One of the purposes of this thesis project is to analyze feasible alternatives to be industrially implemented that help to lower spinel formation in the inclusions but without having a negative impact on the extent of desulphurization. A possibility on this aspect is to reduce the (MgO) content in the slag. In order to see the effect of this process parameter, the coupled kinetic model for the slag-steel and inclusions with a single particle size was used.

The calculations to describe the industrial heats were repeated with the same initial amount of inclusions based on 40 ppm O_T and assuming that all inclusions have the same initial diameter of 5 microns. The only variation for this analysis was the initial wt% of dissolved (MgO) in the slag from the industrial content reported to a lower value of 3 wt %. This modification of the slag chemistry is unlikely to have a drastic effect on the desulphurization process other than a slight reduction on the sulphide capacity (Turkdogan, 1985). The calculated %Mg results for Heat 6, 7, 8 and 15 are in Figures 4-43 to 4-46. The respective measured fractions of Mg are also included.

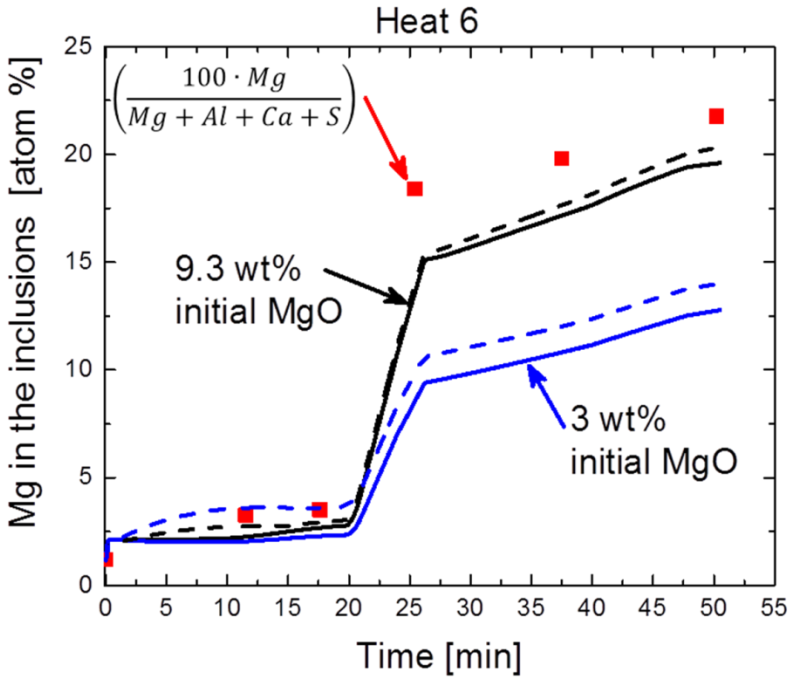

Figure 4-43. Calculated %Mg in the inclusions. The industrial value of MgO in the slag was 9.3 wt%. Continuous lines from the unsteady state scheme, dashed lines are from the Quasi-steady state scheme for the inclusions, Heat 6.

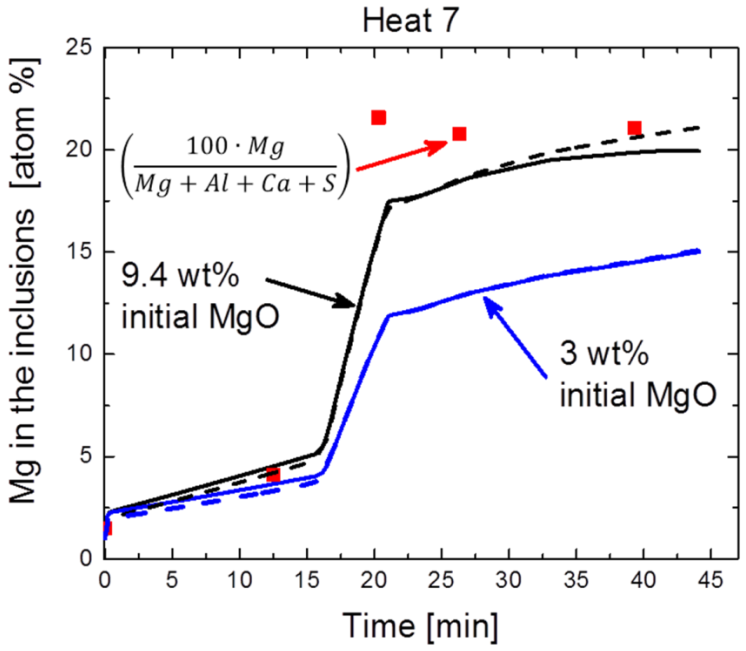

Figure 4-44. Calculated %Mg in the inclusions. The industrial value of MgO in the slag was 9.3 wt%. Continuous lines from the unsteady state scheme, dashed lines are from the Quasi-steady state scheme for the inclusions, Heat 7.

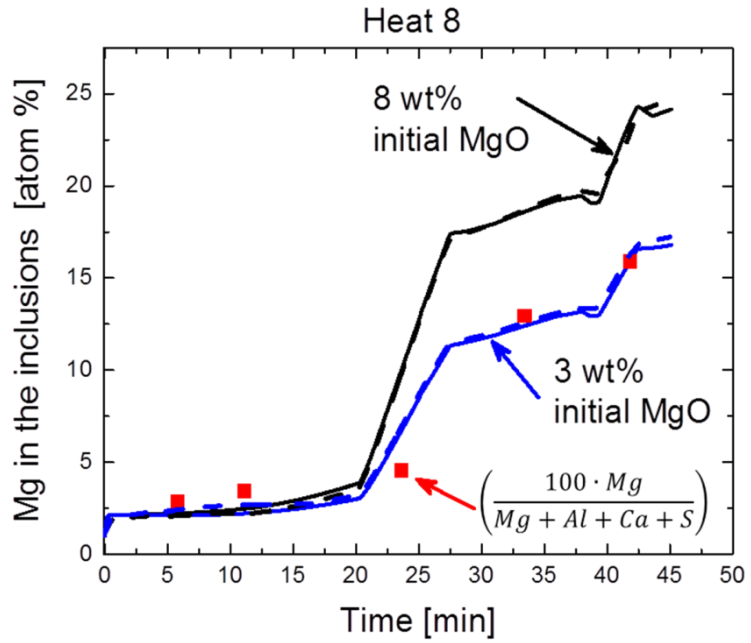

Figure 4-45. Calculated %Mg in the inclusions. The industrial value of MgO in the slag was 9.3 wt%. Continuous lines from the unsteady state scheme, dashed lines are from the Quasi-steady state scheme for the inclusions, Heat 8.

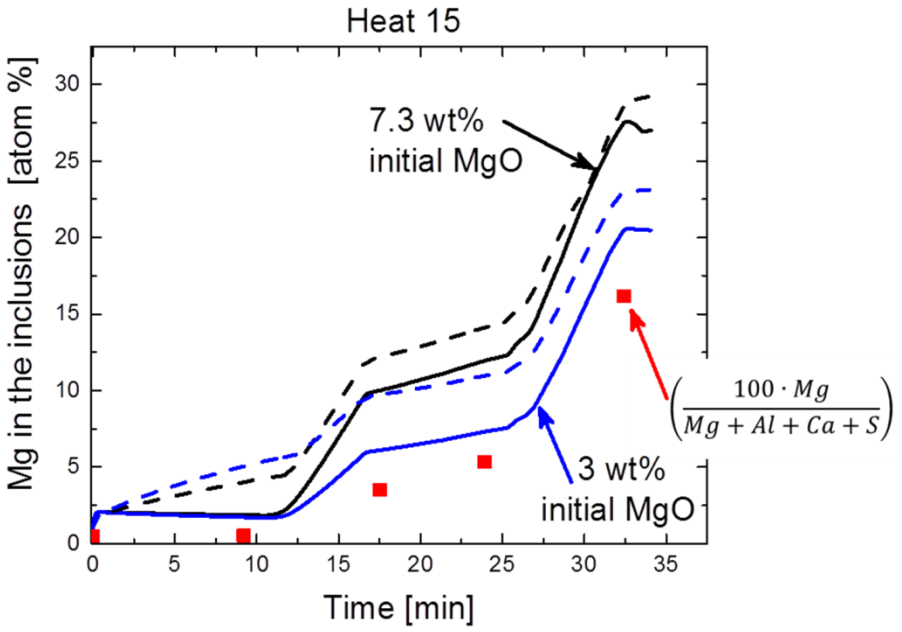

Figure 4-46. Calculated %Mg in the inclusions. The industrial value of MgO in the slag was 9.3 wt%. Continuous lines from the unsteady state scheme, dashed lines are from the Quasi-steady state scheme for the inclusions, Heat 15.

The results indicate a decrease in the amount of spinel in all cases; this is expected since the only source of [Mg] for spinel formation in the model is the top slag. Furthermore, the measured MgO in slag of these industrial heats was in the range of 7 to 10 wt%, for these concentrations the slag is saturated in MgO; that is, the activity of MgO in the slag is very close to unity, $a_{(MgO)in\ slag} \approx 1$. However, from the thermodynamic calculations with the Cell Model, a content of 3 wt% MgO in these industrial multicomponent slags gives an activity closer to $a_{(MgO)in\ slag} \approx 0.5$. Although there is a reduction in the %Mg for the inclusions is not in the same proportion in which the MgO activity is lowered in the slag.

Figure 4-47 shows that the desulphurization in steel in Heat 6 is not significantly affected by this modification of the slag chemistry; similar results were obtained for the other heats. This indicates that control over the MgO in the slag can help to reduce spinel formation but it might require additional processing modifications in order to get lower amounts of spinel in the inclusions.

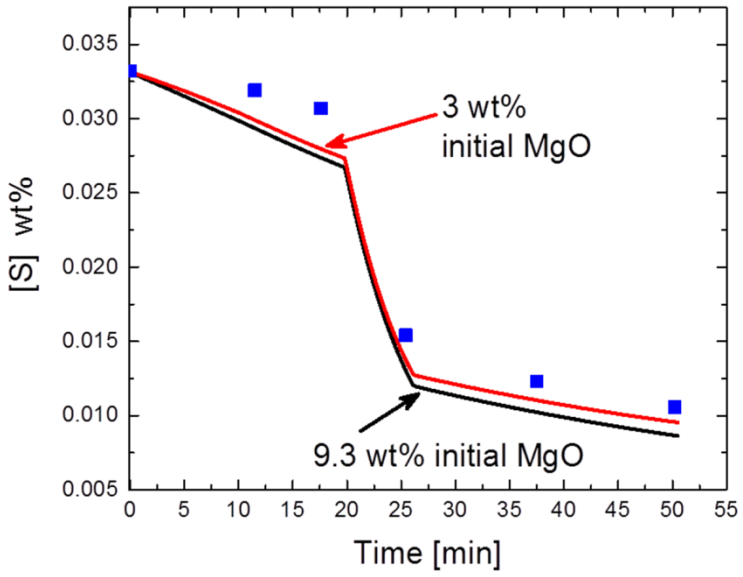

Figure 4-47. Calculated bulk content of [S] in the steel for the reported industrial conditions and with a lower (MgO) in the slag. The measured concentrations are also included. Heat 6.

A similar analysis on the effect of MgO content in the slag for the formation of spinel was made by Harada, et al., (2013b) with the kinetic model that they proposed. These researchers arrived to similar conclusions on the necessity of combining several aspects during the refining process in order to reduce Mg pickup by the inclusions.

4.5 Sensitivity analysis of the kinetic model

As elegantly reviewed by Saltelli, et al., (2012); models of reaction systems are routinely created to understand reaction mechanisms, kinetic properties and process yields under various operating conditions. From this perspective, a model will hopefully help to corroborate or falsify a given description of reality. However, as mentioned by Saltelli, et al., (2012) models are built on the presence of uncertainties of various levels such as the kinetic and thermodynamic values used for the calculations. Determining the strength of the relation between a given uncertain input and the output in the model is the job of a sensitivity analysis.

The present sensitivity analyses focused on two different types of parameters in the kinetic model. The first group of calculations analyzed the conditions during refining in the ladle furnace; this includes the initial composition of the slag and steel, the size and amount of inclusions and the intensity of argon stirring. The second group of analyses determined the effect of the uncertainty in the rate constants for mass transfer and diffusion; specifically, the mass transfer coefficients for convective transport in the slag, the mass transfer coefficients of [Mg], [Al] and [O] in the boundary layer at the inclusions-steel interface and the component diffusivities of the cations Mg^{2+} and Al^{3+} in the spinel product layer.

The mass of steel in these calculations was set to be initially 160000 kg, while the initial mass of slag was 3000 kg. Isothermal conditions were fixed at 1873 K. The initial composition of the steel is in Table 4-1. The initial bulk oxygen concentration is equal to the equilibrium concentration for [Al] deoxidation to form pure alumina, $a_{Al_2O_3} = 1$, therefore the initial oxygen bulk concentration is [O] = 6.01 ppm.

Table 4-1. Initial bulk composition in the steel in wt%, base case.

[C]	[Mn]	[P]	[S]	[Si]	[Cu]	[Ni]	[Cr]	[Sn]	[Mo]
0.05	0.15	0.006	0.035	0.007	0.1	0.03	0.06	0.005	0.012

[Al]	[N]	[Nb]	[Ca]	[B]	[Ti]	[Mg]
0.04	0.0069	0.0002	0.0002	0.0001	0.0007	0.00001

The base case for the initial composition of the tops slag is in Table 4-2. This base slag composition contains 2.5 wt% FeO and 1 wt% MnO; it is also important to note that the slag is MgO saturated due to its initial 8 wt% MgO.

Table 4-2. Initial bulk composition in the slag in wt%, base case.

K_2O	P_2O_5	TiO_2	CaS	FeO	CaO
0.005	0.01	0.3	0.45	2.5	50

MnO	SiO_2	MgO	Al_2O_3	Other
1	5	8	30	3.811

Unless otherwise specified, the mass transfer coefficients of the more easily reduced oxides in the slag FeO, MnO and SiO_2 were obtained from the ratios with the respective species in the steel. The base case values were: $\frac{k_{sl}^{FeO}}{k_m^{Fe}}$ = 0.25, $\frac{k_{sl}^{MnO}}{k_m^{Mn}}$ = 0.1 and $\frac{k_{sl}^{SiO_2}}{k_m^{Si}} = 1 \times 10^{-3}$. These ratios were maintained constant during the course of each analysis.

The initial thickness of the spinel product layer was calculated to represent 1 Mg% in the oxide inclusions. The base case assumed 40 ppm of total oxygen O_T and that all the inclusions have the same initial diameter of 5 microns. The number of particles N_p is held constant for each analysis.

4.5.1 Sensitivity analysis for the processing conditions in the ladle furnace

4.5.1.1 Effect of gas stirring in the ladle furnace

In this analysis the base case was used but with variations in the intensity of argon stirring. The low and high gas stirring regimes were set based on the reported conditions from ArcelorMittal Dofasco. The low gas flowrate was at 5 Nm^3/hr per plug while the high gas flow rate was at 20 Nm^3/hr per plug. The kinetic model was modified to keep a constant bulk concentration of [Al] equal to 0.04 wt%. The results on the variations in %Mg for the inclusions is in Figure 4-48.

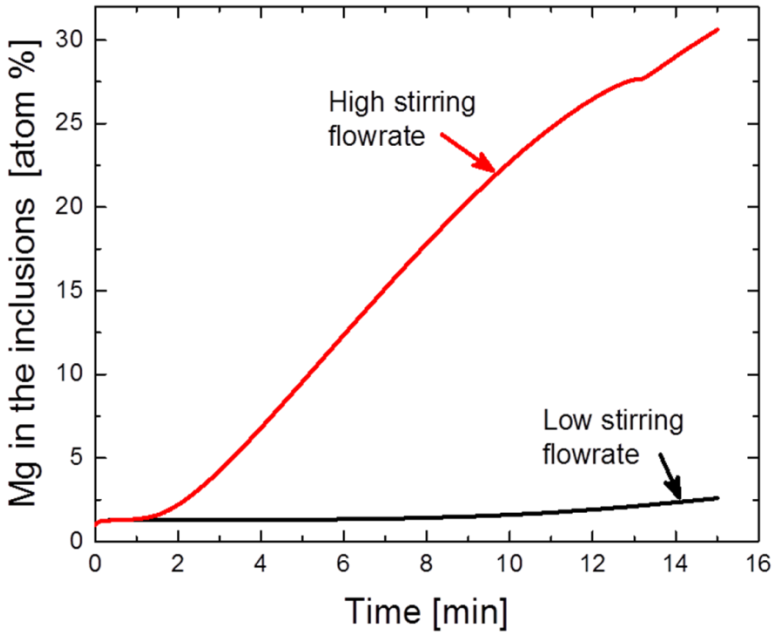

Figure 4-48. Calculated content of Mg in the oxide inclusions for two different values in the gas stirring flowrate.

The inclusions under a low gas flowrate remain mostly as pure alumina. On the contrary, with a high gas flowrate the transformation to spinel in the particles is much closer to completion. The marked effect of high stirring on the inclusions starts after 1.5 minutes; this can be explained with the variations in FeO and MnO for each calculation, Figure 4-49. The high stirring case deoxidizes the top slag faster than the low stirring regime. Once the slag is deoxidized enough then the reduction of other oxides like SiO_2 and MgO proceeds, this is also reflected in the behavior of [Si] in the bulk of steel, Figure 4-50. With a low stirring regime the dissolved [Si] is sent to the slag. On the contrary, the reversion of [Si] is more pronounced in the high stirring scenario once the slag and steel system reach a higher deoxidation level. These results are consistent with the

industrial evidence that the pickup of [Si] is linked to an increase in the formation of spinel and the %Mg in the inclusions, (E. B. Pretorius et al., 2013).

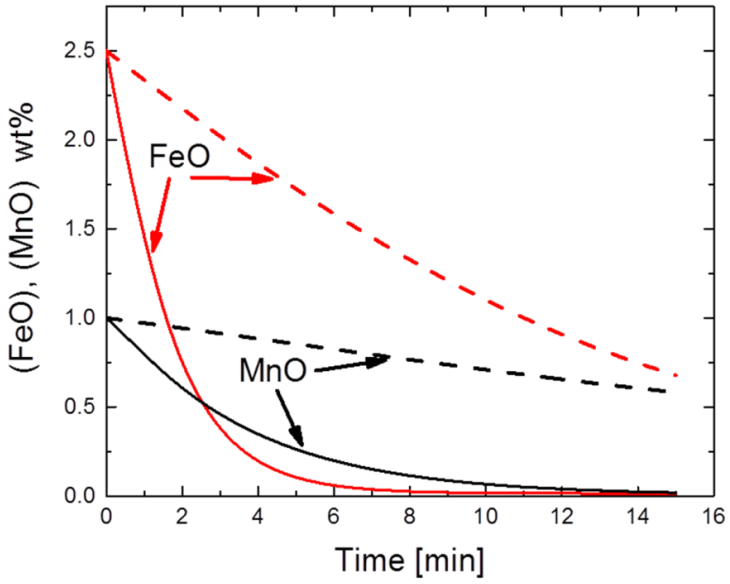

Figure 4-49. Calculated (FeO) and (MnO) levels in the slag. Continuous lines from the high stirring case, dashed lines correspond to the low stirring regime.

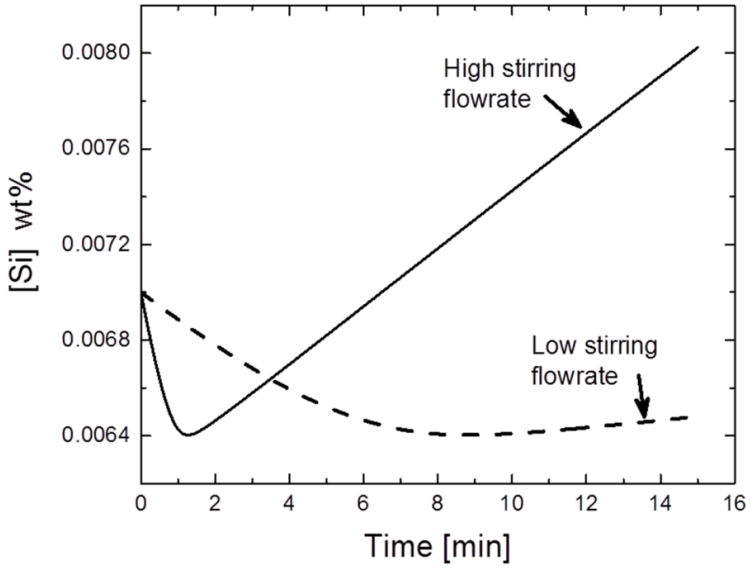

Figure 4-50. Calculated bulk concentration of [Si]. The dashed line is from the low stirring regime.

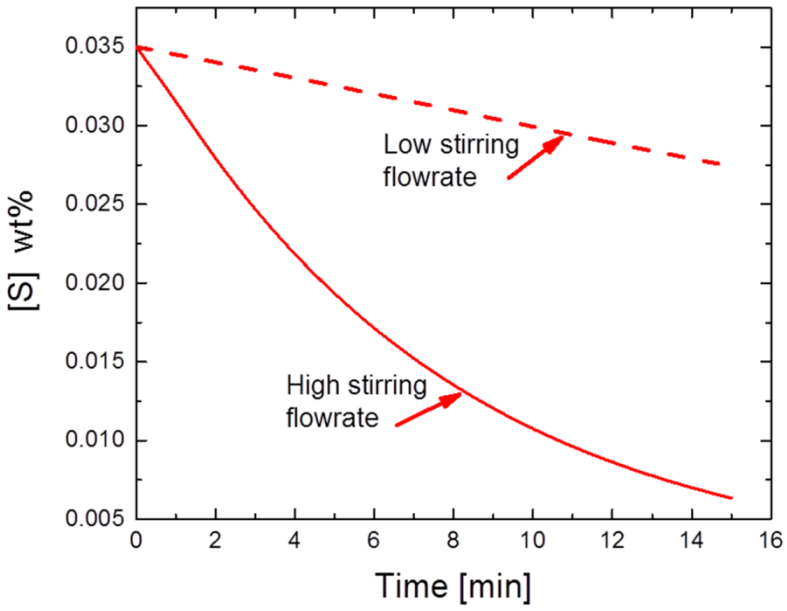

Figure 4-51. Calculated extent of steel desulphurization. The dashed line is from the low stirring regime.

The differences on the calculated desulphurization extents when high argon flowrates are applied are in Figure 4-51; these results highlight one of the main reasons for the industrial practice of using high gas stirring rates in order to provide further steel desulphurization. However, the much higher formation of magnesium aluminate spinel, Figure 4-48, implies that gas stirring can have a strong effect on the inclusions chemistry depending on the slag deoxidation level.

4.5.1.2 Deoxidation level in the top slag

In order to further analyze the slag deoxidation level on the formation of spinel inclusions, the initial slag composition was modified from the base case as listed in Table 4-3.

Table 4-3. Initial slag composition in wt% for several deoxidation levels

Slag	FeO	MnO	FeO + MnO
A	7.143	2.857	10
B	5.714	2.286	8
C	4.285	1.715	6
D	2.857	1.143	4
E	2.143	0.857	3
F	1.428	0.572	2
G	0.715	0.285	1

The compositions in Table 4-3 were chosen to maintain a initial ratio of $FeO/MnO \approx 2.5$; this value is similar to the FeO/MnO ratio of the initial conditions in the industrial heats analyzed. The balance of the initial composition was made by adjustment of the CaO and Al_2O_3 in the slag.

The conditions of stirring with a high and low gas flowrate were used for comparison. For all these calculations the bulk concentration of [Al] was kept at constant at 0.04 wt%. The results on the %Mg for the inclusions when high gas stirring is applied is in Figure 4-52, the respective slag deoxidation progress is in Figure 4-53. The results for a low gas flowrate are in Figure 4-54 and Figure 4-55.

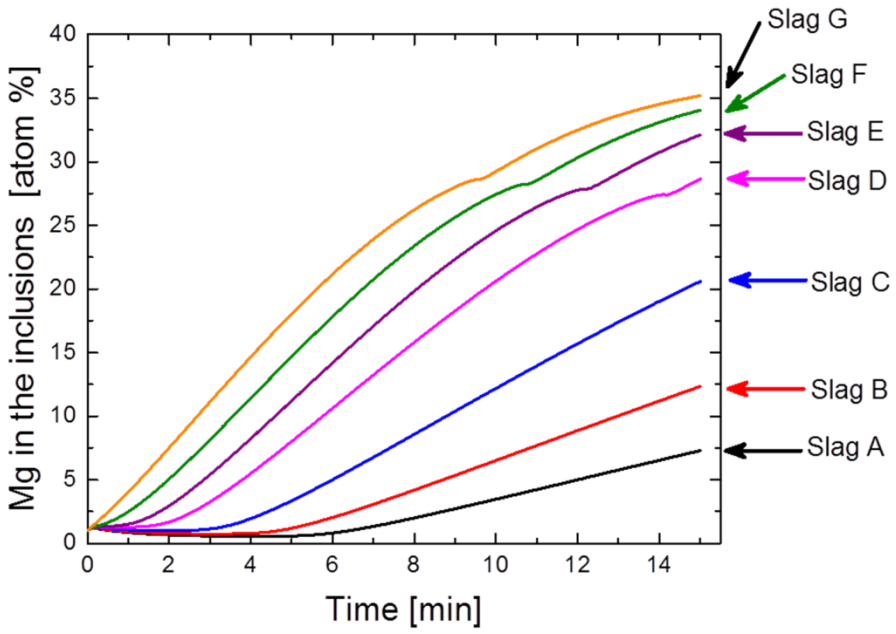

Figure 4-52. Calculated content of Mg in the oxide inclusions for different initial compositions of the slag, high gas stirring flowrate.

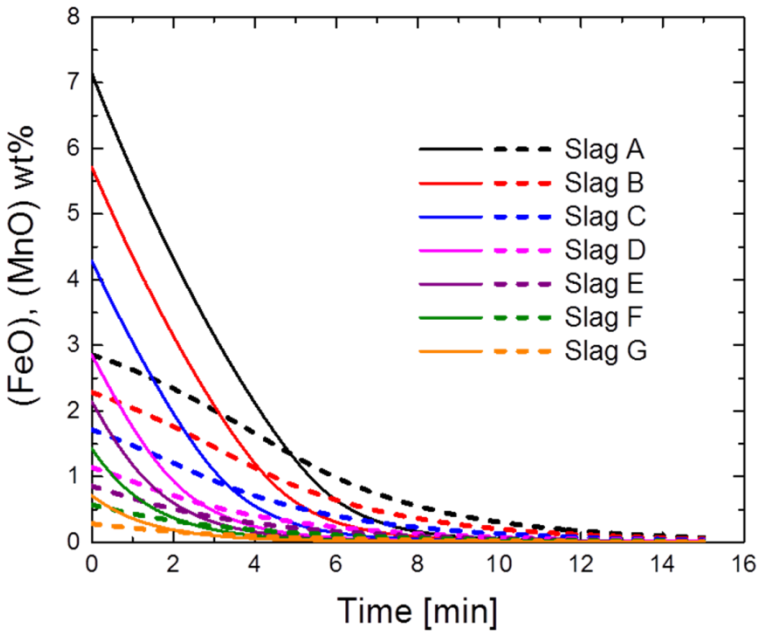

Figure 4-53. Slag deoxidation progress. Continuous lines represent the FeO content, dashed lines are the MnO content, high gas stirring flowrate.

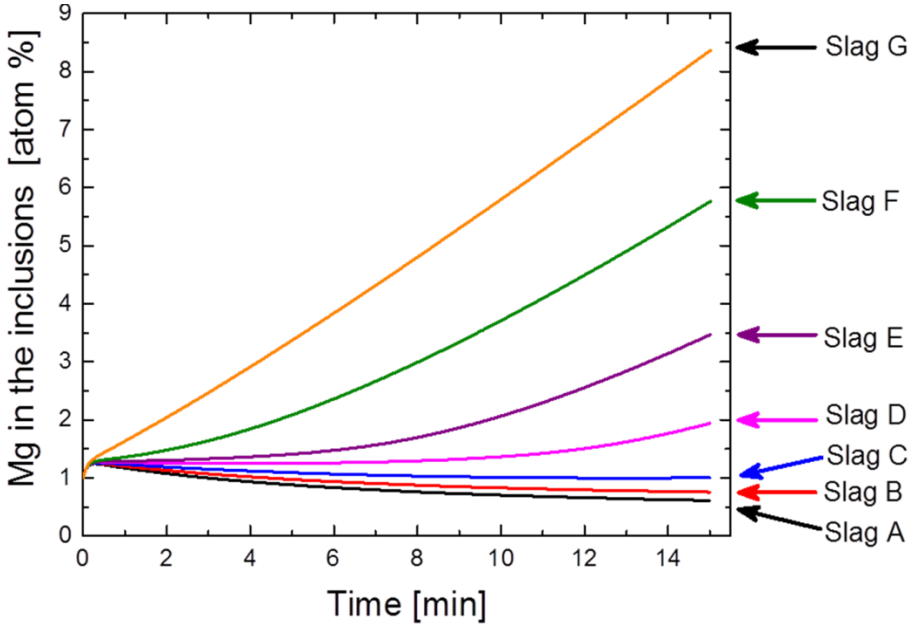

Figure 4-54. Calculated content of Mg in the oxide inclusions for different initial compositions of the slag, low gas stirring flowrate.

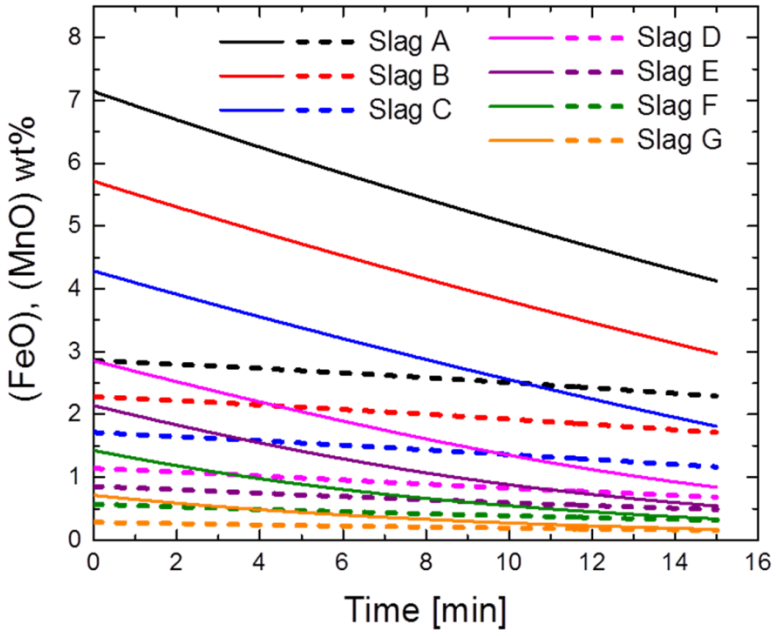

Figure 4-55. Slag deoxidation progress. Continuous lines represent the FeO content, dashed lines are the MnO content, low gas stirring flowrate.

The cases where high stirring was applied reached higher Mg contents in the inclusions; this can be attributed mainly to the more rapid reduction of FeO and MnO compared to the low stirring regime and also high stirring increases the mass transfer process for the release of [Mg] to the steel. In the case of Figure 4-52 for high stirring it is noticeable the delay in the start of Mg pick up by the inclusions when slags A, B and C are used. This delay in the transformation of the inclusions is explained with the more oxidizing conditions at the beginning of the process.

Similar results are obtained for the low gas stirring scenarios. In the cases of well deoxidized slags the low stirring regime slowed down the release of [Mg]. Slags A, B with the higher contents of FeO and MnO did not show Mg pick up by the inclusions after 15 minutes of process; on the contrary, these cases had a reduction in the %Mg since the oxidizing conditions in the system and the lack of [Mg] in the steel make alumina inclusions more stable than spinel.

4.5.1.3 Amount of inclusions in the steel

A sensitivity analysis on the amount of inclusions was made by considering 20, 40 and 60 ppm of initial total oxygen O_T in the calculations. The initial content of FeO and MnO in the slag was equal to slag E in Table 4-3, that is: FeO = 2.14 wt%, MnO= 0.86 wt%. A high gas flowrate for stirring was used. The calculated number of particles N_p for 20 ppm O_T is in the order of

1.9×10^{13}, for 40 ppm O_T is 4.64×10^{13} and for 60 ppm O_T is 7.37×10^{13}. The results on the %Mg for the inclusions are in Figure 4-56.

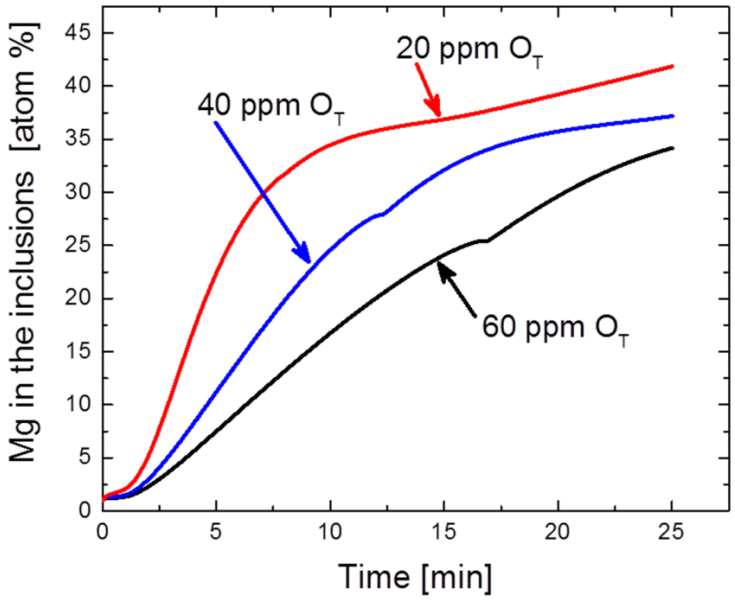

Figure 4-56. Calculated Mg content in the oxide inclusions for three different amounts of particles in the system.

As the number of particles decreases it implies that a similar amount of [Mg] provided by the slag is distributed among the fewer inclusions in the system. Therefore, steel with a smaller amount of inclusions induces a higher amount of Mg pick up and spinel formation in the inclusions.

The results also indicate that an increase on the %Mg is not proportional to the variations in the initial total oxygen content. This difference in proportionality can be attributed to the calculated number of particles N_p for each case as well as on the non-ideal behavior of the activities a_{MgO} and $a_{Al_2O_3}$ in the Al_2O_3-MgO system for spinel. Figure 4-57 shows the time variation of the

activity a_{MgO} at the inclusions-steel interface that satisfies the simultaneous equilibrium deoxidation.

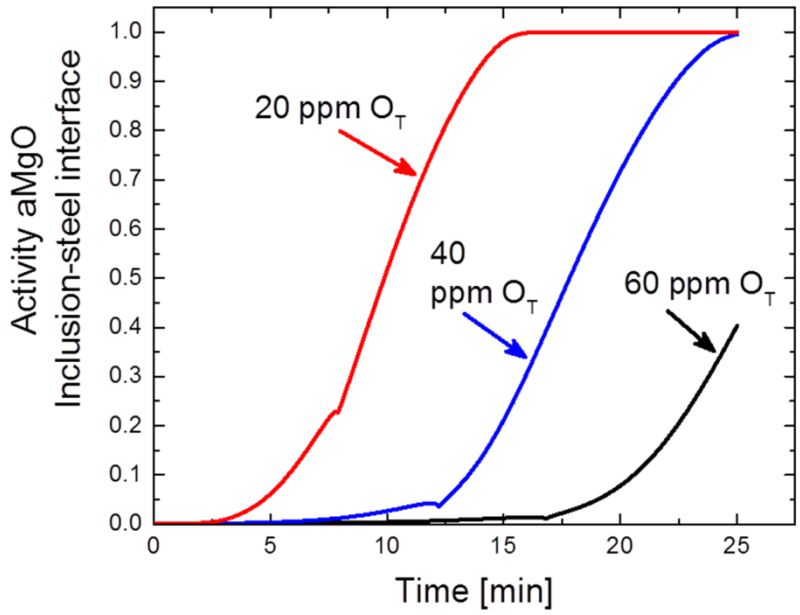

Figure 4-57. Calculated variation in a_{MgO} for three different amounts of inclusions in the system.

Furthermore, in order to achieve higher contents of Mg in the inclusions the mass transfer of Mg^{2+} across the spinel product layer increased. Figure 4-58 illustrates the calculated mass transfer rates $N_{Mg^{2+}}$ and $N_{Al^{3+}}$ at each individual inclusion for the three amounts of particles.

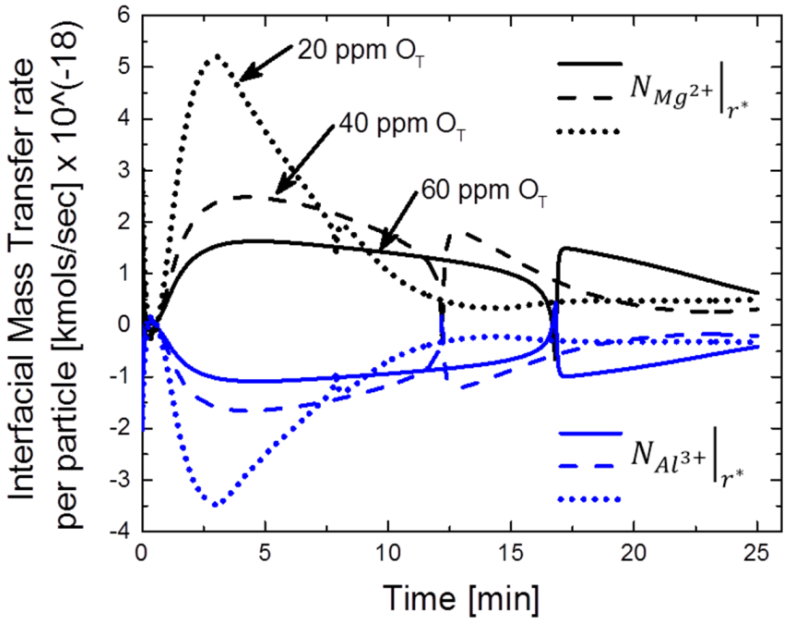

Figure 4-58. Calculated mass transfer rates $N_{Mg^{2+}}$ and $N_{Al^{3+}}$ at the individual inclusion-steel interface for the three initial values of total oxygen.

4.5.1.4 Initial inclusions diameter

In terms of particle size, most of the indigenous inclusions detected by the automated SEM analysis are in the range of 1 to 10 microns of diameter. To verify the effect of the inclusions size in the kinetic model, four different initial particle diameters were used: 2 μm, 5 μm, 10μm and 15μm. The initial composition of slag D was used, that is: 2.86 wt% FeO and 1.14 wt% MnO. The [Al] concentration was kept constant and equal to 0.04 wt% and a high gas flowrate for stirring was considered. This analysis assumed the same initial total oxygen of 40 ppm O_T for all the cases. The calculated Mg contents for the different inclusions are in Figure 4-59.

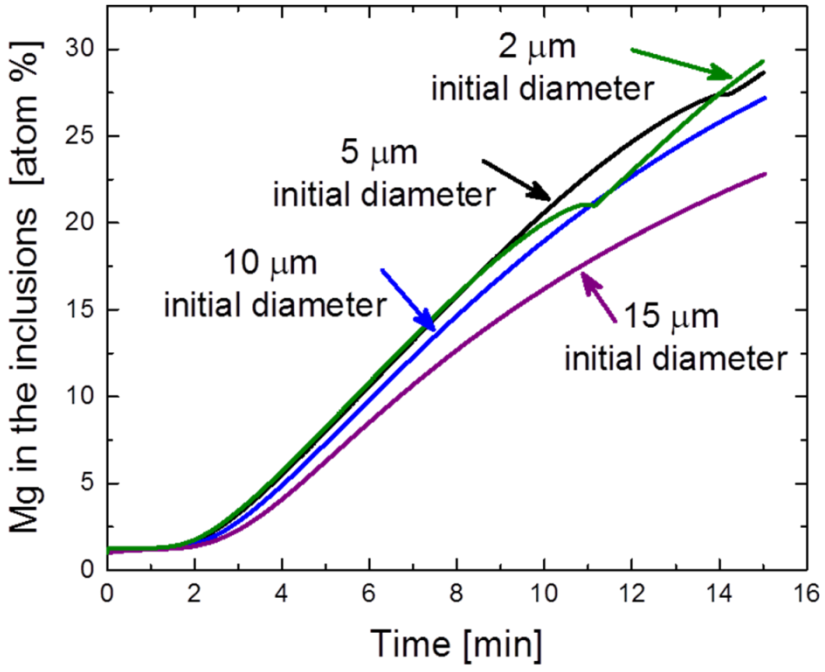

Figure 4-59. Calculated Mg content in the oxide inclusions for different values of initial diameter, same initial total oxygen O_T and a high gas stirring flowrate.

The results indicate that the small inclusions transform faster to spinel than the bigger ones. These differences on the rate of Mg pick up by the inclusions can be attributed to the larger interfacial area between the inclusions and the steel for the case of smaller inclusions. Because the surface area increases with more inclusions, then the respective interfacial mass transfer rates $N_{Mg^{2+}}$ and $N_{Al^{3+}}$ decrease, Figure 4-60.

Overall, the amounts of Mg pick up by the inclusions were very similar in the range size of 2 to 10 microns. For these calculations the initial mass of the inclusions was the same, but different numbers of particles were used. Therefore, this sensitivity analysis for the overall inclusions composition indicates that the

effect of a particle size is not as strong as in the previous analyses of varying the total mass of inclusions.

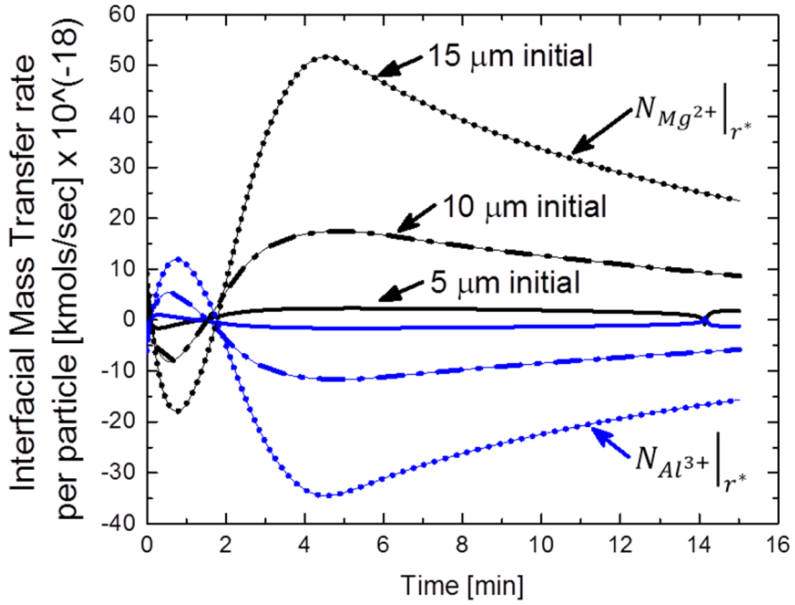

Figure 4-60. Calculated mass transfer rates $N_{Mg^{2+}}$ and $N_{Al^{3+}}$ at the individual inclusion-steel interface for different particle diameters.

4.5.2 Sensitivity analysis of the rate constants for mass transfer and diffusion

4.5.2.1 Diffusivities of Mg^{2+} and Al^{3+} in the spinel product layer

The uncertainties on the diffusivities used for cationic diffusion of Mg^{2+} and Al^{3+} in the spinel product layer exist due to the scarcity of reported values and the different techniques and methodologies to calculate these diffusivities.

The studies of Martinelli et al (1986) and Murphy et al (2009) concluded that Mg^{2+} ions are more mobile than Al^{3+} ions in magnesium aluminate spinel.

The temperature dependence of the diffusivity of Mg^{2+} in spinel has been reported by Lindner & Åkerström (1956) and Sheng et al., (1992); their reported pre-exponential factors and activation energies are summarized in Table 4-4.

Table 4-4. Temperature dependencies of $D_{Mg^{2+}}$ in magnesium aluminate spinel

Reference	D_0 in $\left[\frac{m^2}{s}\right]$	Q in $\left[\frac{kJ}{mol}\right]$	Temperature range
Lindner & Åkerström (1956)	2×10^{-2}	360	1173 – 1573 K
Sheng et al., (1992)	7.46×10^{-3}	384	1534 – 1826 K

The diffusivities $D_{Mg^{2+}}$ and $D_{Al^{3+}}$ obtained by Götze et al., (2009) are based on measurements of solid state diffusion couples and calculations that assume cation counterdiffusion in spinel. Although the measurements in the work of Götze et al., (2009) were at 1623 K, these values were used for all the calculations in this kinetic model for spinel inclusions. In order to estimate the diffusivity of Mg^{2+} at steelmaking temperatures of 1873 K, the correlations in Table 4-4 were used and compared with the respective diffusivities at 1623 K, the results are in Table 4-5.

Table 4-5. Calculated and reported values for $D_{Mg^{2+}}$ at two different temperatures

Temperature	$D_{Mg^{2+}}$ in $\left[\frac{m^2}{s}\right]$	Reference
1623 K	5.2×10^{-14}	Lindner & Åkerström (1956)
1623 K	3.2×10^{-15}	Sheng et al., (1992)
1623 K	1.4×10^{-15}	Götze et al., (2009)
1873 K	1.8×10^{-12}	Lindner & Åkerström (1956)
1873 K	1.4×10^{-13}	Sheng et al., (1992)

These estimations for $D_{Mg^{2+}}$ indicate a span of two to three orders of magnitude. For the sensitivity analyses, two limiting values of $D_{Mg^{2+}}$ were identified, namely: low temperature (1623 K) $D_{Mg^{2+}}\big|_{1623\ K} = 1 \times 10^{-15}$ m^2/sec and high temperature diffusivity (1873 K) $D_{Mg^{2+}}\big|_{1873\ K} = 1 \times 10^{-13}$ m^2/sec.

For the diffusivity of Al^{3+} in spinel, Götze et al., (2009) reported $D_{Al^{3+}} = 3.7 \times 10^{-16}$ m^2/sec which is an order of magnitude lower than their value for Mg^{2+}. In the sensitivity analyses, two cases for the diffusivity of Al^{3+} were defined: $D_{Al^{3+}}$ one order of magnitude smaller than $D_{Mg^{2+}}$ and $D_{Al^{3+}}$ two orders of magnitude smaller than $D_{Mg^{2+}}$. The nomenclature and values of the four diffusivity pairs analyzed are in Table 4-6.

Table 4-6. Estimated orders of magnitude for $D_{Mg^{2+}}$ and $D_{Al^{3+}}$ in spinel

Diffusivity pair	$D_{Mg^{2+}}$ in $\left[\frac{m^2}{s}\right]$	$D_{Al^{3+}}$ in $\left[\frac{m^2}{s}\right]$
Low Temp. estimation A	1×10^{-15}	1×10^{-17}
Low Temp. estimation B	1×10^{-15}	1×10^{-16}
High Temp. estimation A	1×10^{-13}	1×10^{-15}
High Temp. estimation B	1×10^{-13}	1×10^{-14}

The base case scenario for slag composition, total oxygen and inclusions diameter was used to see the variations in the Mg content of the inclusions. Low and high gas stirring conditions were considered in the system, the respective results for the inclusions composition are in Figure 4-61 and 4-62.

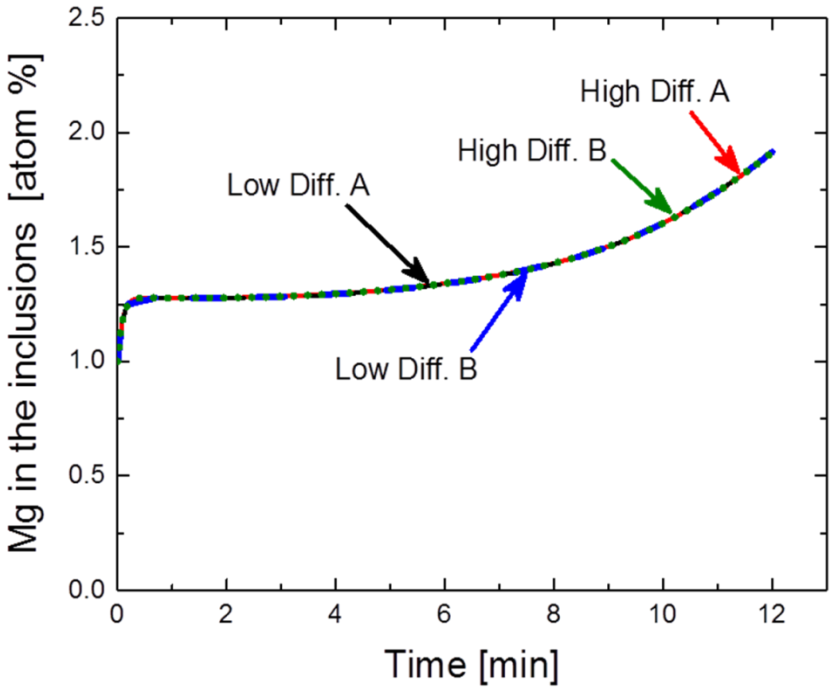

Figure 4-61. Calculated Mg content in the oxide inclusions. Variations in the cation diffusivities across the spinel product layer. Low stirring gas flowrate.

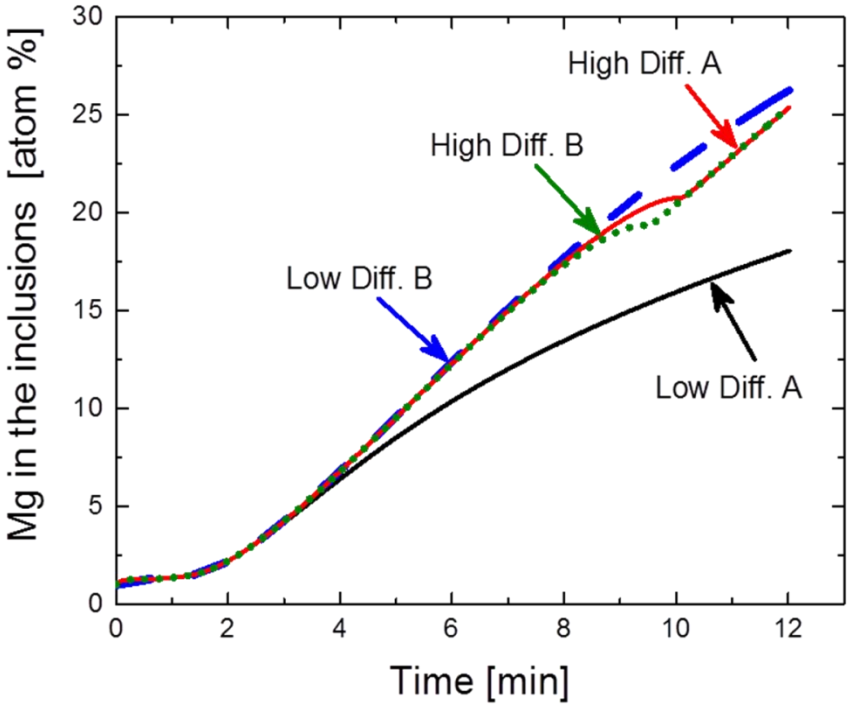

Figure 4-62. Calculated Mg content in the oxide inclusions. Variations in the cation diffusivities across the spinel product layer. High stirring gas flowrate.

Under the low gas stirring conditions, the supply of [Mg] from the slag is more limited in comparison to the high stirring scenario. This restriction on the supply of [Mg] controls the overall kinetics for the formation of spinel and therefore varying the cation diffusivities across the spinel product layer does not have a considerable impact on the inclusions composition.

The analysis for high gas stirring indicates that only for the lowest value of $D_{Al^{3+}}$ the process of transformation from alumina to spinel is delayed. The stronger effect of $D_{Al^{3+}}$ on the growth of the product layer is due to the reduced

mobility of Al^{3+} in spinel. The rest of the calculations provided similar rates of Mg pick up by the inclusions.

The diffusivity values reported by Götze et al., (2009) have the same order of magnitude of the diffusivity pair in the low temperature estimation B. Therefore, when the value of $D_{Al^{3+}}$ is reduced by one order of magnitude as in the calculation with the low temperature estimation A, the inclusions composition shows that the kinetics of the formation of spinel is affected by both the supply of [Mg] and the cationic diffusion in the product layer. This indicates that a condition of mixed control appears if high gas stirring is applied and using the cationic diffusivity pair with the lowest value of $D_{Al^{3+}}$.

Furthermore, the values of $D_{Mg^{2+}}$ and $D_{Al^{2+}}$ are required in the calculation of the change in chemical potential of oxygen $\frac{\partial \mu_O}{\partial r}$ that maintains electroneutrality across the spinel product layer. Although this modifies the calculated driving forces for cationic diffusion $\frac{\partial \mu_{Mg}}{\partial r}$ and $\frac{\partial \mu_{Al}}{\partial r}$, this analysis indicate that varying the diffusivities in the high temperature estimations (1873 K) does not generate a different overall behavior in the inclusions chemistry.

4.5.2.2 Mass transfer in the boundary layer at the inclusions-steel interface

The kinetic step of mass transfer of the dissolved species [Mg], [Al] and [O] through the interfacial boundary layer that surrounds each inclusion was also

analyzed. The mass transfer rates $N_{[Mg]}$, $N_{[Al]}$ and $N_{[O]}$ in steel are a function of the concentrations in the bulk of steel, the concentrations at the inclusion-steel interface, the particles diameter and the respective mass transfer coefficients k_{Mg}, k_{Al} and k_O.

Given the range of sizes for the indigenous inclusions, the inclusions and the steel move with virtually the same velocity. Therefore, this kinetic step neglects the effect of convective transport. In this kinetic model mass transport in the boundary layer considers only the diffusional term; therefore the mass transfer coefficients are calculated assuming a Sherwood number equal to 2 (Oeters, 1994). The Sherwood number of a dissolved species [A] in a fluid and for spherical particles of these sizes is (Szekely & Themelis, 1971):

$$Sh = \frac{k_A d}{D_{[A]}} \tag{4-39}$$

In expression 4-39 d is the diameter of the particle, k_A is the mass transfer coefficient and $D_{[A]}$ is the diffusivity of the species in liquid steel. As reviewed by Nagata, et al., (1988) and Geiger & Poirier (1973), the diffusivities of most species in liquid steel at steelmaking temperatures are in the range of 10^{-9} to 10^{-7} m^2/sec. For all the previous calculations with the kinetic model, the diffusivities used are: $D_{[O]} = 3.1 \times 10^{-9}\, m^2 \cdot s^{-1}$ (Lu, 1992), $D_{[Mg]} = 3 \times 10^{-9}\, m^2 \cdot s^{-1}$ (Irons, et al., 1978) and $D_{[Al]} = 3.5 \times 10^{-9}\, m^2 \cdot s^{-1}$ (Nagata, et al., 1988).

In this sensitivity analysis, the diffusivities $D_{[Mg]}$, $D_{[Al]}$ and $D_{[O]}$ in liquid steel were considered equal and were varied for three different values: $D = 1 \times 10^{-9}$, $D = 1 \times 10^{-7}$ and $D = 1 \times 10^{-9}$ m^2/sec. The base case scenario was implemented for the slag composition, the initial total oxygen was 40 ppm, the initial diameter of the inclusions was 5 μm and the [Al] content was constant and equal to 0.4 wt%. The calculations assumed both high and low gas stirring flowrates. The results for the Mg content in the inclusions are in Figures 4-63 and 4-64.

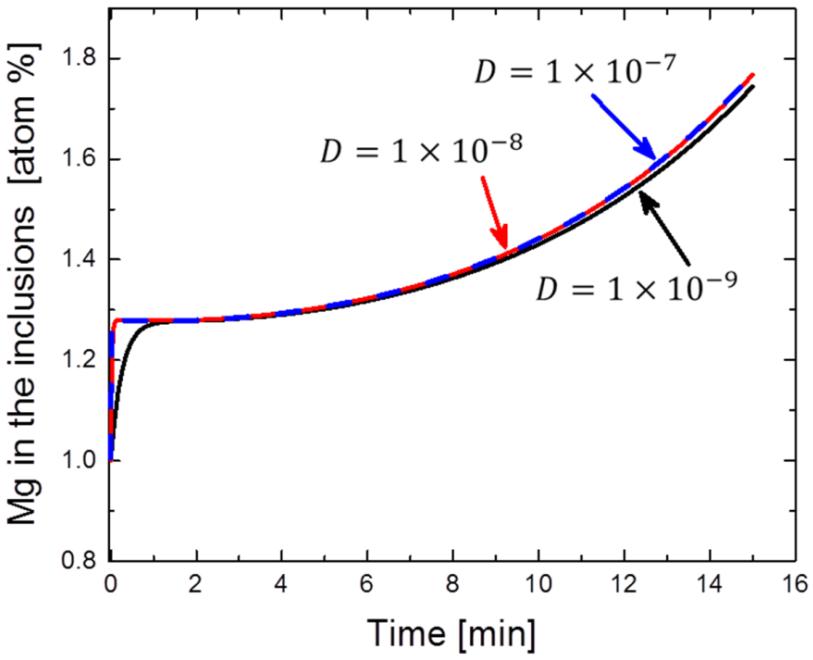

Figure 4-63. Calculated Mg content in the oxide inclusions. Base case scenario but different diffusivities for [Mg], [Al] and [O]. Low stirring gas flowrate.

These results indicate that varying the diffusivities of the dissolved species by three orders of magnitude does not have a significant effect on the overall

composition of the inclusions. The total surface area of the inclusions in steel and most important these results also support the argument that the rate limiting step for the transformation of inclusions from alumina to spinel is the release of [Mg] to the steel from the slag.

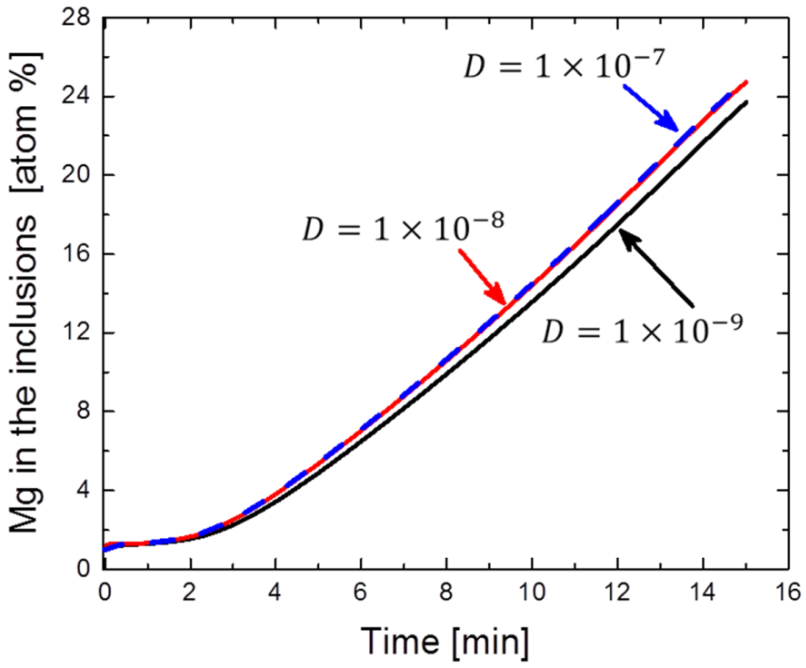

Figure 4-64. Calculated Mg content in the oxide inclusions. Base case scenario but different diffusivities for [Mg], [Al] and [O]. High stirring gas flowrate.

4.5.2.3 Mass transfer coefficients for convective transport in the slag

For this kinetic model, the mass transfer of species between the slag and steel is described by coupling the different slag-steel reactions in order to satisfy the multicomponent equilibrium at the interface and to balance the mass transfer rates in both phases. The model calculates the mass transfer coefficients of the components in the slag $k_{sl}^{M_xO_y}$ from individual ratios with the respective mass

transfer coefficients of the species in the steel $k_{sl}^{M_xO_y} / k_m^M$. Due to the importance of the slag deoxidation level on the transformation of alumina inclusions to spinel, the effect of the ratios k_{sl}^{FeO} / k_m^{Fe} , k_{sl}^{MnO} / k_m^{Mn} and $k_{sl}^{SiO_2} / k_m^{Si}$ on the rate of Mg pickup by the inclusions was analyzed.

In most of the kinetic models for desulphurization or dephosphorization of steel with the slag, the mass transfer coefficients of the species in steel k_m^M are assumed to be the same. The variation of k_m^M with the stirring conditions is obtained from experimental measurements and by using empirical correlations of k_m^M as a function of the stirring energy ε.

The use of mass transfer coefficients ratios to calculate the values of $k_{sl}^{M_xO_y}$ was analyzed in the multicomponent kinetic model of Robertson et al., (1984). In this work, all the different $k_{sl}^{M_xO_y}$ values were assumed the same due to the lack of knowledge on its behavior. Robertson et al., demonstrated based on model calculations for desulphurization of hot metal, that mass transfer resistance in the slag plays an important role only at the beginning of the process where the equilibrium partition coefficient L'_S is much smaller than the larger final L'_S under more reducing conditions. This sensitivity analysis was made by changing the ratio $k_{sl}^{M_xO_y} / k_m^M$ from 1 to $\frac{1}{10}$. In this case, the value of 1 represents the lowest mass transfer resistance for transport of the species in the slag.

The work of Kitamura et al., (1991), implemented a similar kinetic model to the one proposed by Robertson et al., (1984) in order to describe hot metal dephosphorization. Laboratory experiments were made in a 70 kg induction furnace with argon gas stirring. The correlation between the stirring energy ε and k_m^M was obtained by following the desiliconization reaction. The mass transfer coefficients k_{sl} for all the slag components were assumed the same. The specific value of k_{sl} was selected in order to obtain agreement with the dephosphorization progress and the FeO content in the slag. From this study, the ratio $k_{sl}/\ k_m$ was found in the range of $\frac{1}{5}$ to $\frac{1}{10}$. On the other hand, Kitamura et al. could not determine an obvious dependence of the ratio $k_{sl}^{M_xO_y}/\ k_m^M$ with the temperature variations from 1623 to 1873 K or with variations in the stirring energy.

The laboratory study of Okuyama et al., (2000) analyzed different slags from the system CaO-Al_2O_3-MgO-SiO_2 and their effect on the inclusions composition of aluminum killed steel. The experiments were performed in a 20 kg vacuum induction furnace. Although this work did not propose a coupled kinetic model for the slag-steel and inclusions, their model for the slag-steel reactions was also based on the method of Robertson et al., (1984). The ratio $k_{sl}^{M_xO_y}/\ k_m^M$ for all the components in the slag other than SiO_2 was $\frac{1}{20}$. On the contrary, the ratio $k_{sl}^{SiO_2}/\ k_m^M$ was $\frac{1}{100}$. These values were obtained to agree with the experimental results in the steel phase. This study indicated that there is a higher

resistance for the mass transfer of SiO_2 in the slag. Also, they mentioned that for their slag compositions reacting with low carbon aluminum killed steel, the release of [Si] to the steel is kinetically controlled by mass transfer in the slag.

In the work of Graham (2008) and Graham & Irons (2010), their coupled kinetic model for the slag-steel reactions was based on the model of Robertson et al., (1984) but considering the industrial conditions of the ladle metallurgy furnace and the refining of low carbon aluminum killed steel. Graham & Irons (2010) proposed to use separate mass transfer ratios for the transport of species in the slag, that is: k_{sl}^{FeO} / k_m^{Fe}, k_{sl}^{MnO} / k_m^{Mn}, $k_{sl}^{SiO_2} / k_m^{Si}$, $k_{sl}^{TiO_2} / k_m^{Ti}$ and $k_{sl}^{Al_2O_3} / k_m^{Al}$. The value of each ratio was selected in order to obtain agreement with the measured industrial compositions in the slag and steel.

Graham (2008) indicated the case of SiO_2 where a higher mass transfer resistance was observed in comparison with the resistances for FeO and MnO. Furthermore, this analysis mentioned that for several industrial heats, the ratio k_{sl}^{FeO} / k_m^{Fe} required to be reduced after the addition of [Al] in the ladle for additional deoxidation. Also, the same k_{sl}^{FeO} / k_m^{Fe} ratio used required to be reduced during periods of electrical arcing in the case of slags with less than 1 wt % FeO.

Harada et al., (2013a) proposed a kinetic model for the kinetics in the ladle furnace and compared their calculations with the experimental measurements of

Graham & Irons (2010). This work defined the ratio k_{sl}^{CaO} / k_m to be $\frac{1}{10}$. The mass transfer coefficient for the other components M_xO_y in the slag were obtained by multiplying k_{sl}^{CaO} with the ratio $\sqrt{\frac{D_{M_xO_y}}{D_{CaO}}}$, where $D_{M_xO_y}$ and D_{CaO} are the respective diffusivities in the slag. Variations in the mass transfer ratios due to the slag composition, gas stirring or electrical arcing were not mentioned.

For the sensitivity analysis of current kinetic model, the effect of the mass transfer ratios k_{sl}^{FeO} / k_m^{Fe}, k_{sl}^{MnO} / k_m^{Mn} and $k_{sl}^{SiO_2} / k_m^{Si}$ on the pickup of Mg by the inclusions was analyzed. Each ratio was varied from 1 which implies mass transfer control in the metal phase, up to the value of $\frac{1}{100}$ which represents a higher mass transfer resistance in the slag; when an specific ratio was analyzed the value for the other two was set equal to 10^{-3}, this implies an even further restriction to mass transfer in the slag. In this way, the different mass transfer rates can be compared. The initial slag composition was taken from the base case for sensitivity analysis, the initial amount of inclusions was based on 40 ppm O_T, the initial diameter of the inclusions was 5 microns. High stirring conditions were considered. The [Al] concentration in the bulk of the steel was set constant throughout the calculations and equal to 0.04 wt%. The loss of FeO in the slag when k_{sl}^{FeO} / k_m^{Fe} is varied is in Figure 4-65. The respective contents of Mg in the inclusions are in Figure 4-66.

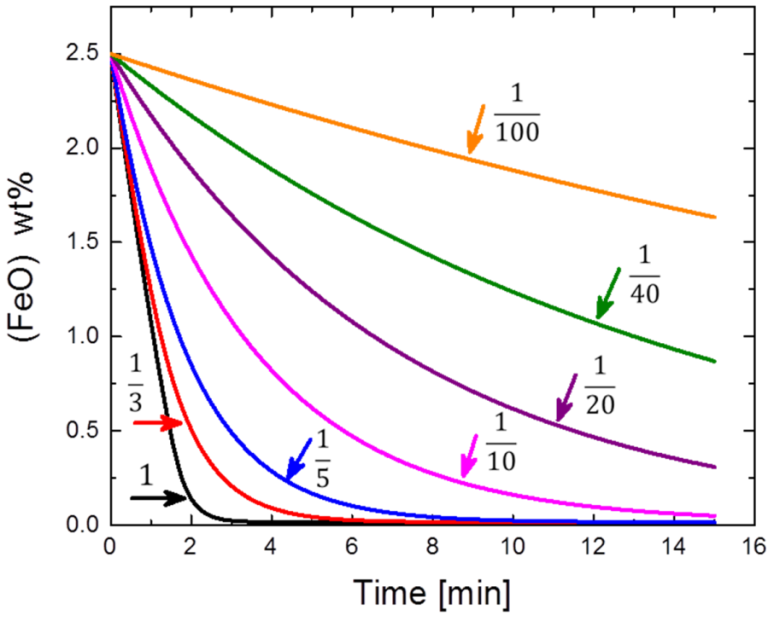

Figure 4-65. Reduction of FeO in the slag for different values of the mass transfer coefficients ratio k_{sl}^{FeO} / k_m^{Fe} .

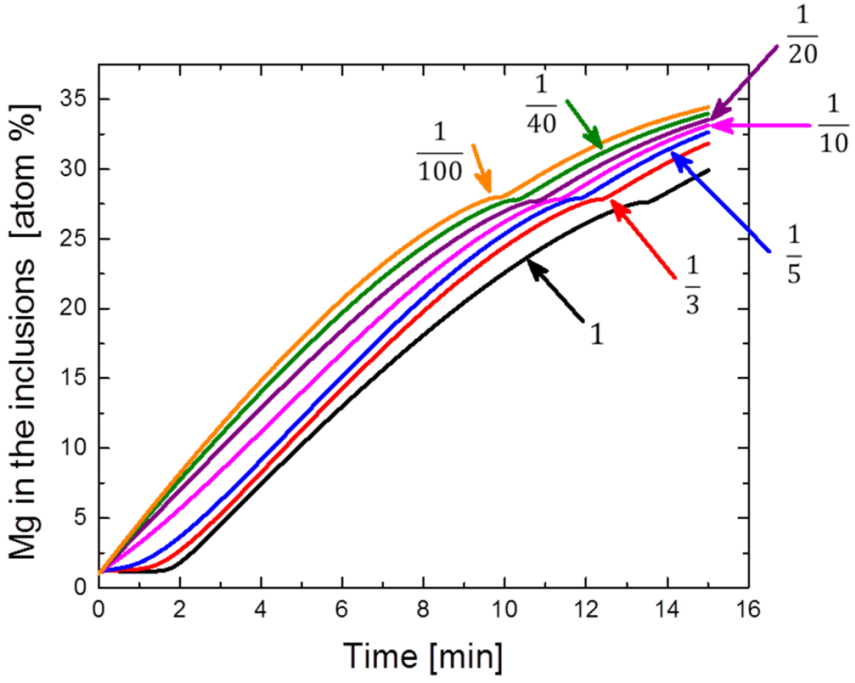

Figure 4-66. Content of Mg in the oxide inclusions for different values of the mass transfer coefficients ratio k_{sl}^{FeO} / k_m^{Fe} .

These results indicate that for the higher rates of FeO reduction the process of Mg pickup by the inclusions is delayed, this is due to the more oxidizing conditions that are provided under a rapid FeO reduction process. That is, [O] is sent from the slag to the steel more rapidly. On the other hand, if the resistance for FeO transport in the slag is increased with a smaller mass transfer coefficient, then the aluminum in steel controls the reduction of MgO in the slag and the Mg pickup in the inclusions starts earlier.

The contents of MnO in the slag when k_{sl}^{MnO} / k_m^{Mn} is varied are in Figure 4-67. The respective contents of Mg in the inclusions are in Figure 4-68. The analysis for the ratio $k_{sl}^{SiO_2} / k_m^{Si}$ is shown in Figures 4-69 and 4-70.

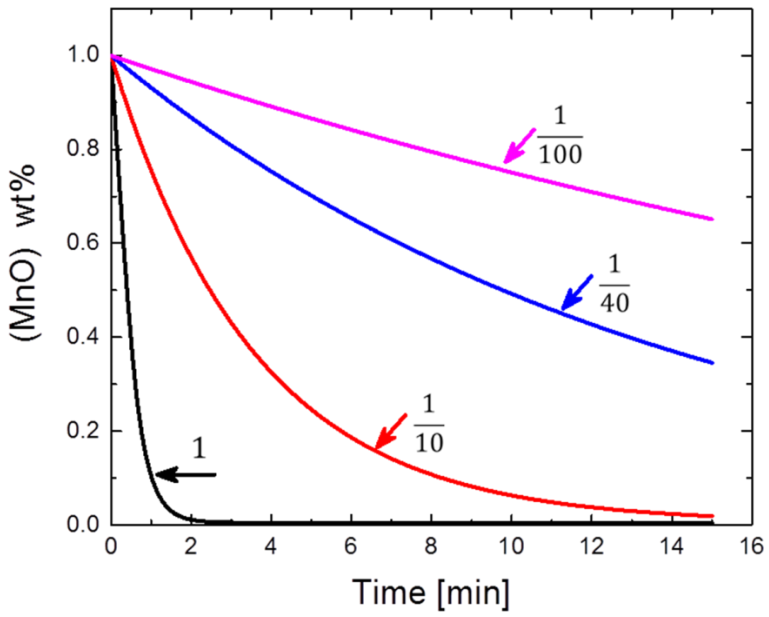

Figure 4-67. Reduction of MnO in the slag for different values of the mass transfer coefficients ratio k_{sl}^{MnO} / k_m^{Mn} .

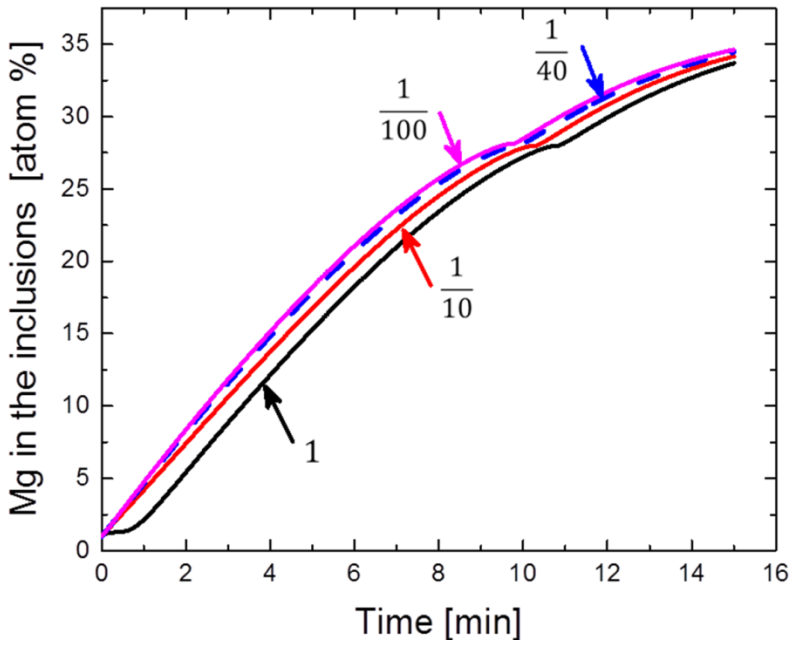

Figure 4-68. Content of Mg in the oxide inclusions for different values of the mass transfer coefficients ratio k_{sl}^{MnO} / k_m^{Mn} .

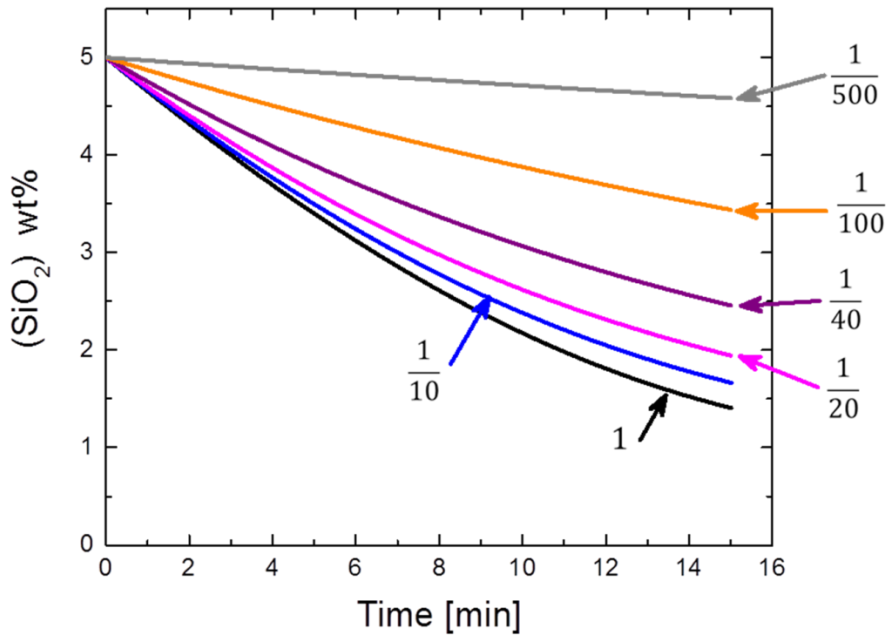

Figure 4-69. Reduction of SiO_2 in the slag for different values of the mass transfer coefficients ratio $k_{sl}^{SiO_2} / k_m^{Si}$.

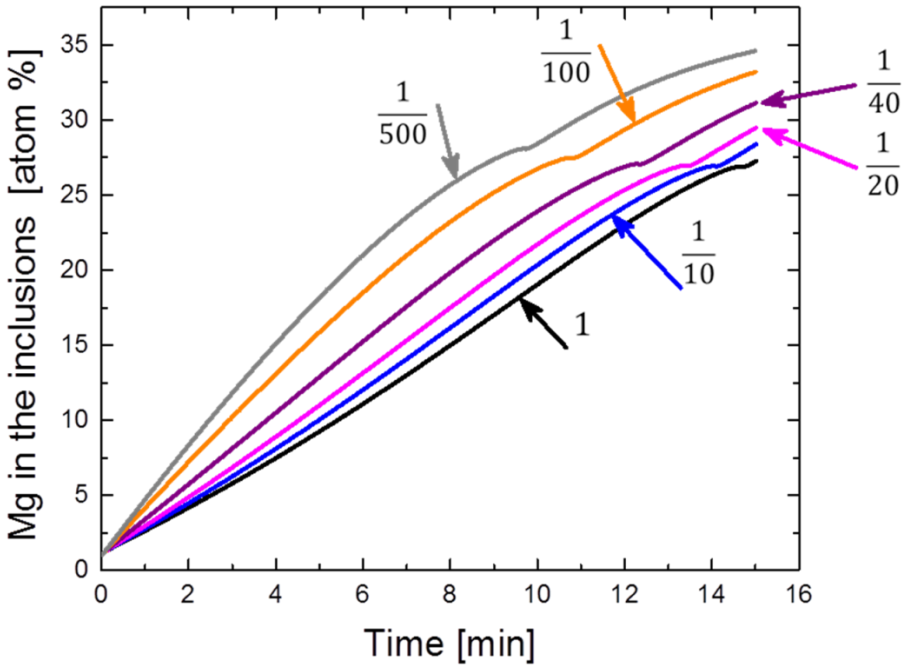

Figure 4-70. Content of Mg in the oxide inclusions for different values of the mass transfer coefficients ratio $k_{sl}^{SiO_2} / k_m^{Si}$.

The results on the inclusions composition for the variation of k_{sl}^{MnO} / k_m^{Mn} have a similar behavior to the variation in the rate of FeO reduction. The faster MnO reduction provides more oxidizing conditions that delay the formation of spinel in the inclusions. The effect of MnO is not as remarkable due to its lower content in the initial top slag composition.

The calculated results for the variation in $k_{sl}^{SiO_2} / k_m^{Si}$ do not show a delay in the pickup of Mg by the inclusions, even with the faster mass transfer rates. The higher content of SiO_2 in the slag can reduce the amount of spinel formed even if the supply of [O] from FeO and MnO is blocked; this also explains the broader range of final Mg contents in the inclusions for the different reduction

rates. Therefore, higher contents of SiO_2 in the slag reduce the amount of spinel in the inclusions. On the other hand, adding SiO_2 to the slag can affect the viscosity properties of the slag with subsequent impacts on the fluidity and different mass transfer coefficients in the slag.

This sensitivity analysis further supports the argument that the time variations in the content of FeO, MnO and SiO_2 in the slag strongly control the release of [Mg] to the steel and the transformation of alumina to spinel inclusions.

Chapter 5

Summary and conclusions

5.1 Summary

The main objectives of this thesis project were to develop a kinetic model for the transformation of alumina inclusions to magnesium aluminate spinel inclusions and the implementation of the inclusions model to a previous kinetic model for the slag-steel reactions in the Ladle Metallurgy Furnace. These two objectives were achieved as demonstrated in Chapters 3 and 4. The important outcomes of this work are:

- A kinetic model for the formation of magnesium aluminate spinel inclusions in the liquid steel. The model is based on a solid state reaction mechanism of cationic counterdiffusion.
- A methodology to calculate local equilibrium concentrations at the inclusions-steel interface for the simultaneous steel deoxidation with [Mg] and [Al].
- The verification of the functionality of the coupled kinetic model for spinel formation under industrial conditions where the changes in the slag and steel are considered.
- A sensitivity analysis of the coupled kinetic model for the slag, steel and inclusions. The analysis compared the effect of the different processing

conditions in the ladle furnace and the uncertainty in the kinetic rate constants and parameters.

This work provides further understanding of the formation of magnesium aluminate inclusions during the refining of steel in the Ladle Furnace. The results of this study are expected to be useful for industrial steelmakers and for research metallurgists in order to have a more complete understanding of the factors that cause and promote the formation of spinel inclusions, more importantly this analysis points out alternatives to mitigate the formation of these inclusions.

5.2 Conclusions

The conclusions from this research are:

1. The Wagner-Schmalzried theory for spinel formation in solid state allows the formulation of kinetic expressions for the growth and concentration variations of the product layer of magnesium aluminate spinel in the inclusions. The driving forces for diffusion of Mg^{2+} and Al^{3+} are expressed as a function of the gradients in the activities of the spinel components a_{MgO} and $a_{Al_2O_3}$.
2. The mass transfer of dissolved oxygen [O] between the inclusions and steel is linked to the external growth or consumption of the spinel product layer at the steel-inclusion interface. This assumption aided on the coupling of the mass transfer rates for Mg^{2+}, Al^{3+}, [Mg], [Al] and [O] at the steel-inclusion

interface. This rigorous analysis for the transport and diffusion of the different species between the steel and the inclusions has not been reported previously. Also, the time variations of the local equilibrium concentrations X_{Mg}^{*}, X_{Al}^{*}, X_{O}^{*}, $a_{Al_2O_3}{}^{*}$, $a_{MgO}{}^{*}$ and $X_{Al_2O_3}{}^{*}$ are obtained for the simultaneous [Mg] and [Al] deoxidation process, but without artificially constraining any of the activities and concentrations in the steel or in the inclusions.

3. The nonstoichiometric changes of magnesium aluminate spinel with the respective variations in the activities of the components a_{MgO} and $a_{Al_2O_3}$ are calculated for the product layer in the inclusions. These composition variations in distance and time are obtained by solving numerically the diffusion equation for Mg^{2+}.
4. The calculated Mg contents in the inclusions from the coupled kinetic model for slag, steel and spinel inclusions had reasonable agreement with most of the measurements from the automated SEM inclusions analysis of the industrial heats. The agreement was achieved in terms of the timing, the amount and the rates of Mg pick up by the oxide inclusions.
5. For the case of the transformation of alumina inclusions to spinel during ladle refining of LCAK steel, there is little difference in the results of the Mg content in the inclusions when the Unsteady state scheme or the Quasi-steady state approximation are used in the spinel product layer. This considerable similarity between the two solutions is significant since the Quasi-steady

scheme separates mathematically the time scales for the slag-steel changes and for the inclusions changes.

6. The coupled model for the slag-steel reactions and the formation of spinel inclusions is one of the first kinetic models that describe changes in the oxide inclusions with a rigorous and detailed approach for diffusion in the solid inclusions.
7. The largest disagreement between the coupled kinetic model and the industrial measurements on the amount of Mg in the inclusions was mostly found to occur during periods of high gas stirring in the ladle furnace. This suggests the possibility of atmospheric reoxidation of having an impact on the contents of [Mg] in the steel and in the inclusions composition.
8. In most of the heats analyzed, the starting FeO and MnO contents in the slag were already low. Therefore, the higher rates of Mg pick up by the inclusions occurred during the periods of high gas stirring.
9. Varying the initial mass of inclusions and the number of particles in the range of 25 to 40 ppm of initial total oxygen O_T showed the influence of this parameter when the industrial heats are modeled. For a given heat, the cases with fewer particles had a higher Mg contents in the inclusions and further transformation to spinel. This occurs because the fewer inclusions distribute the same amount of [Mg] coming from the slag.

For Heats 10 and 17, increasing the initial mass of inclusions to 50 ppm O_T did not provide better agreement between the model and the measurements; this indicates the possibility of other sources of [Mg] loss.

10. Considering a distribution of three particle sizes for the inclusions in the coupled kinetic model indicates that the smaller inclusions reach higher Mg concentrations than the bigger inclusions. The rates of transformation to spinel also increase as the inclusion size is reduced. However, the total %Mg for all the mass of inclusions of the three sizes showed a similar behavior to the %Mg obtained when a reasonable single particle size is assumed in the model. In both the multiparticle and single particle calculations, the initial mass of inclusions was based on 40 ppm O_T. Therefore, having a distribution of particle sizes in the model does not significantly affect the Mg pick up by the total mass of inclusions. This analysis is important since the total atom% of Mg is the value reported by the automated SEM analysis independently of the inclusion size.
11. The calculations for Heats 6, 7, 8 and 15 with a reduced starting MgO in the slag (3 wt %) showed a reduction in the %Mg contents of the inclusions. This variation did not affect the calculated extent of steel desulphurization with the top slag. However, the decrease on the %Mg in the inclusions was not in the same proportion to the decrease in the activity of MgO in the slag and the formation of spinel inclusions was not suppressed.

12. The similarities between the unsteady state scheme and the Quasi-steady state approximation indicate that the rate limiting step for spinel inclusions formation in the overall system is the rate of supply of dissolved [Mg] from the slag-steel reaction. This supply of [Mg] is controlled by the changes at the slag-steel interface.
13. The sensitivity analysis for the variation of the diffusivities of the dissolved species in steel $D_{[Mg]}$, $D_{[Al]}$ and $D_{[O]}$ and the diffusivities $D_{Mg^{2+}}$ and $D_{Al^{3+}}$ with the estimations at 1873 K did not have a significant influence on the formation rate of spinel and the calculated %Mg in the inclusions. This was observed for both the low and high gas stirring conditions. The analysis indicates that the steps of mass transport through the interface boundary layer in the steel and the cationic diffusion across the spinel product layer are not the rate limiting steps. Therefore, the rate control in the formation of spinel inclusions is the supply of [Mg] from the slag-steel reaction; this process is controlled by the changes at the slag-steel interface.
14. Under high gas stirring application and if the value of $D_{Al^{3+}}$ is reduced to the lowest estimation at low temperature, the system shows a condition of mixed control in which the cationic diffusion across the product layer and the supply of [Mg] from the slag have an influence on the formation of spinel in the inclusions.
15. The sensitivity analysis of the coupled kinetic model demonstrated that the formation of spinel inclusions is strongly dependent on the deoxidation level

of the top slag and on the stirring conditions in the ladle. For the slags with higher initial contents of FeO and MnO but under high gas stirring conditions, the inclusions remain as alumina until the slag is deoxidized enough to start the release of [Mg]. In the cases of low gas stirring but high FeO and MnO in the slag, the inclusions did not transform to spinel after 15 minutes of processing. These calculations further support that the alumina to spinel transformation in the inclusions is controlled by the release of [Mg] from the slag.

16. The sensitivity analysis of the kinetic constants and parameters for mass transfer and diffusion indicates that the amount of spinel and Mg in the inclusions is further affected by varying the mass transfer coefficient ratios k_{sl}^{FeO} / k_m^{Fe} , k_{sl}^{MnO} / k_m^{Mn} and $k_{sl}^{SiO_2} / k_m^{Si}$ for transport of FeO, MnO and SiO_2 in the slag than by the variation in the diffusivities of the species in steel $D_{[Mg]}$, $D_{[Al]}$ and $D_{[O]}$ or the cation diffusivities $D_{Mg^{2+}}$ and $D_{Al^{2+}}$ in the spinel product layer. These results also support that the rate limiting kinetic step for the transformation of alumina to spinel inclusions is the release of [Mg] from the slag.

5.3 Suggestions for future work

From this work, the suggested aspects for future analysis and research for the inclusions model and the slag-steel model in the area of Ladle Metallurgy are:

1. Extend the kinetic model for the transformation of oxide inclusions in order to consider the effect of dissolved [Ca] in the steel. Depending on the processing conditions and calcium concentrations, the solid inclusions of alumina or magnesium aluminate spinel inclusions change their composition and transform into liquid inclusions, (Verma et al., 2012). The supply of [Ca] to the steel can be direct or indirect as reviewed by Park & Todoroki, (2010). The intentional calcium injection is applied in order to obtain liquid inclusions to avoid clogging of the nozzle during continuous casting. The indirect supply of [Ca] occurs from the reduction of CaO in the slag when the steel is deoxidized with aluminum.
2. The possibility of modeling different inclusions sizes simultaneously can be extended to calculate the simultaneous variation in the compositions for different inclusions types during the refining of steel. This includes for example oxide, sulphide and nitride indigenous inclusions.
3. A more recent thermodynamic formalism for the deoxidation of steel has been proposed by Jung, Decterov, & Pelton (2004). This formalism called the Associate Model provides a framework for the interaction between oxygen and the dissolved deoxidizers in molten steel. The implementation of this thermodynamic model for the slag-steel and steel-inclusions reactions may

provide better agreement in the case of strong deoxidizers like [Mg] and [Ca]. Furthermore, the Associate Model can be implemented for less strong deoxidizers such as [Al], [Ti], [Cr], [V], [Mn], [Si], [B], [C], [Ce], [Nb] and [Zr], Jung (2010). The applicability of this formalism on several inclusions systems for steelmaking has been reported (Jung, Decterov, & Pelton, 2004).

4. The thermodynamics of the magnesium aluminate spinel solid solution in the quasi-binary system Al_2O_3-MgO can be described with the Compound Energy Formalism, Hillert (2001) and with the assessments for the Al_2O_3-MgO system reported by Hallstedt (1992) and Zienert & Fabrichnaya (2013). Implementing this formalism may provide a more accurate and simpler method to calculate the variation in the chemical potentials $\frac{\partial \mu_{Mg}}{\partial r}$ and $\frac{\partial \mu_{Al}}{\partial r}$ for counterdiffusion of Mg^{2+} and Al^{3+} in the product layer of spinel. The current model uses the chain rule for the variation in the activities a_{MgO} and $a_{Al_2O_3}$ as a function of the mole fraction $X_{Al_2O_3}$.

5. The numerical solution of the diffusion equation for the spinel product layer in the inclusions is made with the Method of Lines. In this kinetic model, the spatial discretization uses finite difference formulas for the first and second derivatives with a truncation error of fourth order $O(h^4)$. Simplifying the spatial derivatives with the formulas for a truncation error of second order $O(h^2)$ may reduce the computation time for both the Unsteady and Quasi-steady state schemes.

6. Comparing the proposed kinetic model for the transformation of alumina inclusions to spinel with kinetic calculations with the DICTRA program. DICTRA is a software package for simulation of diffusion controlled transformations in multicomponent alloys (Ågren, 1992; Andersson, et al., 2002). As reviewed by Saunders & Miodownik (1998), the DICTRA program is based on a numerical solution of multicomponent diffusion equations that assume local thermodynamic equilibrium at phase interfaces. The program is divided into four modules which involve: (1) the solution of the diffusion equations, (2) the calculation of thermodynamic equilibrium by using Thermo-Calc, (3) the solution of flux-balance equations and (4) the displacement of phase interface positions and adjustment of grid points.

   Given the similarities between this kinetic model for spinel inclusions and DICTRA it becomes relevant to compare them. This comparison depends on the availability of databases for the solid oxide solutions and for liquid steel.
7. The modification of the slag-steel kinetic model in order to introduce the effect of atmospheric reoxidation during the periods of high gas stirring when the steel is exposed to the atmosphere. Experimental measurements of the reoxidation effect would be required to develop such model.
8. Further research is required to provide a more complete description of the changes in the mass transfer coefficients of FeO, MnO and SiO_2 in the slag. The simultaneous industrial sampling and analysis of the slag, steel and inclusions can provide additional information on this important topic.

9. For the simulation of reaction kinetics in multicomponent multiphase systems Koukkari & Pajarre (2006a), (2006b) have proposed a method of Gibss Free energy minimization for multicomponent systems that is kinetically constrained by the reaction rates or by mass transport of the species. The method is directly applicable in the commonly used Gibbs energy minimization routines, such as SOLGASMIX (Eriksson, 1975; Eriksson & Hack, 1990; Weber, 1998) or ChemApp (C. W. Bale et al., 2009; Petersen & Hack, 2007). According to Koukkari & Pajarre (2006b), this multicomponent kinetic method is the based on the minimization method of Lagrangian undetermined multipliers constrained with the reaction rates. The implementation of this methodology for the current slag-steel kinetic model can result of useful comparison with the kinetic model proposed by Robertson, et al., (1984). Additionally, the concepts from this approach can be used for the kinetic interaction of the inclusions with the different dissolved species in the steel.

References

Ågren, J. (1992). Computer Simulations of Diffusional Reactions in Complex Steels. *ISIJ International*, *32*(3), 291–296.

Andersson, J. O., Helander, T., Höglund, L., Shi, P., & Sundman, B. (2002). Thermo-Calc & DICTRA, computational tools for materials science. *Calphad: Computer Coupling of Phase Diagrams and Thermochemistry*, *26*(2), 273–312.

Andersson, M. a. T., Jonsson, L. T. I., & Jönsson, P. G. (2000). A Thermodynamic and Kinetic Model of Reoxidation and Desulphurisation in the Ladle Furnace. *ISIJ International*, *40*(11), 1080–1088.

Ando, K., & Oishi, Y. (1974). Self-diffusion coefficients of oxygen ion in single crystals of MgO n Al2O3 spinels. *The Journal of Chemical Physics*, *61*(2), 625–629.

Armijo, J. S. (1969). The kinetics and mechanism of solid-state spinel formation - A review and critique. *Oxidation of Metals*, *1*(2), 171–198.

Bale, C. W., Bélisle, E., Chartrand, P., Decterov, S. A., Eriksson, G., Hack, K., … Petersen, S. (2009). FactSage thermochemical software and databases - recent developments. *Calphad: Computer Coupling of Phase Diagrams and Thermochemistry*, *33*, 295–311.

Bale, C. W., & Pelton, A. D. (1990). The unified interaction parameter formalism: Thermodynamic consistency and applications. *Metallurgical Transactions A*, *21*(7), 1997–2002.

Barsoum, M. . (2002). *Fundamentals of Ceramics* (1 edition.). Taylor & Francis.

Benameur, N., Bernard-Granger, G., Addad, A., Raffy, S., & Guizard, C. (2011). Sintering analysis of a fine-grained alumina-magnesia spinel powder. *Journal of the American Ceramic Society*, *94*(5), 1388–1396.

Bengtson, B., & Jagitsch, R. (1947). Kinetic Studies on Formation of Spinel from Zinc Oxide and Alumina. *Arkiv Kemi, Minerali. Geol.*, *24A*(18), 1–16.

Betts, J. T. (2009). *Practical Methods for Optimal Control and Estimation Using Nonlinear Programming* (2nd editio.). Society for Industrial & Applied Mathematics.

Brabie, V. (1996). Mechanism of Reaction between Refractory Materials and Aluminum Deoxidised Molten Steel. *ISIJ International*, *36*, S109–S112.

Brooks, G. a., Rhamdhani, M. a., Coley, K. S., Subagyo, & Pan, Y. (2009). Transient kinetics of slag metal reactions. *Metallurgical and Materials Transactions B: Process Metallurgy and Materials Processing Science*, *40*(June), 353–362.

Carter, R. (1961). Mechanism of Solid- state Reaction Between Magnesium Oxide and Aluminum Oxide and Between Magnesium Oxide and Ferric Oxide. *Journal of the American Ceramic Society*, *14*(3), 116–120.

Cho, S.-W., & Suito, H. (1994). Assessment of Aluminum-Oxygen Equilibrium in Liquid Iron and Activities in CaO-Al2O3-SiO2 Slags. *ISIJ International*, *34*(2), 177–185.

Crank, J. (1987). *Free and Moving Boundary Problems*. Oxford University Press.

Crank, J., & Gupta, R. S. (1972). A method for solving moving boundary problems in heat flow using cubic splines or polynomials. *IMA Journal of Applied Mathematics*, *10*(3), 296–304.

Deo, B., & Boom, R. (1993). *Fundamentals of steelmaking metallurgy*. Prentice-Hall.

Dimitrov, S., Weyl, A., & Janke, D. (1995). Control of the aluminium-oxygen reaction in pure iron melts. *Steel Research*, *66*(1), 3–7.

Eriksson, G. (1975). Thermodynamic studies of high temperature equilibria. XII. SOLGASMIX, A computer program for calculation of equilibrium compositions in multiphase systems. *Chem. Scr.*, *8*, 100–103.

Eriksson, G., & Hack, K. (1990). ChemSage-A computer program for the calculation of complex chemical equilibria. *Metallurgical Transactions B*, *21*(6), 1013–1023.

Fiquet, G., Richet, P., & Montagnac, G. (1999). High-temperature thermal expansion of lime, periclase, corundum and spinel. *Physics and Chemistry of Minerals*, *27*(2), 103–111.

Frank, La. A. (2001). Castability - From Alumina to Spinels (and More). *AISTech 2001 Proceedings*, 403–416.

Fruehan, R. J., & Pistorius, P. C. (2013). Metallurgical Process Phenomena. In S. Seetharaman (Ed.), *Treatise on Process Metallurgy Volume 2: Process Phenomena* (1st ed., pp. 233–238). Elsevier.

Fujii, K., Nagasaka, T., & Hino, M. (2000). Activities of the constituents in spinel solid solution and free energies of formation of MgO, MgO. Al2O3. *ISIJ International*, *40*(11), 1059–1066.

Fujiwara, H., Hattori, A., & Ichise, E. (1999). Equilibrium between aluminum and oxygen in Fe-36% Ni alloy and liquid iron at 1973K. *Tetsu-To-Hagane / Journal of the Iron and Steel Institute of Japan*, *85*(3), 201–207.

Ganesh, I. (2013). A review on magnesium aluminate (MgAl2O4) spinel: synthesis, processing and applications. *International Materials Reviews*, *58*(2), 63–112.

Ganguly, J. (2002). Diffusion kinetics in minerals: principles and applications to tectono-metamophic processes. In C. M. Grammaccioli (Ed.), *Energy Modelling in Minerals, Volume 4* (pp. 271–309). European Mineralogical Union.

Gaye, H., Lehmann, J., Matsumiya, T., & Yamada, W. (1992). A statistical thermodynamics model of slags: applications to systems containing S, F, P2O5 and Cr oxides. *4th International Conference on Molten Slags and Fluxes*.

Gaye, H., & Welfringer, J. (1984). Modelling of the Thermodynamic Properties of Complex Metallurgical Slags. In *The Second International Symposium on Metallurgical Slags and Fluxes* (pp. 357–366).

Geiger, G. H., & Poirier, D. R. (1973). Transport phenomena in metallurgy. Addison-Wesley.

Ghosh, A. (2000). *Secondary Steelmaking: Principles and Applications* (1st Ed.). CRC Press.

Gorobets, A. P. (1980). Investigation into the Thermodynamics of the De-Oxidation of Iron by a Magnesium Solution. *Metall. Koksokhim*, *69*, 34–37.

Gottlieb, S., Ketcheson, D., & Shu, C.-W. (2011). *Strong Stability Preserving Runge-Kutta and Multistep Time Discretizations*. World Scientific Publishing.

Götze, L. C., Abart, R., Rybacki, E., Keller, L. M., Petrishcheva, E., & Dresen, G. (2009). Reaction rim growth in the system MgO-Al2O3-SiO2 under uniaxial stress. *Mineralogy and Petrology*, *99*(3-4), 263–277.

Graham, K. J. (2008). *Integrated Ladle Metallurgy Control*. McMaster University.

Graham, K. J., & Irons, G. A. (2010). Coupled Kinetic Phenomena in Ladle Metallurgy. In *International Symposium on Highly Innovative Novel Operations "Future Steelmaking Metallurgy"* (pp. 65–74). Tokyo.

Gustafsson, K. (1991). Control theoretic techniques for stepsize selection in explicit Runge-Kutta methods. *ACM Transactions on Mathematical Software (TOMS)*, *17*(4), 533–554.

Gustafsson, S., & Mellberg, P.-O. (1980). On the Free Energy Interaction Between Some Strong Deoxidizers, Especially Calcium, and Oxygen in Liquid Iron. *Scandinavian Journal of Metallurgy*, *9*(3), 111–116.

Hairer, E. (n.d.). Fortran and Matlab Codes. Retrieved April 6, 2015, from http://www.unige.ch/~hairer/software.html

Hairer, E., Nørsett, S. P., & Wanner, G. (2011). *Solving Ordinary Differential Equations I Nonstiff Problems* (2nd Editio.). Springer-Verlag Berlin Heidelberg.

Hairer, E., & Wanner, G. (2002). *Solving Ordinary Differential Equations II Stiff and Differential-Algebraic Problems* (2nd Editio.). Springer-Verlag Berlin Heidelberg.

Hallstedt, B. (1992). Thermodynamic assessment of the system MgO–Al2O3. *Journal of the American Ceramic Society*, (196322), 1497–1507.

Han, Q., Zhou, D., & Xiang, C. (1997). Determination of dissolved sulfur and Mg-S, Mg-O equilibria in molten iron. *Steel Research*, *68*(1), 9–14.

Harada, A., Maruoka, N., Shibata, H., & Kitamura, S. (2013a). A Kinetic Model to Predict the Compositions of Metal, Slag and Inclusions during Ladle Refining: Part 1. Basic Concept and Application. *ISIJ International*, *53*(12), 2110–2117.

Harada, A., Maruoka, N., Shibata, H., & Kitamura, S. (2013b). A Kinetic Model to Predict the Compositions of Metal, Slag and Inclusions during Ladle Refining: Part2. Condition to Control the Inclusion Composition. *ISIJ International*, *53*(12), 2118–2125.

Hillert, M. (2001). The compound energy formalism. *Journal of Alloys and Compounds*, *320*(2), 161–176.

Hino, M., & Ito, K. (Eds.). (2010). *Thermodynamic Data for Steelmaking - The Japan Society for the Promotion of Science*. Tohoku University Publishing Co.

Holappa, L. (2014). Secondary Steelmaking. In S. Seetharaman (Ed.), *Treatise on Process Metallurgy, Volume 3: Industrial Processes* (1st ed., Vol. 3, pp. 301–345). Elsevier.

Holappa, L., & Wijk, O. (2014). Inclusion Engineering. In S. Seetharaman (Ed.), *TTreatise on Process Metallurgy, Volume 3: Industrial Processes* (1st ed., Vol. 3, pp. 347–372). Elsevier.

Hundsdorfer, W., & Verwer, J. G. (2007). *Numerical Solution of Time-Dependent Advection-Diffusion-Reaction Equations* (1st Editio.). Springer-Verlag Berlin Heidelberg.

Inoue, R., & Suito, H. (1994). Thermodynamics of O, N, and S in liquid Fe equilibrated with CaO-AI2O3-MgO slags. *Metallurgical and Materials Transactions B*, *25*(April), 235–244.

Irons, G. A., Chang, C. W., Guthrie, R. I., & Szekely, J. (1978). The Measurement and Prediction of the Vaporization of Magnesium from an Inductively Stirred Melt. *Metallurgical and Materials Transactions Transactions B*, *9*(1), 151–154.

Itoh, H., Hino, M., & Ban-Ya, S. (1997). Thermodynamics on the formation of spinel nonmetallic inclusion in liquid steel. *Metallurgical and Materials Transactions B*, *28*(5), 953–956.

Jo, S., Song, B. O., & Kim, S. (2002). Thermodynamics on the Formation of Spinel (MgO и Al 2 O 3) Inclusion in Liquid Iron Containing Chromium, *33*(October), 703–709.

Jung, I., Decterov, S. A., & Pelton, A. D. (2004). Computer Applications of Thermodynamic Databases to Inclusion Engineering. *ISIJ International*.

Jung, I. H. (2010). Overview of the applications of thermodynamic databases to steelmaking processes. *Calphad: Computer Coupling of Phase Diagrams and Thermochemistry*, *34*(3), 332–362.

Jung, I.-H., Decterov, S. a., & Pelton, A. D. (2004a). A thermodynamic model for deoxidation equilibria in steel. *Metallurgical and Materials Transactions B*, *35*(June), 493–507.

Jung, I.-H., Decterov, S. a., & Pelton, A. D. (2004b). Critical Thermodynamic Evaluation and Optimization of the MgO-Al2O3, CaO-MgO-Al2O3, and MgO-Al2O3-SiO2 Systems. *Journal of Phase Equilibria & Diffusion*, *25*(4), 329–345.

Kapoor, M. L., & Frohberg, M. G. (1973). Theoretical treatment of activities in silicate melts. In *Internat. Symposium on Chemical Metallurgy of Iron and Steel* (pp. 17–22).

Kaushik, P., Lehmann, J., & Nadif, M. (2012). State of the Art in Control of Inclusions, Their Characterization, and Future Requirements. *Metallurgical and Materials Transactions B*, *43*(4), 710–725.

Kaushik, P., Pielet, H., & Yin, H. (2009). Inclusion characterisation – tool for measurement of steel cleanliness and process control: Part 1. *Ironmaking & Steelmaking*, *36*(8), 561–571.

Kelley, C. T. (1987). *Solving Nonlinear Equations with Newton's Method*. Society for Industrial & Applied Mathematics,U.S.

Kitamura, S., Kitamura, T., Shibata, K., Mizukami, Y., Mukawa, S., & Nakagawa, J. (1991). Effect of Stirring Energy, Temperature and Flux Composition on Hot Metal Dephosphorization Kinetics. *ISIJ International*, *31*(11), 1322–1328.

Koch, E., & Wagner, C. (1936). Formation of Ag2HgI4 from AgI and HgI2 by Reaction in Solid State. *Z. Physik. Chem.*, (B34), 317–321.

Kofstad, P., & Truls, N. (2007). *Defects and transport in crystalline solids*. Oslo, Norway: University of Oslo.

Kor, G. J. W., & Glaws, P. C. (1998). Ladle Refining and Vacuum Degassing. In R. J. Fruehan (Ed.), *The Making, Shaping and Treating of Steel, Vol. 2: Steelmaking and Refining Volume* (11th ed.). Pittsburgh, PA: AISE Steel Foundation.

Koukkari, P., & Pajarre, R. (2006a). Calculation of constrained equilibria by Gibbs energy minimization. *Calphad: Computer Coupling of Phase Diagrams and Thermochemistry*, *30*(1), 18–26.

Koukkari, P., & Pajarre, R. (2006b). Introducing mechanistic kinetics to the Lagrangian Gibbs energy calculation. *Computers and Chemical Engineering*, *30*(6-7), 1189–1196.

Krishnapisharody, K., & Irons, G. A. (2007). A study of spouts on bath surfaces from gas bubbling: Part I. Experimental investigation. *Metallurgical and Materials Transactions B: Process Metallurgy and Materials Processing Science*, *38*, 367–375.

Kulikov, I. S. (1985). Iron Deoxidation by Alkaline-Earth Metals. *Izv. Akad. Nauk SSSR, Met*, *6*, 9–15.

Lange, K. W. (1988). Thermodynamic and kinetic aspects of secondary steelmaking processes. *International Materials Reviews*.

Lehmann, J., & Gaye, H. (1993). Modeling of Thermodynamic Properties of Sulphur Bearing Metallurgical Slags. *Revue Internationale Des Hautes Temperatures et Des Refractaires*, *28*(3), 81 – 90.

Lehmann, J., & Nadif, M. (2011). Interactions Between Metal and Slag Melts: Steel Desulfurization. *Reviews in Mineralogy and Geochemistry*, *73*, 493–511.

Levenspiel, O. (1998). *Chemical Reaction Engineering* (3rd Editio.). Wiley.

LeVeque, R. (2007). *Finite Difference Methods for Ordinary and Partial Differential Equations: Steady-State and Time-dependent Problems*. Society for Industrial and Applied Mathematics.

Liddell, Kn. C. (2005). Shrinking core models in hydrometallurgy: What students are not being told about the pseudo-steady approximation. *Hydrometallurgy*, *79*(1-2), 62–68.

Lindner, R., & Åkerström, Å. (1956). Self-Diffusion and Reaction in Oxide and Spinel Systems. *Zeitschrift Für Physikalische Chemie*, *6*(3_4), 162–177.

Lu, D.-Z. D. (1992). *Kinetics, mechanisms and modelling of calcium treatment of steel*. McMaster University.

Luikov, A. V. (1968). *Analytical Heat Diffusion Theory*. Academic Press.

Lupis, C. H. P. (1983). *Chemical Thermodynamics of Materials*. New York: Elsevier Science Ltd.

Martinelli, J., Sonder, E., Weeks, R., & Zuhr, R. (1986). Mobility of cations in magnesium aluminate spinel. *Physical Review B*, *33*(8), 5698–5701.

Mehrer, H. (2007). *Diffusion in Solids: Fundamentals, Methods, Materials, Diffusion-Controlled Processes* (1st Ed.). Springer.

Mendez, J., Gómez, A., Capurro, C., Donayo, R., & Cicutti, C. (2012). Effect of process conditions on the evolution of MgO content of inclusions during the production of calcium treated, aluminum killed steels. In *8th International Conference on Clean Steel*. Budapest, Hungary.

Mitchell, T. E. (1999). Dislocations and Mechanical Properties of MgO–Al2O3 Spinel Single Crystals. *Journal of the American Ceramics Society*, *82*, 3305–3316.

Mizuno, K., Todoroki, H., Noda, M., & Tohge, T. (2001). Effects of Al and Ca in ferrosilicon alloys for deoxidation on inclusion composition in type 304 stainless steel. *Iron & Steelmaker*, *28*(8), 93–101.

Murphy, S. T., Uberuaga, B. P., Ball, J. B., Cleave, a. R., Sickafus, K. E., Smith, R., & Grimes, R. W. (2009). Cation diffusion in magnesium aluminate spinel. *Solid State Ionics*, *180*(1), 1–8.

Nadif, M., & Gatellier, C. (1986). Influence d'une Addition de Calcium ou de Magnesium sur la Solubilite de l'Oxygen et du Soufre dan l'Acier Liquid. *Revue de Metallurgie*, 377–394.

Nagata, K., Ono, Y., Ejima, T., & Yamamura, T. (1988). Chapter 7 - Diffusion. In Y. Kawai & Y. Shiraishi (Eds.), *Handbook of Physico-chemical Properties at High Temperatures*. Tokyo: ISIJ.

Nakano, M., Yamaguchi, G., & Saito, K. (1971). Role of Oxygen from in Spinel and Formation MgO and Al2O3. *Yogyo - Kyokai -Shi, Journal of the Ceramic Society of Japan*, *79*(3), 92 – 96.

Navias, L. (1961). Preparation and Properties of Spinel Made by Vapor Transport and Diffusion in the System MgO-Al2O3. *Journal of the American Ceramic Society*, *44*(9), 434–446.

Nishi, T., & Shinme, K. (1998). Formation of Spinel Inclusions in Molten Stainless Steel under Al Deoxidation with Slags. *Tetsu-to-Hagane(Journal of the Iron and Steel Institute of Japan)*, *84*(12), 837–843.

Oeters, F. (1994). *Metallurgy of Steelmaking*. Dusselderf: Verlag Stahleisen mbH.

Ohta, H., & Suito, H. (1997). Deoxidation equilibria of calcium and magnesium in liquid iron. *Metallurgical and Materials Transactions B*, *28*(December), 1131–1139.

Okuyama, G., Yamaguchi, K., Takeuchi, S., & Sorimachi, K. (2000). Effect of Slag Composition on the Kinetics of Formation of Al2O3 MgO Inclusions in Aluminum Killed Ferritic Stainless Steel. *ISIJ International*.

Ono, H., Nakajima, K., Ibuta, T., & Usui, T. (2010). Equilibrium Relationship between the Oxide Compounds in MgO–Al2O3–Ti2O3 and Molten Iron at 1 873 K. *ISIJ International*, *50*, 1955–1958.

Paar, A., Schneider, R., Zeller, P., Reiter, G., Paul, S., & Würzinger, P. (2014). Effect of Electrical Parameters on Type and Content of Non-Metallic Inclusions after Electro-Slag-Remelting. *Steel Research International*, *85*(4), 570–578.

Park, J. H., & Kim, D. S. (2005). Effect of CaO-Al2O3-MgO slags on the formation of MgO-Al2O3 inclusions in ferritic stainless steel. *Metallurgical and Materials Transactions B*, *36*(4), 495–502.

Park, J., & Todoroki, H. (2010). Control of MgO· Al2O3 Spinel Inclusions in Stainless Steels. *ISIJ International*, *50*(10), 1333–1346.

Pelton, A. D., & Bale, C. W. (1986). A Modified Interaction Parameter Formalism for Non-Dilute Solutions. *Metallurgical Transactions A*, *17*(7), 1211–1215.

Peter, J., Peaslee, K. D., Robertson, D. G. C., & Thomas, B. G. (2005). Experimental Study of Kinetic Processes During the Steel Treatment at two LMF ' s. In *AIST Tech Conference Proceedings* (Vol. 1, pp. 959–967).

Petersen, S., & Hack, K. (2007). The thermochemistry library ChemApp and its applications. *International Journal of Materials Research*, *98*(10), 935–945.

Pfeiffer, T., & Schmalzried, H. (1989). Spinel Formation: A Detailed Analysis. *Zeitschrift Für Physikalische Chemie*, *161*(Part_1_2), 1–17.

Pluschkell, W. (1981). Grundoperationen Pfannenmetallurgischer Prozesse. *Stahl Und Eisen*, *101*(13-14), 97–103.

Pretorius, E. B., Oltmann, H. G., & Schart, B. T. (2013). An Overview of Steel Cleanliness From an Industry Perspective. In *AISTech 2013 Proceedings* (pp. 993–1026).

Pretorius, E., Oltmann, H., & Cash, T. (2010). The effective modification of spinel inclusions by Ca treatment in LCAK steel. *Iron & Steel Technology*, *Vol. 7*(No. 7), 31–44.

Reddy, K., & Cooper, A. (1981). Oxygen diffusion in magnesium aluminate spinel. *Journal of the American Ceramic …*, *65*(12), 634–638.

Reimanis, I., & Kleebe, H.-J. (2009). A Review on the Sintering and Microstructure Development of Transparent Spinel (MgAl 2 O 4). *Journal of the American Ceramic Society*, *92*(7), 1472–1480.

Rickert, H. (1982). *Electrochemistry of Solids* (Vol. 7). Springer Berlin Heidelberg.

Robertson, D., Deo, B., & Ohguchi, S. (1984). Multicomponent Mixed-Transport Control Theory for Kinetics of Coupled Slag/Metal and Slag/Metal/Gas Reactions: Application to Desulphurization of Molten Iron. *Ironmaking and Steelmaking*, *11*(1), 41–55.

Robertson, D. G. C. (1995). The computation of the kinetics of reactions between multiple phases. In *EPD Congress* (pp. 347–361).

Rossi, R. C., & Fulrath, R. M. (1963). Epitaxial Growth of Spinel by Reaction in the Solid State. *Journal of the American Ceramic Society*, *46*(3), 145–149.

Rubat Du Merac, M., Kleebe, H. J., Müller, M. M., & Reimanis, I. E. (2013). Fifty years of research and development coming to fruition; Unraveling the complex interactions during processing of transparent magnesium aluminate (MgAl 2 O 4) spinel. *Journal of the American Ceramic Society*, *96*(11), 3341–3365.

Saltelli, A., Ratto, M., Tarantola, S., & Campolongo, F. (2012). Update 1 of: Sensitivity analysis for chemical models. *Chemical Reviews*, *112*(5), 1–21.

Saunders, N., & Miodownik, A. P. (1998). *CALPHAD (Calculation of Phase Diagrams): A Comprehensive Guide*. Pergamon.

Schiesser, W. E. (1991). *The numerical method of lines : integration of partial differential equations*. Academic Press.

Schmalzried, H. (1995). *Chemical kinetics of solids* (1st ed.). VCH Verlag, Weinheim.

Schmalzried, H., & Pfeiffer, T. (1986). The Build-Up of Internal Pressures During Compound Formation. *Zeitschrift Für Physikalische …*, *148*(1), 21–32.

Seo, J.-D., & Kim, S.-H. (2000). Thermodynamic assessment of Mg deoxidation reaction of liquid iron and equilibria of [Mg]-[Al]-[O] and [Mg]-[S]-[O]. *Steel Research*, *71*(4), 101–106.

Seo, J.-D., Kim, S.-H., & Lee, K.-R. (1998). Thermodynamic assessment of the Al deoxidation reaction in liquid iron. *Steel Research*, *69*(2), 49–53.

Shacham, M. (1986). Numerical solution of constrained non-linear algebraic equations. *International Journal for Numerical Methods in Engineering*, *23*(8), 1455–1481.

Sheng, Y. ., Wasserburg, G. ., & Hutcheon, I. . (1992). Self-diffusion of magnesium in spinel and in equilibrium melts: Constraints on flash heating of silicates. *Geochimica et Cosmochimica Acta*, *56*(6), 2535–2546.

Sheshukov, O. Y., Nekrasov, I. V., Sivtsov, a. V., Tsymbalist, M. M., Egiazar'yan, D. K., & Metelkin, a. a. (2014). Dynamic monitoring of slag oxidation and thickness in the ladle-furnace unit. *Steel in Translation*, *44*(1), 43–46.

Silebi, C. A., & Schiesser, W. E. (1992). *Dynamic Modeling of Transport Process Systems* (1st Editio.). Academic Press.

Söderlind, G. (2002). Automatic control and adaptive time-stepping. *Numerical Algorithms*, *31*(1-4), 281–310.

Sohn, H. Y. (2014). Process Modeling in Non-Ferrous Metallurgy. In S. Seetharaman (Ed.), *Treatise on Process Metallurgy* (1st ed., Vol. 3, pp. 701–838). Elsevier.

Sohn, H. Y., & Wadsworth, M. E. (1979). *Rate Processes of Extractive Metallurgy* (1st ed.). Springer US.

Story, S. R., Smith, S. M., & Fruehan, R. (2004). Application of Rapid Inclusion Identification and Analysis. In *AISTech 2004 Proceedings - Volume II AISTech 2004 Proceedings - Volume II* (Vol. II, pp. 1147–1156).

Story, S.-R., Goldsmith, G.-E., & Klepzig, G.-L. (2008). Study of cleanliness and castability in Ti-stabilized ultra low carbon steels using automated SEM inclusion analysis. *Revue de Métallurgie*, *105*, 272–279.

Szekely, J., Evans, J. W., & Sohn, H. Y. (1976). Gas-solid reactions. New York: Academic Press.

Szekely, J., & Themelis, N. J. (1971). *Rate phenomena in process metallurgy*. New York: John Wiley & Sons Inc.

Takata, R., Yang, J., & Kuwabara, M. (2007). Characteristics of Inclusions Generated during Al–Mg Complex Deoxidation of Molten Steel. *ISIJ International*, *47*(10), 1379–1386.

Taler, J., & Duda, P. (2006). *Solving Direct and Inverse Heat Conduction Problems*. Springer Berlin Heidelberg.

Thomas, B. G., & Brimacombe, J. K. (1997). Process Modeling. In *Advanced Physical Chemistry for Process Metallurgy* (pp. 253–280).

Todoroki, H., & Mizuno, K. (2004). Effect of Silica in Slag on Inclusion Compositions in 304 Stainless Steel Deoxidized with Aluminum. *ISIJ International*, *44*(8), 1350–1357.

Turkdogan, E. T. (1985). Slags and fluxes for ferrous ladle metallurgy. *Ironmaking and Steelmaking*, *12*(2), 64–78.

Van Orman, J. a., & Crispin, K. L. (2010). Diffusion in Oxides. *Reviews in Mineralogy and Geochemistry*, *72*(1), 757–825.

Verma, N., Pistorius, P. C., Fruehan, R. J., Potter, M. S., Oltmann, H. G., & Pretorius, E. B. (2012). Calcium Modification of Spinel Inclusions in Aluminum-Killed Steel: Reaction Steps. *Metallurgical and Materials Transactions B*, *43*(4), 830–840.

Viertel, H. U., & Seifert, F. (1979). Physical properties of defect spinels in the system MgAl2O4–Al2O3. *Neues Jahrb. Mineral., Abh.*, *134*(2), 167–182.

Wagner, C. (1938). Uber den Mechanismus von doppelten Umsetzungen durch Reaktion im festen Zustand. *Zeitschrift Fur Anorganische Und Allgemeine Chemie*, *236*(1), 320–338.

Wagner, C. (1952). *Thermodynamics of Alloys*. Addison-Wesley.

Wagner, C. (1975). Equations for transport in solid oxides and sulfides of transition metals. *Progress in Solid State Chemistry*, *10*, 3–16.

Watson, E. B., & Price, J. D. (2002). Kinetics of the reaction MgO + Al2O3 → MgAl2O4 and Al-Mg interdiffusion in spinel at 1200 to 2000°C and 1.0 to 4.0 GPa. *Geochimica et Cosmochimica Acta*, *66*(12), 2123–2138.

Weber, C. F. (1998). Convergence of the Equilibrium Code SOLGASMIX. *Journal of Computational Physics*, *145*(2), 655–670.

Wei, G. C., Jeon, S. J., Sung, C., & Rhodes, W. H. (1998). Characterization of second phases in translucent alumina by analytical transmission electron microscopy. In A. P. Tomsia & A. M. Glaeser (Eds.), *Ceramic Microstructures: Control at the Atomic Level* (pp. 311–322). Springer US.

Wen, C. Y. (1968). Noncatalytic heterogeneous solid-fluid reaction models. *Industrial & Engineering Chemistry*, *60*(9), 34–54.

Whitney, W. P., & Stubican, V. S. (1971a). Interdiffusion in the System MgO-MgAl2O4. *Journal of the American Ceramic Society*, *54*(7), 349–352.

Whitney, W. P., & Stubican, V. S. (1971b). Interdiffusion studies in the system MgO□Al2O3. *Journal of Physics and Chemistry of Solids*, *32*(2), 305–312.

Wouwer, A. Vande, Saucez, P., & Schiesser, W. E. (2001). *Adaptive Method of Lines* (1st Editio.). Chapman and Hall/CRC.

Wu, S., & Zhang, J. (2008). Mathematical Model for Growth of Inclusion in Deoxidization on the Basis of Unreacted Core Model. *Journal of Iron and Steel Research, International*, *15*(6), 24–28.

Yamaguchi, G., & Tokuda, T. (1967). Some Aspects of Solid State Reactions between Oxides. *Bulletin of the Chemical Society of Japan*, *40*(4), 843–851.

Yang, S., Wang, Q., Zhang, L., Li, J., & Peaslee, K. (2012). Formation and Modification of MgO·Al2O3-Based Inclusions in Alloy Steels. *Metallurgical and Materials Transactions B*, *43*(4), 731–750.

Yang, W., Zhang, L., Wang, X., Ren, Y., Liu, X., & Shan, Q. (2013). Characteristics of Inclusions in Low Carbon Al-Killed Steel during Ladle Furnace Refining and Calcium Treatment. *ISIJ International*, *53*(8), 1401–1410.

Young, D. J. (2008). *High Temperature Oxidation and Corrosion of Metals* (1st ed.). Elsevier.

Young, R. W., Duffy, J. A., Hassall, G. J., & Xu, Z. (1992). Use of optical basicity concept for determining phosphorus and sulphur slag− metal partitions. *Ironmaking & Steelmaking*, *19*(3), 201–219.

Zhang, L., & Thomas, B. G. (2003). State of the Art in Evaluation and Control of Steel Cleanliness. *ISIJ International*, *43*(3), 271–291.

Zhang, P., Debroy, T., & Seetharaman, S. (1996). Interdiffusion in the MgO-Al2O3 spinel with or without some dopants. *Metallurgical and Materials …*, *27*(August).

Zienert, T., & Fabrichnaya, O. (2013). Thermodynamic assessment and experiments in the system MgO–Al2O3. *Calphad*, *40*, 1–9.

Appendix A

Method to calculate the inclusion-steel interfacial equilibrium

With the assumption of local equilibrium at the inclusion-steel interface, a methodology is proposed to calculate the interfacial activities and concentrations of the components involved in the simultaneous deoxidation with [Mg] and [Al]. This procedure couples the mass transfer rates in the steel and inclusions phases and satisfies the equilibrium constraints.

A.1 System of equations

From the analysis of cationic diffusion in the product layer based on the Wagner- Schmalzried theory for spinel formation, the mass transfer rates of Mg^{2+} and Al^{3+} at the inclusion-steel interface in the product layer are:

$$N_{Mg^{2+}}\Big|_{r*} = 4\pi r^{*2}\frac{\delta^{*}\upsilon^{*}\cdot D_{Mg}D_{Al}}{4\delta^{*}D_{Mg}+9\upsilon^{*}D_{Al}}\cdot\frac{1}{V_m^{Sp}}\left[9\frac{\partial \ln a_{MgO}}{\partial r}\Big|_{r*}-3\frac{\partial \ln a_{Al_2O_3}}{\partial r}\Big|_{r*}\right] \quad \text{(A-1)}$$

$$N_{Al^{3+}}\Big|_{r*} = 4\pi r^{*2}\frac{\delta^{*}\upsilon^{*}\cdot D_{Mg}D_{Al}}{4\delta^{*}D_{Mg}+9\upsilon^{*}D_{Al}}\cdot\frac{1}{V_m^{Sp}}\left[2\frac{\partial \ln a_{Al_2O_3}}{\partial r}\Big|_{r*}-6\frac{\partial \ln a_{MgO}}{\partial r}\Big|_{r*}\right] \quad \text{(A-2)}$$

Where r* is the radius of the inclusions at the interface with steel, $\delta*$ and $\nu*$ are the indexes of the composition of spinel in equilibrium with steel

$Mg_{\delta^*}Al_{\upsilon^*}O_4$, D_{Mg} and D_{Al} are the diffusivities of Mg^{2+} and Al^{3+} in spinel as components and V_m^{Sp} is the molar volume of spinel.

In this model, the magnesium aluminate spinel is considered as a solid solution between Al_2O_3 and MgO, therefore $\delta*$ and $\nu*$ can be defined:

$$\delta^* = \frac{4 - 4X^*_{Al_2O_3}}{1 + 2X^*_{Al_2O_3}} \tag{A-3}$$

$$\upsilon^* = \frac{8X^*_{Al_2O_3}}{1 + 2X^*_{Al_2O_3}} \tag{A-4}$$

This implies that the equilibrium composition of spinel corresponds to the mole fraction $X^*_{Al_2O_3}$ in the Al_2O_3 and MgO system. Substituting (A-3) and (A-4) in expressions (A-1) and (A-2), the interfacial mass transfer rates are:

$$N_{Mg^{2+}}\Big|_{r*} = 4\pi r^{*2}\frac{D_{Mg}D_{Al}\left(32X^*_{Al_2O_3} - 32{X^*_{Al_2O_3}}^2\right)}{\left(72D_{Mg}X^*_{Al_2O_3} - 16D_{Mg}X^*_{Al_2O_3} + 16D_{Mg}\right)\left(1 + 2X^*_{Al_2O_3}\right)} \times \frac{1}{V_m^{Sp}}\left[9\frac{\partial \ln a_{MgO}}{\partial r}\Big|_{r*} - 3\frac{\partial \ln a_{Al_2O_3}}{\partial r}\Big|_{r*}\right] \tag{A-5}$$

$$N_{Al^{3+}}\Big|_{r*} = 4\pi r^{*2}\frac{D_{Mg}D_{Al}\left(32X^*_{Al_2O_3} - 32{X^*_{Al_2O_3}}^2\right)}{\left(72D_{Mg}X^*_{Al_2O_3} - 16D_{Mg}X^*_{Al_2O_3} + 16D_{Mg}\right)\left(1 + 2X^*_{Al_2O_3}\right)} \times \frac{1}{V_m^{Sp}}\left[2\frac{\partial \ln a_{Al_2O_3}}{\partial r}\Big|_{r*} - 6\frac{\partial \ln a_{MgO}}{\partial r}\Big|_{r*}\right] \tag{A-6}$$

In order to calculate the gradients in the activities of Al_2O_3 and MgO in the product layer at r*, the derivatives are approximated using finite differences. In this way, the region of the spinel product layer $r' \leq r \leq r^*$ is spatially discretized in n equidistant nodes located at distances r_i according to:

$$h = \frac{r^* - r'}{n-1} \tag{A-7}$$

$$r_i = r' + (i-1)h \qquad i = 1, \dots, n \tag{A-8}$$

If the function $f(r)$ represents a physical property in the product layer its values can be sampled at the nodes $f_i = f(r_i)$. Then, the fourth order backward approximation for the first the derivative at the interfacial node $\mathrm{r}_n = \mathrm{r}^*$ is (Betts, 2009):

$$f_n' = \frac{1}{12h}\left[25f_n - 48f_{n-1} + 36f_{n-2} - 16f_{n-3} + 3f_{n-4}\right] \tag{A-9}$$

An equivalent form is:

$$f_n' = \frac{25}{12h}\left[\, f_n - Af_{n-1} - Bf_{n-2} - Cf_{n-3} - Df_{n-4} \,\right] \tag{A-10}$$

Where $A = \frac{48}{25}, B = -\frac{36}{25}, C = \frac{16}{25}$ and $D = -\frac{3}{25}$. Therefore, the change in the activities at the interface can be approximated according to:

$$\left.\frac{\partial \ln a_{MgO}}{\partial r}\right|_{r*} = \frac{25}{12h}\left[\ln a_{MgO^*} - A \ln a_{MgO_{n-1}} - B \ln a_{MgO_{n-2}} - C \ln a_{MgO_{n-3}} - D \ln a_{MgO_{n-4}}\right] \tag{A-11}$$

$$\left.\frac{\partial \ln a_{Al_2O_3}}{\partial r}\right|_{r*} = \frac{25}{12h}\left[\ln {a_{Al_2O_3}}^{*} - A \ln a_{Al_2O_3\,n-1} - B \ln a_{Al_2O_3\,n-2} - C \ln a_{Al_2O_3\,n-3} - D \ln a_{Al_2O_3\,n-4}\right] \tag{A-12}$$

If the activities at the nodes adjacent to the interface are known values, the derivatives can be expressed as:

$$\left.\frac{\partial \ln a_{MgO}}{\partial r}\right|_{r*} = \frac{25}{12h}\left[\ln {a_{MgO}}^{*} + C_{MgO}\right] \tag{A-13}$$

$$\left.\frac{\partial \ln a_{Al_2O_3}}{\partial r}\right|_{r*} = \frac{25}{12h}\left[\ln {a_{Al_2O_3}}^{*} + C_{Al_2O_3}\right] \tag{A-14}$$

Where C_{MgO} and $C_{Al_2O_3}$ group the local available information of the activities of MgO and Al_2O_3 respectively:

$$C_{MgO} = -A \ln a_{MgO\,n-1} - B \ln a_{MgO\,n-2} - C \ln a_{MgO\,n-3} - D \ln a_{MgO\,n-4} \tag{A-15}$$

$$C_{Al_2O_3} = -A \ln a_{Al_2O_3\,n-1} - B \ln a_{Al_2O_3\,n-2} - C \ln a_{Al_2O_3\,n-3} - D \ln a_{Al_2O_3\,n-4} \tag{A-16}$$

Substituting the derivatives (A-13) and (A-14) in the expressions for the mass transfer rates (A-5) and (A-6) and organizing terms we obtain:

$$N_{Mg^{2+}}\big|_{r*} = 4\pi {r^*}^2 \cdot \frac{D_{Mg} D_{Al}\left(32X^*_{Al_2O_3} - 32{X^*_{Al_2O_3}}^2\right)}{\left(72D_{Mg}X^*_{Al_2O_3} - 16D_{Mg}X^*_{Al_2O_3} + 16D_{Mg}\right)\left(1 + 2X^*_{Al_2O_3}\right)} \times \frac{1}{V_m^{Sp}}\left(\frac{25}{12h}\right)\left[9 \ln {a_{MgO}}^{*} - 3 \ln {a_{Al_2O_3}}^{*} + \alpha_{Mg}\right] \tag{A-17}$$

(A-18)

$$N_{Al^{3+}}|_{r*} = 4\pi {r^*}^2 \cdot \frac{D_{Mg} D_{Al}\left(32X^*_{Al_2O_3} - 32{X^*_{Al_2O_3}}^2\right)}{\left(72D_{Mg}X^*_{Al_2O_3} - 16D_{Mg}X^*_{Al_2O_3} + 16D_{Mg}\right)\left(1 + 2X^*_{Al_2O_3}\right)}$$

$$\times \frac{1}{V_m^{Sp}}\left(\frac{25}{12h}\right)\left[2\ln {a_{Al_2O_3}}^* - 6\ln {a_{MgO}}^* + \alpha_{Al}\right]$$

Where the terms $\alpha_{Mg}$and α_{Al} group the known values of C_{MgO} and $C_{Al_2O_3}$ according to:

$$\alpha_{Mg} = 9C_{MgO} - 3C_{Al_2O_3} \quad \text{(A-19)}$$

$$\alpha_{Al} = 2C_{Al_2O_3} - 6C_{MgO} \quad \text{(A-20)}$$

Equations (A-17) and (A-18) express the cationic mass transfer rates at the interface in terms of the activities in equilibrium with the species in steel ${a_{Al_2O_3}}^*$ and ${a_{MgO}}^*$, the equilibrium spinel composition defined with the mole fraction ${X_{Al_2O_3}}^*$, the known values of activities at the nodes inside the product layer and the kinetic coefficients.

Coupling of the interfacial mass transfer rates in the inclusions and steel phase is proposed to occur according to:

$$N_{[Mg]} = N_{Mg^{2+}}\Big|_{r*} + \frac{\delta^*}{4}N_{[O]} \quad \text{(A-21)}$$

$$\frac{\upsilon^*}{4}N_{[O]} = -N_{Al^{3+}}|_{r*} + N_{[Al]} \quad \text{(A-22)}$$

Where $N_{[Mg]}$, $N_{[Al]}$ and $N_{[O]}$ are the mass transfer rates across the interface boundary layer of the [Mg], [Al] and [O] dissolved in liquid steel.

$$N_{[Mg]} = 4\pi r^{*2} \cdot k_{Mg} C_{Vm}\left(X_{Mg}^{b} - X_{Mg}^{*}\right) \tag{A-23}$$

$$N_{[Al]} = 4\pi r^{*2} \cdot k_{Al} C_{Vm}\left(X_{Al}^{b} - X_{Al}^{*}\right) \tag{A-24}$$

$$N_{[O]} = 4\pi r^{*2} \cdot k_{O} C_{Vm}\left(X_{O}^{b} - X_{O}^{*}\right) \tag{A-25}$$

Where X_{Mg}^{*}, X_{Al}^{*}, and X_{O}^{*} are the interfacial mole fraction concentrations in equilibrium with the spinel product layer; X_{Mg}^{b}, X_{Al}^{b} and X_{O}^{b} are the concentrations in the bulk of the steel; k_{Mg}, k_{Al}, and k_{O} are the mass transfer coefficients for diffusion in the boundary layer and C_{Vm} is the total molar concentration in the steel.

Substituting the expression for each equation of mass transfer as well as for δ∗ and ν∗ , the interfacial mass balance for deoxidation with magnesium in the spinel is obtained from equations (A-3), (A-17), (A-21), (A-23) and (A-25); after some rearrangement it becomes:

(A-26)

$$\begin{aligned} k_{Mg} C_{Vm}\left(X_{Mg}^{b} - X_{Mg}^{*}\right) = {} & \frac{D_{Mg} D_{Al}\left(32 X_{Al_2O_3}^{*} - 32 {X_{Al_2O_3}^{*}}^{2}\right)}{\left(72 D_{Mg} X_{Al_2O_3}^{*} - 16 D_{Mg} X_{Al_2O_3}^{*} + 16 D_{Mg}\right)\left(1 + 2 X_{Al_2O_3}^{*}\right)} \\ & \times \frac{1}{V_m^{Sp}} \left(\frac{25}{12h}\right) \left[9 \ln {a_{MgO}}^{*} - 3 \ln {a_{Al_2O_3}}^{*} + \alpha_{Mg}\right] \\ & + \frac{1 - X_{Al_2O_3}^{*}}{1 + 2 X_{Al_2O_3}^{*}} \cdot k_{O} C_{Vm}\left(X_{O}^{b} - X_{O}^{*}\right) \end{aligned}$$

From equations (A-4), (A-18), (A-22), (A-24) and (A-25), the mass balance at the interface for deoxidation with aluminum in spinel is:

$$\frac{2X^*_{Al_2O_3}}{1+2X^*_{Al_2O_3}} \cdot k_O C_{Vm}(X^b_O - X^*_O) = k_{Al} C_{Vm}(X^b_{Al} - X^*_{Al}) - \frac{D_{Mg}D_{Al}\left(32X^*_{Al_2O_3} - 32{X^*_{Al_2O_3}}^2\right)}{\left(72D_{Mg}X^*_{Al_2O_3} - 16D_{Mg}X^*_{Al_2O_3} + 16D_{Mg}\right)\left(1+2X^*_{Al_2O_3}\right)} \times \frac{1}{V_m^{Sp}}\left(\frac{25}{12h}\right)\left[2\ln {a_{Al_2O_3}}^* - 6\ln {a_{MgO}}^* + \alpha_{Al}\right] \quad \text{(A-27)}$$

Thermodynamic equilibrium is assessed at the inclusion-steel interface from the equilibrium relationships. In the case of the deoxidation reaction with magnesium is:

$$K_{MgO} = \frac{a_{MgO}\,*}{\left[\frac{X^*_{Mg} f^*_{Mg} \cdot n_T \cdot Mw_{Mg} \cdot 100}{St_{mass}}\right]\left[\frac{X^*_O f^*_O \cdot n_T \cdot Mw_O \cdot 100}{St_{mass}}\right]} \quad \text{(A-28)}$$

Where Mw_{Mg} and Mw_O are the molar weights of Mg and O, n_t is the total number of moles in the steel phase and St_{mass} is the total mass of steel in kilograms. The activity coefficients at the interface f^*_{Mg}, f^*_{Al} and f^*_O are obtained with the Unified Interaction Parameter formalism. Since the inclusions-steel model steps in time with an explicit scheme the values of the activity coefficients are calculated with the interfacial concentrations of the previous time step. Then, the equilibrium relation in equation (A-28) can be formulated as:

$$K_{MgO} = \frac{a_{MgO}\,*}{X^*_{Mg} \cdot X^*_O}\theta \quad \text{(A-29)}$$

Where the coefficient θ is:

$$\theta = \frac{1}{\left[\frac{f_{Mg}^{*} \cdot n_T \cdot Mw_{Mg} \cdot 100}{St_{mass}}\right]\left[\frac{f_O^{*} \cdot n_T \cdot Mw_O \cdot 100}{St_{mass}}\right]} \tag{A-30}$$

For the deoxidation reaction with aluminum the equilibrium relation is:

$$K_{Al_2O_3} = \frac{a_{Al_2O_3}\,*}{\left[\frac{X_{Al}^{*} f_{Al}^{*} \cdot n_T \cdot Mw_{Al} \cdot 100}{St_{mass}}\right]^2 \left[\frac{X_O^{*} f_O^{*} \cdot n_T \cdot Mw_O \cdot 100}{St_{mass}}\right]^3} \tag{A-31}$$

The equilibrium condition in (A-31) is expressed as:

$$K_{Al_2O_3} = \frac{a_{Al_2O_3}\,*}{X_{Al}^{*\,2} \cdot X_O^{*\,3}}\,\varepsilon \tag{A-32}$$

Where the coefficient ε is:

$$\varepsilon = \frac{1}{\left[\frac{f_{Al}^{*} \cdot n_T \cdot Mw_{Al} \cdot 100}{St_{mass}}\right]^2 \left[\frac{f_O^{*} \cdot n_T \cdot Mw_O \cdot 100}{St_{mass}}\right]^3} \tag{A-33}$$

The activities of the oxide components $a_{Al_2O_3}$ and a_{MgO} in the binary system Al_2O_3-MgO are represented using sigmoidal functions. Therefore, the interfacial activity of Al_2O_3 must correspond to the equilibrium composition $X_{Al_2O_3}^{*}$ according to the function:

$$a_{Al_2O_3}\,* \;= a_1 - (a_1 - b_1) \cdot exp\left[-\left(k_1 \cdot X_{Al_2O_3}^{*}\right)^{d_1}\right] \tag{A-34}$$

Where $a_1 = 1$, $b_1 = 0.034$, $k_1 = 1.862$ and $d_1 = 15.131$. In the case of the interfacial activity of MgO the function that must be satisfied is:

$$a_{MgO}\,* = \frac{b_2}{\left[1 + \left(\frac{c_2}{X_{Al_2O_3}^{*}}\right)^{h_2}\right]^{s_2}} \tag{A-35}$$

Where the value of the parameters in function (A-35) are: $b_2 = 1$, $c_2 = 0.462$, $h_2 = -143.245$ and $s_2 = 0.127$.

Equations (A-26), (A-27), (A-29), (A-32), (A-34) and (A-35) constitute a non-linear system of six equations where the unknowns are: X_{Mg}^*, X_{Al}^*, X_O^*, $a_{Al_2O_3}{}^*$, $a_{MgO}{}^*$ and $X_{Al_2O_3}{}^*$.

In order to find a solution for the system of several variables all the equations have to be equated to zero. Therefore, from equation (A-26):

$$F_1 = \frac{D_{Mg}D_{Al}\left(32X_{Al_2O_3}^* - 32X_{Al_2O_3}^{*\,2}\right)}{\left(72D_{Mg}X_{Al_2O_3}^* - 16D_{Mg}X_{Al_2O_3}^* + 16D_{Mg}\right)\left(1 + 2X_{Al_2O_3}^*\right)} \qquad \text{(A-36)}$$

$$\times \frac{1}{V_m^{Sp}}\left(\frac{25}{12h}\right)\left[9\ln a_{MgO}{}^* - 3\ln a_{Al_2O_3}{}^* + \alpha_{Mg}\right]$$

$$+ \frac{1 - X_{Al_2O_3}^*}{1 + 2X_{Al_2O_3}^*} \cdot k_O C_{Vm}(X_O^b - X_O^*)$$

$$- k_{Mg}C_{Vm}\left(X_{Mg}^b - X_{Mg}^*\right)$$

From equation (A-27):

$$F_2 = \frac{D_{Mg}D_{Al}\left(32X_{Al_2O_3}^* - 32X_{Al_2O_3}^{*\,2}\right)}{\left(72D_{Mg}X_{Al_2O_3}^* - 16D_{Mg}X_{Al_2O_3}^* + 16D_{Mg}\right)\left(1 + 2X_{Al_2O_3}^*\right)} \qquad \text{(A-37)}$$

$$\times \frac{1}{V_m^{Sp}}\left(\frac{25}{12h}\right)\left[2\ln a_{Al_2O_3}{}^* - 6\ln a_{MgO}{}^* + \alpha_{Al}\right]$$

$$+ \frac{2X_{Al_2O_3}^*}{1 + 2X_{Al_2O_3}^*} \cdot k_O C_{Vm}(X_O^b - X_O^*)$$

$$-k_{Al}C_{Vm}(X_{Al}^b - X_{Al}^*)$$

From equation (A-29):

$$F_3 = K_{MgO} \cdot X_{Mg}^* \cdot X_O^* - \theta \cdot a_{MgO} * \tag{A-38}$$

From equation (A-32)

$$F_4 = K_{Al_2O_3} \cdot {X_{Al}^*}^2 \cdot {X_O^*}^3 - \varepsilon \cdot a_{Al_2O_3} * \tag{A-39}$$

From equation (A-34)

$$F_5 = a_1 - (a_1 - b_1) \cdot exp\left[-\left(k_1 \cdot X_{Al_2O_3}^*\right)^{d_1}\right] - a_{Al_2O_3} * \tag{A-40}$$

From equation (A-35)

$$F_6 = \frac{b_2}{\left[1 + \left(\frac{c_2}{X_{Al_2O_3}^*}\right)^{h_2}\right]^{s_2}} - a_{MgO} * \tag{A-41}$$

Solving the multivariable system of non-linear equations implies to find the values that make equations F_1, F_2, F_3, F_4, F_5 and F_6 equal to zero simultaneously; in order to accomplish such task, an iterative numerical method is used.

A.2 Numerical method to solve the system of equations

In order to approximate a solution for the system of non-linear equations Newton's Method for several variables is used. The system of six equations **F** as function of the six variables **X** becomes:

$$\mathbf{F}(\boldsymbol{X}) = \begin{bmatrix} F_1(\boldsymbol{X}) \\ F_2(\boldsymbol{X}) \\ F_3(\boldsymbol{X}) \\ F_4(\boldsymbol{X}) \\ F_5(\boldsymbol{X}) \\ F_6(\boldsymbol{X}) \end{bmatrix} \tag{A-42}$$

The vector of variables contains the unknown interfacial activities and concentrations:

$$\mathbf{X} = \begin{bmatrix} X_{Al}^* \\ X_{Mg}^* \\ X_O^* \\ a_{Al_2O_3}{}^* \\ a_{MgO}{}^* \\ X_{Al_2O_3}^* \end{bmatrix} \tag{A-43}$$

Newton's Method approximates $\mathbf{F}(\boldsymbol{X})$ by using a local linearization at each iteration k (Kelley, 1987), therefore the system evaluated at $\boldsymbol{X}^{k+1}$ is:

$$\mathbf{F}(\boldsymbol{X^{k+1}}) = \mathbf{F}(\boldsymbol{X^k}) + \mathbf{F}'(\boldsymbol{X^k})(\boldsymbol{X^{k+1}} - \boldsymbol{X^k}) \tag{A-44}$$

Here, $\mathbf{F}'(\boldsymbol{X^k})$ is the Jacobian matrix of the system:

$$\mathbf{F}'(\boldsymbol{X}) = \begin{bmatrix} \frac{\partial F_1}{\partial X_{Al}^*} & \frac{\partial F_1}{\partial X_{Mg}^*} & \frac{\partial F_1}{\partial X_O^*} & \frac{\partial F_1}{\partial a_{Al_2O_3}{}^*} & \frac{\partial F_1}{\partial a_{MgO}{}^*} & \frac{\partial F_1}{\partial X_{Al_2O_3}^*} \\ \frac{\partial F_2}{\partial X_{Al}^*} & \frac{\partial F_2}{\partial X_{Mg}^*} & \frac{\partial F_2}{\partial X_O^*} & \frac{\partial F_2}{\partial a_{Al_2O_3}{}^*} & \frac{\partial F_2}{\partial a_{MgO}{}^*} & \frac{\partial F_2}{\partial X_{Al_2O_3}^*} \\ \vdots & & & & & \\ \frac{\partial F_6}{\partial X_{Al}^*} & \frac{\partial F_6}{\partial X_{Mg}^*} & \frac{\partial F_6}{\partial X_O^*} & \frac{\partial F_6}{\partial a_{Al_2O_3}{}^*} & \frac{\partial F_6}{\partial a_{MgO}{}^*} & \frac{\partial F_6}{\partial X_{Al_2O_3}^*} \end{bmatrix} \tag{A-45}$$

The elements of the Jacobian matrix for the first row are:

$$\frac{\partial F_1}{\partial X_{Al}^*} = 0 \tag{A-46.1}$$

$$\frac{\partial F_1}{\partial X_{Mg}^*} = k_{Mg} C_{Vm} \tag{A-46.2}$$

$$\frac{\partial F_1}{\partial X_{O}^*} = -\frac{1 - X_{Al_2O_3}^*}{1 + 2X_{Al_2O_3}^*} \cdot k_O C_{Vm} \tag{A-46.3}$$

(A-46.4)

$$\frac{\partial F_1}{\partial a_{Al_2O_3}\,*} = \frac{D_{Mg} D_{Al}\left(32X_{Al_2O_3}^* - 32{X_{Al_2O_3}^*}^2\right)}{\left(72D_{Mg}X_{Al_2O_3}^* - 16D_{Mg}X_{Al_2O_3}^* + 16D_{Mg}\right)\left(1 + 2X_{Al_2O_3}^*\right)} \times \frac{1}{V_m^{Sp}}\left(\frac{25}{12h}\right)\left(\frac{-3}{a_{Al_2O_3}\,*}\right)$$

(A-46.5)

$$\frac{\partial F_1}{\partial a_{MgO}\,*} = \frac{D_{Mg} D_{Al}\left(32X_{Al_2O_3}^* - 32{X_{Al_2O_3}^*}^2\right)}{\left(72D_{Mg}X_{Al_2O_3}^* - 16D_{Mg}X_{Al_2O_3}^* + 16D_{Mg}\right)\left(1 + 2X_{Al_2O_3}^*\right)} \times \frac{1}{V_m^{Sp}}\left(\frac{25}{12h}\right)\left(\frac{9}{a_{MgO}\,*}\right)$$

(A-46.6)

$$\frac{\partial F_1}{\partial X_{Al_2O_3}^*} = \frac{-4D_{Mg} D_{Al}\left({X_{Al_2O_3}^*}^2\left(27D_{Al} - 2D_{Mg}\right) + 4D_{Mg}X_{Al_2O_3}^* - 2D_{Mg}\right)}{\left(1 + 2X_{Al_2O_3}^*\right)^2\left(X_{Al_2O_3}^*\left(9D_{Al} - 2D_{Mg}\right) + 2D_{Mg}\right)^2} \times \frac{1}{V_m^{Sp}}\left(\frac{25}{12h}\right)\left[9\ln {a_{MgO}}^* - 3\ln {a_{Al_2O_3}}^* + \alpha_{Mg}\right] - \frac{3}{\left(1 + 2X_{Al_2O_3}^*\right)^2} \cdot k_O C_{Vm}\left(X_O^b - X_O^*\right)$$

The elements of the Jacobian matrix for the second row are:

$$\frac{\partial F_2}{\partial X_{Al}^*} = k_{Al} C_{Vm} \tag{A-47.1}$$

$$\frac{\partial F_2}{\partial X_{Mg}^*} = 0 \tag{A-47.2}$$

$$\frac{\partial F_2}{\partial X_{O}^*} = -\frac{2X_{Al_2O_3}^*}{1 + 2X_{Al_2O_3}^*} \cdot k_O C_{Vm} \tag{A-47.3}$$

(A-47.4)

$$\frac{\partial F_2}{\partial a_{Al_2O_3}{}^*} = \frac{D_{Mg} D_{Al}\left(32X_{Al_2O_3}^* - 32{X_{Al_2O_3}^*}^2\right)}{\left(72D_{Mg}X_{Al_2O_3}^* - 16D_{Mg}X_{Al_2O_3}^* + 16D_{Mg}\right)\left(1 + 2X_{Al_2O_3}^*\right)} \times \frac{1}{V_m^{Sp}}\left(\frac{25}{12h}\right)\left(\frac{2}{a_{Al_2O_3}{}^*}\right)$$

(A-47.5)

$$\frac{\partial F_2}{\partial a_{MgO}{}^*} = \frac{D_{Mg} D_{Al}\left(32X_{Al_2O_3}^* - 32{X_{Al_2O_3}^*}^2\right)}{\left(72D_{Mg}X_{Al_2O_3}^* - 16D_{Mg}X_{Al_2O_3}^* + 16D_{Mg}\right)\left(1 + 2X_{Al_2O_3}^*\right)} \times \frac{1}{V_m^{Sp}}\left(\frac{25}{12h}\right)\left(\frac{-6}{a_{MgO}{}^*}\right)$$

(A-47.6)

$$\frac{\partial F_2}{\partial X_{Al_2O_3}^*} = \frac{-4D_{Mg} D_{Al}\left({X_{Al_2O_3}^*}^2\left(27D_{Al} - 2D_{Mg}\right) + 4D_{Mg}X_{Al_2O_3}^* - 2D_{Mg}\right)}{\left(1 + 2X_{Al_2O_3}^*\right)^2\left(X_{Al_2O_3}^*\left(9D_{Al} - 2D_{Mg}\right) + 2D_{Mg}\right)^2} \times \frac{1}{V_m^{Sp}}\left(\frac{25}{12h}\right)\left[2\ln a_{Al_2O_3}{}^* - 6\ln a_{MgO}{}^* + \alpha_{Al}\right] + \frac{2X_{Al_2O_3}^*}{1 + 2X_{Al_2O_3}^*} \cdot k_O C_{Vm}\left(X_O^b - X_O^*\right)$$

The elements of the Jacobian matrix for the third row are:

$$\frac{\partial F_3}{\partial X_{Al}^*} = 0 \tag{A-48.1}$$

$$\frac{\partial F_3}{\partial X_{Mg}^*} = K_{MgO} \cdot X_O^* \tag{A-48.2}$$

$$\frac{\partial F_3}{\partial X_O^*} = K_{MgO} \cdot X_{Mg}^* \tag{A-48.3}$$

$$\frac{\partial F_3}{\partial a_{Al_2O_3}\,*} = 0 \tag{A-48.4}$$

$$\frac{\partial F_3}{\partial a_{MgO}\,*} = -\theta \tag{A-48.5}$$

$$\frac{\partial F_3}{\partial X_{Al_2O_3}^*} = 0 \tag{A-48.6}$$

The elements of the Jacobian matrix for the fourth row are:

$$\frac{\partial F_4}{\partial X_{Al}^*} = 2K_{Al_2O_3} \cdot X_{Al}^* \cdot {X_O^*}^3 \tag{A-49.1}$$

$$\frac{\partial F_4}{\partial X_{Mg}^*} = 0 \tag{A-49.2}$$

$$\frac{\partial F_4}{\partial X_O^*} = 3K_{Al_2O_3} \cdot {X_{Al}^*}^2 \cdot {X_O^*}^2 \tag{A-49.3}$$

$$\frac{\partial F_4}{\partial a_{Al_2O_3}\,*} = -\varepsilon \tag{A-49.4}$$

$$\frac{\partial F_4}{\partial a_{MgO}\,*} = 0 \tag{A-49.5}$$

$$\frac{\partial F_4}{\partial X_{Al_2O_3}^*} = 0 \tag{A-49.6}$$

The elements of the Jacobian matrix for the fifth row are:

$$\frac{\partial F_5}{\partial X_{Al}^*} = 0 \tag{A-50.1}$$

$$\frac{\partial F_5}{\partial X_{Mg}^*} = 0 \tag{A-50.2}$$

$$\frac{\partial F_5}{\partial X_{O}^*} = 0 \tag{A-50.3}$$

$$\frac{\partial F_5}{\partial a_{Al_2O_3}\,*} = -1 \tag{A-50.4}$$

$$\frac{\partial F_5}{\partial a_{MgO}\,*} = 0 \tag{A-50.5}$$

(A-50.6)

$$\frac{\partial F_5}{\partial X_{Al_2O_3}^*} = (a_1 - b_1)\left[k_1 \cdot d_1\left(k_1 \cdot X_{Al_2O_3}^*\right)^{(d_1-1)}\right] \cdot exp\left[-\left(k_1 \cdot X_{Al_2O_3}^*\right)^{d_1}\right]$$

The elements of the Jacobian matrix for the sixth row are:

$$\frac{\partial F_6}{\partial X_{Al}^*} = 0 \tag{A-51.1}$$

$$\frac{\partial F_6}{\partial X_{Mg}^*} = 0 \tag{A-51.2}$$

$$\frac{\partial F_6}{\partial X_{O}^*} = 0 \tag{A-51.3}$$

$$\frac{\partial F_6}{\partial a_{Al_2O_3}\,*} = 0 \tag{A-51.4}$$

$$\frac{\partial F_6}{\partial a_{MgO}\,*} = -1 \tag{A-51.5}$$

(A-51.6)

$$\frac{\partial F_6}{\partial X^*_{Al_2O_3}} = s_2 h_2 c_2 \cdot \left(\frac{1}{{X^*_{Al_2O_3}}^2}\right) \cdot \frac{b_2}{\left[1+\left(\frac{c_2}{X^*_{Al_2O_3}}\right)^{h_2}\right]^{s_2}} \cdot \left(\frac{c_2}{X^*_{Al_2O_3}}\right)^{h_2-1}$$

By making $\mathbf{F}(\boldsymbol{X^{k+1}}) = \mathbf{0}$ in equation (A-41) the iteration procedure of Newton's Method becomes:

$$\boldsymbol{X^{k+1}} = \boldsymbol{X^k} + \Delta \boldsymbol{X^k} \tag{A-52}$$

Where $\Delta \boldsymbol{X^k}$ is the complete iteration step calculated according to:

$$\Delta \boldsymbol{X^k} = -[\mathbf{F}'(\boldsymbol{X^k})]^{-1}\mathbf{F}(\boldsymbol{X^k}) \tag{A-53}$$

When non-linear systems are solved it is important to insure that the functions and the elements of the Jacobian matrix are not evaluated at discontinuities during the iterations. Shacham (1986) proposed a strategy to prevent this to happen by considering the 'absolute constraints' of the system, where the absolute constraints refers to cases when the functions $f(x_i)$ are undefined for $x_i = 0$ or for $x_i < 0$ such as in $1/x_i$, $\ln(x_i)$ and others. The method of Shacham (1986) involves to use a damping scalar parameter λ^k to restrict the length of the complete iteration step according to:

$$\boldsymbol{X^{k+1}} = \boldsymbol{X^k} + \lambda^k \Delta \boldsymbol{X^k} \tag{A-54}$$

Considering that each variable is updated with:

$$x_i^{k+1} = x_i^k + \Delta x_i \tag{A-55}$$

The scalar step length λ^k is defined as:

$$\lambda^{\boldsymbol{k}} = \min_j \left| \frac{\alpha \cdot x_j}{\Delta x_j} \right| \tag{A-56}$$

Where α=0.99 and j represents the index of all the variables for which absolute constraints must to be preserved. In the solution of the Inclusion-Steel interface these cautions are taken for $a_{Al_2O_3}$*, a_{MgO}* and $X_{Al_2O_3}$* since during the iterations these variables cannot be less or equal to zero.

The algorithm to calculate the next iteration step with restricted length is then (Shacham, 1986):

1. Solve the linear approximation (A-53) for the complete iteration step $\Delta \boldsymbol{X}^{\boldsymbol{k}}$.
2. Calculate λ^k with equation (A-56).
3. Compute the next iterate with expression (A-54).

The convergence criteria of the method is based on the considerations of Shacham (1986). In this way, each element of the vector of errors $\mathbf{E^k}$ is calculated as the relative difference between two iterations:

$$E_i^k = \frac{\left| x_i^{k+1} - x_i^k \right|}{\left| x_i^{k+1} \right|} \tag{A-57}$$

If one of the elements of the vector of variables $\mathbf{X}$ is zero, then the relative error is calculated with:

$$E_i^k = \left| x_i^{k+1} - x_i^k \right| \tag{A-58}$$

The iteration stops when the calculated norms of the vector of functions and errors satisfy $\left\| \mathbf{F}(\boldsymbol{X}^{\boldsymbol{k}}) \right\| \leq tol_1$ and $\left\| \mathbf{E^k} \right\| \leq tol_2$ simultaneously.

Appendix B

Numerical solution of the PDE model for cationic diffusion

The model for diffusion of Mg^{2+} in the spinel product layer assuming that the driving force is the gradient in the chemical potential of Mg with constant diffusivity D_{Mg} is mathematically expressed as:

$$\frac{\partial C_{Mg^{2+}}}{\partial t} = \frac{D_{Mg}}{RT}\left[\frac{2}{r}C_{Mg}\left(\frac{\partial \mu_{Mg}}{\partial r}\right) + \left(\frac{\partial C_{Mg}}{\partial r}\right)\left(\frac{\partial \mu_{Mg}}{\partial r}\right) + C_{Mg}\left(\frac{\partial^2 \mu_{Mg}}{\partial r^2}\right)\right] \qquad \text{(B-1)}$$

$$r' \leq r \leq r^*$$

The diffusion equation (B-1) is constrained by the interfacial boundary conditions at r*, the equilibrium concentration at r' and the non-linear variation of the chemical potential with concentration in magnesium aluminate spinel. This time-dependent non-linear partial differential equation is solved numerically using the method of lines approach in which the first step is the spatial discretization of the equation and the second step is the time integration of the system obtained.

B.1 Spatial discretization of the diffusion equation

Once the thickness and spatial domain in which equation (B-1) applies is defined the location of the discretizing equidistant nodes $U_i = U(r_i)$ is calculated with:

$$h = \frac{r^* - r'}{n-1} \tag{B-2}$$

$$r_i = r' + (i-1)h \qquad i = 1, \dots, n \tag{B-3}$$

Here n is the total number of nodes and h is the distance between each node, r^* is the radius of the inclusion at the interface with steel and r' is the radius at the inner boundary where the product layer is in equilibrium with the alumina unreacted core. In this way the molar Mg concentration in the product layer is modeled at each node i and a time step q as:

$$C_{Mg}(i,q) = U\left(r_i,\ t_q\right) \tag{B-4}$$

The purpose of the spatial discretization is to calculate the terms in the PDE model $\left.\frac{\partial \mu_{Mg}}{\partial r}\right|_{i,t}$, $\left.\frac{\partial^2 \mu_{Mg}}{\partial r^2}\right|_{i,t}$ and $\left.\frac{\partial C_{Mg}}{\partial r}\right|_{i,t}$ at each node for a given time step. Once the molar Mg concentration C_{Mg} at each node is known the respective mole fraction concentration $X_{Al_2O_3}$ in the Al_2O_3-MgO quasi-binary system is:

$$X_{Al_2O_3} = \frac{4 - V_m^{Sp} \cdot C_{Mg}}{4 + 2V_m^{Sp} \cdot C_{Mg}} \tag{B-5}$$

Here V_m^{Sp}, the molar volume of spinel, is assumed constant. Subsequently, with the mole fraction $X_{Al_2O_3}$ and molar concentration C_{Mg}, the respective stoichiometric indices of spinel $Mg_\delta Al_\upsilon O_4$ are calculated:

$$\delta = C_{Mg} \cdot V_m^{Sp} \tag{B-6}$$

$$\upsilon = \frac{8X_{Al_2O_3}}{1 + 2X_{Al_2O_3}} \tag{B-7}$$

The mole concentration of Al^{3+} is:

$$C_{Al} = \frac{\upsilon}{V_m^{Sp}} \tag{B-8}$$

Furthermore the activities of the components Al_2O_3 and MgO is calculated at each node using the sigmoidal functions that were obtained by fitting the reported activities of Fujii, et al., (2000) at 1873 K:

$$a_{Al_2O_3} = a_1 - (a_1 - b_1) \cdot exp\left[-\left(k_1 \cdot X_{Al_2O_3}\right)^{d_1}\right] \tag{B-9}$$

$$a_{MgO} = \frac{b_2}{\left[1 + \left(\frac{c_2}{X_{Al_2O_3}}\right)^{h_2}\right]^{s_2}} \tag{B-10}$$

Where the parameters of the functions are: are: a_1 = 1, b_1 = 0.034, k_1 = 1.862, d_1 = 15.131, b_2 = 1, c_2 = 0.462, h_2 = -143.245 and s_2 = 0.127. Therefore, for a given time step the values of $X_{Al_2O_3}$, δ, υ, C_{Mg}, C_{Al}, a_{MgO} and $a_{Al_2O_3}$ are known at each node.

From the definition of chemical potential and the formation reaction of MgO, the variation in the chemical potential $\frac{\partial \mu_{Mg}}{\partial r}$ at each node i is:

$$\left(\frac{\partial \mu_{Mg}}{\partial r}\right)_i = RT\left(\frac{\partial \ln a_{MgO}}{\partial r}\right)_i - \left(\frac{\partial \mu_O}{\partial r}\right)_i \tag{B-11}$$

Therefore:

$$\left(\frac{\partial^2 \mu_{Mg}}{\partial r^2}\right)_i = RT\left(\frac{\partial^2 \ln a_{MgO}}{\partial r^2}\right)_i - \left(\frac{\partial^2 \mu_O}{\partial r^2}\right)_i \tag{B-12}$$

The variation in the chemical potential of oxygen is calculated by coupling the mass transfer rates of Mg^{2+} and Al^{3+} to maintain electroneoutrality in spinel; this method was suggested by Schmalzried and Pfeiffer (1986), from that analysis:

$$\left(\frac{\partial \mu_O}{\partial r}\right)_i = RT \frac{\delta_i \cdot D_{Mg}\left(\frac{\partial \ln a_{MgO}}{\partial r}\right)_i + \frac{3}{4} v_i \cdot D_{Al}\left(\frac{\partial \ln a_{Al_2O_3}}{\partial r}\right)_i}{\delta_i \cdot D_{Mg} + \frac{9}{4} v_i \cdot D_{Al}} \tag{B-13}$$

Equation (B-13) is equivalent to:

$$\left(\frac{\partial \mu_O}{\partial r}\right)_i = RT \frac{C_{Mg_i} \cdot D_{Mg}\left(\frac{\partial \ln a_{MgO}}{\partial r}\right)_i + \frac{3}{4} C_{Al_i} \cdot D_{Al}\left(\frac{\partial \ln a_{Al_2O_3}}{\partial r}\right)_i}{C_{Mg_i} \cdot D_{Mg} + \frac{9}{4} C_{Al_i} \cdot D_{Al}} \tag{B-14}$$

The second derivative for the chemical potential of oxygen from (B-14) is:

$$\begin{aligned}
&\left(\frac{\partial^2 \mu_O}{\partial r^2}\right)_i \\
&= RT \left\{ \left[C_{Mg_i} D_{Mg} + \frac{9}{4} C_{Al_i} D_{Al}\right] \right. \\
&\cdot \left[C_{Mg_i} D_{Mg}\left(\frac{\partial^2 \ln a_{MgO}}{\partial r^2}\right)_i + D_{Mg}\left(\frac{\partial C_{Mg}}{\partial r}\right)_i \left(\frac{\partial \ln a_{MgO}}{\partial r}\right)_i + \frac{3}{4} C_{Al_i} D_{Al}\left(\frac{\partial^2 \ln a_{Al_2O_3}}{\partial r^2}\right)_i \right. \\
&\left. + \frac{3}{4} D_{Al}\left(\frac{\partial C_{Al}}{\partial r}\right)_i \left(\frac{\partial \ln a_{Al_2O_3}}{\partial r}\right)_i \right] - \left[C_{Mg_i} D_{Mg}\left(\frac{\partial \ln a_{MgO}}{\partial r}\right)_i + \frac{3}{4} C_{Al_i} D_{Al}\left(\frac{\partial \ln a_{Al_2O_3}}{\partial r}\right)_i \right] \\
&\left. \cdot \left[D_{Mg}\left(\frac{\partial C_{Mg}}{\partial r}\right)_i + \frac{9}{4} D_{Al}\left(\frac{\partial C_{Al}}{\partial r}\right)_i \right] \right\} \times \left(\frac{1}{C_{Mg_i} D_{Mg} + \frac{9}{4} C_{Al_i} D_{Al}}\right)^2
\end{aligned} \tag{B-15}$$

The different derivatives required for (B-11), (B-12), (B-14) and (B-15) are calculated for each node based on the chain rule, therefore:

$$\left(\frac{\partial \ln a_{MgO}}{\partial r}\right) = \left(\frac{1}{a_{MgO}}\right)\left(\frac{\partial a_{MgO}}{\partial X_{Al_2O_3}}\right)\left(\frac{\partial X_{Al_2O_3}}{\partial C_{Mg}}\right)\left(\frac{\partial C_{Mg}}{\partial r}\right) \tag{B-16}$$

$$\left(\frac{\partial \ln a_{Al_2O_3}}{\partial r}\right) = \left(\frac{1}{a_{Al_2O_3}}\right)\left(\frac{\partial a_{Al_2O_3}}{\partial X_{Al_2O_3}}\right)\left(\frac{\partial X_{Al_2O_3}}{\partial C_{Mg}}\right)\left(\frac{\partial C_{Mg}}{\partial r}\right) \tag{B-17}$$

$$\begin{aligned}\left(\frac{\partial^2 \ln a_{MgO}}{\partial r^2}\right) = {} & \left(\frac{-1}{{a_{MgO}}^2}\right)\left(\frac{\partial a_{MgO}}{\partial X_{Al_2O_3}}\right)^2\left(\frac{\partial X_{Al_2O_3}}{\partial C_{Mg}}\right)^2\left(\frac{\partial C_{Mg}}{\partial r}\right)^2 \\ & + \left(\frac{1}{a_{MgO}}\right)\left(\frac{\partial^2 a_{MgO}}{\partial {X_{Al_2O_3}}^2}\right)\left(\frac{\partial X_{Al_2O_3}}{\partial C_{Mg}}\right)^2\left(\frac{\partial C_{Mg}}{\partial r}\right)^2 \\ & + \left(\frac{1}{a_{MgO}}\right)\left(\frac{\partial a_{MgO}}{\partial X_{Al_2O_3}}\right)\left(\frac{\partial^2 X_{Al_2O_3}}{\partial {C_{Mg}}^2}\right)\left(\frac{\partial C_{Mg}}{\partial r}\right)^2 \\ & + \left(\frac{1}{a_{MgO}}\right)\left(\frac{\partial a_{MgO}}{\partial X_{Al_2O_3}}\right)\left(\frac{\partial X_{Al_2O_3}}{\partial C_{Mg}}\right)\left(\frac{\partial^2 C_{Mg}}{\partial r^2}\right)\end{aligned} \tag{B-18}$$

$$\begin{aligned}\left(\frac{\partial^2 \ln a_{Al_2O_3}}{\partial r^2}\right) = {} & \left(\frac{-1}{{a_{Al_2O_3}}^2}\right)\left(\frac{\partial a_{Al_2O_3}}{\partial X_{Al_2O_3}}\right)^2\left(\frac{\partial X_{Al_2O_3}}{\partial C_{Mg}}\right)^2\left(\frac{\partial C_{Mg}}{\partial r}\right)^2 \\ & + \left(\frac{1}{a_{Al_2O_3}}\right)\left(\frac{\partial^2 a_{Al_2O_3}}{\partial {X_{Al_2O_3}}^2}\right)\left(\frac{\partial X_{Al_2O_3}}{\partial C_{Mg}}\right)^2\left(\frac{\partial C_{Mg}}{\partial r}\right)^2 \\ & + \left(\frac{1}{a_{Al_2O_3}}\right)\left(\frac{\partial a_{Al_2O_3}}{\partial X_{Al_2O_3}}\right)\left(\frac{\partial^2 X_{Al_2O_3}}{\partial {C_{Mg}}^2}\right)\left(\frac{\partial C_{Mg}}{\partial r}\right)^2 \\ & + \left(\frac{1}{a_{Al_2O_3}}\right)\left(\frac{\partial a_{Al_2O_3}}{\partial X_{Al_2O_3}}\right)\left(\frac{\partial X_{Al_2O_3}}{\partial C_{Mg}}\right)\left(\frac{\partial^2 C_{Mg}}{\partial r^2}\right)\end{aligned} \tag{B-19}$$

For expressions (B-16), (B-17), (B-18) and (B-19) the following derivatives are calculated analytically according to:

(B-20)

$$\frac{\partial a_{MgO}}{\partial X_{Al_2O_3}} = s_2 h_2 c_2 \cdot \left(\frac{1}{X_{Al_2O_3}{}^2}\right) \cdot \left[\frac{b_2}{\left[1+\left(\frac{c_2}{X_{Al_2O_3}}\right)^{h_2}\right]^{s_2}}\right] \cdot \left(\frac{c_2}{X_{Al_2O_3}}\right)^{h_2-1}$$

(B-21)

$$\frac{\partial^2 a_{MgO}}{\partial X_{Al_2O_3}{}^2} = s_2 h_2 c_2 \times \left\{ \left(\frac{-2}{X_{Al_2O_3}{}^3}\right) \cdot \left[\frac{b_2}{\left[1+\left(\frac{c_2}{X_{Al_2O_3}}\right)^{h_2}\right]^{(s_2+1)}}\right] \cdot \left(\frac{c_2}{X_{Al_2O_3}}\right)^{(h_2+1)} + C_2 b_2 h_2 \cdot (s_2+1) \right.$$

$$\cdot \left(\frac{1}{X_{Al_2O_3}{}^4}\right) \cdot \left(\frac{c_2}{X_{Al_2O_3}}\right)^{(2h_2-2)} \cdot \left[\frac{1}{\left[1+\left(\frac{c_2}{X_{Al_2O_3}}\right)^{h_2}\right]^{s_2}}\right] + \left(\frac{-1}{X_{Al_2O_3}{}^4}\right) \cdot c_2$$

$$\left. \cdot (h_2-1) \cdot \left(\frac{c_2}{X_{Al_2O_3}}\right)^{(h_2-2)} \cdot \left[\frac{b_2}{\left[1+\left(\frac{c_2}{X_{Al_2O_3}}\right)^{h_2}\right]^{(s_2+1)}}\right] \right\}$$

(B-22)

$$\frac{\partial a_{Al_2O_3}}{\partial X_{Al_2O_3}} = (a_1 - b_1)\left[k_1 \cdot d_1\left(k_1 \cdot X_{Al_2O_3}\right)^{(d_1-1)}\right] \cdot exp\left[-\left(k_1 \cdot X_{Al_2O_3}\right)^{d_1}\right]$$

$$\frac{\partial^2 a_{Al_2O_3}}{\partial {X_{Al_2O_3}}^2} = (a_1 - b_1) \cdot \left({k_1}^{d_1}\right) \cdot d_1 \times \left\{\left(\left(X_{Al_2O_3}\right)^{(d_1-1)}\right) \cdot \left(-d_1 k_1 \left(k_1 \cdot X_{Al_2O_3}\right)^{(d_1-1)}\right) \cdot exp\left[-\left(k_1 \cdot X_{Al_2O_3}\right)^{d_1}\right] + (d_1 - 1) \cdot \left(X_{Al_2O_3}\right)^{(d_1-2)} \cdot exp\left[-\left(k_1 \cdot X_{Al_2O_3}\right)^{d_1}\right]\right\} \tag{B-23}$$

$$\frac{\partial X_{Al_2O_3}}{\partial C_{Mg}} = \frac{-12\, V_m^{Sp}}{\left(4 + 2V_m^{Sp} \cdot C_{Mg}\right)^2} \tag{B-24}$$

$$\frac{\partial^2 X_{Al_2O_3}}{\partial {C_{Mg}}^2} = \frac{48\, V_m^{Sp}}{\left(4 + 2V_m^{Sp} \cdot C_{Mg}\right)^3} \tag{B-25}$$

For the calculation of $\left(\frac{\partial C_{Mg}}{\partial r}\right)_i$, $\left(\frac{\partial C_{Al}}{\partial r}\right)_i$, and $\left(\frac{\partial^2 C_{Mg}}{\partial r^2}\right)_i$ fourth order finite differences approximations are used considering that the values of C_{Mg} and C_{Mg} are known at each equidistant node. The respective formulas for the first derivative are (Betts, 2009):

$$\left.\frac{\partial U}{\partial r}\right|_1 = \frac{1}{12h}[-25U_1 + 48U_2 - 36U_3 + 16U_4 - 3U_5] \tag{B-26.1}$$

$$\left.\frac{\partial U}{\partial r}\right|_2 = \frac{1}{12h}[-3U_1 - 10U_2 + 18U_3 - 6U_4 + U_5] \tag{B-26.2}$$

$$\left.\frac{\partial U}{\partial r}\right|_i = \frac{1}{12h}[-U_{i+2} + 8U_{i+1} - 8U_{i-1} + U_{i-2}] \qquad i = 3, \dots, (n-2) \tag{B-26.3}$$

$$\left.\frac{\partial U}{\partial r}\right|_{n-1} = \frac{1}{12h}[-U_{n-4} + 6U_{n-3} - 18U_{n-2} + 10U_{n-1} + 3U_n] \quad \text{(B-26.4)}$$

$$\left.\frac{\partial U}{\partial r}\right|_{n} = \frac{1}{12h}[+3U_{n-4} - 16U_{n-3} + 36U_{n-2} - 48U_{n-1} + 25U_n] \quad \text{(B-26.5)}$$

The formulas for the second derivative at each node are:

$$\left.\frac{\partial^2 U}{\partial r^2}\right|_{1} = \frac{1}{12h^2}[45U_1 - 154U_2 + 214U_3 - 156U_4 + 61U_5 - 10U_6] \quad \text{(B-27.1)}$$

$$\left.\frac{\partial^2 U}{\partial r^2}\right|_{2} = \frac{1}{12h^2}[10U_1 - 15U_2 - 4U_3 + 14U_4 - 6U_5 + U_6] \quad \text{(B-27.2)}$$

$$\left.\frac{\partial^2 U}{\partial r^2}\right|_{i} = \frac{1}{12h^2}[-U_{i-2} + 16U_{i-1} - 30U_i + 16U_{i+1} - U_{i+2}] \quad \text{(B-27.3)}$$

$$i = 3, \dots, (n-2)$$

$$\left.\frac{\partial^2 U}{\partial r^2}\right|_{n-1} = \frac{1}{12h^2}[U_{n-5} - 6U_{n-4} + 14U_{n-3} - 4U_{n-2} - 15U_{n-1} + 10U_n] \quad \text{(B-27.4)}$$

$$\left.\frac{\partial^2 U}{\partial r^2}\right|_{n} = \frac{1}{12h^2}[-10U_{n-5} + 61U_{n-4} - 156U_{n-3} + 214U_{n-2} - 154U_{n-1} + 45U_n] \quad \text{(B-27.5)}$$

Once the different terms necessary to calculate the variation in chemical potential of Mg are calculated according to (B-11) and (B-12) the spatial discretization at a time step is complete.

B.2 Boundary conditions of the PDE model

The two interfacial boundary conditions at the position r^* express the interaction of the diffusion process in the product layer with the changes of [Mg], [Al] and [O] in the steel phase. The boundary conditions are:

$$\left.\frac{\partial C_{Mg^{2+}}}{\partial r}\right|_{r^*,\ t} = \left(\frac{\partial C_{Mg^{2+}}}{\partial r}\right)^* \tag{B-28}$$

$$C_{Mg^{2+}}(r^*, t) = C_{Mg^{2+}}^{equilib} \tag{B-29}$$

B.2.1 Calculation of the interfacial boundary conditions values

The numerical values for both conditions are calculated at each time step. From the calculation of the coupled deoxidation equilibria the activities and concentrations obtained for the interface between the product layer and steel are: X_{Mg}^*, X_{Al}^*, X_O^*, $a_{Al_2O_3}$*, a_{MgO}* and $X_{Al_2O_3}$* . In this way the value of $C_{Mg^{2+}}^{equilib}$ in (B-29) is obtained from the knowledge of $X_{Al_2O_3}$*. On the other hand, the different interfacial mass transfer rates and fluxes are easily calculated once the equilibrium activities are known, this allows to obtain the value of $\left(\frac{\partial C_{Mg^{2+}}}{\partial r}\right)^*$. With the definition of chemical potential and based on the formation reaction of MgO the following relation holds at the interface of spinel with steel:

$$\left(\frac{\partial \mu_{Mg}}{\partial r}\right)^* = RT\left(\frac{\partial \ln a_{MgO}}{\partial r}\right)^* - \left(\frac{\partial \mu_O}{\partial r}\right)^* \tag{B-30}$$

From the Wagner-Schmalzried theory for spinel formation it has been previously demonstrated that the flux of Mg^{2+} at the spinel-steel interface r^* is defined as:

$$J_{Mg^{2+}}\big|_{r^*} = \frac{D_{Mg} C_{Mg}{}^*}{RT}\left(\frac{\partial \mu_{Mg}}{\partial r}\right)^* \tag{B-31}$$

In the analysis for the numerical solution of the deoxidation equilibria and interface mass balance the flux $J_{Mg^{2+}}\big|_{r^*}$ in the product layer is expressed as:

$$J_{Mg^{2+}}\big|_{r*} = \frac{D_{Mg} D_{Al}\left(32 X^*_{Al_2O_3} - 32 X^*_{Al_2O_3}{}^2\right)}{\left(72 D_{Mg} X^*_{Al_2O_3} - 16 D_{Mg} X^*_{Al_2O_3} + 16 D_{Mg}\right)\left(1 + 2X^*_{Al_2O_3}\right)} \times \frac{1}{V_m^{Sp}}\left(\frac{25}{12h}\right)\left[9 \ln a_{MgO}{}^* - 3 \ln a_{Al_2O_3}{}^* + \alpha_{Mg}\right] \tag{B-32}$$

The term α_{Mg} contains information of the nodes adjacent to the interface and is defined in Appendix A. Therefore, the variation in the chemical potential at the interface is obtained from (B-31) and (B-32) with:

$$\left(\frac{\partial \mu_{Mg}}{\partial r}\right)^* = \frac{J_{Mg^{2+}}\big|_{r*} \times RT}{D_{Mg} \cdot C_{Mg}{}^*} \tag{B-33}$$

Also from the coupling of the mass transfer rates for Mg^{2+} and Al^{3+}, the variation in the chemical potential of oxygen at r^* is:

$$\left(\frac{\partial \mu_O}{\partial r}\right)^* = RT \frac{C_{Mg}{}^* D_{Mg}\left(\frac{\partial \ln a_{MgO}}{\partial r}\right)^* + \frac{3}{4} C_{Al}{}^* D_{Al}\left(\frac{\partial \ln a_{Al_2O_3}}{\partial r}\right)^*}{C_{Mg}{}^* D_{Mg} + \frac{9}{4} C_{Al}{}^* D_{Al}} \tag{B-34}$$

The variation in the component activities is obtained from the chain rule:

$$\left(\frac{\partial \ln a_{MgO}}{\partial r}\right)^* = \left(\frac{1}{a_{MgO}{}^*}\right)\left(\frac{\partial a_{MgO}}{\partial X_{Al_2O_3}}\right)^*\left(\frac{\partial X_{Al_2O_3}}{\partial C_{Mg}}\right)^*\left(\frac{\partial C_{Mg}}{\partial r}\right)^* \tag{B-35}$$

$$\left(\frac{\partial \ln a_{Al_2O_3}}{\partial r}\right)^* = \left(\frac{1}{a_{Al_2O_3}{}^*}\right)\left(\frac{\partial a_{Al_2O_3}}{\partial X_{Al_2O_3}}\right)^*\left(\frac{\partial X_{Al_2O_3}}{\partial C_{Mg}}\right)^*\left(\frac{\partial C_{Mg}}{\partial r}\right)^* \tag{B-36}$$

To obtain $\left(\frac{\partial a_{MgO}}{\partial X_{Al_2O_3}}\right)^*$ and $\left(\frac{\partial a_{Al_2O_3}}{\partial X_{Al_2O_3}}\right)^*$ the respective analytical derivatives as a function of $X_{Al_2O_3}{}^*$ are used, while for $\left(\frac{\partial X_{Al_2O_3}}{\partial C_{Mg}}\right)^*$ the derivative is:

$$\left(\frac{\partial X_{Al_2O_3}}{\partial C_{Mg}}\right)^* = \frac{-12 \cdot V_m^{Sp}}{\left(4 + 2C_{Mg}{}^* \cdot V_m^{Sp}\right)^2} \tag{B-37}$$

From expression (B-30) and considering (B-34), (B-35) and (B-36) the variation in chemical of Mg at the interface becomes:

(B-38)

$$\left(\frac{\partial \mu_{Mg}}{\partial r}\right)^* = RT \cdot F_{MgO}\left(\frac{\partial C_{Mg}}{\partial r}\right)^* - RT\left[B_{MgO}\left(\frac{\partial C_{Mg}}{\partial r}\right)^* + B_{Al_2O_3}\left(\frac{\partial C_{Mg}}{\partial r}\right)^*\right]$$

The coefficients in expression (B-38) are:

$$F_{MgO} = \left(\frac{1}{a_{MgO}{}^*}\right)\left(\frac{\partial a_{MgO}}{\partial X_{Al_2O_3}}\right)^*\left(\frac{\partial X_{Al_2O_3}}{\partial C_{Mg}}\right)^* \tag{B-39}$$

$$B_{MgO} = \frac{C_{Mg}{}^* D_{Mg}\left(\frac{1}{a_{MgO}{}^*}\right)\left(\frac{\partial a_{MgO}}{\partial X_{Al_2O_3}}\right)^*\left(\frac{\partial X_{Al_2O_3}}{\partial C_{Mg}}\right)^*}{C_{Mg}{}^* D_{Mg} + \frac{9}{4}C_{Al}{}^* D_{Al}} \tag{B-40}$$

$$B_{Al_2O_3} = \frac{\frac{3}{4} {C_{Al}}^* \, D_{Al} \left(\frac{1}{{a_{Al_2O_3}}^*}\right) \left(\frac{\partial a_{Al_2O_3}}{\partial X_{Al_2O_3}}\right)^* \left(\frac{\partial X_{Al_2O_3}}{\partial C_{Mg}}\right)^*}{{C_{Mg}}^* \, D_{Mg} + \frac{9}{4} {C_{Al}}^* \, D_{Al}} \tag{B-41}$$

Finally, with the value of $\left(\frac{\partial \mu_{Mg}}{\partial r}\right)^*$ from (B-33), the interfacial gradient of the molar concentration is:

$$\left(\frac{\partial C_{Mg}}{\partial r}\right)^* = \frac{\left(\frac{\partial \mu_{Mg}}{\partial r}\right)^*}{RT\left[F_{MgO} - B_{MgO} - B_{Al_2O_3}\right]} \tag{B-42}$$

B.2.2 Enforcement of the interfacial boundary conditions in the discretization

The spatial approximation of the boundary conditions is made by using fictitious nodes. These nodes are outside the spatial domain and are used to enforce the boundary conditions (Silebi & Schiesser, 1992). For the PDE model (B-1) the spatial discretization uses fourth order finite difference formulas (B-26) and (B-27) to approximate the first and second derivatives at each node. For the nodes U_i where $i = 3, \ldots, (n-2)$ central differences formulas are applied. However, for U_{n-1} and the node at the interface with steel U_n the central differences formulas require two additional nodes, these fictitious nodes are U_{n+1} and U_{n+2} .

If the initial concentration C_{Mg} of the system is known at every node then the second order central difference formula for the first derivative at U_n becomes:

$$\left(\frac{\partial C_{Mg}}{\partial r}\right)^* = \left.\frac{\partial U}{\partial r}\right|_n = \frac{1}{2h}[U_{n+1} - U_{n-1}] \tag{B-43}$$

The fictituous node U_{n+1} is then:

$$U_{n+1} = 2h \cdot \left(\frac{\partial C_{Mg}}{\partial r}\right)^{*} + U_{n-1} \tag{B-44}$$

Similarly, the fourth order approximation for the first derivative using central differences must satisfy the boundary condition at the interface:

$$\left(\frac{\partial C_{Mg}}{\partial r}\right)^{*} = \left.\frac{\partial U}{\partial r}\right|_{n} = \frac{1}{12h}[-U_{n+2} + 8U_{n+1} - 8U_{n-1} + U_{n-2}] \tag{B-45}$$

Therefore the fictituous node U_{n+2} is:

$$U_{n+2} = -12h \cdot \left(\frac{\partial C_{Mg}}{\partial r}\right)^{*} + 8U_{n+1} - 8U_{n-1} + U_{n-2} \tag{B-46}$$

The fictituous nodes assure that boundary condition (B-28) holds at the interface and allow to use central differences formulas at the node U_{n-1} .

To impose boundary condition (B-29) the equilibrium concentration $C_{Mg^{2+}}^{equilib}$ is assigned to the interfacial node U_n and that value is kept constant only during the integration of the respective time step.

B.3 Time integration of the diffusion equation

B.3.1 Implementation of the explicit Runge-Kutta method DOP853

For the time integration of the PDE equation, all the nodes except the ones at the boundaries U_1 and U_n are integrated from time t_q to t_{q+1}. In order to do so, the PDE is evaluated at a number of intermediate stages necessary for the explicit Runge-Kutta method of Prince & Dormand DOP853 described in (Hairer, Nørsett, & Wanner, 2011) and (Hairer & Wanner, 2002). The evaluation of the diffusion equation (B-1) at each node is then:

$$F(U_i) = \frac{D_{Mg}}{RT}\left[\frac{2}{r}U_i\left(\frac{\partial \mu_{Mg}}{\partial r}\right)_i + \left(\frac{\partial U}{\partial r}\right)_i\left(\frac{\partial \mu_{Mg}}{\partial r}\right)_i + U_i\left(\frac{\partial^2 \mu_{Mg}}{\partial r^2}\right)_i\right] \tag{B-47}$$

The terms to evaluate $F(U_i)$ are obtained at every time integration stage and for each node with the spatial discretization and boundary condition enforcement previously described.

Defining y_q as the known vector of values of the molar concentration C_{Mg} for the inner nodes at time t_q :

$$y_q = C_{Mg}(i)\big|_{t=t_q} \qquad i = 2, \dots, n-1 \tag{B-48}$$

The time integration step involves twelve stages that use the integration constants and the time step Δt_q , the stages proceed according to:

$$y_1 = y_q \tag{B-49.1}$$

$$k_1 = F(y_1) \tag{B-49.2}$$

$$y_2 = y_q + \left(a_{2,1} \cdot k_1\right)\Delta t_q \tag{B-49.3}$$

$$k_2 = F(y_2) \tag{B-49.4}$$

$$y_3 = y_q + \left(a_{3,1} \cdot k_1 + a_{3,2} \cdot k_2\right)\Delta t_q \tag{B-49.5}$$

$$k_3 = F(y_3) \tag{B-49.6}$$

$$y_4 = y_q + \left(a_{4,1} \cdot k_1 + a_{4,3} \cdot k_3\right)\Delta t_q \tag{B-49.7}$$

$$k_4 = F(y_4) \tag{B-49.8}$$

$$y_5 = y_q + \left(a_{5,1} \cdot k_1 + a_{5,3} \cdot k_3 + a_{5,4} \cdot k_4\right)\Delta t_q \tag{B-49.9}$$

$$k_5 = F(y_5) \tag{B-49.10}$$

$$y_6 = y_q + \left(a_{6,1} \cdot k_1 + a_{6,4} \cdot k_4 + a_{6,5} \cdot k_5\right)\Delta t_q \tag{B-49.11}$$

$$k_6 = F(y_6) \tag{B-49.12}$$

$$y_7 = y_q + \left(a_{7,1} \cdot k_1 + a_{7,4} \cdot k_4 + a_{7,5} \cdot k_5 + a_{7,6} \cdot k_6\right)\Delta t_q \tag{B-49.13}$$

$$k_7 = F(y_7) \tag{B-49.14}$$

$$y_8 = y_q + \left(a_{8,1} \cdot k_1 + a_{8,4} \cdot k_4 + a_{8,5} \cdot k_5 + a_{8,6} \cdot k_6 + a_{8,7} \cdot k_7\right)\Delta t_q \tag{B-49.15}$$

$$k_8 = F(y_8) \tag{B-49.16}$$

$$y_9 = y_q + \left(a_{9,1} \cdot k_1 + a_{9,4} \cdot k_4 + a_{9,5} \cdot k_5 + a_{9,6} \cdot k_6 + a_{9,7} \cdot k_7 + a_{9,8} \cdot k_8\right) \Delta t_q \tag{B-49.17}$$

$$k_9 = F(y_9) \tag{B-49.18}$$

$$y_{10} = y_q + \left(a_{10,1} \cdot k_1 + a_{10,4} \cdot k_4 + a_{10,5} \cdot k_5 + a_{10,6} \cdot k_6 + a_{10,7} \cdot k_7 + a_{10,8} \cdot k_8 + a_{10,9} \cdot k_9\right)\Delta t_q \tag{B-49.19}$$

$$k_{10} = F(y_{10}) \tag{B-49.20}$$

$$y_{11} = y_q + \left(a_{11,1} \cdot k_1 + a_{11,4} \cdot k_4 + a_{11,5} \cdot k_5 + a_{11,6} \cdot k_6 + a_{11,7} \cdot k_7 + a_{11,8} \cdot k_8 + a_{11,9} \cdot k_9 + a_{11,10} \cdot k_{10}\right)\Delta t_q \tag{B-49.21}$$

$$k_{11} = F(y_{11}) \tag{B-49.22}$$

$$y_{12} = y_q + \left(a_{12,1} \cdot k_1 + a_{12,4} \cdot k_4 + a_{12,5} \cdot k_5 + a_{12,6} \cdot k_6 + a_{12,7} \cdot k_7 + a_{12,8} \cdot k_8 + a_{12,9} \cdot k_9 + a_{12,10} \cdot k_{10} + a_{12,11} \cdot k_{11}\right)\Delta t_q \tag{B-49.23}$$

$$k_{12} = F(y_{12}) \tag{B-49.24}$$

$$Q_4 = b_1 \cdot k_1 + b_6 \cdot k_6 + b_7 \cdot k_7 + b_8 \cdot k_8 + b_9 \cdot k_9 + b_{10} \cdot k_{10} + b_{11} \cdot k_{11} + b_{12} \cdot k_{12} \tag{B-49.25}$$

The integration constants $a_{i,j}$ and b_i are reported in the freely accessible software codes (Hairer, n.d.).

The 8th order time step approximation is finally obtained with:

$$Q_5 = y_q + Q_4 \cdot \Delta t_q \tag{B-49.25}$$

If the time step integration satisfies the accuracy and stability control tolerances then the step is accepted and Δt_q increases to Δt_{q+1} for the next step according to the time step control strategy, therefore:

$$y_{q+1} = Q_5 \tag{B-50}$$

If the step is rejected then Δt_q is reduced with the time step control strategy and the current time step is repeated until the step is accepted.

B.3.2 Adaptive time-step control strategy

To accept or reject a time step integration and adaptive time-step method for Δt_q is implemented. The method is based on the modified PI control algorithm proposed by Gustafsson (1991) where P stands for 'proportional feedback' and I for 'integral feedback'. In this way, if the PDE model is in a region of few changes then the time step can be increased to save computational efforts. On the contrary, if many diffusional changes occur in the product layer the time step of the model is reduced to maintain stability and accuracy.

In order to evaluate a given time step integration the Runge-Kutta method DOP853 calculates two error estimations of 5th and 3rd order respectively (Hairer & Wanner, 2002):

$$Err_5 = \|\hat{y}_i - y_i\| = \mathcal{O}(\Delta t^6) \tag{B-51}$$

$$Err_3 = \|\tilde{y}_i - y_i\| = \mathcal{O}(\Delta t^4) \tag{B-52}$$

The vectors of error estimations are calculated with:

$$Err_5 = E_1 \cdot k_1 + E_6 \cdot k_6 + E_7 \cdot k_7 + E_8 \cdot k_8 + E_9 \cdot k_9 + E_{10} \cdot k_{10} + E_{11} \cdot k_{11} + E_{12} \cdot k_{12} \tag{B-53}$$

$$Err_3 = Q_4 - b_1^{Err} \cdot k_1 - b_2^{Err} \cdot k_9 - b_3^{Err} \cdot k_{12} \tag{B-54}$$

The constants in E_i and b_i^{Err} for (B-53) and (B-54) are reported in the available software codes (Hairer, n.d.). The "stretched" error estimator for DOP853 was proposed by Hairer & Wanner (2002) and is calculated at each node according to:

$$Err = Err_5 \cdot \frac{Err_5}{\sqrt{(Err_5)^2 + 0.01(Err_3)^2}} = \mathcal{O}(\Delta t^8) \tag{B-55}$$

The value of the error per step EPS is then:

$$EPS = max(Err) \tag{B-56}$$

To adjust the time step, Gustafsson (1991) described the outline of the time-step control strategy that uses an standard control algorithm (B-57) and the PI control algorithm (B-58):

If a time step is rejected, the standard algorithm shortens Δt_q with:

$$\Delta t_q = \left(\frac{tol}{EPS}\right)^{\frac{1}{K}} \Delta t_q \tag{B-57}$$

If the step is accepted, Δt_q increases with the PI algorithm:

$$\Delta t_{q+1} = \left(\frac{0.8 \cdot tol}{EPS}\right)^{K_I} \left(\frac{EPS_{old}}{EPS}\right)^{K_P} \Delta t_q \tag{B-58}$$

In this case EPS_{old} is the value of the error esimation from the previous time step integration and tol is the tolerance limit that assures accuracy and stability. As mentioned by Söderlind (2002), the choice of $K \cdot K_I$ and $K \cdot K_P$ is based on theoretical considerations as well as computational performance. Since the EPS value is used in (B-57) and (B-58) then $K = P$ and in this case $P = 7$ because a local extrapolation of the 8th order error estimation is used for DOP853 (Hairer & Wanner, 2002). The values of K_I and K_P refer to the proportional gain and are related according to (Hairer & Wanner, 2002):

$$\alpha = K_I + K_P \tag{B-59.1}$$

$$\beta = K_P \tag{B-59.2}$$

Based on numerical studies for the Runge-Kutta method DOP853, Hairer & Wanner (2002) proposed to use the values $\alpha = \frac{1}{P}$ and $\beta = 0.08$.

Appendix C

Comparison of the kinetic coupled model with the plant data measurements

The validation of the kinetic coupled model for the slag, steel and oxide inclusions was made by considering the processing conditions in the Ladle Metallurgy Furnace station at ArcelorMittal Dofasco. This appendix includes the comparison between the calculated and measured concentrations for the species in the slag, steel and the %Mg concentration in the inclusions. The value of %Mg represents the amount of magnesium aluminate spinel in the inclusions.

Plots with the specific processing conditions and additions of each heat are also part of this appendix as well as the measurements and estimations that were input to start the calculations with the model: initial steel mass, estimation of the initial slag mass and steel temperature. The used ratios of the mass transfer coefficients of the components in the slag with the mass transfer coefficient of the species in steel $k_{sl}^{M_xO_y} / k_m^M$ are included for FeO, MnO and SiO_2. The refining heats are identified with the same nomenclature used in the previous kinetic model implemented in the thesis of Graham (2008).

Finally, the results on the size, composition and class distribution from the automated SEM inclusions analysis of the analyzed heats are also presented.

Heat 6

Initial steel mass	Estimation of initial slag mass	Initial Temp. for calculations
164513 Kg	2587 Kg	1608 K

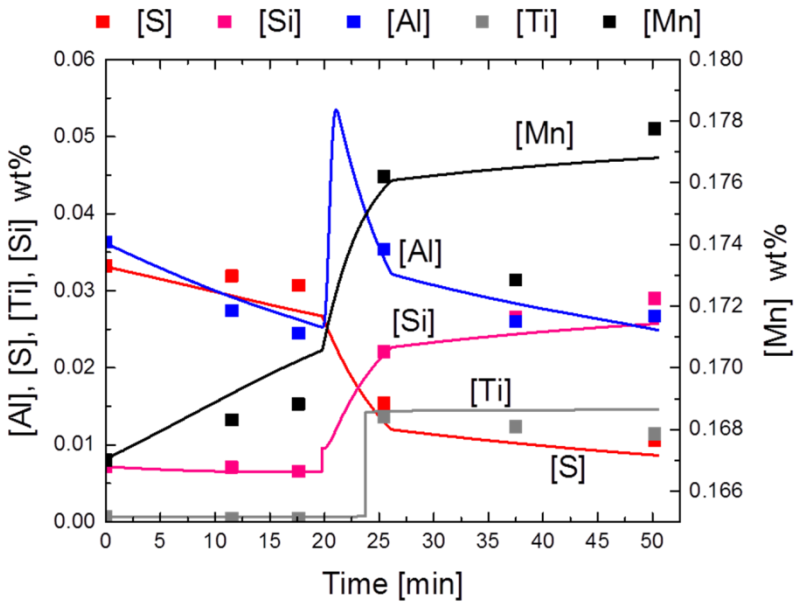

Figure C-1. Measured and calculated bulk concentrations in the steel phase, Heat 6.

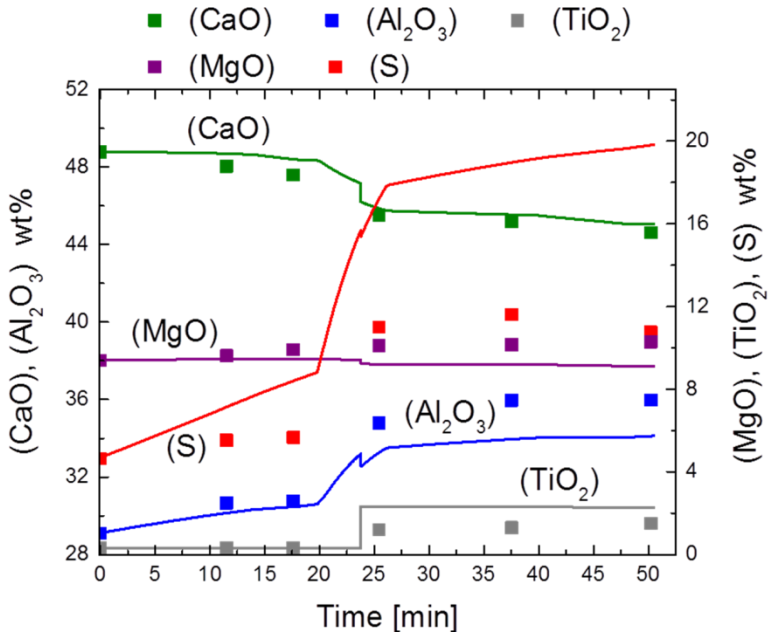

Figure C-2. Measured and calculated bulk concentrations in the slag phase, Heat 6.

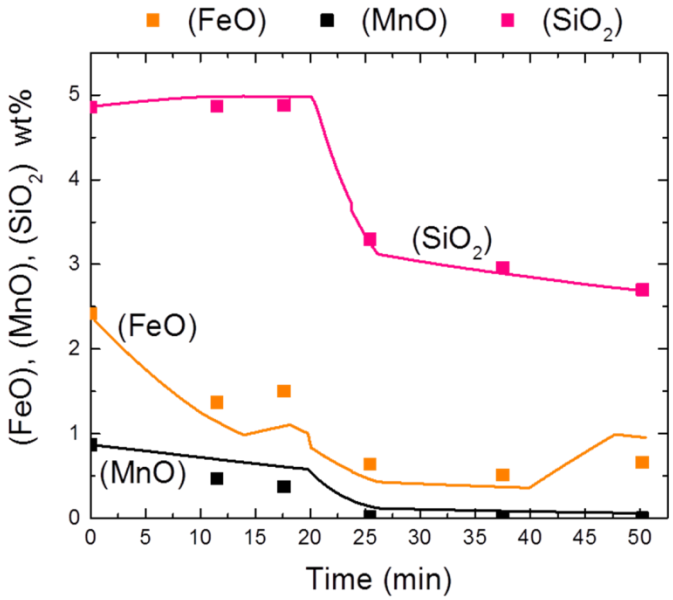

Figure C-3. Measured and calculated bulk values for FeO, MnO and SiO_2 in the slag phase, Heat 6.

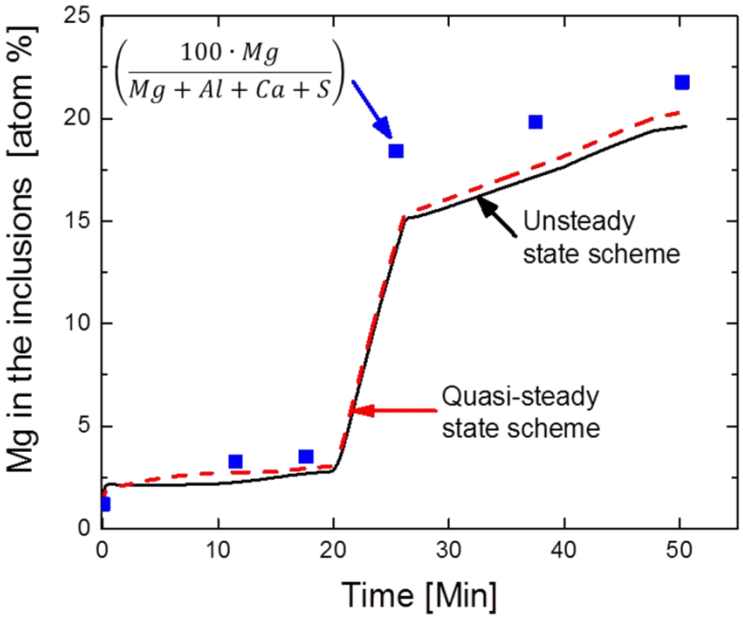

Figure C-4. Measured and calculated content of Mg in the oxide inclusions, Heat 6.

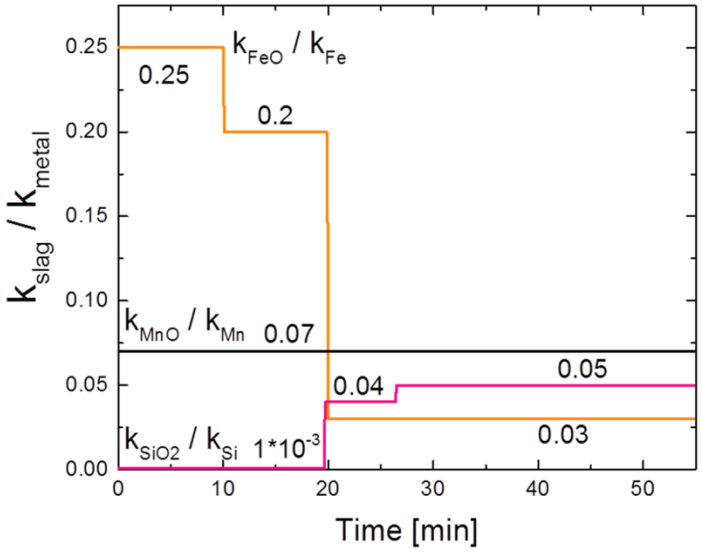

Figure C-5. Ratios of the slag mass transfer coefficients with the respective mass transfer coefficient of the species in steel, Heat 6.

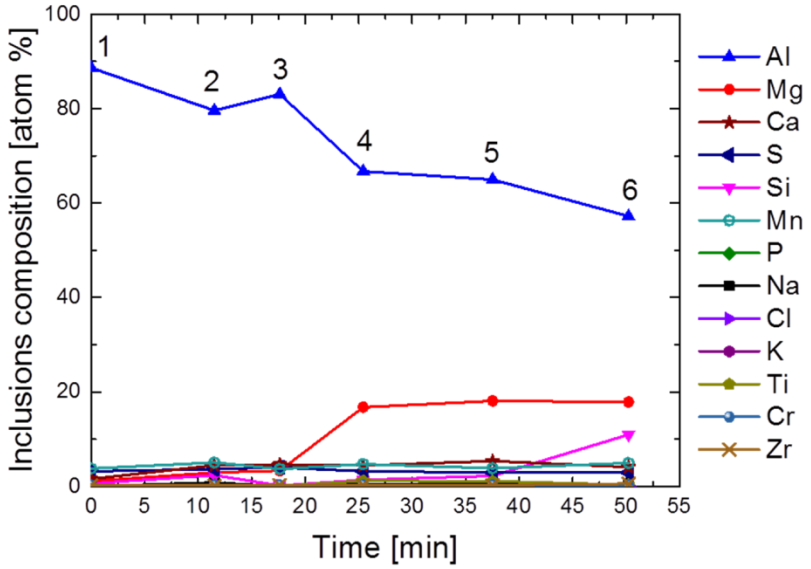

Figure C-6. Automated SEM analysis, average composition of the inclusions in atomic percentaje. Sample numbers during the course of Heat 6.

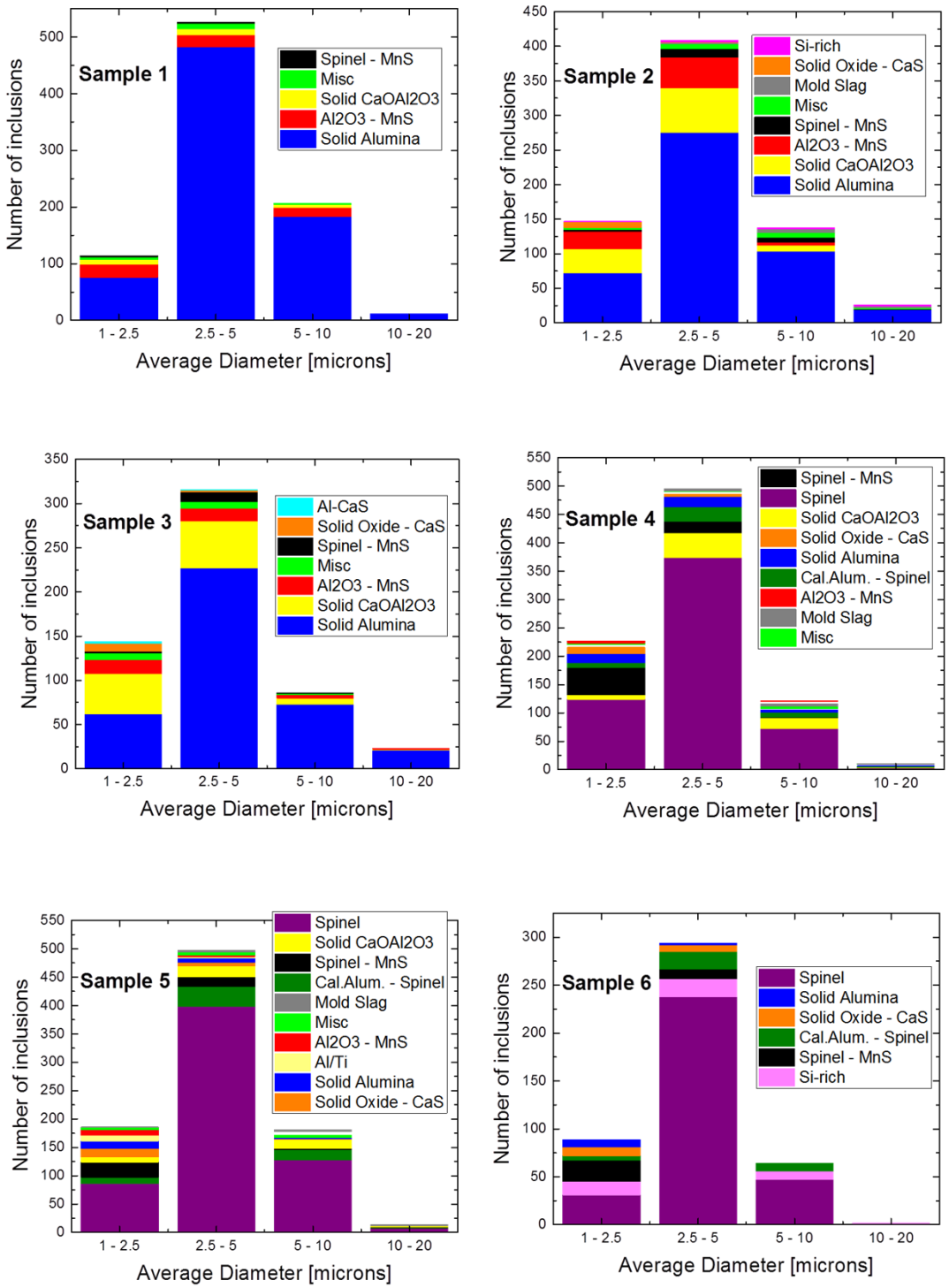

Figure C-7. Measured results from the automated SEM inclusions analysis. Number Distribution by average diameter (microns), Heat 6. Sample numbers correspond to Figure C-6.

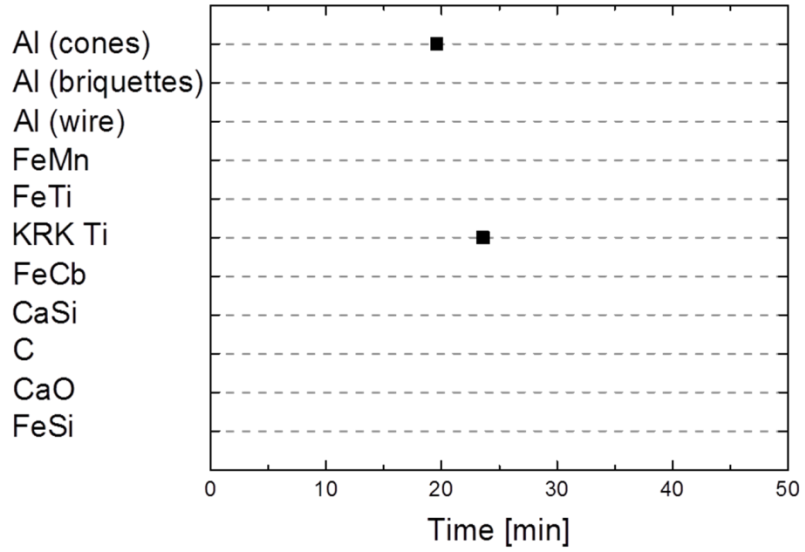

Figure C-8. Additions for the slag and steel during treatment in the LMF, Heat 6.

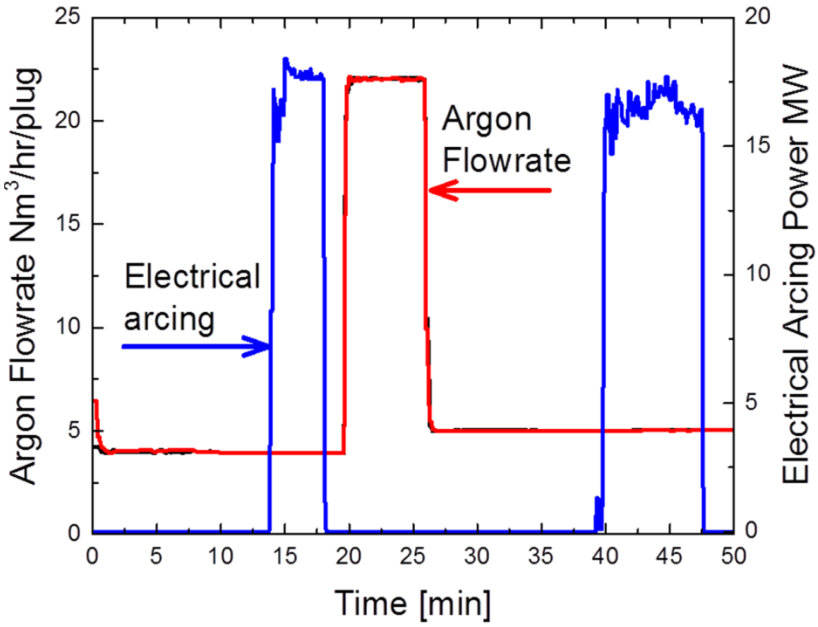

Figure C-9. Argon gas stirring and electrical heating during treatment in the LMF, Heat 6.

Heat 7

Initial steel mass	Estimation of initial slag mass	Initial Temp. for calculations
161458 Kg	2842 Kg	1625 K

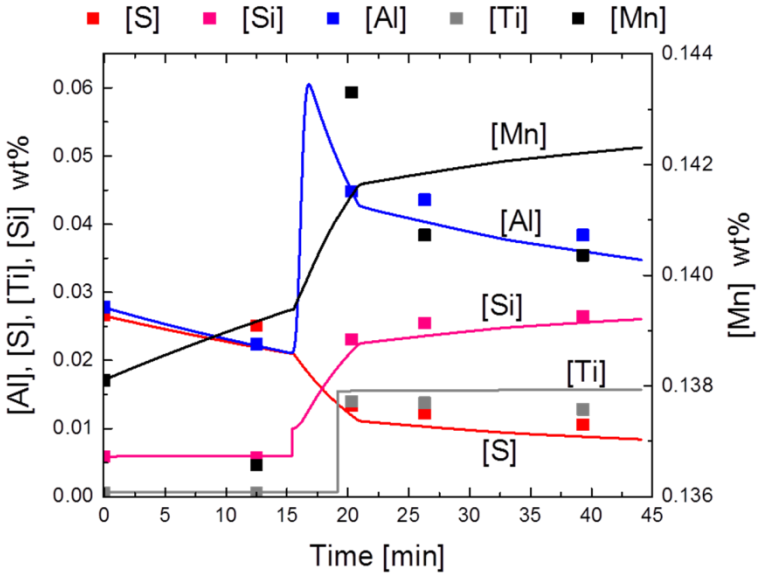

Figure C-10. Measured and calculated bulk concentrations in the steel phase, Heat 7.

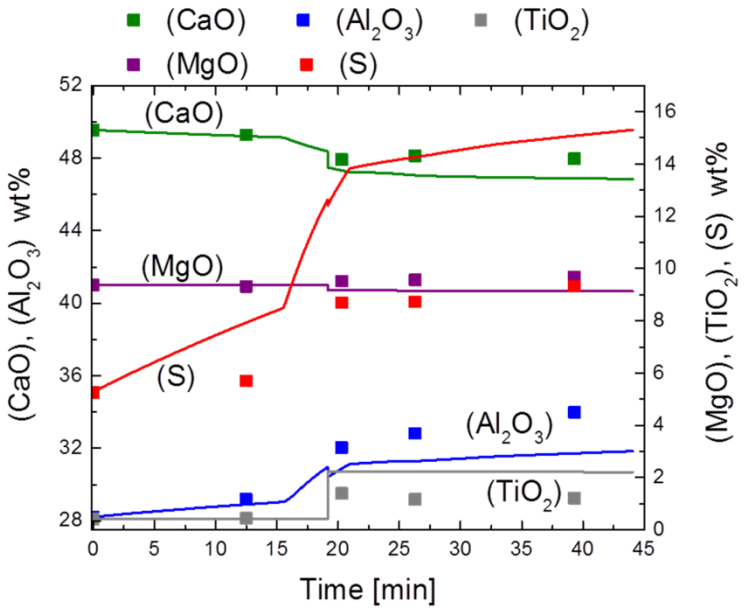

Figure C-11. Measured and calculated bulk concentrations in the slag phase, Heat 7.

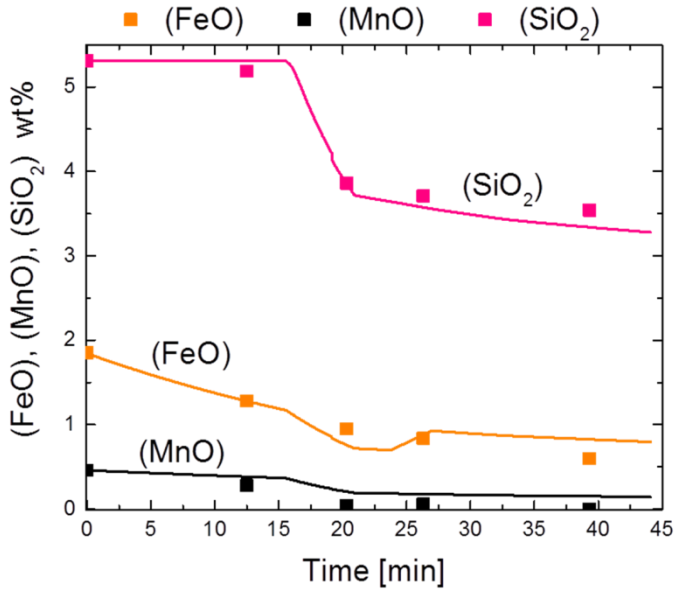

Figure C-12. Measured and calculated bulk values for FeO, MnO and SiO_2 in the slag phase, Heat 7.

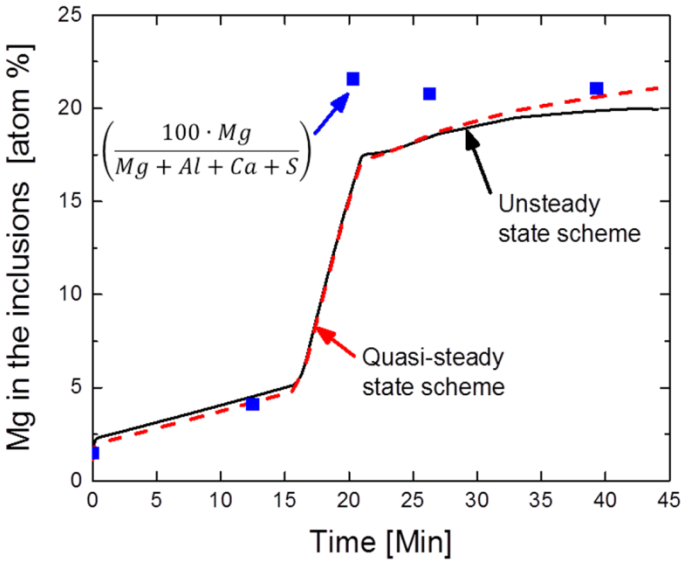

Figure C-13. Measured and calculated content of Mg in the oxide inclusions, Heat 7.

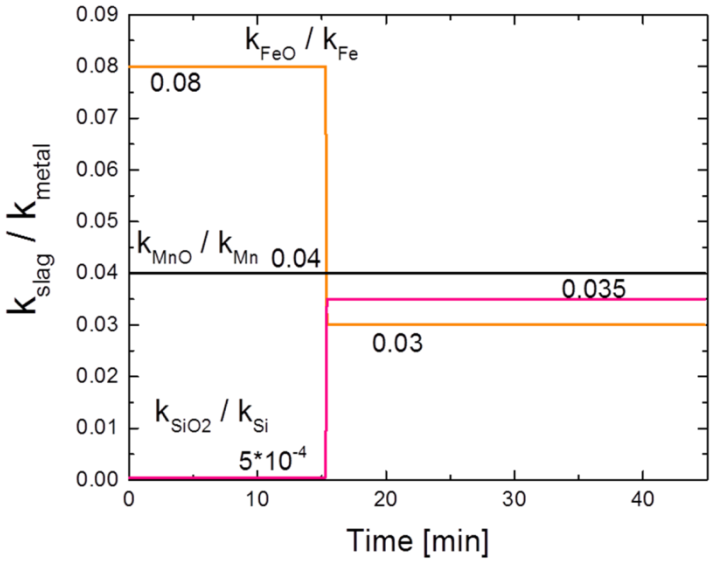

Figure C-14. Ratios of the slag mass transfer coefficients with the respective mass transfer coefficient of the species in steel, Heat 7.

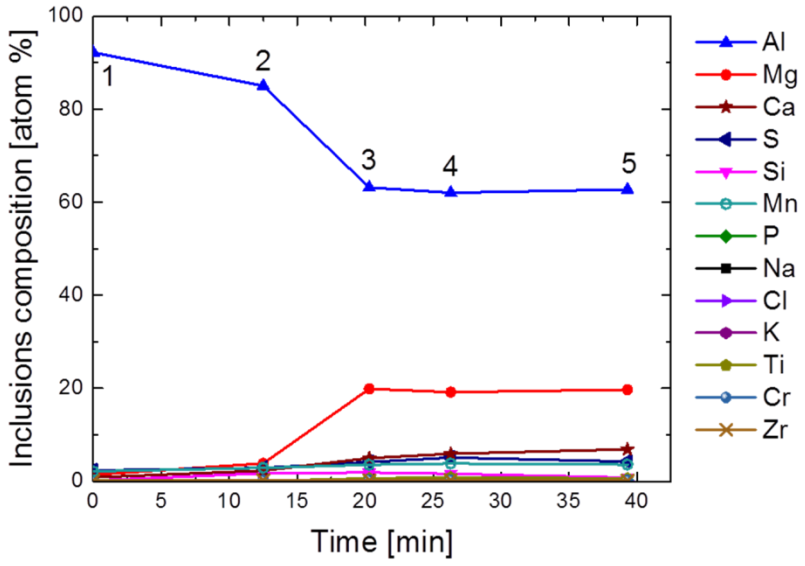

Figure C-15. Automated SEM analysis, average composition of the inclusions in atomic percentaje. Sample numbers during the course of Heat 7.

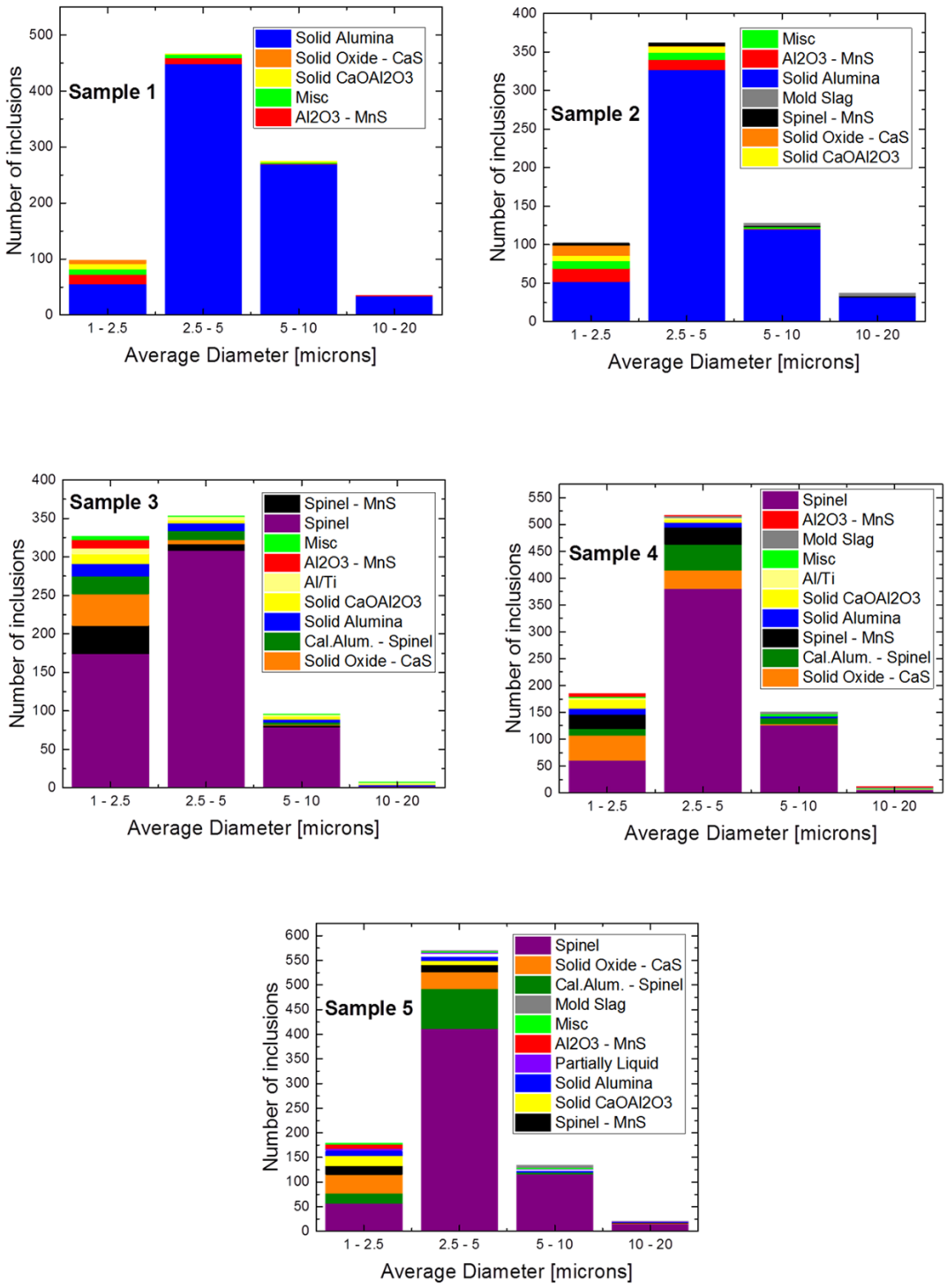

Figure C-16. Measured results from the automated SEM inclusions analysis. Number Distribution by average diameter (microns), Heat 7. Sample numbers correspond to Figure C-15.

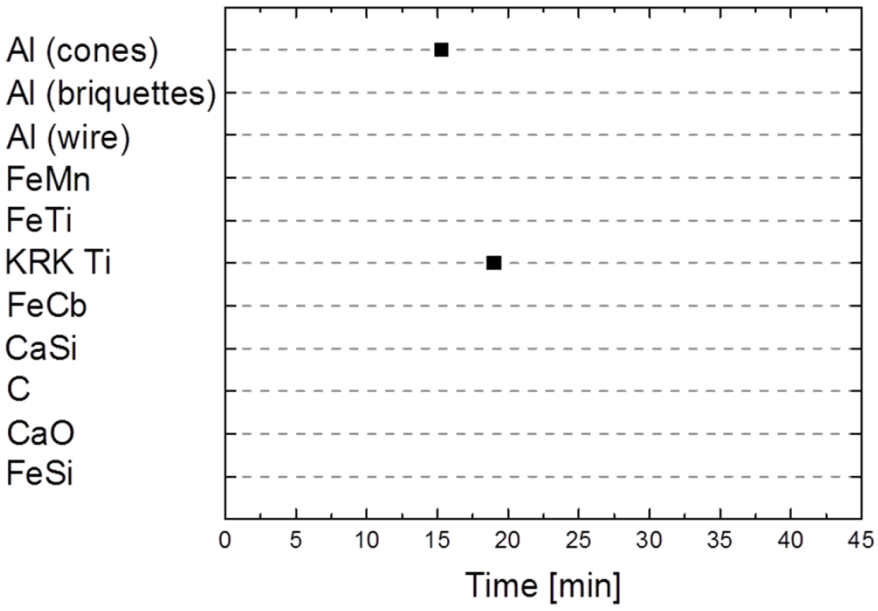

Figure C-17. Additions for the slag and steel during treatment in the LMF, Heat 7.

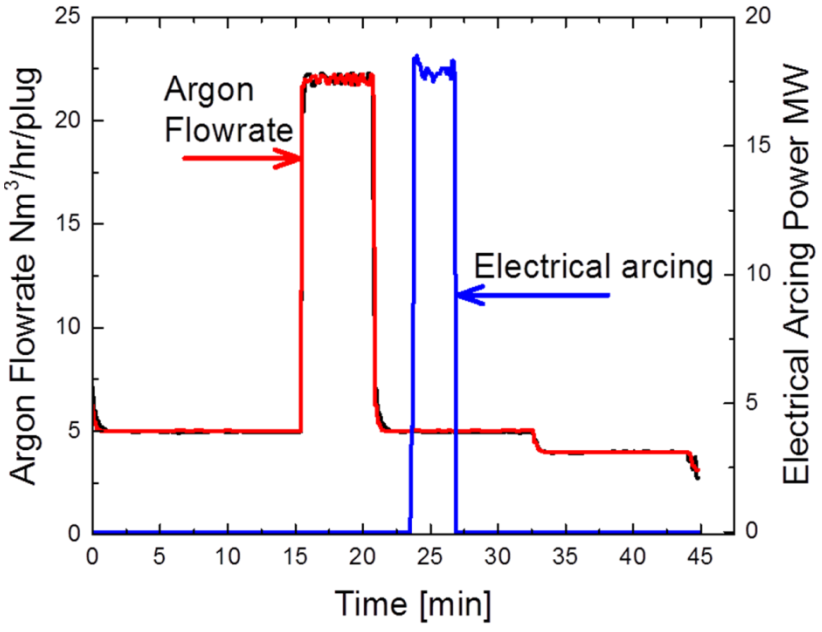

Figure C-18. Argon gas stirring and electrical heating during treatment in the LMF, Heat 7.

Heat 8

Initial steel mass	Estimation of initial slag mass	Initial Temp. for calculations
165549 Kg	4151 Kg	1603 K

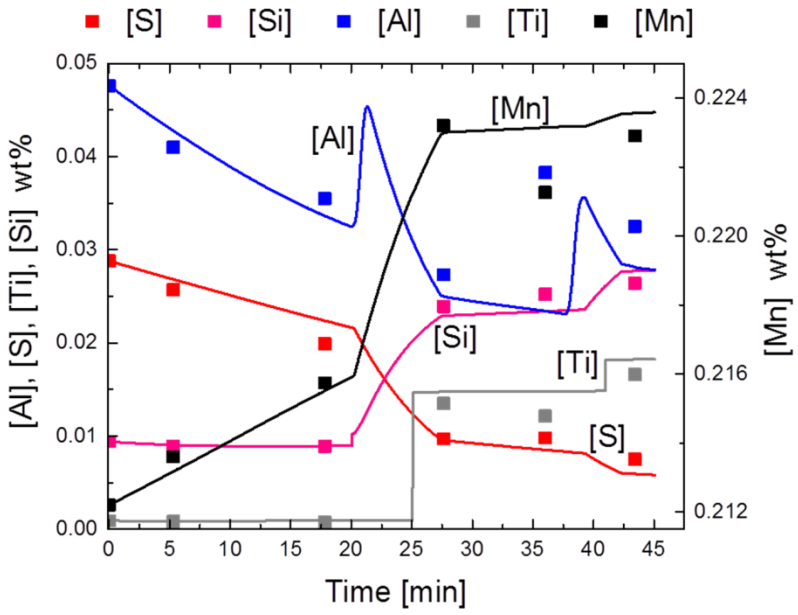

Figure C-19. Measured and calculated bulk concentrations in the steel phase, Heat 8.

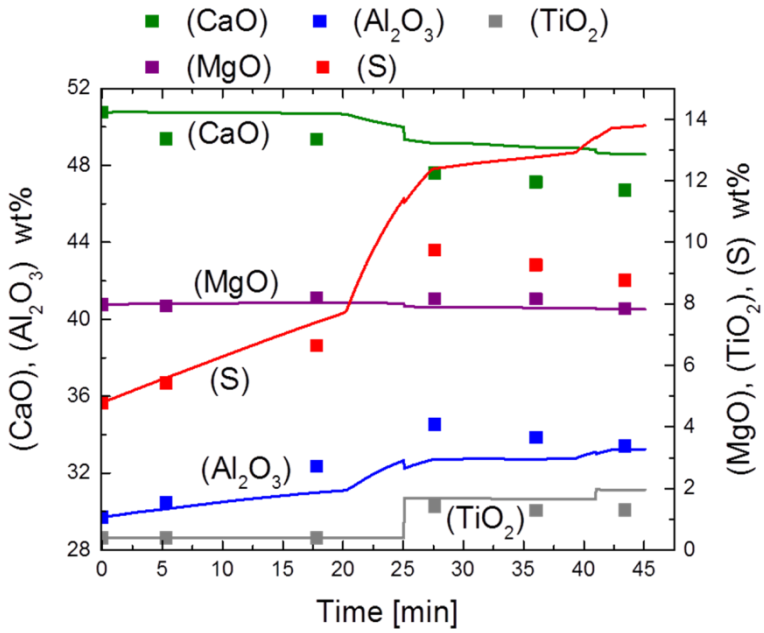

Figure C-20. Measured and calculated bulk concentrations in the slag phase, Heat 8.

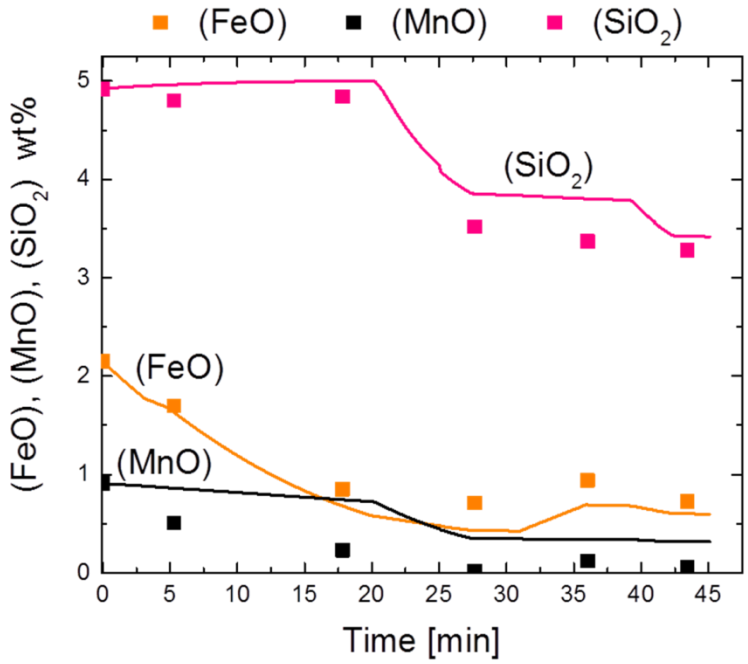

Figure C-21. Measured and calculated bulk values for FeO, MnO and SiO_2 in the slag phase, Heat 8.

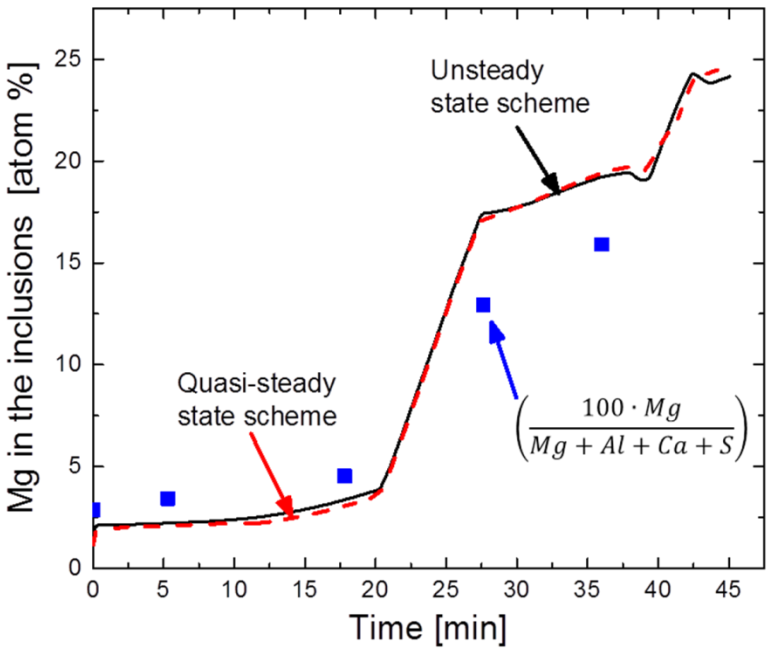

Figure C-22. Measured and calculated content of Mg in the oxide inclusions, Heat 8.

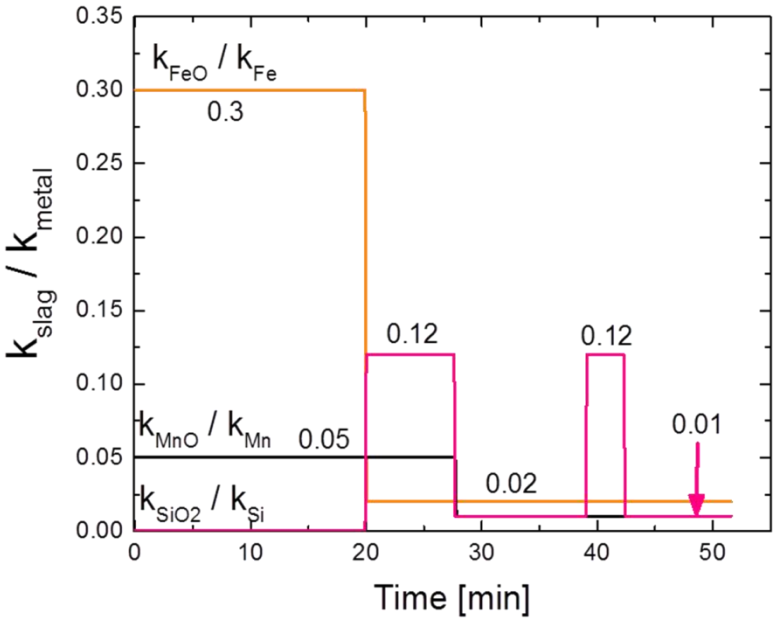

Figure C-23. Ratios of the slag mass transfer coefficients with the respective mass transfer coefficient of the species in steel, Heat 8.

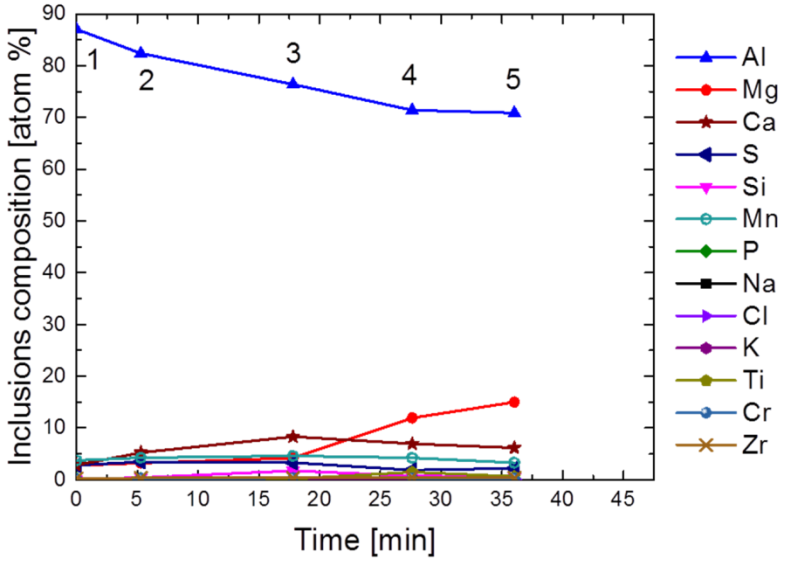

Figure C-24. Automated SEM analysis, average composition of the inclusions in atomic percentaje. Sample numbers during the course of Heat 8.

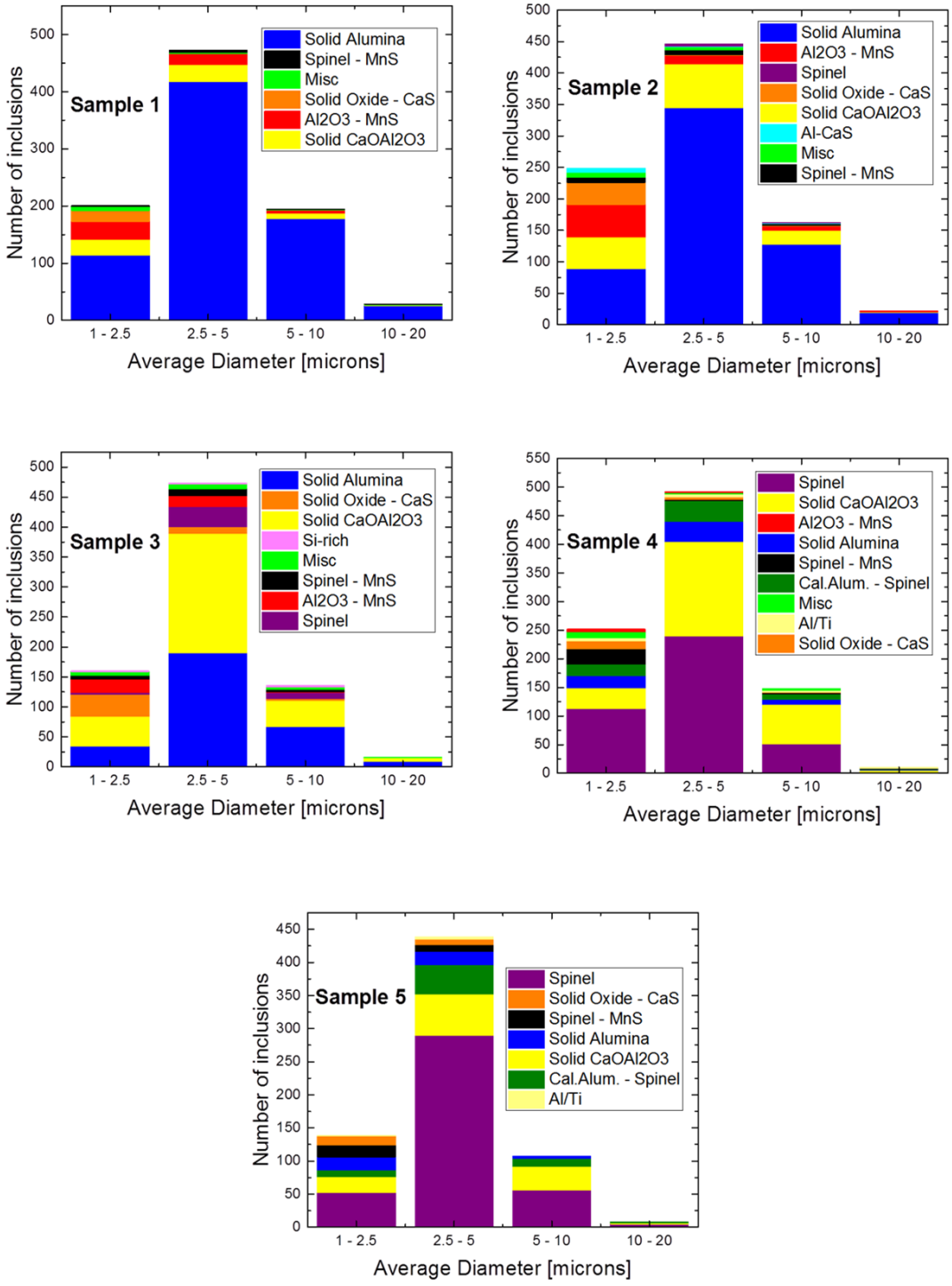

Figure C-25. Measured results from the automated SEM inclusions analysis. Number Distribution by average diameter (microns), Heat 8. Sample numbers correspond to Figure C-24.

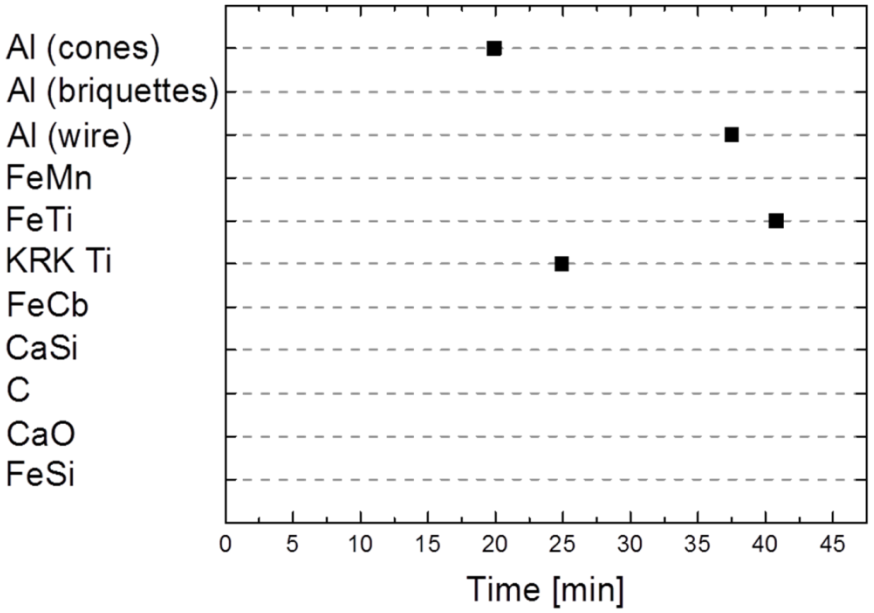

Figure C-26. Additions for the slag and steel during treatment in the LMF, Heat 8.

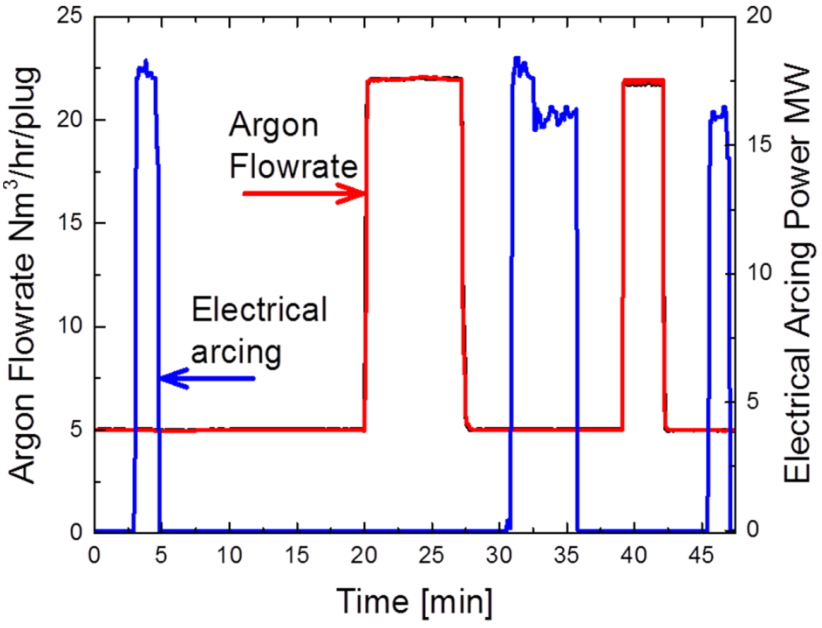

Figure C-27. Argon gas stirring and electrical heating during treatment in the LMF, Heat 8.

Heat 10

Initial steel mass	Estimation of initial slag mass	Initial Temp. for calculations
162629 Kg	3271 Kg	1582 K

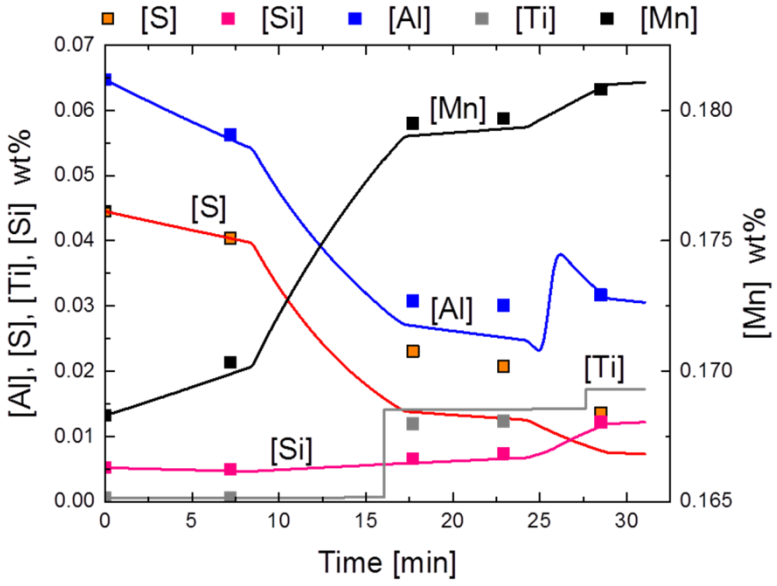

Figure C-28. Measured and calculated bulk concentrations in the steel phase, Heat 10.

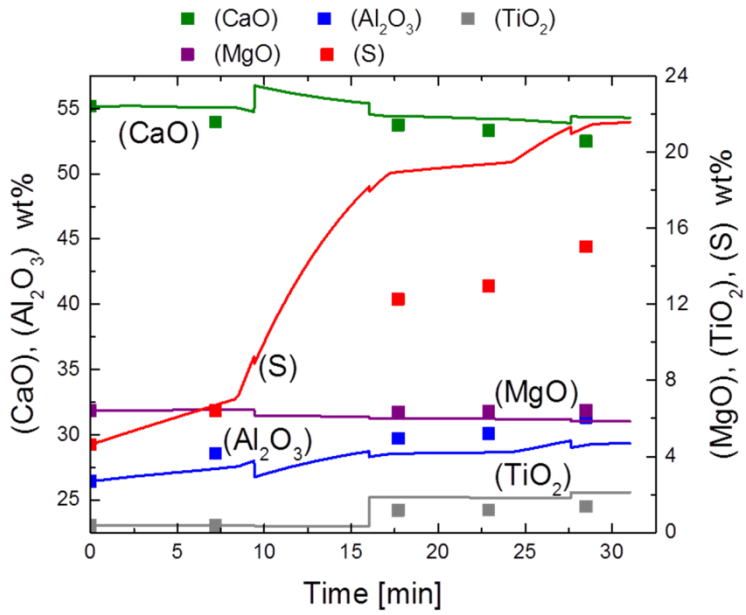

Figure C-29. Measured and calculated bulk concentrations in the slag phase, Heat 10.

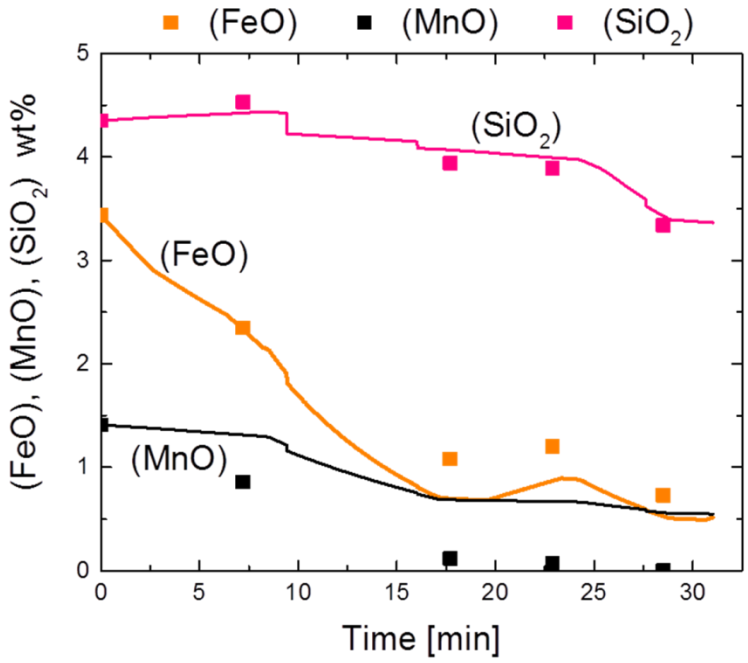

Figure C-30. Measured and calculated bulk values for FeO, MnO and SiO_2 in the slag phase, Heat 10.

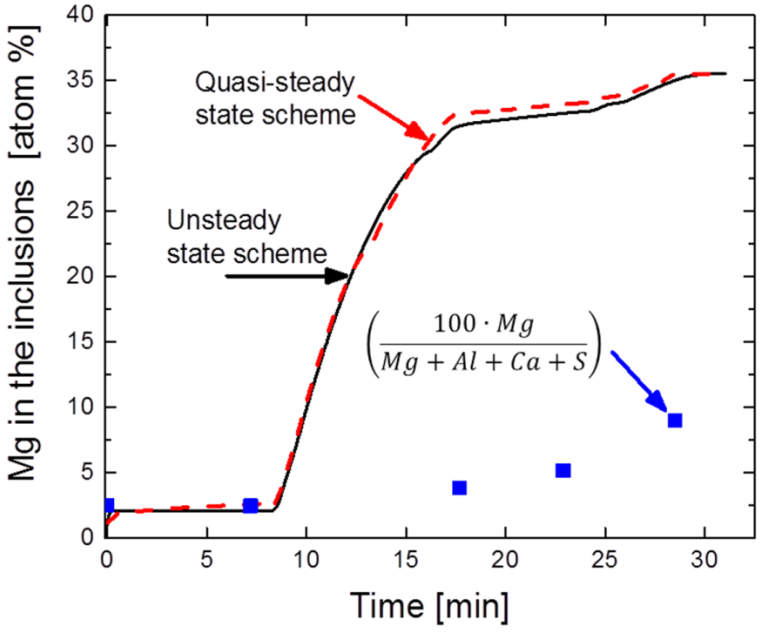

Figure C-31. Measured and calculated content of Mg in the oxide inclusions, Heat 10.

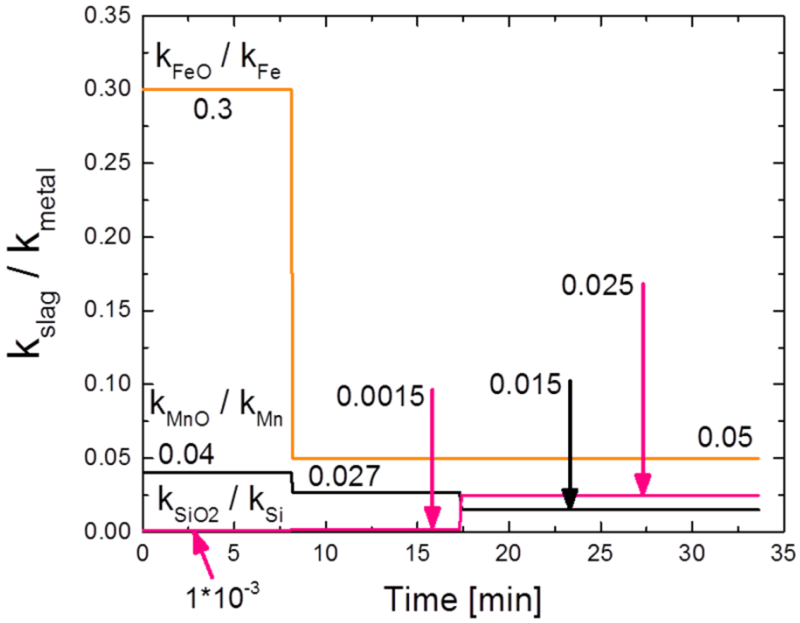

Figure C-32. Ratios of the slag mass transfer coefficients with the respective mass transfer coefficient of the species in steel, Heat 10.

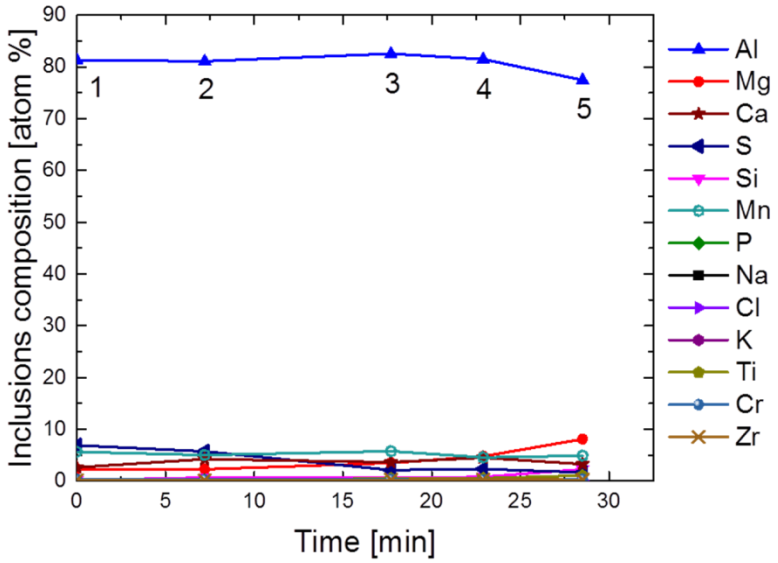

Figure C-33. Automated SEM analysis, average composition of the inclusions in atomic percentaje. Sample numbers during the course of Heat 10.

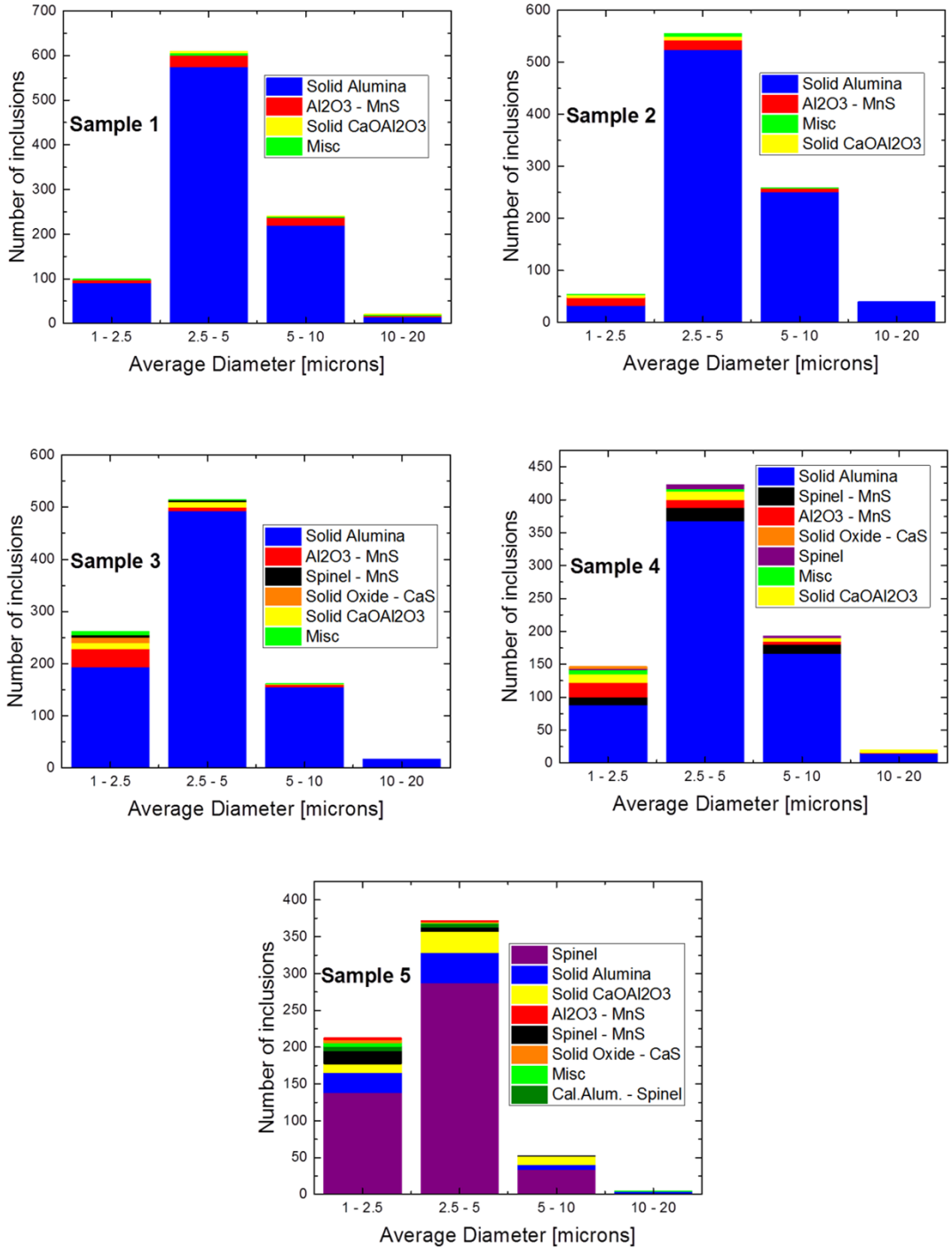

Figure C-34. Measured results from the automated SEM inclusions analysis. Number Distribution by average diameter (microns), Heat 10. Sample numbers correspond to Figure C-33.

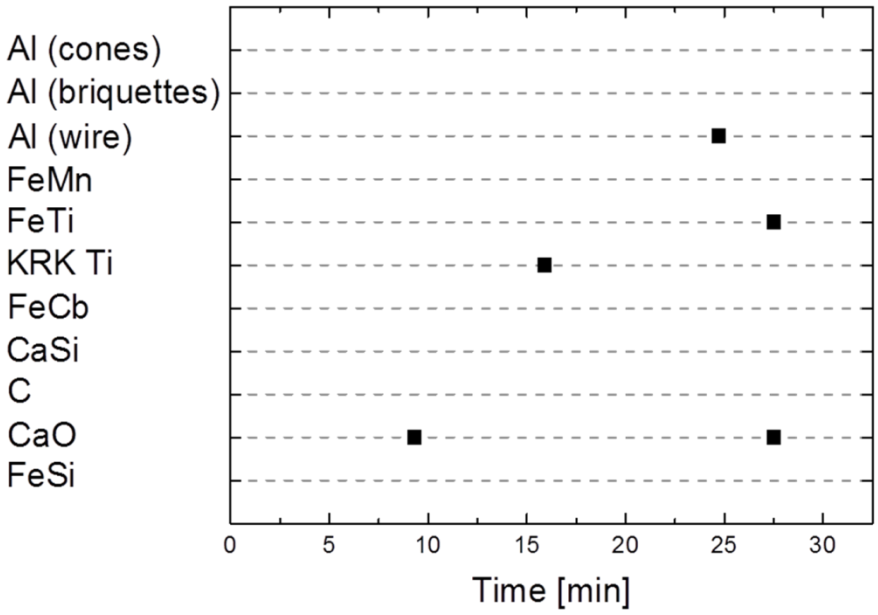

Figure C-35. Additions for the slag and steel during treatment in the LMF, Heat 10.

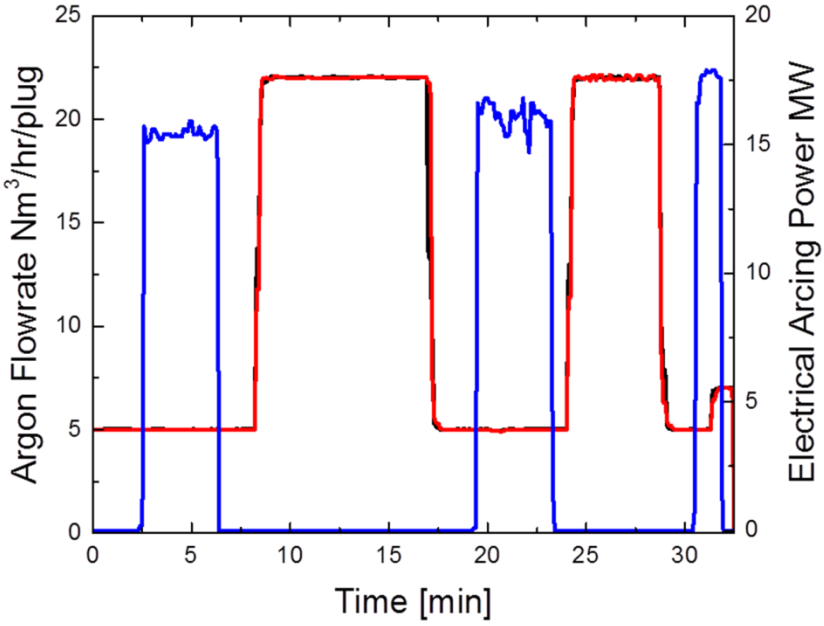

Figure C-36. Argon gas stirring and electrical heating during treatment in the LMF, Heat 10.

Heat 15

Initial steel mass	Estimation of initial slag mass	Initial Temp. for calculations
163277 Kg	2623 Kg	1569 K

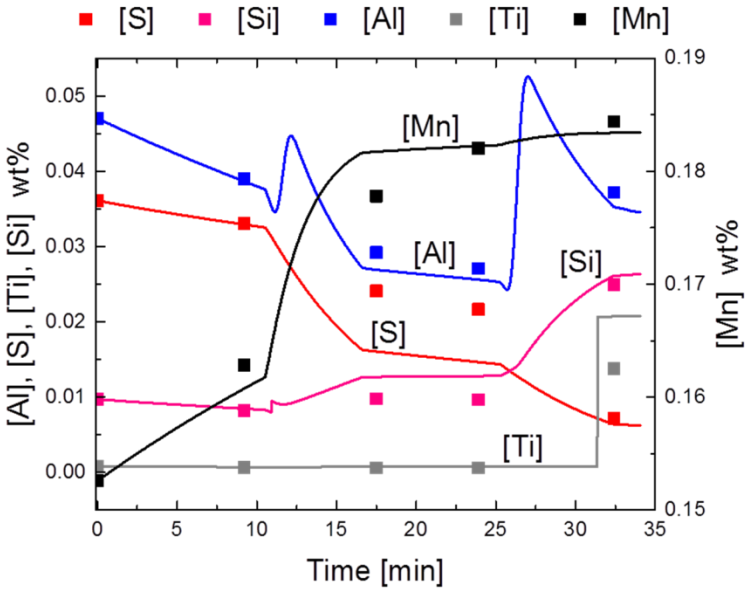

Figure C-37. Measured and calculated bulk concentrations in the steel phase, Heat 15.

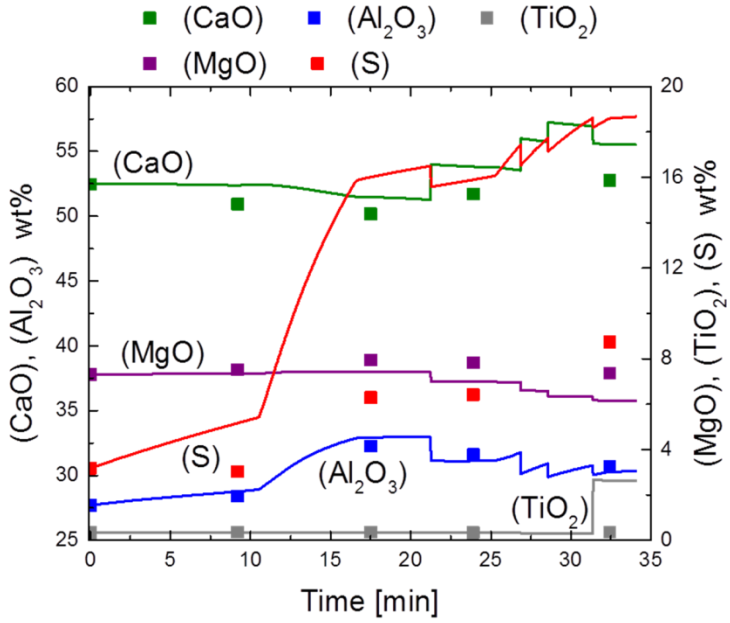

Figure C-38. Measured and calculated bulk concentrations in the slag phase, Heat 15.

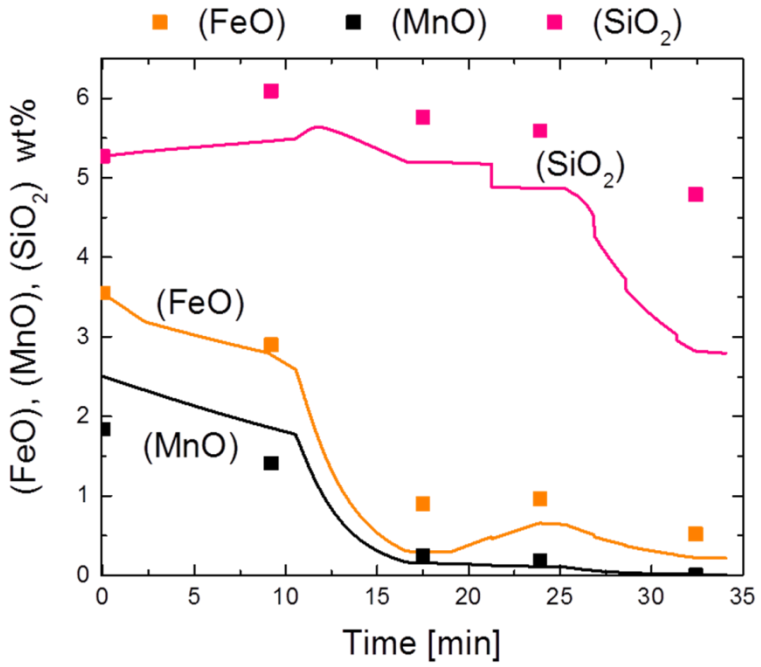

Figure C-39. Measured and calculated bulk values for FeO, MnO and SiO_2 in the slag phase, Heat 15.

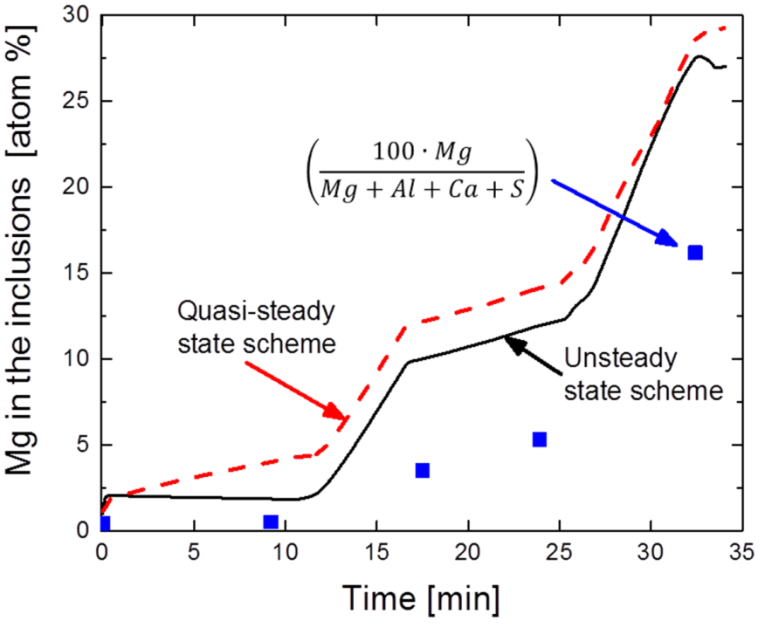

Figure C-40. Measured and calculated content of Mg in the oxide inclusions, Heat 15.

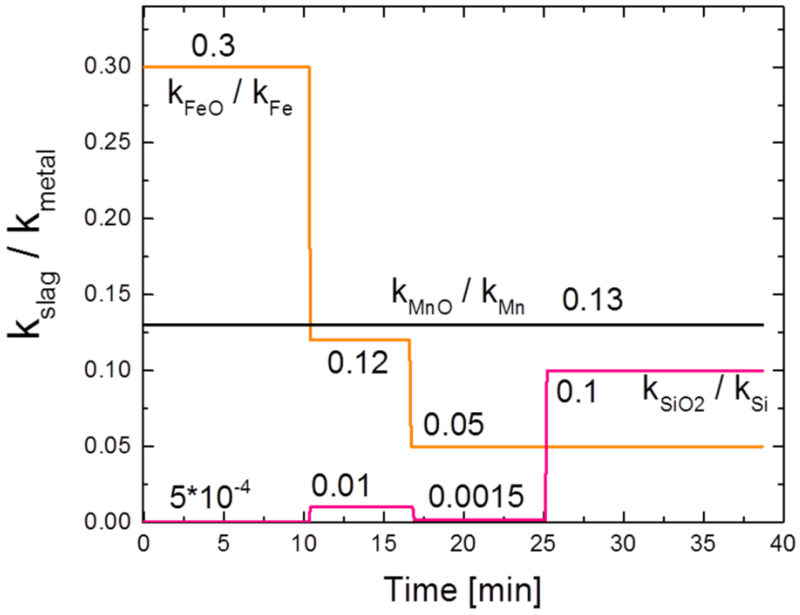

Figure C-41. Ratios of the slag mass transfer coefficients with the respective mass transfer coefficient of the species in steel, Heat 15.

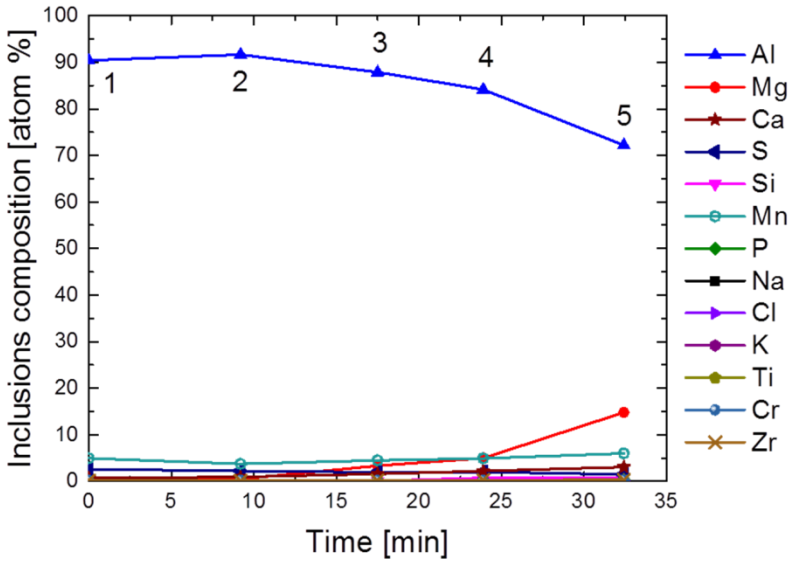

Figure C-42. Automated SEM analysis, average composition of the inclusions in atomic percentaje. Sample numbers during the course of Heat 15.

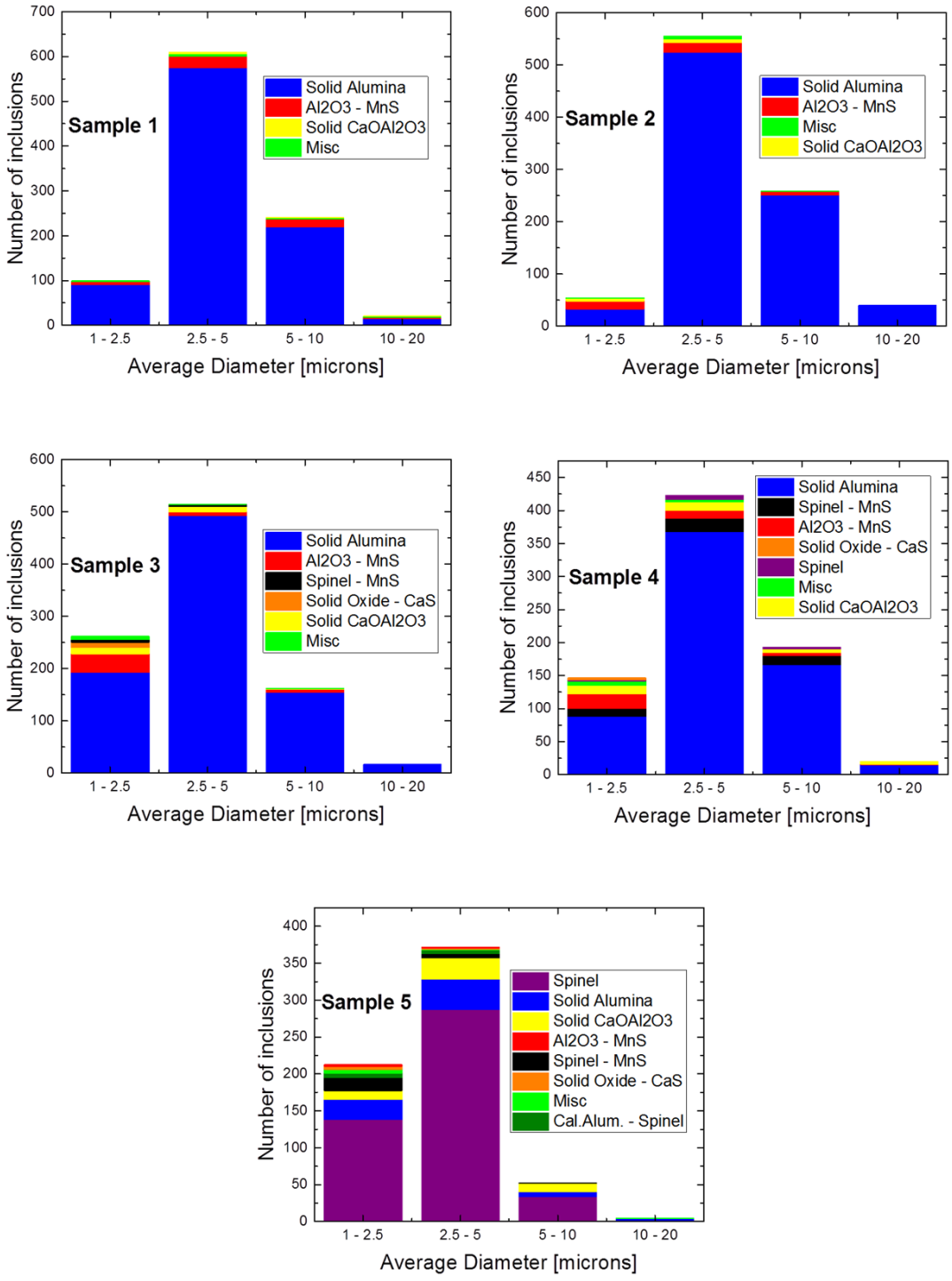

Figure C-43. Measured results from the automated SEM inclusions analysis. Number Distribution by average diameter (microns), Heat 15. Sample numbers correspond to Figure C-42.

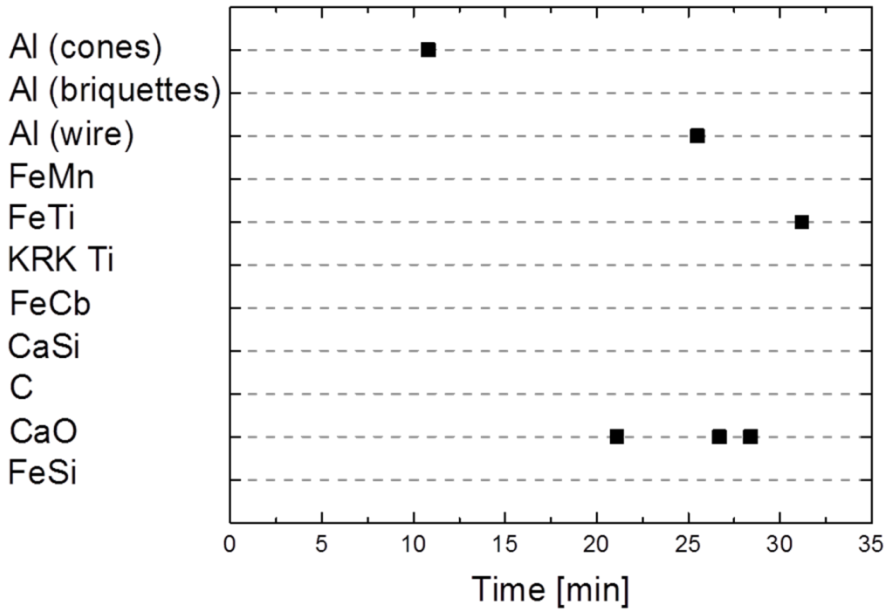

Figure C-44. Additions for the slag and steel during treatment in the LMF, Heat 15.

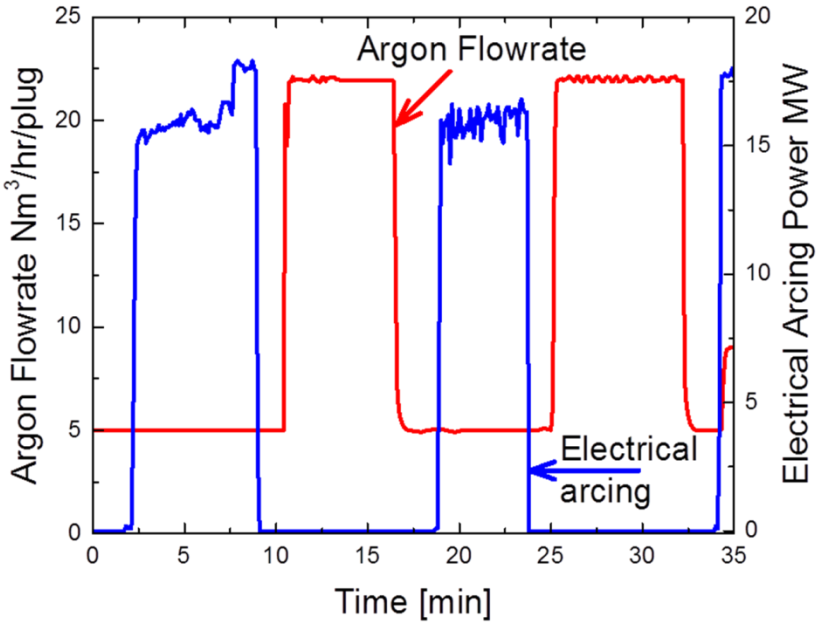

Figure C-45. Argon gas stirring and electrical heating during treatment in the LMF, Heat 15.

Heat 17

Initial steel mass	Estimation of initial slag mass	Initial Temp. for calculations
160343 Kg	2557 Kg	1580 K

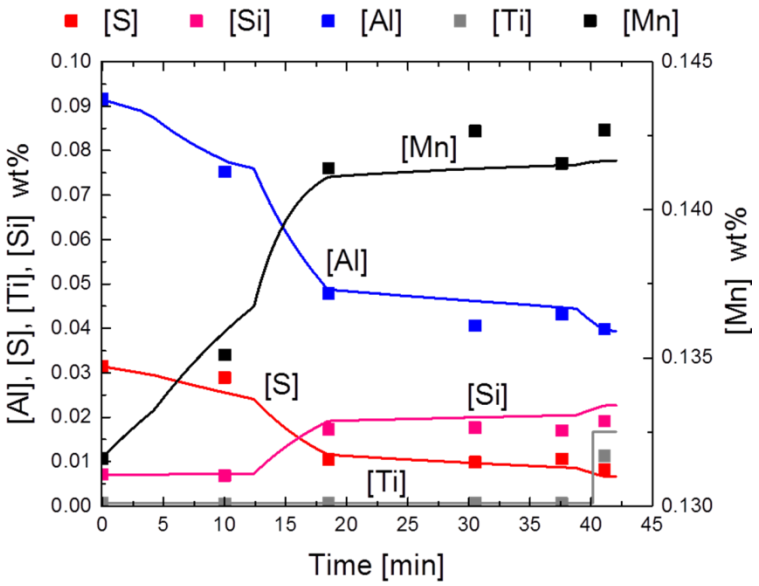

Figure C-46. Measured and calculated bulk concentrations in the steel phase, Heat 17.

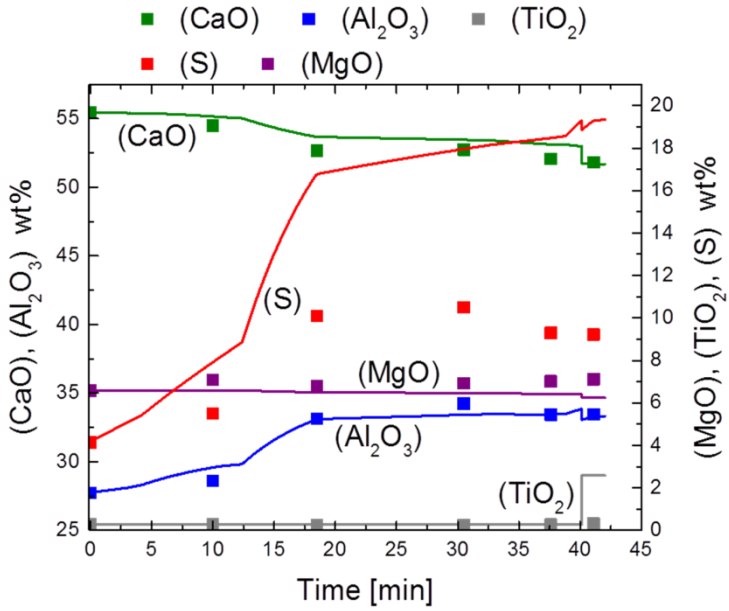

Figure C-47. Measured and calculated bulk concentrations in the slag phase, Heat 17.

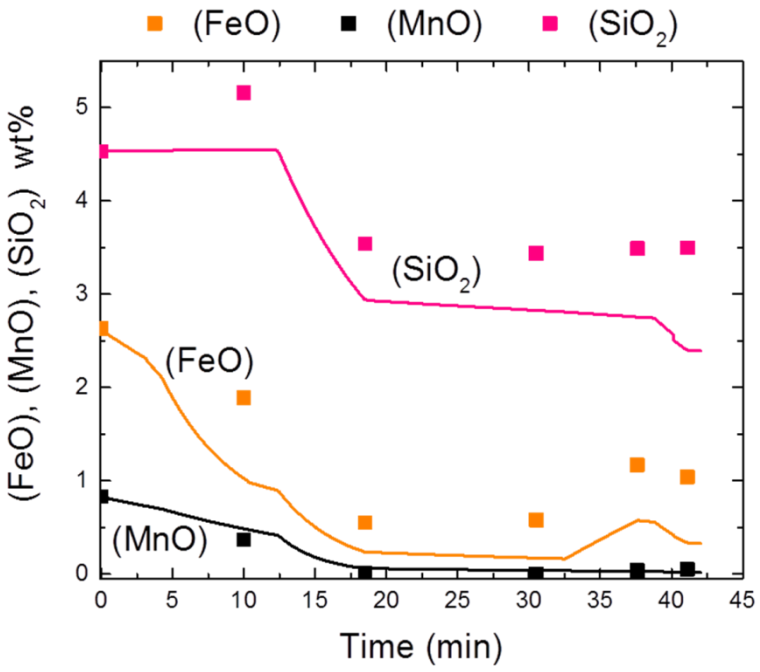

Figure C-48. Measured and calculated bulk values for FeO, MnO and SiO_2 in the slag phase, Heat 17.

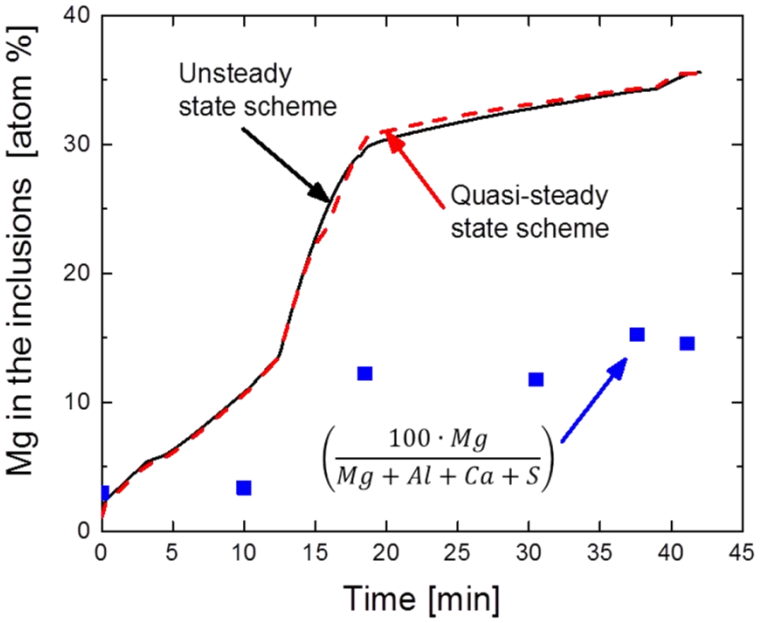

Figure C-49. Measured and calculated content of Mg in the oxide inclusions, Heat 17.

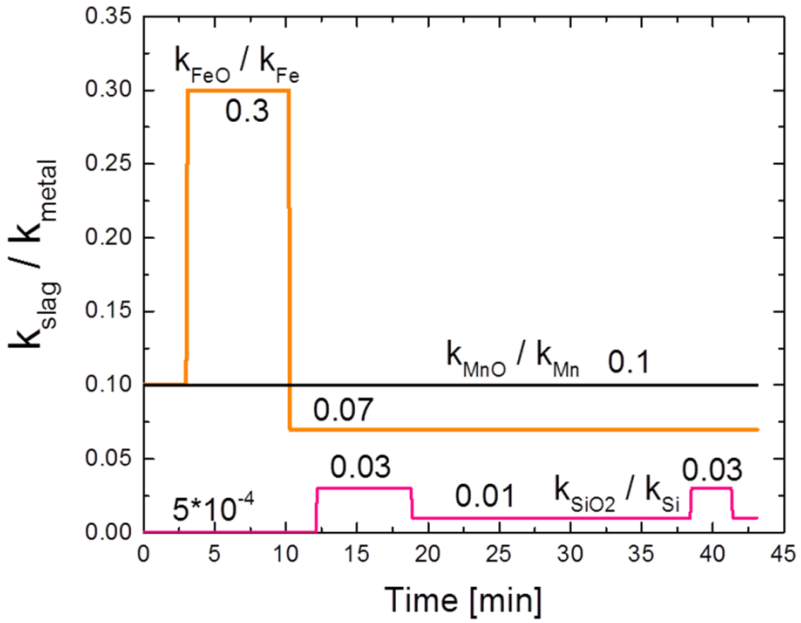

Figure C-50. Ratios of the slag mass transfer coefficients with the respective mass transfer coefficient of the species in steel, Heat 17.

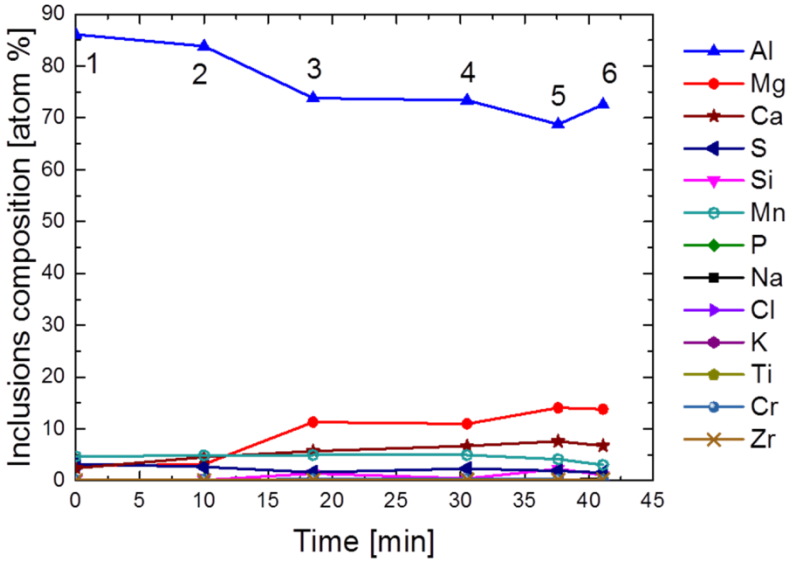

Figure C-51. Automated SEM analysis, average composition of the inclusions in atomic percentaje. Sample numbers during the course of Heat 17.

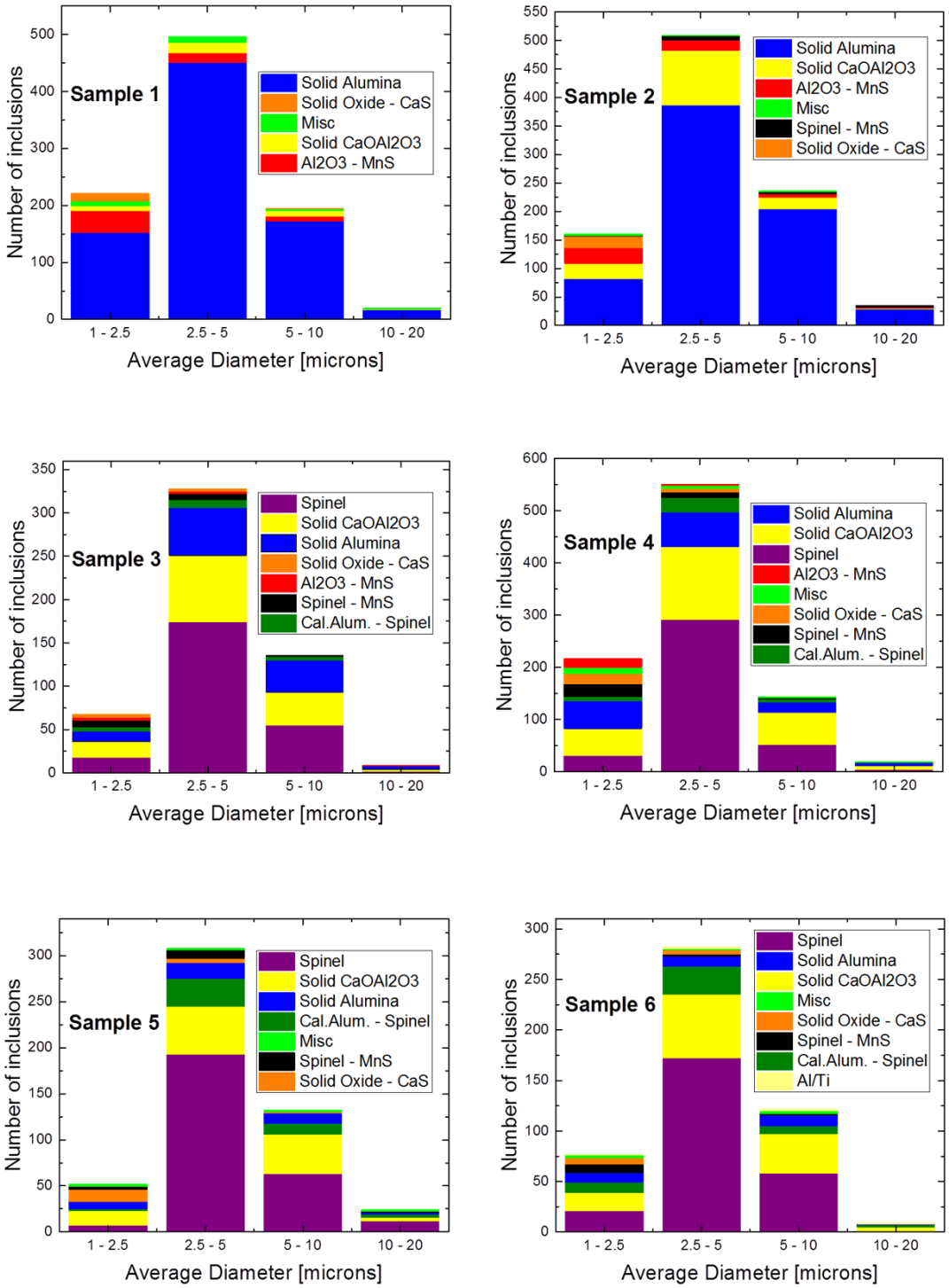

Figure C-52. Measured results from the automated SEM inclusions analysis. Number Distribution by average diameter (microns), Heat 17. Sample numbers correspond to Figure C-51.

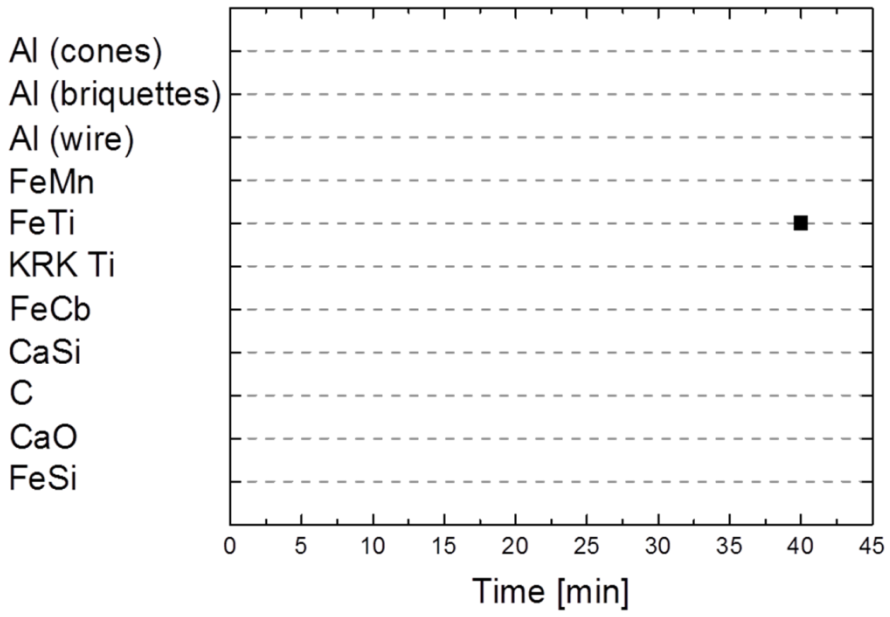

Figure C-53. Additions for the slag and steel during treatment in the LMF, Heat 17.

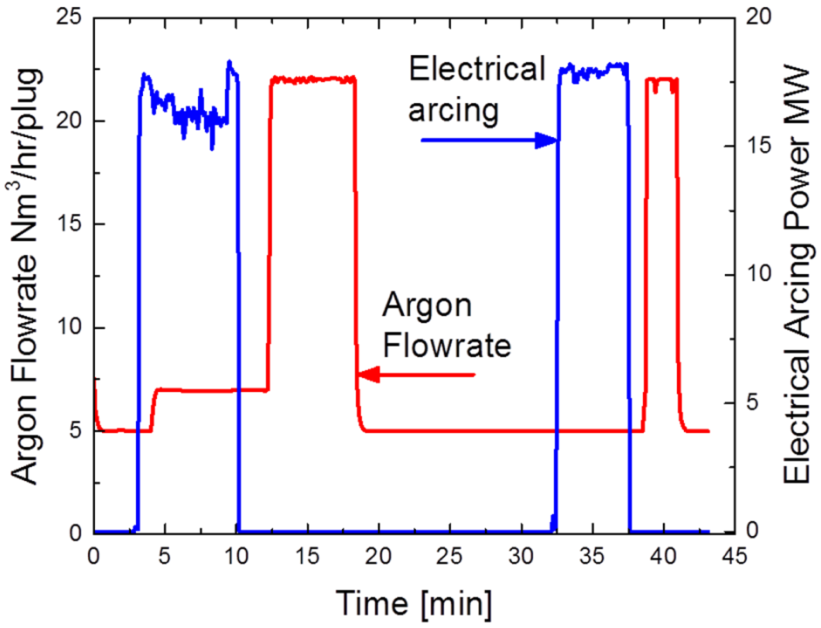

Figure C-54. Argon gas stirring and electrical heating during treatment in the LMF, Heat 17.

Heat 18

Initial steel mass	Estimation of initial slag mass	Initial Temp. for calculations
160752 Kg	2848 Kg	1592 K

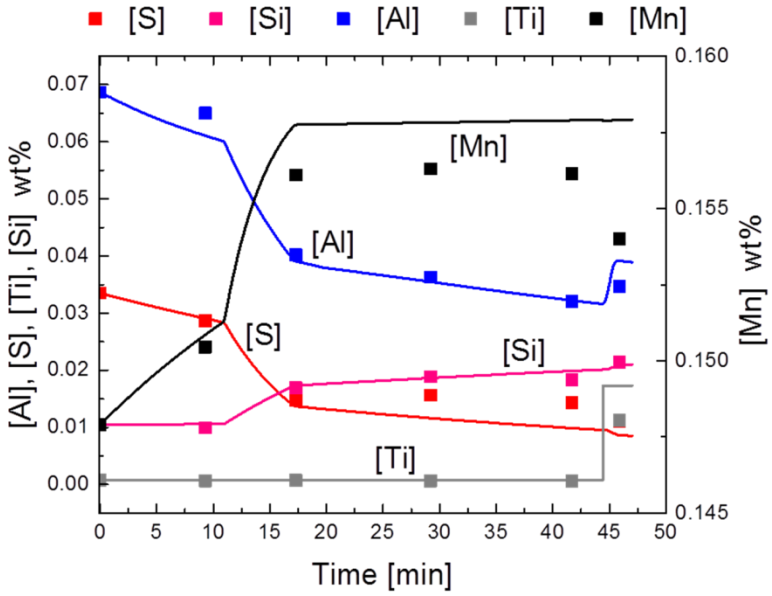

Figure C-55. Measured and calculated bulk concentrations in the steel phase, Heat 18.

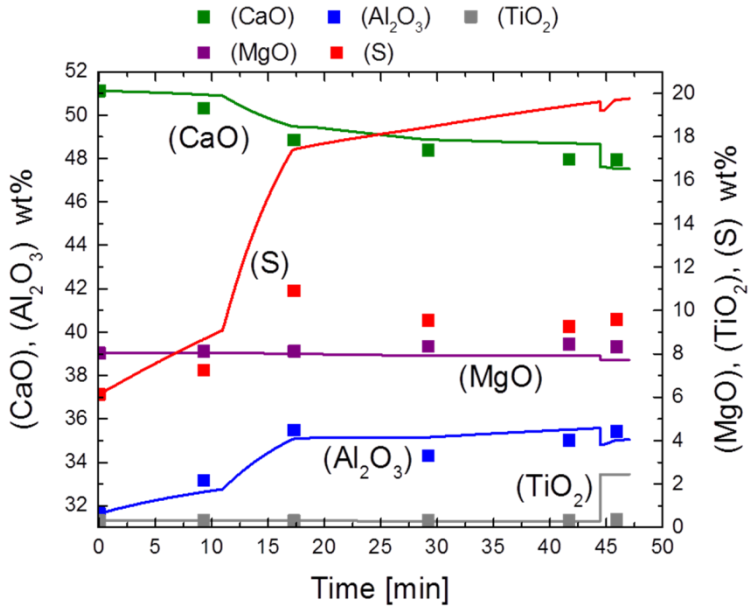

Figure C-56. Measured and calculated bulk concentrations in the slag phase, Heat 18.

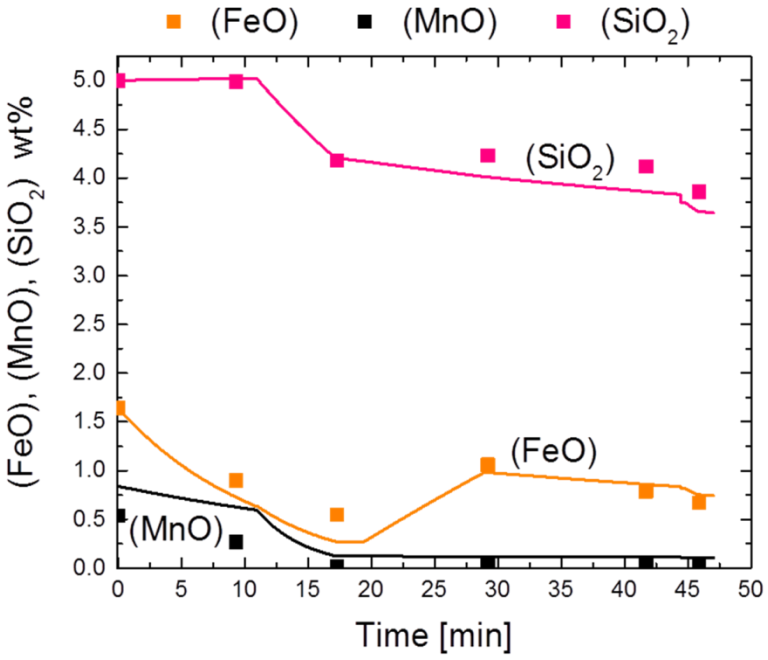

Figure C-57. Measured and calculated bulk values for FeO, MnO and SiO_2 in the slag phase, Heat 18.

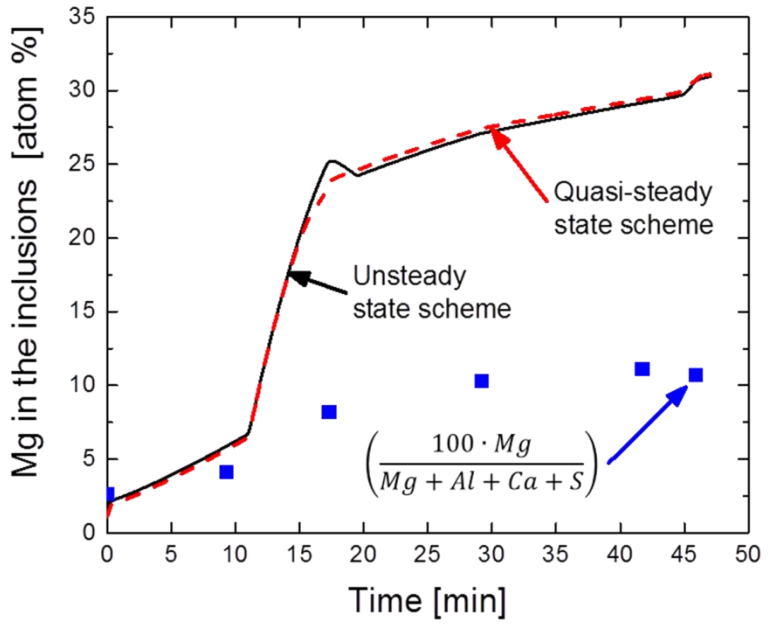

Figure C-58. Measured and calculated content of Mg in the oxide inclusions, Heat 18.

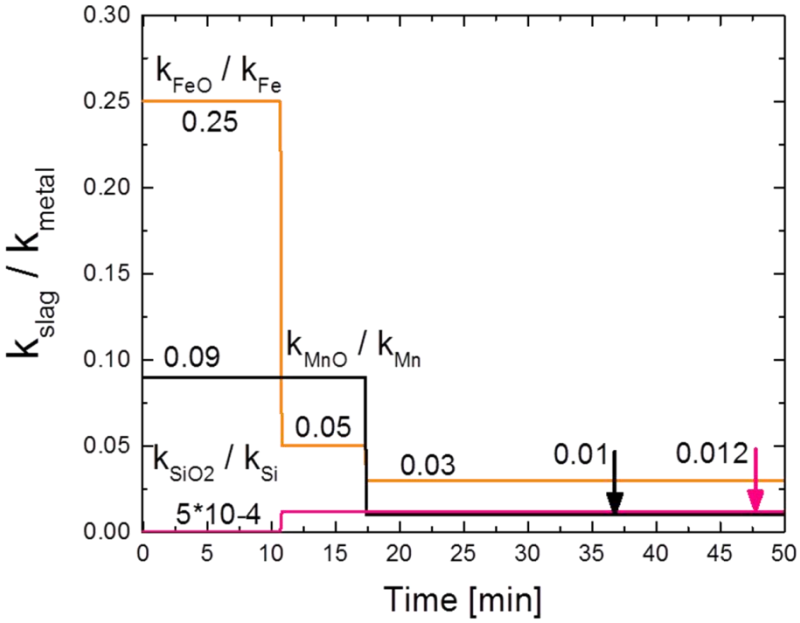

Figure C-59. Ratios of the slag mass transfer coefficients with the respective mass transfer coefficient of the species in steel, Heat 18.

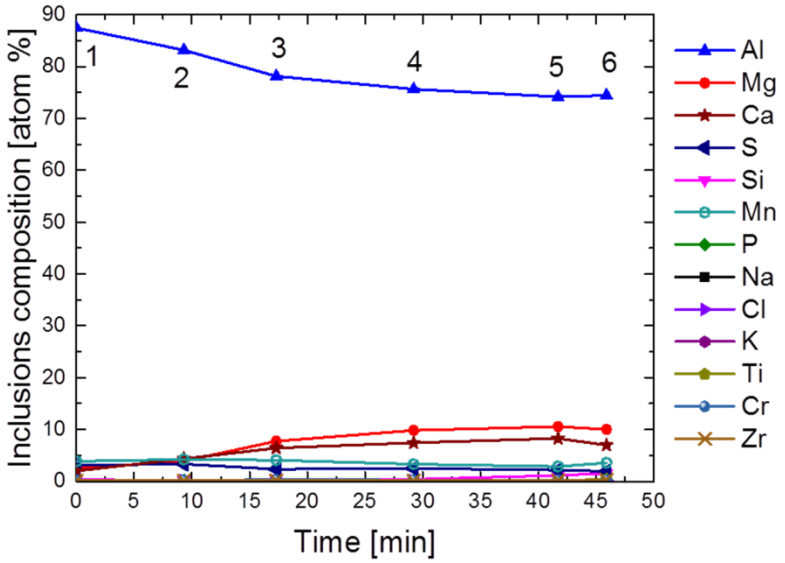

Figure C-60. Automated SEM analysis, average composition of the inclusions in atomic percentaje. Sample numbers during the course of Heat 18.

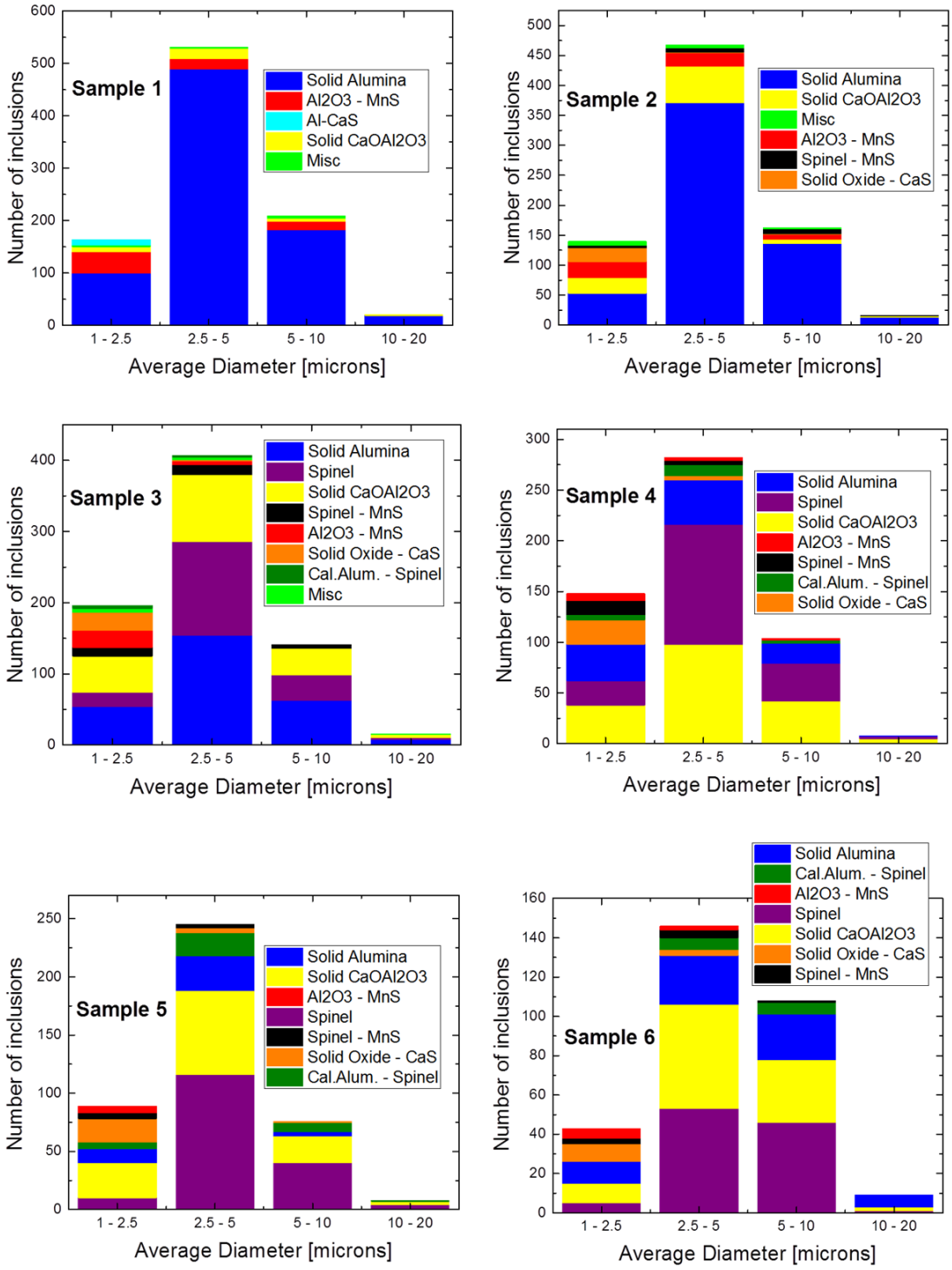

Figure C-61. Measured results from the automated SEM inclusions analysis. Number Distribution by average diameter (microns), Heat 18. Sample numbers correspond to Figure C-60.

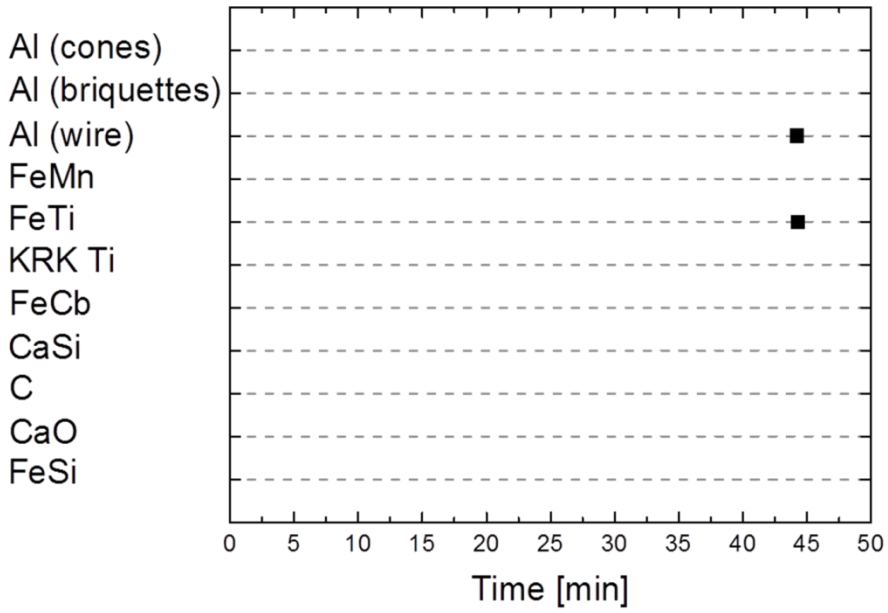

Figure C-62. Additions for the slag and steel during treatment in the LMF, Heat 18.

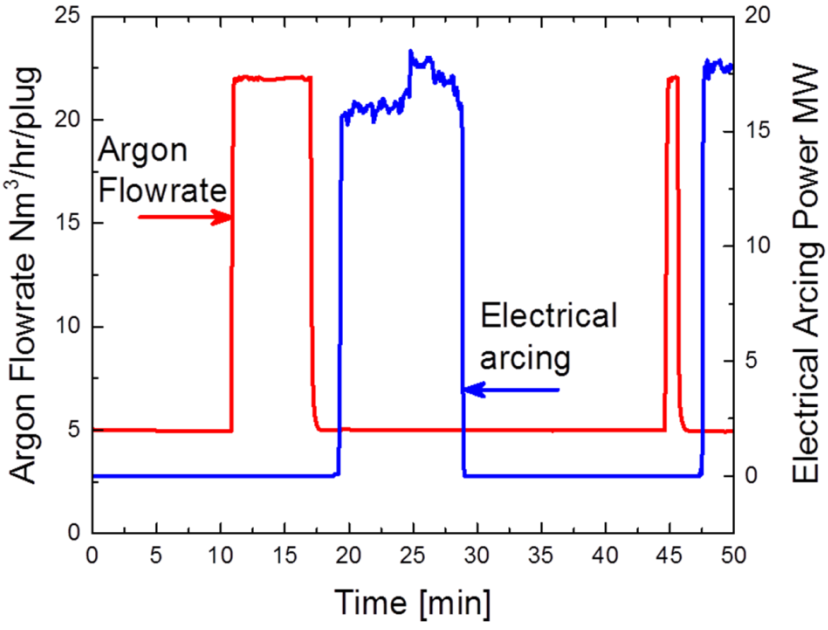

Figure C-63. Argon gas stirring and electrical heating during treatment in the LMF, Heat 18.